THE UNIVERSITY *of* EDINBURGH

Optical studies of diatomic molecules at extreme conditions

Veronika Afonina

Doctor of Philosophy
The University of Edinburgh
April 2018

Abstract

The formidable progress achieved in the research at extreme conditions led to important discoveries of many unusual and interesting physical and chemical phenomena. Materials with high compressibility were and still are of particular interest due to a significant reduction of volume which could result in unexpected changes of bonding and/or electronic properties. Among highly compressible materials simple diatomic molecules such as H_2, N_2, and O_2 are particularly interesting because they form new types of solids at high pressure.

Hydrogen, being the most abundant element in the universe, possesses simple electronic structure, therefore, the study of hydrogen systems is of special interest. In the last three decades, there were subsequently explored and described several high-pressure phases of hydrogen up to 400 GPa. However, there is still a vast area of unexplained effects, which requires further analysis.

The contributed work discusses Raman experiments in a wide pressure and temperature range where rotational and lattice phonon excitations have been measured in the Raman spectrum of solid H_2 and D_2 at 10, 77, 150 and 300 K from 2 to 180 GPa and up to 380 GPa at 300 K. Analysis of the Raman spectra allows to model how the rotational modes change with pressure and temperature and how the mass scaling laws evolve as the density increases in both hydrogen and deuterium. Comparison of vibrational frequencies of the isotopes appears to be extremely useful for estimation of equivalent pressures for both isotopes.

Nitrogen and oxygen are archetypal elements possessing unique features such as extremely strong triple bond in case of N_2 and magnetic moment in O_2 . Both N_2 and O_2 exhibit rich polymorphism, with additional phases of O_2 derived from its electronic and magnetic properties. N_2 /O_2 mixtures (for example, 20.9% O_2 and 78% N_2 mixture is air that we breathe) have been studied up to 12 GPa at

300 K experimentally and explored up to 500 GPa at 0 K theoretically. In the current project, N_2 /O_2 molecular systems are examined at 300 K up to 150 GPa. Rich polymorphism is observed, with seven phases exhibiting drastically different Raman spectra for concentrations below 45% of O_2 and a more stable area with three phases in the concentration range from 45% to 80% of oxygen at pressures above 12 GPa. Moreover, characteristic Raman spectra obtained for the mix with 25% O_2 after laser heating to approximately 2000 K at 25 and 96 GPa reveals pronounced peaks indicating the potential formation of new compounds.

Lay Summary

In order to understand behavior of complex materials, it is very useful to begin with exploration of simpler molecules, which are smaller in size and posses fewer electrons. The study of such simple diatomic molecules as H2, O2, N2, at conditions represented by extreme pressures and temperatures is of great importance for fundamental and applied sciences. Through advances in high-pressure experimental equipment and methods, experimentalists got access to studies of the changes of crystal structure of materials, induced by extreme conditions. Compression of materials results in decrease of distances between molecules, and valence electrons which are responsible for material's properties, interact with each other. And as a result of structural changes, caused by pressure increase, material obtains new properties.

In this work, simple molecular systems of hydrogen, deuterium and nitrogen/oxygen are studied in their solid phases at high pressures and extreme temperatures. High pressures are achieved by means of diamond anvil cells, low temperatures are reached in cryostat, and high temperatures are generated by laser heating. The present work consists of two projects, where one is focused on exploration of properties of hydrogen and its isotope deuterium, and the other is dedicated to investigation of nitrogen/oxygen mixtures. In the hydrogen and deuterium section we analyse behavior of the molecules under compression and at various temperatures. We observe that with pressure increase it is becoming harder for molecules of hydrogen and deuterium in solid phases to rotate freely, and they gradually freeze within the crystal lattice. On the other hand, in nitrogen/oxygen mixtures, exposed to high pressures and temperatures, we witness formation of many novel phases and compound, which have not been observed before. These phases can be characterised by new crystal structures, resulting in unique properties of the materials.

Declaration

I declare that this thesis was composed by myself, that the work contained herein is my own except where explicitly stated otherwise in the text, and that this work has not been submitted for any other degree or professional qualification except as specified.

(*Veronika Afonina, April 2018*)

Acknowledgements

I would like to record my thanks to all those who have helped me in the course of this work. In particular, the following:

Prof. Eugene Gregoryanz for his always positive support, wise guidance which gave me enough freedom to take decisions myself, encouragement throughout my studies, inspiring life stories and his patient attitude to all my other interests outside of science.

Dr. Ross T. Howie and Dr. Philip Dalladay-Simpson for their constant support, coaching, and assistance with experiments as well as precious help for acclimating to the new countries and new surroundings.

Dr. Miriam Pena Alvarez for her exceptional support, coaching and fruitful collaboration, all while being a great friend.

Dr. Xiao-Di Liu, Dr. Jack Binns, Dr. Mungo Frost, Robin Turnbull, Edward Pace for help and companionship through experiments and on the beamtimes.

Future Dr. Ryan McManus for heated debates about almost everything and help with English, Maths, Physics, and LaTex while introducing me to the world of quality films.

Dr. Uriel Urquiza for fueling my interest in science and research.

To the technical staff at the physics workshop who had to put up with job requests for the course of the work.

To SUPA for financial support.

To the Center for High-Pressure Science and Technology Advanced Research, Shanghai, China and Institute of Solid State Physics, CAS, Hefei, China for the opportunity to conduct some of my experiments in China.

To my big and cheerful (although a little bit nuclear) family, starting from my grandmother and finishing my younger brothers and sisters, and especially to my mother, Poe and Joe for their unfailing encouragement and support throughout, in the most difficult times.

Finally, to my friends from all-over-the-world, for still being with me, even separated by borders, time zones, and all our personal lives.

This thesis is dedicated to my father. Sometimes, even if I do not want to admit it, he knows what is right for me. Maybe because he loves all his big family so much.

Contents

List of Figures

List of Tables

Chapter 1

Introduction

With the volume change, that is the alteration of the density, occurring as a consequence of compression or temperature variation, atoms and molecules of the initial system come closer to each other and might be forced to change their location in the crystal lattice for more efficient packing. Exposure to extreme conditions can also result in the change of intermolecular or interatomic interaction. Phases with new arrangements of atoms or molecules exhibit new and often radically different characteristics. In the case when phases are formed by different elements, resulting structure might be dependent on the difference of the size and type of atoms and molecules as well as on the compositions of the phase. Research of polymorphism of materials at such extreme conditions as pressure and temperature is of great importance for various fields of investigation.

Studies of archetypal diatomic molecular systems such as H_2, N_2, and O_2 at high densities are of great interest both in fundamental physical/chemical and geo- and planetary sciences. Each of these pure elements, characterized by unique and diverse properties, has already been studied quite extensively experimentally and theoretically. On the contrary, there was just few research devoted to studying of nitrogen/oxygen system in spite of potential interest in this system due to the tremendously altered reactivity of nitrogen oxides by high pressures.

In the present thesis, studies of H_2, D_2, and N_2/O_2 systems in wide pressure and temperature range were conducted with the help of Raman spectroscopy. Raman spectroscopy is a very efficient method, which permits to investigate the pressure-

induced changes over a range of frequencies by measuring changes in relative positions and intensities in the Raman spectra. Raman spectra can be very informative for characterization of crystal structure and phase transitions through the rotational and vibrational selection rules which possess high sensitivity to the atomic sites depending on their symmetry as well as vibrational coupling and orientational ordering.

The contributed work consists of separate projects examining properties of molecular systems of simple diatomics employing optical spectroscopy. For the convenience of the reader, present thesis consists of seven chapters including this introductory chapter which are briefly outlined below. Each chapter is also divided into sections in order to organize information in a more structured way and finalized with a summary. Chapter 2 briefly introduces the experimental methods and technics applied in this project as well as gives a general background on Raman spectroscopy and Raman setup.

Chapter 3 serves as an introduction to molecular systems of hydrogen, nitrogen, oxygen and N_2/O_2 mixtures under compression at normal and extreme temperatures. This chapter comprises sections which separately review each molecular system.

Chapter 4 discusses the attempts to gain a better understanding of the nature of low-frequency excitations in hydrogen and deuterium and suggests the method of comparison of hydrogen and deuterium systems.

Chapter 5 details studies of the P-x phase diagram of the nitrogen/oxygen molecular system at room temperature and pressures up to 150 GPa. This experimental research leads to the design of the extended phase diagram of the N_2/O_2 system with the new phases observed for the first time in this study.

Chapter 6 focuses on the discussion of the high-temperature experiments with specific N_2/O_2 mixtures at pressures from 25 GPa to 96 GPa with the focus on novel phases and compounds, which have not been formed in previously published experimental research.

Finally, chapter 7 summarizes the main results and highlights questions important for further investigation.

Chapter 2

High pressure experimental survey

Studies of low-z molecular systems such as hydrogen, nitrogen, and oxygen under extreme conditions such as high pressure and extreme temperatures are of paramount interest and importance for modern science. The recent development of the experimental high-pressure techniques improved access to the exploration of unique behaviour of these systems. This chapter briefly describes the experimental techniques and methods used for high-pressure research, specifically applied at the current study.

2.1 High-pressure Techniques

2.1.1 The Diamond Anvil Cell and High-Pressure Lever Arm

Diamond anvil cells and experimental techniques with their application were developed in 1959. However, due to the difficulties with the pressure determination and temperature limitations, a significant amount of the research in this area appeared only in the last decades. Development of the *in-situ* cryogenic and laser heating methods together with various methods of spectroscopy radically

expanded the possibilities of the experimental study of deep planetary matter with extreme parameters. Devices with diamond anvil cell (diamond anvil cell DAC), developed in the late 1950's [Weir 59] are considered to be one of the most convenient and compact devices for the *in-situ* experiments aimed at the investigation of matter exposed to high pressure or extreme temperature jointly by the methods of infrared, Raman spectroscopy, X-ray diffraction, etc. [Eremets 96]. During the last few decades, the apparatus with diamond anvils became the most successful device for the creation of pressures above 400 GPa in the laboratory conditions [Dubrovinsky 15, Akahama 07] [Duffy 05, Dubrovibsky 07. A pressure of more than 1 TPa can be reached with the device with the two-stage design [Dubrovinsky 12, Dubrovinsky 15] in the range of temperatures from 0 K [Webb 76] to 7000 K [Boehler 00]. Principal scheme of the DAC is presented in Figure 2.1. Diamonds are glued to the supporting seats, which are installed on the opposite parts of the cell. A sample is confined to the sample chamber in the gasket, fixed between the diamonds.

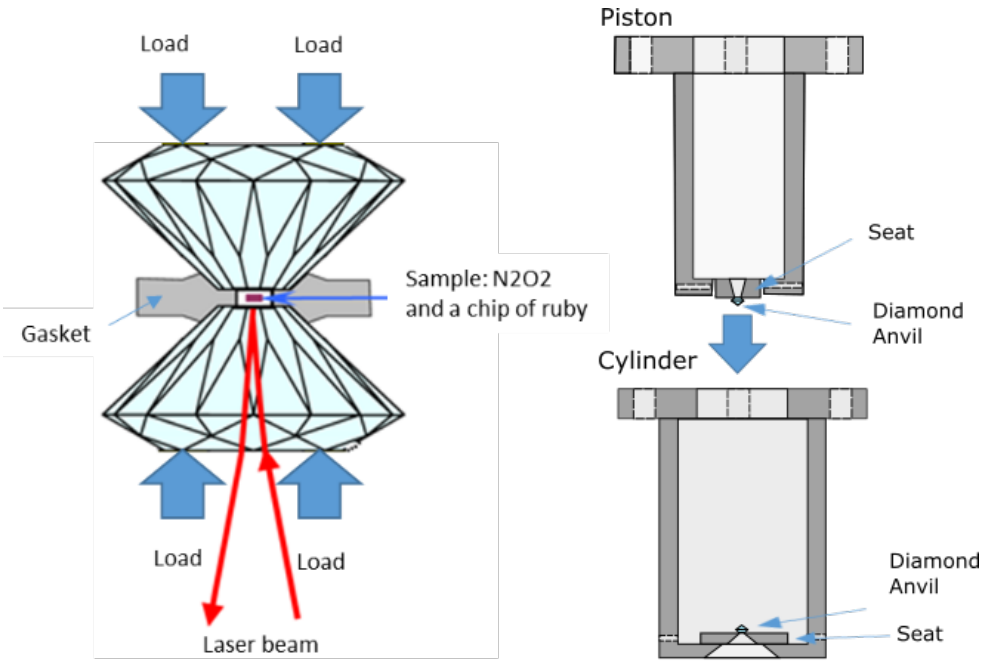

Figure 2.1 *Left: Standard diamond anvil cell schematics. Right: Diagram of Mao and Bell piston-cylinder type of DAC, middle section view. Dark grey areas represent solid, light grey areas are for openings. Dashed lines are for the threaded openings with screws.*

Diamond is the most common material for anvils due to its exceptional hardness and superior chemical inertness. Diamond is not the only material suitable for application in high-pressure devices. To date, some cheaper alternative materials are known, although inferior to diamond in the range of achievable pressures.

The most widespread among them are synthetic sapphire (Al_2O_3, moissanite (SiC), and fianit (cubic ZrO_2) [Wang 10, Xu 00]. Another important property of diamond apart from hardness is high transparency in the wide range of spectra which makes several types of research methods available for the study of materials at extreme conditions. In the case of Raman spectroscopy experiments, the diamond anvils must be ultra-pure, low fluorescence diamonds (usually type Ia), which are also suitable for X-Ray studies. To achieve highest strength, rough diamonds are polished according to the (100)-crystal orientation. For high-pressure experiments, beveled diamonds are normally used.

The best stability is offered by Boehler-Almax design introduced in 2004 [Boehler 04]. Nonetheless, this design is more expensive and requires usage of specific seats with precise dimensions. This construction assures optimized mechanical support of the crown, which allows significantly higher loads (see Figure 2.2 for comparison of different types) [Boehler 06]. Initially, high-pressure experiments for solid materials were conducted by squeezing materials directly between the anvils. However, this method is applicable only for solids, and besides, it has such a downside as significant pressure anisotropy. These issues were successfully solved by introducing gasket material between the anvils [Vincenzo 13].

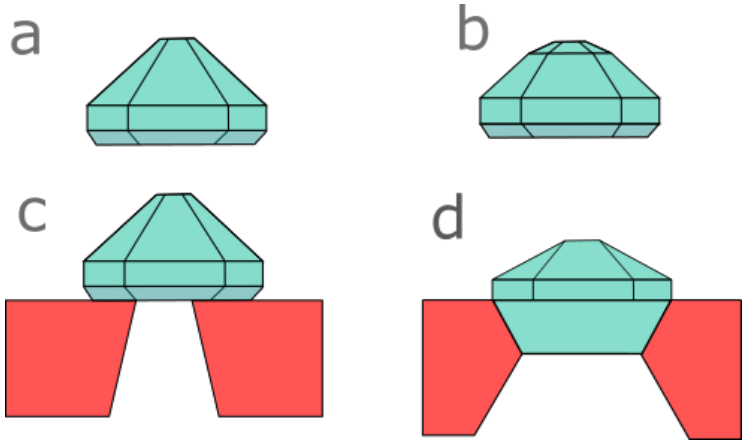

Figure 2.2 *Types of diamond culets and seats employed in the conducted experimental work. (a), (b)- standard and bevelled diamond tips respectively. (c), (d) - conventional and Boehler-Almax backing plates with different supporting geometries [Boehler 04].*

A gasket serves as the pressure transfer medium and seals a sample in the sample chamber. Choice of the gasket material is mainly dictated by such parameters as rigidity, plasticity and chemical inertness. For the high-temperature experiments, the thermal stability of the gasket is also of high importance. The gasket

withstands a huge pressure gradient changing from the minimum at the edge of the culet to the maximum at its centre. Usually, for the solid samples, the pressure transmitting medium is introduced into the sample chamber. It is needed to ensure that the sample is subjected to a hydrostatic pressure with the stress evenly spread all over the sample. Conveniently, when samples are loaded in the liquid or gaseous phases, it is possible to avoid using an additional medium. Nevertheless, upon compression, the pressure is transmitted through the solid medium as the sample solidifies. This requires supplementary measurements in different parts of the sample due to pressure anisotropy, inhomogeneity, and gradient [Shen 16]. The sample chamber is formed through a pulsed IR laser drilling method after preliminary indenting to approximately half of the desired pressure [Dunstan 89]. The thickness of the chamber is measured using interferometry and tailored to the experiment, usually 10% of the culet size. Therefore, the typical sample chamber is specified by the gasket thickness (usually from 30 μm to 6 μm for the diamonds with the culet size from 300 μm to 60 μm, 5-10% of the culet size) and the diameter of the central hole (usually 30-50% of the culet size).

High pressures can be generated in the cells of different construction, specifically designed for different types of experiments. The construction of the cell is crucial for the experiment, because in many cases the failure of the anvils occurs not because of the high stress, but due to the flows in construction of cells.

Among the popular types of DACs are Mao and Bell piston-cylinder DACs and their modifications [Mao 76] and Merrill-Bassett type cells [Merrill 74]. Merrill-Bassett type cells and their various modifications are very well suited for X-Ray diffraction measurements due to their small size, which allows to mount them on X-Ray setups. Mao-Bell type DACs possess high stability and versatility. Moreover, their application allows achieving pressures as high as 300 GPa. Cell design strongly depends on the specific application. For example, for X-Ray experiments size of the cell is crucial. For resistive heating experiments cell shape should allow to connect seats to the heating setup. Cryogenic experiments with the application of lever arm as a pressure control mechanism require cut piston-cylinder cells due to the size of the inner chamber of the cryostat.

There are several ways to control pressure in this type of DACs. The load on the cell, and therefore the force applied to the diamonds, can be controlled by several means. Firstly, that can be the screws which the cell is equipped with. The screws can be efficiently used at low pressures, especially when the sample

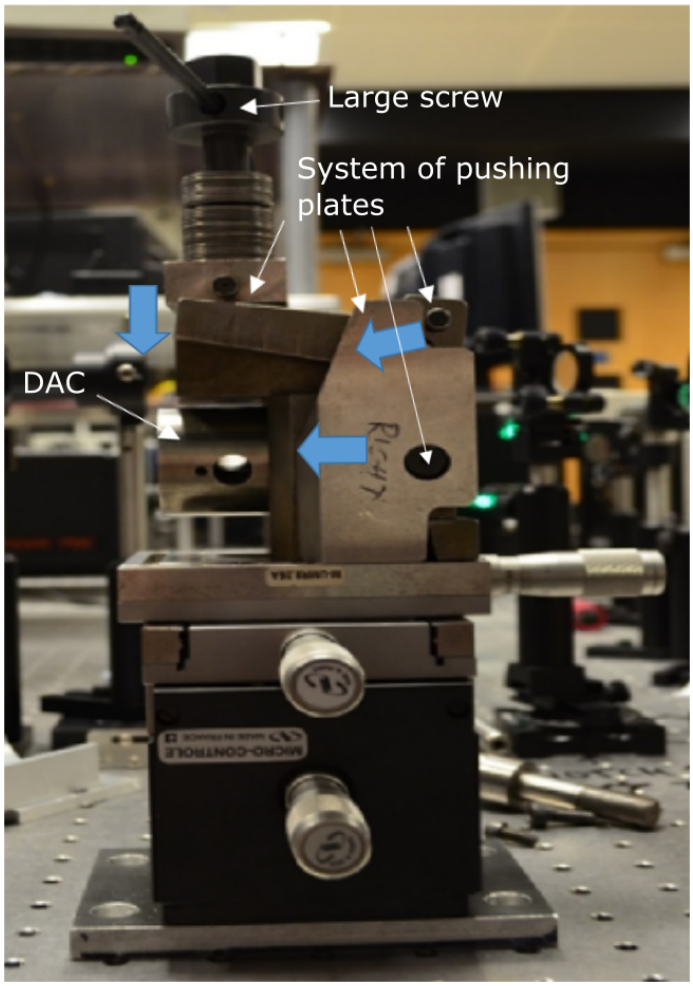

Figure 2.3 *Lever arm system at work.The Large screw pushes the system of pushing plates, which move the piston part of the cell (DAC) closer in the cylinder part (see blue arrows for the direction of the motion). Even distribution of pressure on the cylinder is achieved by engaging pushing plates.*

is still fluid. However, they do not apply load evenly through the cell. This can cause misalignment of the anvils and consequent loss of the sample. To achieve symmetric compression of the sample and very fine pressure control gas driven membranes can be applied [Letoullec 88]. Pressure membranes can be used with specifically designed DACs compatible with membranes. In our experiments with piston-cylinder cells we used an alternative method as external lever arm setup. This setup guarantees strictly translatory motion of the diamonds in the cell (Figure 2.5). Fine and precise pressure control can be achieved by engaging the large screw which then pushes a pushing plate, evenly distributing the load on all the sides of the diamond culets. The lever arm setup can also be employed in the low-temperature experiments in a cryostat with a system of external pressure control. This method was mainly used due to the application of the piston-

cylinder cells in our experiments.

In the experiments performed for this project, I used the custom in-house built modified Mao and Bell piston-cylinder type DACs. Due to the range of desired pressures from 5 to 150 GPa diamonds of standard design, modified brilliant cut, and Boehler-Almax design were used. Culet sizes ranged from 40 μm to 300 μm for the experiments aiming at pressures around 150 GPa and around 50 GPa respectively. Both rhenium and tungsten gaskets were used.

2.1.2 Gas loading and cryogenic loading

Gas loading has an advantage of loading gas mixtures without phase separation due to the compounds being well-mixed in the gaseous phase. The gas-loading method [Dalladay-Simpson 16, Mills 80, Rivers 08] can be described as clamping of precompressed to 1500-2000 bar gases in the gasket hole in the pressure vessel. The gas is pumped into steel "bomb" which contains the cell with the gearbox mechanism. The cell can be closed from outside. This method allows to obtain samples compressed to low pressures, around 0.1-1 GPa. This guarantees the stability of any other materials placed in the sample chamber, such as ruby ball or chip. One of the limitations of this method is compressor compatibility with the chosen gases; the gas-loading systems used in this study were hydrogen and deuterium-proof, but it was not possible to gas load N_2/O_2 mixtures with the high content of oxygen due to its explosiveness.

A simple alternative is to use liquid nitrogen cooling to liquefy gases inside the DAC. Cryogenic loading is sufficiently safer than gas loading. Yet, introducing liquid into the sample chamber can cause washing out other parts of the sample (as ruby calibrants), involve contamination or be a reason for not evenly mixed samples if loaded quickly from pure gases. This method is also limited by the temperature liquefaction of N_2 which condenses at 77 K and thus can be applied to gases and mixture with the boiling temperature above 77 K. The fundamental principle of its work will be described on the example of loading of N_2/O_2 mixtures. The DAC is placed in the copper pot, which is hermetically closed and steeped in a reservoir with industrial liquid nitrogen. The nitrogen gas then flows through a copper capillary wound round the pot and connected at the base, that allows an overpressure of gas in the pot. Once the DAC and the pot have reached the liquefaction temperature of nitrogen (77 K), the nitrogen

gas begins to liquefy. Upon reaching the desired level of liquefied nitrogen in the pot, gaseous oxygen is added. O_2 condenses immediately in the pot as a result of O_2 having a higher boiling point (90.2 K) than nitrogen (77 K). As soon as the pot is filled with N_2/O_2 mixture, it is opened, and the DAC is closed by the screws on the DAC assembly so that the sample is captured between the diamonds within the gasket hole. The DAC is then placed in a lever arm setup for further compression. The ratio of N_2: O_2 is calculated from the relative intensity of the molecular vibrational modes (vibrons) in the Raman spectra.

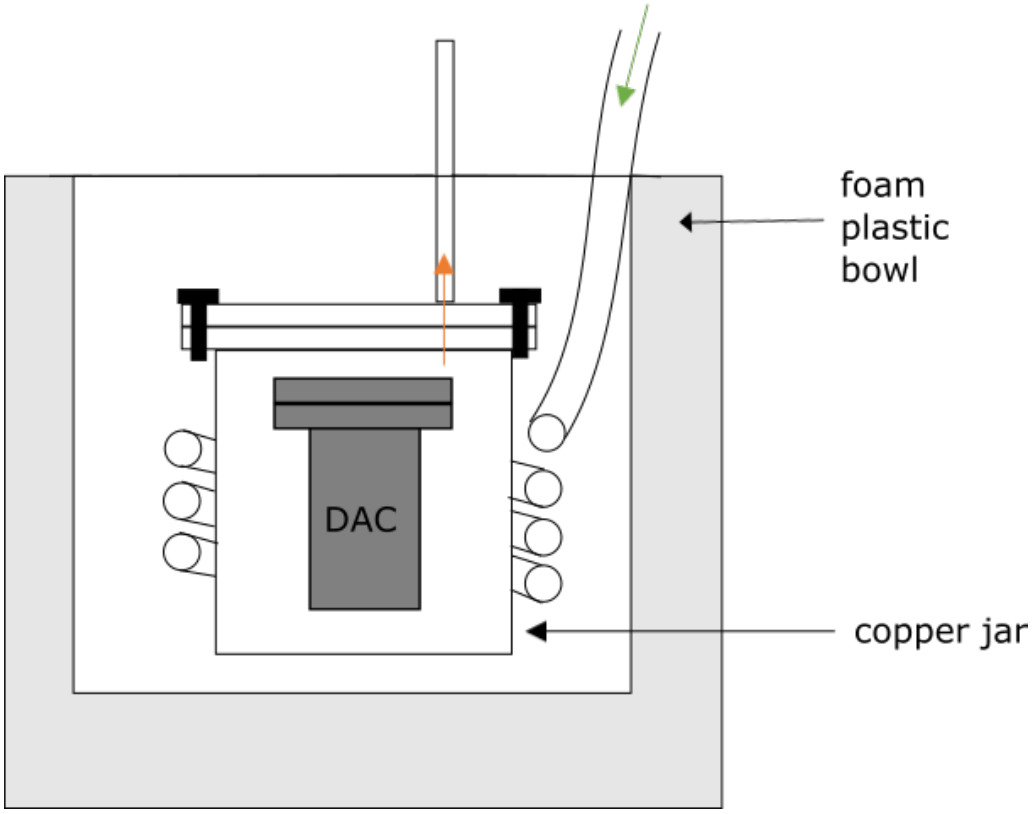

Figure 2.4 *Cross section schematics of the cryogenic loading setup. Slightly opened DAC is sealed in the copper jar, which is located in the foam plastic bowl filled with liquid nitrogen. Gas flows in the copper jar (green arrow), fills the jar and liquefies. Extra pressure is released through the outer pipe (orange arrow). When the liquefied gas fills the copper jar to the top, the jar is opened and screws on the DAC are tightened.*

Both methods were applied for the experiments discussed in the present work. Hydrogen and deuterium samples were only gas loaded. For nitrogen/oxygen samples both cryo-loading and gas-loading were applied.

2.1.3 Extreme temperature experiments

Extreme conditions are defined as hostile to human beings. Examples can be not only high pressures, magnetic fields, acidity, but also extremely low and high temperatures. The contributing work included both types of extreme temperature experiments.

Hydrogen and deuterium were studied in the range of temperatures from 20 K to 300 K. A vertically loaded He/N_2 flow custom built cryostat which allows conducting *in-situ* optical measurements from 300 to 5 K employed in the experiments was the same as in reference [Liu 17]. Experiments were carried out in the Key Laboratory of Materials Physics, Chinese Academy of Sciences, Hefei, China with the help of Dr. Liu. Generally, experiments in the cryostat are conducted in the following way. Once the sample is loaded, the DAC in the lever arm assembly is mounted in the cryostat. The chamber held under ultra-high vacuum is cooled by the heat-exchange gas (either N_2 or He depending on the desired temperature). During the experiment, the temperature is monitored continuously through the use of two sensors attached to the lever arm and rods of the cryostat. To minimize temperature variations, the temperature in the chamber is stabilized by adjusting heating and cooling settings and holding the sample for some time at stabilized conditions before obtaining Raman spectra.

Nitrogen-oxygen mixtures were studied at room temperature and temperatures close to 2000 K obtained by laser heating. Laser heating is a very powerful technique [Sanloup 13]. Two most common types of solid-state lasers are Nd: YAG (Nd^{3+}-doped yttrium aluminum garnet) or Nd: YLF (Nd^{3+}-doped yttrium lithium fluoride), and CO_2 gas laser. Application of the specific type of laser is dictated by the absorption of the sample. For example, ND: YAG and Nd: YFL emitting approximately at 1μm (1.064 μm for Nd: YAG and 1.053 μm for Nd: YFL) are usually employed for heating of metallic absorbers. Whereas CO_2 laser which generates emission lines in IR (10.64 μm) is more common for transparent materials, oxides, molecular systems.

In our experiments, sample heating is achieved by locally striking the surface of the material with high power laser, when sample absorbs infra-red radiation. But because diamonds have extremely high thermal conductivity, it is difficult to keep the temperature of the sample. Therefore, to reach temperatures above

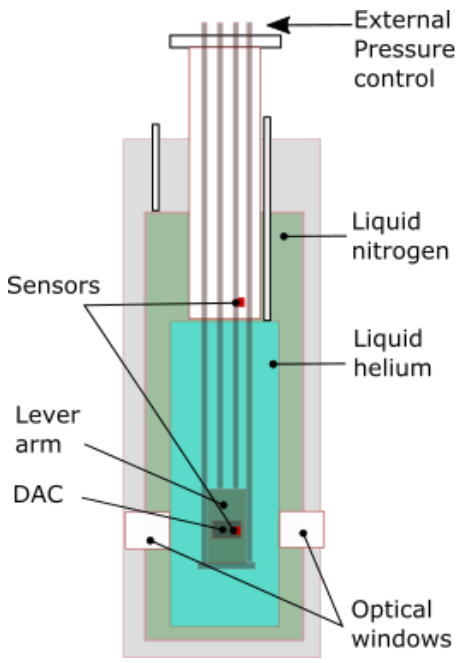

Figure 2.5 *Schematics of the He/N_2 flow cryostat. Such construction allows to achieve temperatures close to 5 K. Pressure control is executed via lever arm, placed in the vacuum chamber of the cryostat. The pushing plate of the lever arm is moved by engaging screws with the help of rods on the external pressure control. In this type of cryostat mainly shortened piston-cylinder cells are used. Attached sensors are used for temperature analysis in the chamber. Laser beam reaches sample in a DAC through the optical windows.*

1000 K high power lasers are required. A construction of laser setup with either a beam splitter or a second laser allows applying heating to both sides of the sample simultaneously to produce homogeneously heated areas across the sample. In case of transparent samples, such as N_2/O_2 mixtures, additional materials (Au and Ag) which act as a laser absorber and so convey heat to the transparent sample are used . Introduction of couplers in the sample chamber also ensures very local heating of the sample in the central area, preventing it from reaction with the gasket material. The laser spot size is usually between 10 to 40 μm. The laser heating experiments were executed in CSEC laboratory using Nd: YAG laser (λ = 1064 nm) and at BL10XU beamline of SPring-8 using the double sided-laser heating system with Nd: YAG laser and Nd: YLF laser [Yagi 01].

2.2 Vibrational Spectroscopy

Various methods of molecular spectroscopy are used for determination of the energy structure of atoms and molecules, which serve as fingerprints of specific elements and compounds. Molecular spectroscopy is based on the analysis of the spectral lines which appear as a result of the change of energy of a molecule, reflected by emission or absorption of a photon.

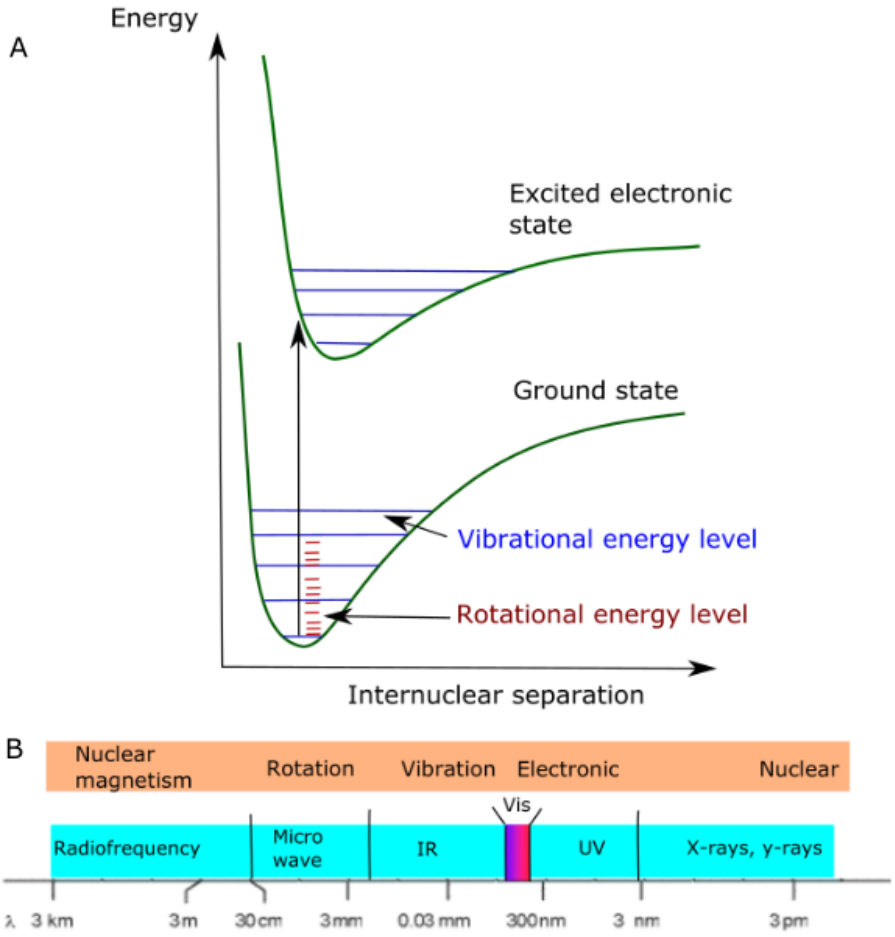

Figure 2.6 *A. Molecules are characterized by electronic, vibrational and rotational levels. Schematically, a molecule comprises two or more atoms, interacting via electrons on the outer shells. Separation between molecules is determined by the sum of all forces between the atoms. When the molecule receives some extra energy, atoms are excited and vibrate around equilibrium state. Therefore, radiation is emitted when atoms go from the excited state to a lower (ground) state. Molecules B. The electromagnetic spectrum and classification of the regions of spectra. Specific spectral regions identify different types of transitions that can be detected there.*

Energy of a molecule is dependent not only on its electronic state and transitions, but also on its rotational and vibrational states. Pure rotational spectra, for example, for the motion observed in hydrogen and deuterium in gaseous phase, are characteristic for gases. In order to analyze changes in rotational energy levels of molecules microwave and far-infrared spectroscopy is usually applied as well as Raman scattering. In the liquid and solid samples rotational motion becomes hidden by stronger vibrational motion.

Main methods of vibrational spectroscopy are Raman (scattering) and Infrared (IR) (absorption) spectroscopy. Raman and IR methods are generally complimentary to each other and have different selection rules. Vibrational Raman spectra can be obtained for the molecules which polarizability varies with the intramolecular distance. And vibrations are IR active when the molecular dipole moment varies with the vibration.

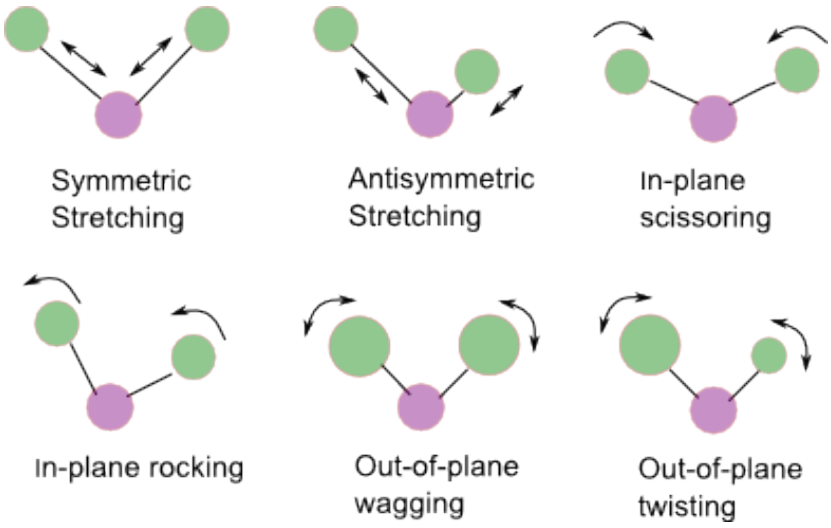

Figure 2.7 *Bonded atoms on a molecule vibrate around the equilibrium state. Some types of molecular vibrations are illustrated above. Stretching appears when the interatomic distance changes along the bond axis. Bending, which includes scissoring, rocking, wagging, and twisting is a change of the angle between two bonds.*

IR and Raman spectroscopic analysis of rotational and vibrational motion of molecules can be used for determination of the molecular structure. In case of analysis of the gas phase of small molecules, rotational spectra can give information about intramolecular bonds and angles, where usually the model of a free rotor is applied. Analysis of liquid and solid samples of diatomic molecules is based on the model of harmonic oscillator and helps to estimate the bond length as well as allows to obtain information about molecular symmetry and functional

groups. However, as can be seen on Fig. 2.6, actual behavior of the molecule deviates from the model, and anharmonicity becomes crucial. This results in such features on the Raman spectra as overtones [Gorelli 01], when transitions between higher vibration levels than fundamental are observed, or frequency turnover [Hanfland 92, Mao 94], when intramolecular distances decrease with compression to certain point and then increase again.

Generally, vibrations can be following types: symmetric stretching, antisymmetric stretching, bending, in-plane scissoring, rocking, wagging and twisting (Fig. 2.7). Depending on the changes of polarizability and dipole moment in a specific molecule, these vibrations can be IR and Raman active or inactive, which is determined by the shape of the molecule.

As long as the main method applied in the present project was Raman spectroscopy, further we will focus just on this method.

2.3 Principles of Raman Spectroscopy and description of Raman Setup

Raman spectroscopy is one of the principal tools for analysis of materials in chemistry, physics, and biochemistry allowing the execution of chemical analysis and facilitating the study of material structure and composition. Raman Effect was originally predicted by Smekal in 1923 [Smekal 23]. Experimentally it was discovered independently in 1928 by Raman and Krishnan in liquids [Raman 28a, Raman 28b] and Mandelshtam and Landsberg in crystals [Landsberg 28].

There are two possible approaches to explain Raman Effect. According to the classical model, substance possesses electrons which are kept together due to a number of forces, among which is Coulomb force. Thus, when an element is exposed to the impact of the electromagnetic wave, these electrons can be separated and then become oscillating dipoles which will emit with the frequency of oscillation. Thereby, when a molecule is irradiated by monochromatic light with the frequency ν_0, due to the induced electronic polarization, it scatters emission with the frequency ν_0 as well as with frequencies $\nu_0 \pm \nu_1$, where ν_1 is the oscillation frequency. Raman effect is built upon the polarizability of molecules, which displays the ability of electron cloud of a molecule to be affected by an

electric field. As a result of interaction with the molecule, the laser beam, which is an oscillating electromagnetic wave, induces an electric dipole moment:

$$\mu = \alpha E \tag{2.1}$$

where alpha is polarizability and E is applied electric field intensity. The frequency dependence of E is given as:

$$E = E_0 cos(\omega_0 t) \tag{2.2}$$

with the induced dipole oscillating with the frequency ω_0. Using these relations, the first equation can be reformulated in the form:

$$\mu_{ind}(t) = \alpha E_0 cos(\omega_0 t) \tag{2.3}$$

Due to the time dependence of the polarizability which comes from the internal motion of the molecule,the polarizability can be introduced as a sum of the time-dependent part and a constant

$$\alpha = \alpha_0 + \alpha_1 cos(\omega_{mol} t) \tag{2.4}$$

where α_0 is the constant term, α_1 it the amplitude of the oscillating term, ω_{mol}-angular frequency of the molecular vibration. Using trigonometric relations, one can derive:

$$\begin{aligned} \mu_{ind} &= (\alpha_0 + \alpha_1 cos(\omega_{mol} t)) E_0 cos(\omega_0 t) = \\ &\alpha_0 E_0 cos(\omega_0 t) + \alpha_1 \frac{E_0}{2} (cos((\omega_0 - \omega_{mol})t) + cos((\omega_0 + \omega_{mol})t)) \end{aligned} \tag{2.5}$$

In other words:

$$\mu_{ind} = \mu(\omega_0 t) + \mu((\omega_0 - \omega_{mol})t) + \mu((\omega_0 + \omega_{mol})t) \tag{2.6}$$

which implies, that the induced dipole moment fluctuates with three different frequencies, emitting radiation. First term $\mu_{ind}(\omega_0 t)$ accounts for Rayleigh scattering, second term $\mu_{ind}((\omega_0 - \omega_{mol})t)$ accounts for Stokes Raman scattering, and $\mu_{ind}((\omega_0 + \omega_{mol})t)$ accounts for anti-Stokes Raman scattering.

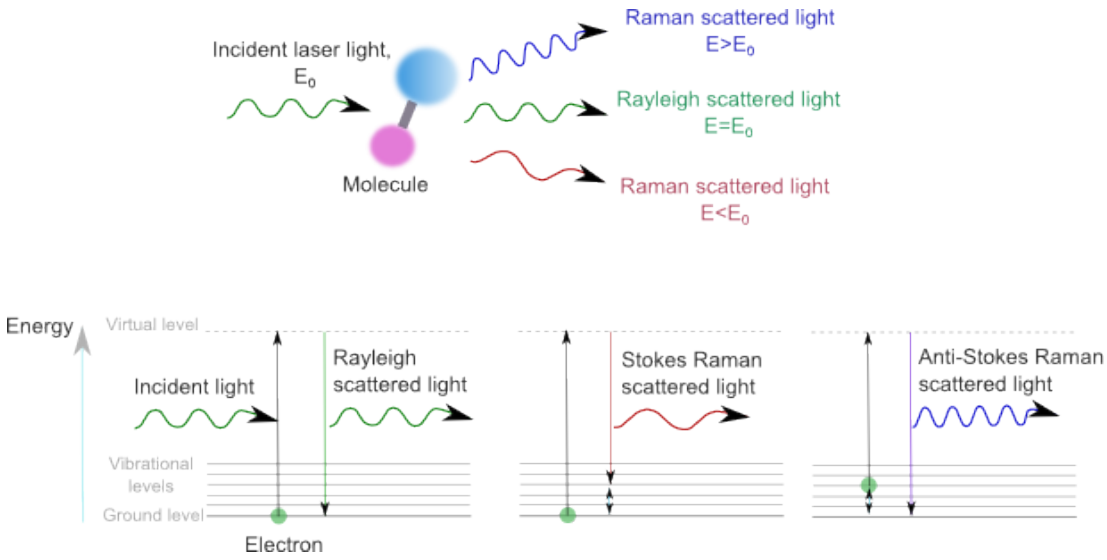

Figure 2.8 *Energy level diagram indicating the states involved in Raman signal.*

From the point of view of quantum theory, emission with frequency ν is considered as a flow of photons with energy $h\nu$ (h- Planck constant). When colliding with molecules photons are scattered. In case of elastic scattering, only the direction of movement will be changed, whereas energy of photon will remain unchanged (Rayleigh scattering). Otherwise, there will appear exchange of energy between photon and molecule after the collision. Moreover, a molecule, in this case, can both acquire and lose energy in accordance with the quantization principles, where ΔE is a residual of its allowed states. Hereby, for Stokes Effect photon frequency is lower than the frequency of incoming radiation, whereas Anti-Stokes photon is characterized with the higher frequency (Figure 2.8). The intensity of Anti-Stokes radiation is usually lower than the intensity of Stokes.

Although the position of the Raman peak on a spectrum is important for the further analysis of materials, a lot can be deduced from its shape. The width of the peak points at the level of crystallinity or the nature of interactions between atoms or molecules. The direction of the shift of Raman peak might indicate the

level of stress and compression of the crystal structure. The intensity of peaks is a good indicator of the composition of mixed or non-uniform samples.

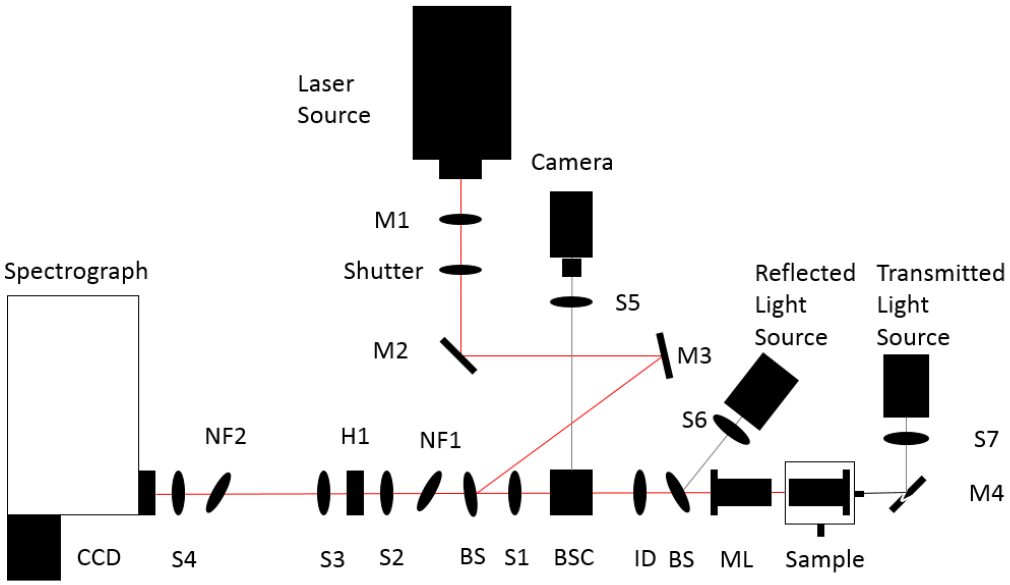

Figure 2.9 *Scheme of the typical experimental Raman setup. Laser beam is generated in the laser source. Laser beam then passes through the set of correction optics and filters. M1, M2, M3, BS are mirrors which uplift and redirect laser beam. S1, S2, S3, S4, H1, BSC, ML- correction optics for the laser beam, consisting of various lenses and filters. NF1 and NF2 -notch filters, serving for cutting off Rayleigh scattering signal. S6, BS, S7, M4- lenses and filers used for directing light from the reflected and transmitted light sources to the sample. Raman signal obtained from the sample eventually reaches the spectrograph and is recorded on the CCD.*

As a light source for Raman Spectroscopy lasers are typically used because laser light is generally monochromatic. Very narrow range of laser wavelength guarantees well-defined Raman bands. A sample is normally illuminated with a laser beam in the ultraviolet (UV), visible (Vis) or near infrared (NIR) range. In the experiments presented in this study, Argon-ion lasers with excitation lines of 488 nm and 514 nm and Krypton-ion laser of 647 nm are used. Owing to the small size of the focused laser beam, experiments can probe a tiny sample volume, e.g. high-pressure experiments with solid hydrogen required a sample size of 2μm -10μm.

A typical Raman setup is demonstrated in Figure 2.9 and normally has following structure: 1. Excitation source (laser); 2. Correction optics and filters; 3. Detector (CCD). On the schematics 2.9 is an imaging system, which consists of two light sources, focusing lenses and a video camera. One of the light sources

serves as a reflected light source which passes through the focusing lens SS, beam splitter BS, and Mitutoyo objective lens. Another light source is used as a source of transmitted light. A sample is illuminated with laser light, which comes from the excitation source through the mirrors for redirection and uplifting of the beam to the 50:50 beam splitter cube (BSC) after which the beam is pointed on the sample through the Mitutoyo long working distance objective lens (ML). The beam then passes towards the spectrometer through a spatial filter, consisting of two plano-convex spherical lenses (S2-focusing lens and S3-collimator) and pinhole (H1), which is located in the focal point of both lenses. As far as strong stray light from Rayleigh scattering can corrupt Raman scattering signal, a special filter should be used to avoid its influence by cutting off its spectral range. Normally, for this purpose two interference (notch) filters are used (NF1 and NF2). Finally, the laser beam is focused in the Spectrograph window with the help of the focal lens S4. Spectrum is then recorded in the CCD (charge-coupled device) which allow multichannel operations, resulting in Raman spectrum being detected in a single acquisition. Depending on the desired range, different gratings can be used. For example, in order to cover bigger area from 0 to 3000 cm^{-1} grating of 300gr/mm can be applied. And in order to obtain more detailed image with the higher accuracy, but in a smaller wavenumber range, normally 1800gr/mm is used. CCD is a very sensitive device, which needs cooling in order to obtain high resolution images. To achieve optimal quality of the obtained spectra, various techniques can be used. One of them is binning, which combines charges of the neighbouring pixels of the CCD, which results in the faster readout speeds and enhanced signal to noise ratio.

2.4 Pressure calibration

Although pressure can be estimated directly from the load applied to a specific surface, this method can potentially be used only at very low pressures. This method is not reliable when applied to piston-cylinder cells due to the friction between parts of the cell and internal friction associated with the solid-medium environment of the sample chamber together with the significant pressure gradients.

One of the most prolific methods for pressure determination in high-pressure experiments is the ruby fluorescence (Cr^{3+} doped Al_2O_3) calibration. Since

the fluorescence shift of ruby is pressure-dependent, pressure in the DAC can be determined by the calculation of $\Delta\lambda(P)$, which is the difference between initial and resulting wavelengths of ruby fluorescence. Ruby spectra at ambient pressure have two peaks (R1 and R2) with wavelengths of 692.7 nm and 694.2 nm respectively. Pressure dependence for ruby fluorescence was proposed by Forman et al. [Forman 72] and later described in details [Piermarini 75, Mao 76, Xu 86]. According to [Piermarini 75], in the range of pressures up to 29 GPa the R2 behaviour is linear and can be described by the following equation:

$$P = A\Delta\lambda \tag{2.7}$$

where P is a pressure (GPa), $\Delta\lambda(P)$ is wavelength shift (nm), and A is a constant of proportionality equal to 0.0274 GPa/nm. Under the pressures beyond 29 GPa fluorescence dependence on pressure becomes non-linear and follow relation:

$$P = 380.8[(\frac{\Delta\lambda}{694.2})^5 - 1] \tag{2.8}$$

Quality of the Ruby fluorescence spectrum also depends on ruby hydrostatical sensitivity. It means that pressure increase results in the reduction of the sample hydrostaticity, which will result in broadening of R1 and R2 lines. Consequently, this method cannot be applied at pressures above 100 GPa due to the significant broadening of the peaks and weak signal. Temperature correction is necessary for temperatures above 100 K where 6 K variation is equivalent to 1 kbar in terms of ruby fluorescence shift [Vos 91, Rekhi 99].

Pressure calibration via Raman mode of diamond phonon also can be applied for the high-pressure experiments. Diamond has two atoms per primitive unit cell and thus exhibits an optical phonon at frequency of 1332 cm^{-1} under ambient conditions [Robertson 30]. The pressure shift of the first order diamond Raman band was proposed in 1985 [Hanfland 85] and calibrated in several works with the latest of Akahama et al. calibrating up to pressures of 410 GPa [Akahama 10a]. According to their work, following expression quite accurately describes the dependence of the diamond mode on pressure up to 300 GPa which will be used in the current project:

$$P = A\frac{\Delta\omega}{\omega_0}[1 + \frac{1}{2}(B-1)\frac{\Delta\omega}{\omega_0}] \tag{2.9}$$

where P is pressure (GPa), ω_0 is the edge frequency at ambient pressure, which was determined as 1333 cm^{-1}, A and B are the frequency constants, equal to 547 GPa and 3.75 respectively. Temperature correction for this method is not known.

Another pressure calibration method, proposed recently, is based on hydrogen and deuterium vibron frequencies as pressure sensors [Howie 13]. As is evident from the method, it can be applied only for pure hydrogen and deuterium experiments. However, temperature influence is not considered there. Therefore there is still a chance for discrepancies in pressure estimations.

Chapter 3

Review of pure H_2, N_2, O_2 molecular systems and N_2/O_2 mixtures at extreme conditions

3.1 Introduction. Molecular systems.

Low-z molecular systems are among the most abundant in the solar system. Depending on their complexity, molecular materials exhibit a variety of interactions between atoms - from weak intermolecular interaction (such as Van der Waals, hydrogen bonding, quadrupole interaction) to strong covalent, ionic (Coulomb forces) and metallic type [Hemley 00]. The main difference between molecular and non-molecular solids is the strength of the bond and electronic characteristics such as delocalization of electrons [Fahlman 11]. Compared to non-molecular crystals based on ionic or covalent bonds, molecular crystals are "softer" in terms of isothermal compressibility, and thermal expansion arises from the weaker interaction between the molecules [Hemley 00]. Pure molecular solids are insulators, yet by doping they can become conductive. In hydrogen, quantum effects play a paramount role, whereas in the systems of heavier diatomics such as nitrogen and oxygen quantum effects are significantly reduced (including orientation ordering and coupling to electronic excitations). Hence, the dynamics in such systems can be treated using classical theory [Hemley 00]. In the present chapter, systems of pure hydrogen, nitrogen and oxygen at extreme conditions

will be described in details. In addition to that, there will be a summary of research conducted on binary nitrogen /oxygen system and study of its phase diagram as well as an outline of nitrogen oxides exposed to extreme temperatures and high pressures.

3.2 Hydrogen and Deuterium

Hydrogen is the simplest element, which possesses a range of unique properties. The hydrogen molecule is formed by exchange interaction. Hydrogen atoms are separated by approximately 0.74 Å. One of the hydrogen isotopes is deuterium, which has similar properties but has a mass greater by a factor 2. Molecular hydrogen exists in two spin modifications - as ortho and para hydrogen. Ortho-hydrogen has parallel nuclei spins with total nuclear spin I=1 and can have only odd rotational states with quantum numbers J, m, whereas, for para hydrogen with I=0, spins are aligned antiparallel and rotational states are even [Silvera 80]. Graphically, molecular rotational energy states for ortho and para species in hydrogen and deuterium are represented in figure 3.1. At normal temperature ortho to para ratio is 3:1 for hydrogen and is 1:2 for deuterium. Such difference occurs as a result of isotopic difference between hydrogen and deuterium. In hydrogen, the triplet orthohydrogen state has a total nuclear spin I=1, with the three values of M_I=1, 0, -1. Therefore orthohydrogen has a nuclear spin degeneracy of three. Whereas singlet parahydrogen state is characterized with the nuclear spin quantum numbers I=0, and M_I=0, with the spin degeneracy of one. On the other hand, in deuterium spin of nucleon I_N=1 (whereas in hydrogen I_N=1/2). Therefore ortho deuterium has a total nuclear spin I=0, 2, and para deuterium has a total nuclear spin I=1 [Silvera 80].

While conversion from ortho to para hydrogen for isolated molecules is forbidden, it can occur in solids. The conversion rate is strongly dependent on isotope and can vary with pressure and temperature [Silvera 80].

Previous research gives detailed theoretical information about hydrogen and its isotopes. Thus, Kolos and Wolniewicz [Kolos 68a, Kolos 68b, Wolniewicz 66] calculated vibrational and rotational excited states for H_2, HD, and D_2. The fundamental vibrational excitations of hydrogen are intramolecular stretches (vibrons), intramolecular rotations (rotons), lattice vibrations (phonons). Rotational energies show very week dependence on pressure, whereas molecular vibron is characterized by strong pressure dependence. Because of the various nature of excitations, their relationship in two isotopes is also different. Proceeding from the fact that rotational bands are modeled as a free rigid motor with energy levels:

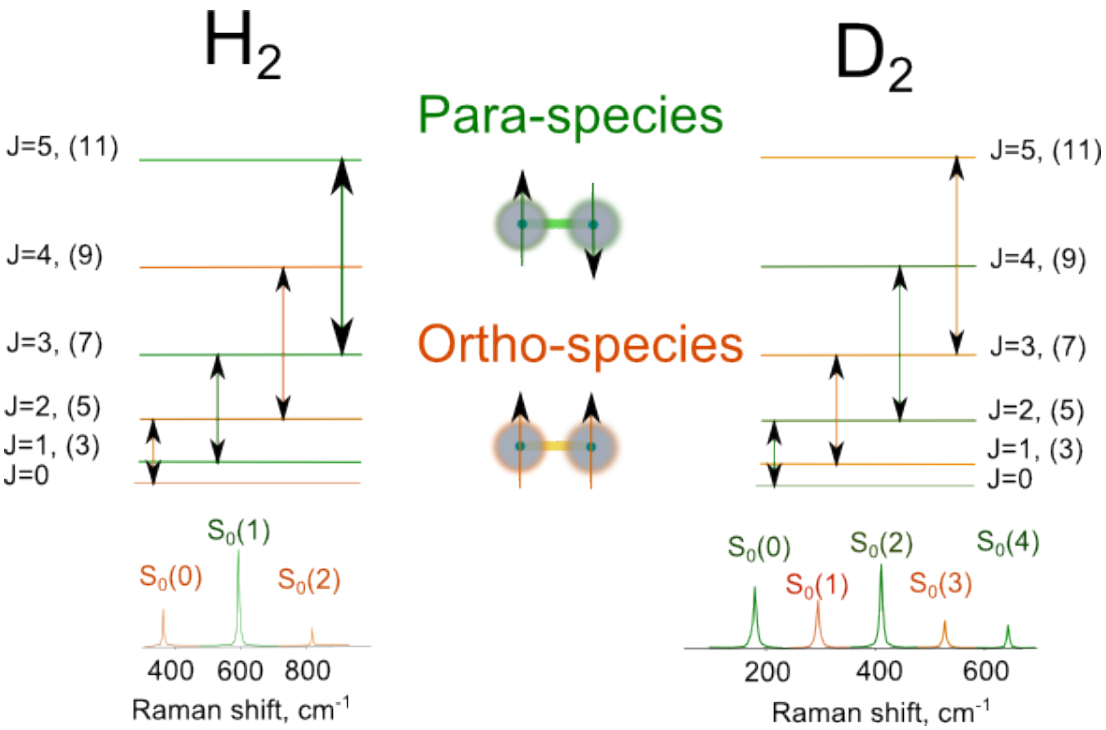

Figure 3.1 *Schematic representation of the molecular rotational energy levels and corresponding Raman spectra in the unbound hydrogen and deuterium molecules. Green represents allowed levels for para-species, while orange is for ortho-species. A number in parenthesis indicates the m degeneracies. Differences between hydrogen and deuterium are due to the larger moment of inertia in deuterium and total nuclear spins, i.e., I=0, 2 for o-D_2 and I=1 for o-H_2, while I =1 and I=0 for p-D_2 and p-H_2 respectively.*

$$E_J = BJ(J+1) \tag{3.1}$$

with rotational constant

$$B = B_{H_2} = \frac{h^2}{\mu r^2 8\pi^2} \tag{3.2}$$

where $\mu = \frac{m_1 m_2}{(m_1+m_2)}$ - reduced mass, h - Planck constant, r - distance between molecules, and therefore

$$B_{H_2} = 2B_{D_2} \tag{3.3}$$

On the other hand, phonon bands represent harmonic oscillation with natural

frequency:

$$\nu = \frac{1}{2\pi c}\sqrt{\frac{k}{\mu}} \tag{3.4}$$

with k - force constant, and μ - reduced mass. Due to the mass difference of isotopes the relation between their reduced masses can be introduced as:

$$\mu_{H_2} = 0,5\mu_{D_2} \tag{3.5}$$

Taking equation 3.3 and successively substituting into 3.2 and 3.1, while substituting 3.5 into 3.4, the following ratios for change of rotational energy (3.6) and vibrational frequency (3.7) of isotopes can be obtained:

$$\frac{\Delta E_{H_2}}{\Delta E_{D_2}} = 2 \tag{3.6}$$

$$\frac{\nu_{H_2}}{\nu_{D_2}} = \sqrt{2} \tag{3.7}$$

Interestingly, that even using the theoretical vibron frequency values at ambient conditions (P_0), $\nu_{D_2}(P_0)$ =2993.96 cm^{-1} and $\nu_{H_2}(P_0)$=4162.06 cm^{-1} [Kolos 68b, Kolos 68a], the ratio differs to $\sqrt{2}$:

$$\frac{\nu_{H_2}(P_0)}{\nu_{D_2}(P_0)} = \frac{4162.06}{2993.96} = 1.39 \tag{3.8}$$

These ratios are very useful for analysis of the type of the observed excitations, as it will be shown in the following chapters.

The phase diagram of solid hydrogen under compression, shown in figure 3.2, has been extensively studied both theoretically and experimentally. Phases I, II and III, which are characterized by weak intermolecular and strong intramolecular interaction evolve into layered phases IV, IV' and V with increased strength of intermolecular interactions and weakened intramolecular bonds [Mao 94]. Phase

I is considered to be a quantum molecular solid with hexagonal close-packed structure with freely rotating spherical molecules [Hazen 87]. Its Raman features include broadened rotational modes, E_2g phonon, and vibrational mode. Due to temperature and pressure broadening, rotational bands are most clearly defined at low pressures and low temperatures. The lowest energy bands are associated with $S_0(0)$ (ΔJ =2, J=0) and $S_0(1)$ (ΔJ=2, J= 1) rotational transitions [Silvera 80, Hemley 90]. Curiously, the first peak was shown to be split into three components due to the influence of the crystal field of hexagonal structure on $M_j = \pm 1, \pm 2, 0$ sublevel transitions [Van Kranendonk 83]. Under compression, the frequency of rotational modes slightly increases. As a result of the high sensitivity of experimental data to the conditions of the experiment and significant broadening of the peaks, interpretation of experimental results differs quite a lot in the publications by different research groups. For example, works by Hemley et al. and Mazin et al. [Hemley 90, Mazin 97] suggested hydrogen $S_0(0)$ peak consisting only of two contributions at pressures above 25 GPa. On the other hand, fitting $S_0(0)$ peak with three contributions of hydrogen is proposed at pressures below 25 GPa and 4 K [Hemley 90], and only with one contribution for deuterium in the pressure range from 0 to 150 GPa at 77 K [Hemley 93].

E_{2g} phonon persists to high pressures and demonstrates strong pressure dependence [Hemley 90], which implies that molecular solid does not undergo any major structural transformations. As for vibrational mode, it shifts continuously with pressure, although experiencing turnover around 40 GPa, related to the weakening of intramolecular bonds with increasing role of intermolecular interactions.

At temperatures below 150 K and pressures from 20 to 110 GPa hydrogen and deuterium transform to a broken symmetry phase with restricted molecular rotations [Silvera 81, Lorenzana 90, Mao 94, Goncharov 11] which occurs upon the orientational ordering of the molecules. Crystal structure remains hexagonal [Goncharenko 05]. Importantly, I to II phase transformation strongly depends on the spin of the molecules, in other words, on the proportion of para to ortho species as well as isotopic mass. In pure para-hydrogen transformation is delayed to about 110 GPa, whereas in the mixed state it occurs at about 60 GPa. Transition in deuterium happens even earlier, at approximately 20 GPa. Recently proposed new phase II' is unique for deuterium [Liu 17]. Its presence was attributed to lower zero-point energy and stronger intermolecular interactions. Phase II is characterized by rich low-frequency Raman spectra, with notable differences between isotopes. Above 150 GPa phase I and II exhibit

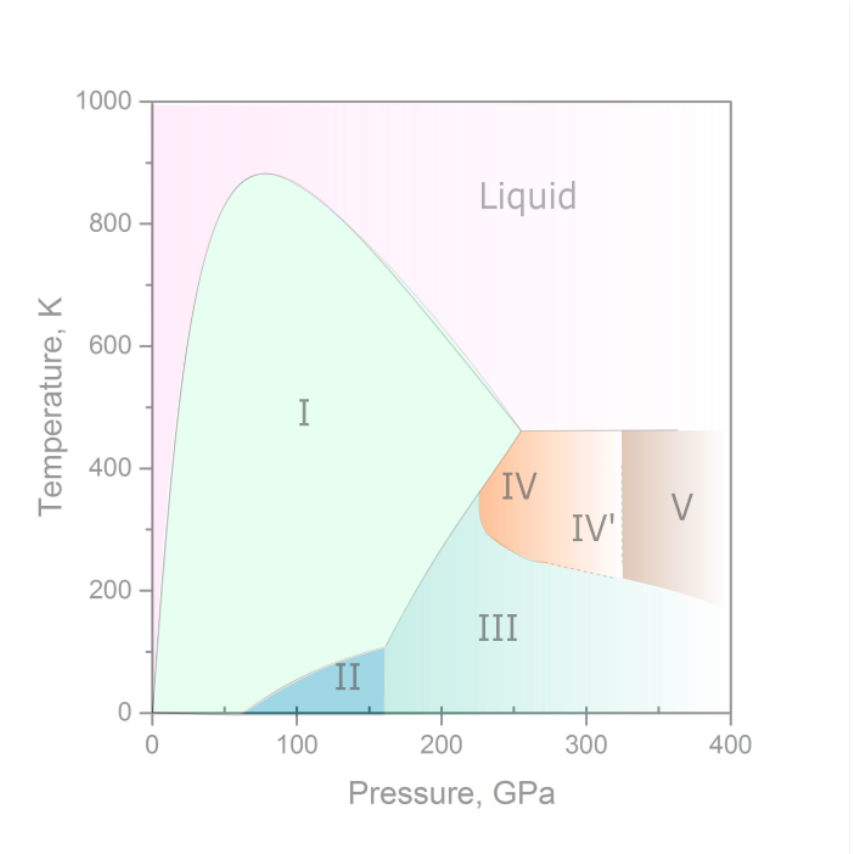

Figure 3.2 *Schematic representation of the phase diagram of hydrogen [Dalladay-Simpson 16]. Deuterium undergoes similar transformations, although shifted in pressure.*

transformation to hexagonal phase III almost simultaneously for both isotopes, which points at its classical nature [Akahama 10b, Mazin 97]. Phase III is beyond the scope of this study.

Theoretical calculations proposed $P6_3/m$ structure for phase I [Pickard 07], $P2_1/c - 24$ structure for phase II and $C2/c - 24$ structure for phase III [Drummond 15].

At temperatures above 300 K and pressures above 220 GPa, phase I and II alternate to layered phases IV, IV' and V [Howie 12b, Howie 12a, Dalladay-Simpson 16]. Transitions are characterized by the change of slope of ν_1 vibrational-mode with respect to pressure and its considerable broadening, which are accompanied by the appearance of well-defined low-frequency modes and second vibrational mode [Howie 12b, Dalladay-Simpson 16]. Theoretical studies predicted layered Pc structure comprising rings with six atoms and freely rotating molecules [Pickard 12]. Phase IV' features additional low-frequency mode and change of

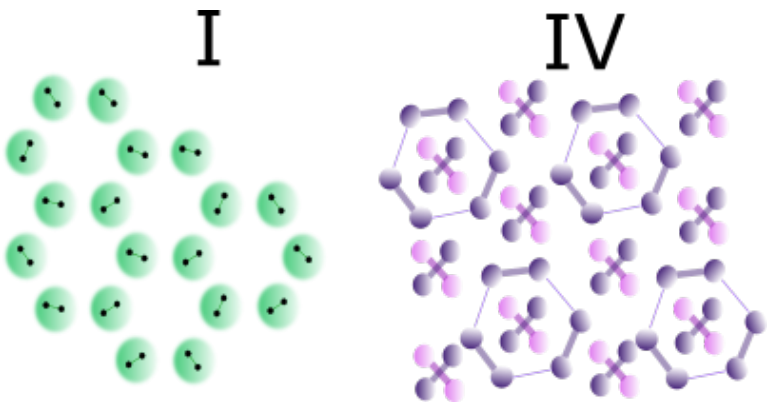

Figure 3.3 *Examples of potential structures of hydrogen and deuterium. Phase I is characterized by freely rotating molecules, whereas phase IV presumably comprises a layered structure with the freely rotating molecules between the layers.*

gradient of the frequency of ν_1 mode with respect to pressure, with other features similar to phase VI. Therefore, phase IV' most likely structurally resembles phase IV. Weakening of the vibrational Raman modes, change of the slope of the ν_1 frequency-pressure curve and arguable disappearance of low-energy band L3 mark transformation to phase V. Due to significant pressure shifts observed in hydrogen and deuterium to achieve similar phases, phase V of deuterium has not been documented yet. Phases IV, IV', V were interpreted as mixed molecular and atomic state, with phase V being a precursor to a non-molecular state.

3.3 Nitrogen

Nitrogen forms an archetypal diatomic molecule with a triple bond. The triple nitrogen bond is one of the strongest known (dissociation energy of 226 kcal/mol, with only 38 kcal/mol for single N-N bond)[Vincenzo 13]. Polynitrogen compounds where nitrogen atoms are bound by single or by single and double bonds are highly unstable. There was extensive research on various polynitrogen clusters. It is expected that the ultimate high-density energy phase of nitrogen should consist of a polymeric array of single-bonded nitrogen atoms, based on the aforementioned significant difference in energy bonding [Uddin 06] which will allow using the stored chemical energy in a controlled way.

Although molecular structure of nitrogen is rather simple, its phase diagram appears to be quite intricate (see figure 3.4). This is a common feature for simple molecular systems, where modest variations of intermolecular interactions can lead to significant changes in crystal packing and consequently to phase transitions. In nitrogen phase transitions, kinetics plays a crucial role. The sequence of phase transitions highly depends on the starting point, which was proven to be especially crucial for low-temperature metastable phases [Frost 16]. Considering the formation of high-temperature phases, we have to take into account the level of activation energy required for breaking nitrogen triple bonds, which implies that these phases can be stable after cooling. Summary of phases of nitrogen is presented in table 3.1.

At low pressures and low temperatures, quadrupole interactions dominate, resulting in two phases: the cubic $Pa3$ structure (α-nitrogen) and γ-tetragonal ($P4_2/mnm$), representing an alternative way of packing [Hemley 00].

Following pressure and temperature increase, the system transforms to a sequence of phases with decreasing symmetry of the lattice with pressure. A hexagonal close-packed and orientationally disordered β-phase has a hexagonal $P6_3/mmc$ structure with two molecules per unit cell [Schiferl 83]. However, depending on the P-T path, the λ-phase can be formed [Frost 16]. λ can be synthesized by compression at low temperatures and exists in a vast P-T domain from 1 to 140 GPa. It is characterized by a layered structure which has a distinctive optical signature suggesting intense intermolecular interactions. The typical Raman spectrum consists of four well-pronounced low-frequency modes, indicating highly

Table 3.1 *Summary of structures of nitrogen. Parameters: lattice constants a, b, c; z-number of molecules per unit cell.*

Phase	Structure properties	Reference
α	cubic $Pa\bar{3}$	[Donohue 61]
β	hexagonal $P6_3/mmc$ a=3.595(1) Å, c=5.845(1) Å; z=2	[Schiferl 83]
β	tetragonal $P4_2/mnm$	[Schuch 70]
δ	cubic Pm3n; a= 6.112(4) Å; z=8	[Hanfland 98] [Stinton 09]
δ_{loc}	tetragonal structure presumably $P4_2/ncm$; a= 8.063(5) Å, c= 5.685(5) Å at 14.5 GPa and 293 K; z=16	[Hanfland 98] [Stinton 09]
ϵ	rhombohedral $R\bar{3}c$; z=8	[Hanfland 98]
ζ	primitive orthorhombic cell, Pmma; a=6.533(0.013) Å, b=2.574(0.005) Å, c=6.844(0.013) Å; z=8	[Gregoryanz 07]
κ	monoclinic A=6.918±0.014 Å, b=6.202±0.014 Å, c=2.289±0.003Å, β =91.774°	[Gregoryanz 07]
ι	orthorhombic primitive;	[Gregoryanz 02]
θ	orthorhombic; a =56.797(4) Å, b=57.756(5) Å, c=53.761(1) Å; z=16; possible groups Pma2, $Pmn2_1$, $Pmc2_1$, Pnc2, $P2_12_12$	[Gregoryanz 02]
λ	Monoclinic $P2_1/c$; a = 3.051(7) Å, b = 3.066(5) Å, c = 5.705(13) Å, β=131.65(5)°	[Frost 16]
η	amorphous	[Gregoryanz 01]
Cubic gauche	$I2_13$, a =3.4542 Å;	[Eremets 04a] [Gregoryanz 07]
Layered polymeric	Cubic Pba2; a = 4.1602 Å, b = 4.2481 Å, c = 4.3689 Å	[Tomasino 14]

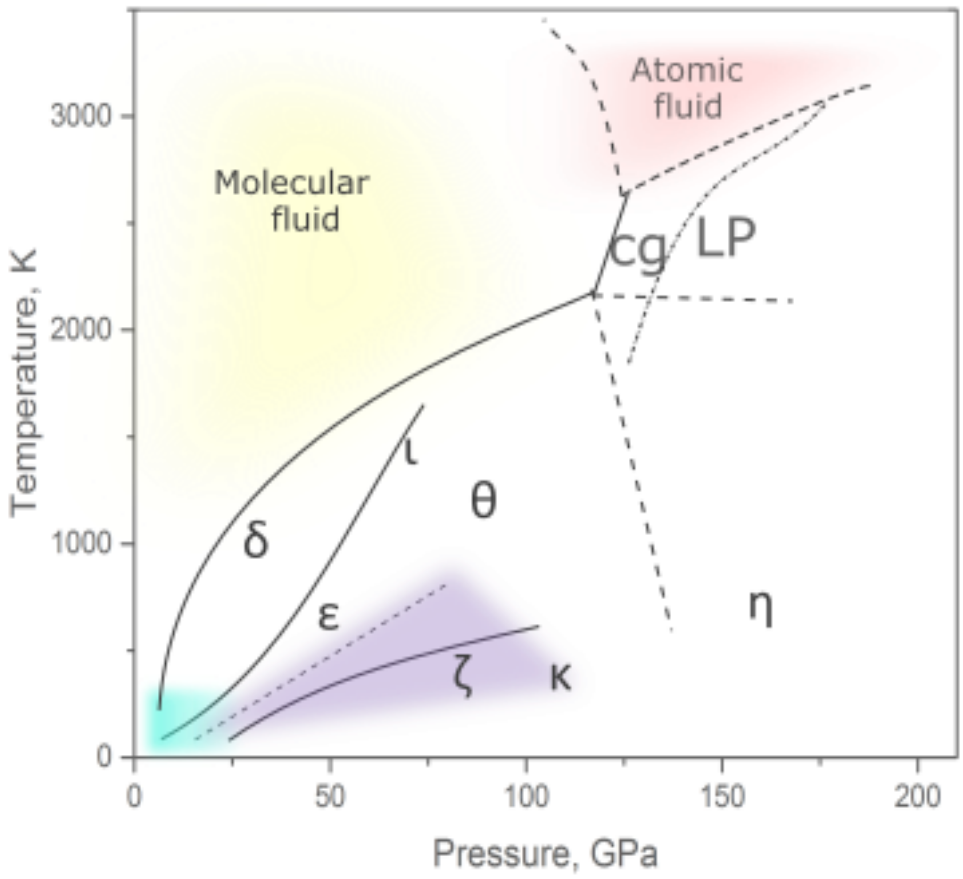

Figure 3.4 *Schematic representation of transformations in nitrogen in the wide range of temperatures and pressures. Figure is based on references [Gregoryanz 07, Goncharov 08, Tomasino 14, Frost 16, Weck 17]. The blue area represents the domain of low-temperature phases α, β, and γ. The purple section and dashed line show observed transitions from λ-nitrogen.*

ordered structure, and three vibrons.

At ambient temperature with further compression, quadruple interactions become less dominant, therefore triggering a phase transition to high-pressure phase δ-nitrogen ($Pm3n$) [Cromer 81, Hanfland 98, Stinton 09]. The molecules occupy two sites of different symmetries and are subject to various intermolecular potentials forming six disklike and two spherically disordered molecules. The two types of molecules give rise to two vibron bands ν_1 and ν around 2360 cm^{-1}.

Another structural modification δ_{loc} with presumably tetragonal structure ($P4_2/ncm$

with 16 molecules per cell) is a distortion of the δ-nitrogen phase [Hanfland 98, Stinton 09].

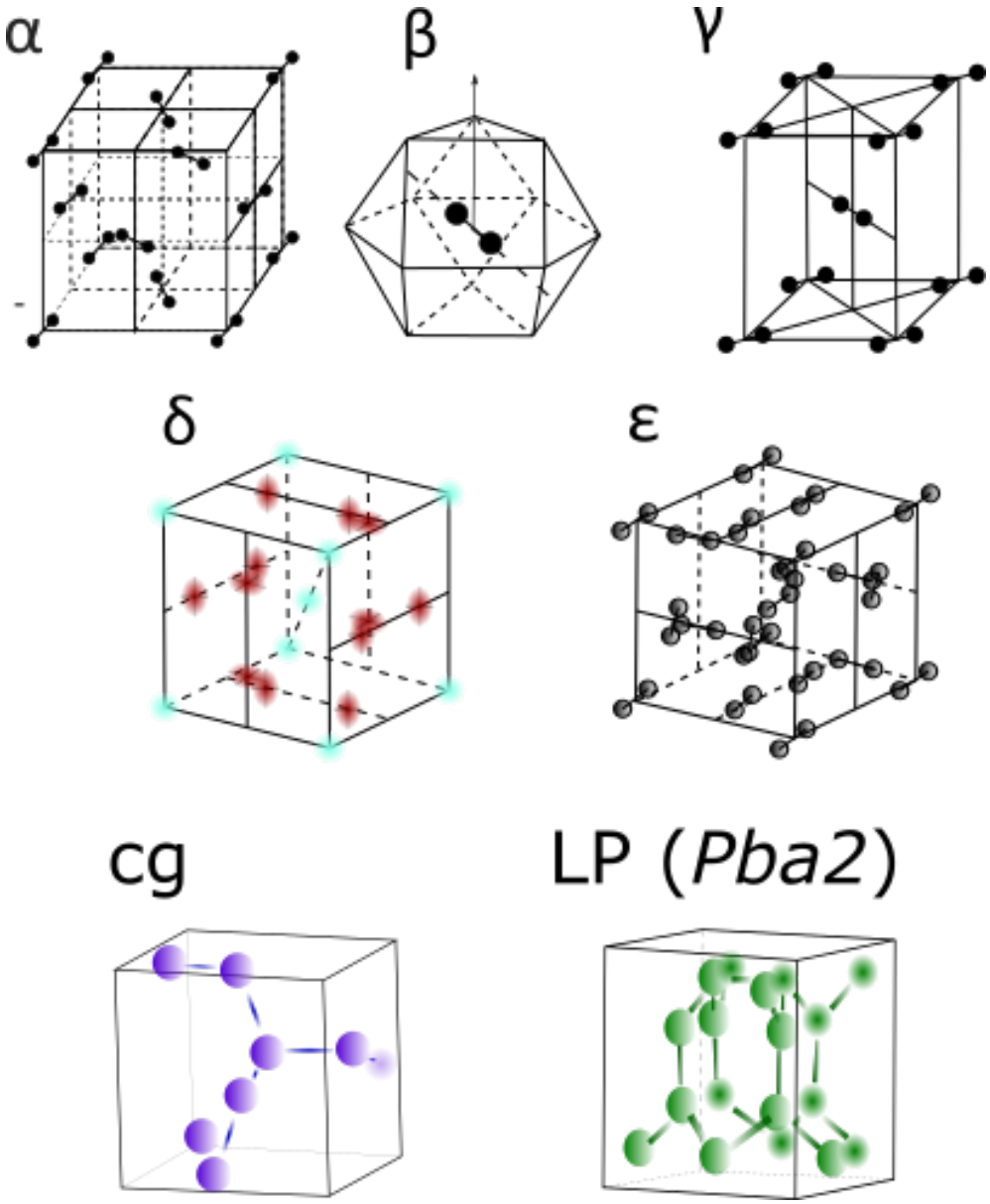

Figure 3.5 *Selected crystal structures of nitrogen [Hemley 00, Stinton 09, Tomasino 14, Eremets 04a].*

At higher pressure, the ϵ-nitrogen phase (rhombohedral, $R\bar{3}c$ with eight molecules per cell; 6 molecules on C_2 symmetry sites and two molecules on S_6 symmetry sites) [Mills 86, Hanfland 98, Bini 00, Gregoryanz 07] is present. According to the terminology for the δ-phase, one ν_1 stretching mode corresponds to sphere-like orientation, while three ν_2 modes (two Raman, one infrared) are related to disklike molecules. ν_2 mode splits into several bands upon the phase transition. Splitting first occurs as an emergence of a weak shoulder on a high-frequency

side due to reductions of symmetry because vibrations with different polarization possess different symmetry and potentially different energies. The rise of new low-frequency bands around and splitting of major vibrational bands is also detected in the low-frequency part of the spectra [Bini 00]. Further experiments indicated transition to the ζ-nitrogen phase with orthorhombic structure ($Pmma$ space group), which results from a slight distortion of the rhombohedral structure [Gregoryanz 07]. Raman vibron spectra become richer due to the increased number of sites with marked molecular site symmetries.

Above 115 GPa the new dense κ-phase is observed, supposedly with monoclinic structure [Gregoryanz 07].The ϵ, ζ and κ phases have closely related structures, derived from ϵ by lowering symmetry [Gregoryanz 07]. In contrast, the transition from the ζ and κ phases to the non-molecular polymeric phase should be accompanied by a full reorganization of the chemical bonding eventually resulting in a cubic gauche form.

At pressures above 150 GPa the black amorphous η-phase is formed [Gregoryanz 01, Goncharov 00]. Experiments showed that at 300 K above 150 GPa the vibron band characteristic to a molecular phase disappears thus confirming transformation to an amorphous non-molecular phase [Goettel 89, Gregoryanz 01, Eremets 01]. Interestingly, with the pressure increase samples darken which can be explained by having a mixture of single and double bonded molecules.

The high-temperature high-pressure phases of nitrogen are ι and θ. The high P-T phase ι forms either by heating ϵ-nitrogen [Gregoryanz 02] to 800 K at 65 GPa or by quenching melt [Goncharov 08].

The θ-phase can be reached by heating ϵ-nitrogen at 95 GPa to 600 K [Gregoryanz 02]. Another path is to heat lambda-nitrogen above 800 K at 70 GPa [Frost 16].

At high pressure, molecular nitrogen has long been predicted to dissociate into atomic phases [McMahan 85, Mailhiot 92, Barbee III 93] as a result of electron delocalization due to the increase of electron kinetic energy. Although the transformation to atomic solid was theoretically predicted at pressures already above 50 GPa [McMahan 85, Mailhiot 92, Pickard 09] with a huge variety of single-bonded polymeric forms of nitrogen [Martin 86, Lewis 92, Mattson 04, Zahariev 05, Yao 08, Ma 09, Sun 13, Kotakoski 08, Wang 12], experimentally it

has not been proven until reaching 110 GPa and temperatures around 1400 K-2000 K with formation of cubic gauche structure [Eremets 04a, Gregoryanz 07, Lipp 07]. Semiconducting cubic gauche nitrogen is a superhard colorless material built by a strong covalent N-N bond [Eremets 07]. Its slightly distorted cubic structure can be characterized by space group $I2_13$ [Eremets 04a]. All nitrogen atoms are three-fold coordinated, and bond lengths are the same for all pairs of bonded atoms [Eremets 04a].

Single-bonded cg-N features the characteristic Raman peak at 820 cm^{-1} [Eremets 04a, Gregoryanz 07, Lipp 07, Tomasino 14], which correlates well with theoretical predictions [Mailhiot 92, Barbee III 93].

Another transparent nonmolecular crystalline phase was discovered recently. It appears to be a layered polymeric (LP) solid [Tomasino 14] and is formed by a 3D-to-2D structural transition at pressures beyond 120 GPa heated above 2000 K where it coexists with cg-N.The LP structure is comprised of single-bonded nitrogen layers with the suggested $Pba2$ structure of seven-membered N-N (N7) rings. Characteristic Raman spectra feature immense phonon bands at $\sim$ 1000 and 1300 cm^{-1}, reflecting two different locations of nitrogen atoms - in the body and on the surface of the layer [Tomasino 14].

Therefore, high temperatures and high pressures are required to overcome the kinetic barriers to transition resulting in a break in the nitrogen triple bond.

3.4 Oxygen

Among the simple diatomics, oxygen requires the lowest pressure of 96 GPa to become metallic [Desgreniers 90, Akahama 95]. In addition to this, at low temperatures, it exhibits a transition to a superconducting state [Shimizu 98]. In most diatomic molecules the ground state is characterized by the total spin S=0 (H_2, N_2). However,an oxygen molecule has a total spin S=1 resulting from two unpaired electrons which makes it a magnetic system. Furthermore, magnetic exchange interaction happens together with weak Van der Waals forces having a significant share in the total lattice energy, which results in a close connection between magnetic and lattice properties [Freiman 04]. Therefore, we observe a rich phase diagram with unique magnetic and optical properties. Under compression, oxygen changes colour from transparent gas, to blue liquid, then blue crystal and eventually becomes red, getting darker to 40 GPa. Upon compression to the metallic phase retaining diatomic molecular structure, oxygen becomes reflecting [Freiman 04]. Unlike nitrogen, quadrupole interactions are almost negligible in oxygen. This leads to the formation of layered structures in the α, β and δ phases of oxygen.

Recent investigations under extreme P-T conditions showed that oxygen demonstrates high polymorphism (figure 3.6). Up to date, all known phases of oxygen are molecular. The list of oxygen phases is provided in table 3.2. At room temperature, fluid oxygen crystallizes into the pale blue β-phase at 5.5 GPa [Schiferl 83]. The rhombohedral β-phase is paramagnetic with primitive rhombohedral cell $R\bar{3}m$, z=1 obtained as an fcc structure distorted by packing of dumbbell molecules (instead of spherical) along cube diagonals [Schiferl 83, Freiman 04].

The low-temperature α-phase is orientationally and magnetically ordered: it is monoclinic $C2/m$ and antiferromagnetic with one molecule in the unit cell [Akahama 01, Jodl 85, Desgreniers 90]. Modest deformation of this structure results in another low-temperature magnetic phase δ. Both α and β phases are considered to be of the first-order type. They both were predicted to have single Raman vibrons, although there should be two Raman active librons in the α-phase and one in the β-phase [Freiman 04].

Transition to the cubic γ-phase, which is also paramagnetic, is followed by

Table 3.2 *Summary of structures of oxygen. Parameters: lattice constants a, b, c ; Z-number of molecules per unit cell.*

Phase	Properties	Reference
α	Antiferromagnetic; Primitive monoclinic C2/m	[Freiman 04] [Barrett 67] [Burakhovich 77]
β	Paramagnetic primitive rhomboedral R$\bar{3}$m a = 2.8467(2) Å, c = 10.2249(8) Å z=3	[Schiferl 81]
γ	Paramagnetic cubic Pm3n a=6.83±0.05 Å z=8	[Jordan 64] [Gorelli 00]
δ	Orthorhombic Fmmm a=4.2151(6) Å, b=2.9567(4) Å, c=6.6897(17) Å z=4	[Schiferl 83]
ϵ	Monoclinic C2/m a=7.770(10) Å, b=5.501(5) Å, c=3.657(3) Å, β =116.4(1)° z=8	[Lundegaard 06] [Fujihisa 06]
η	Hexagonal P6$_3$/mmc a= 2.561(2)Å, c=6.575(6) Å at 15.9 GPa and 625 K. z=2	[Lundegaard 09]
η'	Hexagonal P6$_3$/mmc c=2.301(2) Å, a=6.264(4) Å z=2	[Goncharov 11]
ζ	Metallic molecular, not isostructural to ϵ-phase	[Weck 02] [Goncharov 03]

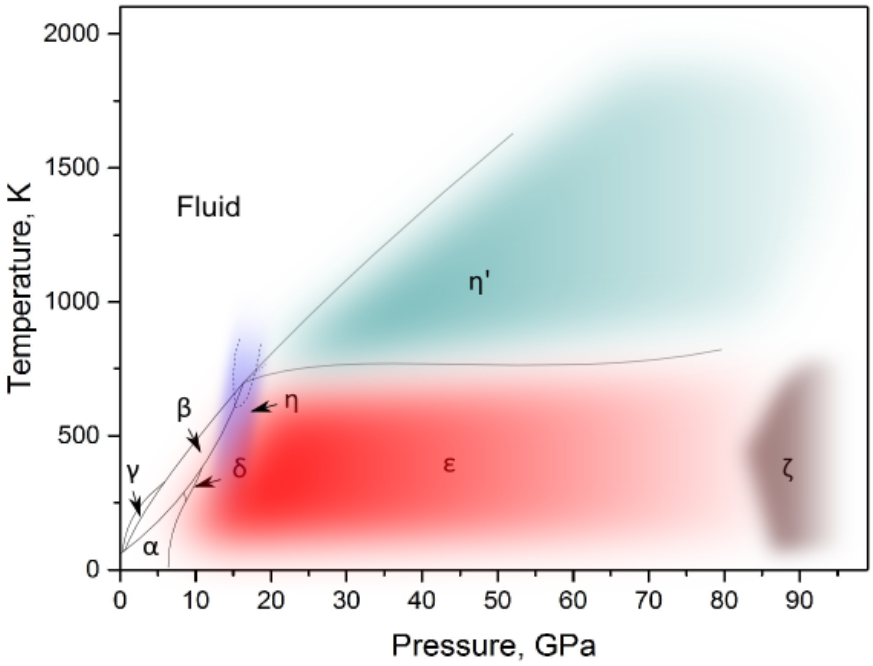

Figure 3.6 *Schematic P-T phase diagram of oxygen based on references [Goncharov 03, Santoro 04, Lundegaard 09, Goncharov 11]. The purple area between dashed lines represents the domain of the high-temperature phase η, regarding which there was some disagreement in the literature [Santoro 04, Lundegaard 09].*

significant volume change [Young 91]. It belongs to the orientationally disordered structure with $Pm3n$ group. As in the case with δ-nitrogen, two molecules are located in the sites with a spherically symmetric distribution of electron density, while six molecules have a disk-shape [Jordan 64]. Raman spectra of γ-phase thus feature oxygen vibron doublet due to the different orientation of molecules with intensity ratio 3:1 and no librons but a hump at low frequencies [Freiman 04]. This phase is similar to the δ-nitrogen phase.

Transformation to the orange δ-phase [Nicol 79] happens at 9.6 GPa at 300 K [Schiferl 83]. It possesses orthorhombic $Fmmm$ structure [Schiferl 83]. Gorelli et al. suggested that the δ-phase has an antiferromagnetic ordering of the molecular spins [Gorelli 00].

Upon further compression, the δ-phase undergoes phase transition to ϵ-oxygen

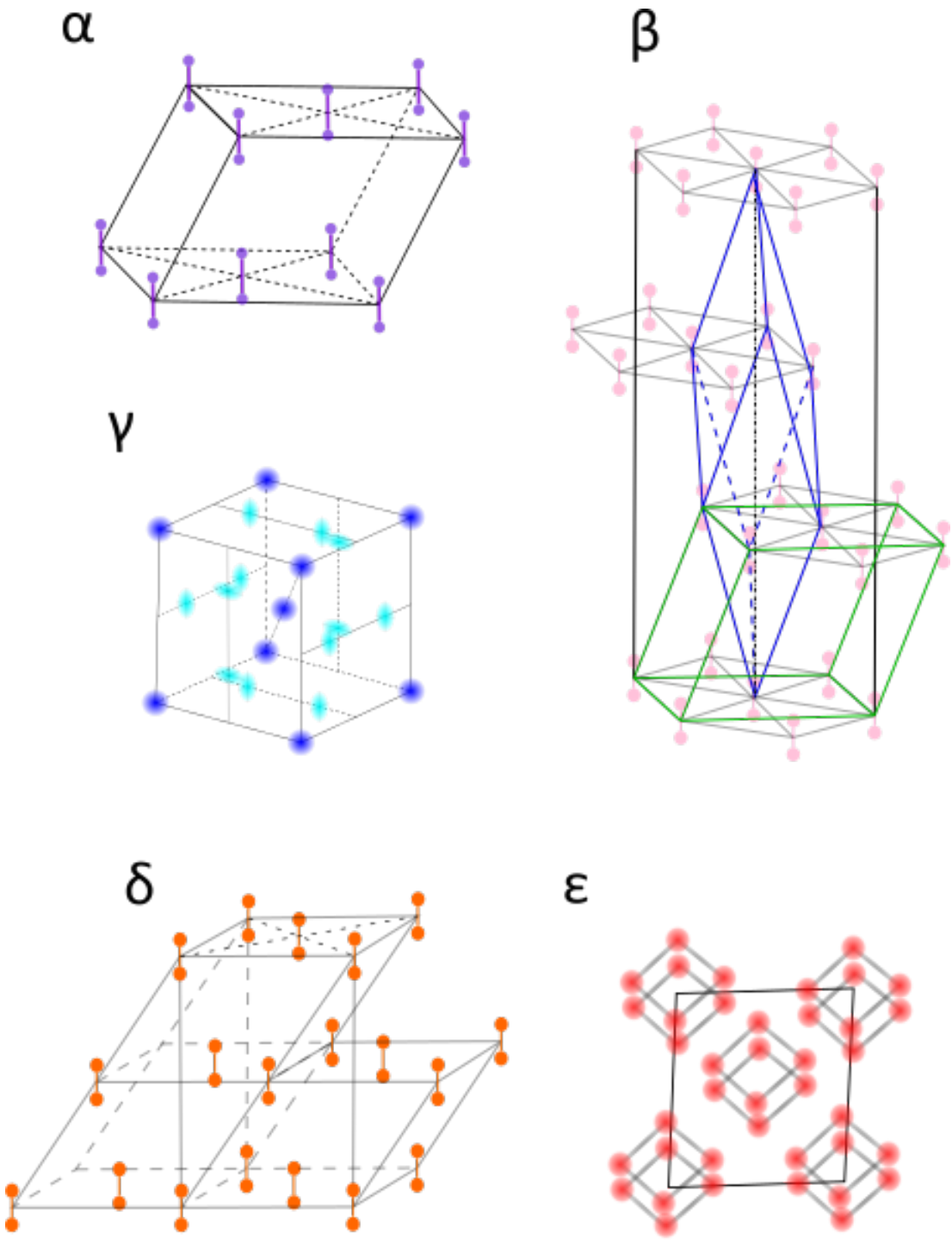

Figure 3.7 *Selected crystal structures of oxygen [Hemley 00, Lundegaard 06].*

at 9.9 GPa at 300 K [Fujihisa 06, Lundegaard 06] followed by visually distinguishable changes of color from orange to red. This phase is stable in the vast pressure domain from 10 to 96 GPa at room temperature. It was suggested that the ϵ-phase consists of diamagnetic oxygen forming clusters [Gorelli 99]. Recent works resolved the structure by providing X-Ray measurements [Fujihisa 06,

Lundegaard 06]. They demonstrated that association of molecules into clusters containing four O_2 molecules with bond lengths 1.20 Å and 2.20 Å is probably due to weak chemical bonds. Unlike the β and δ phases, where structures can be described by deformation of the monoclinic cell of the α phase, the δ to ϵ transition happens due to the relative displacement of half of the molecules in each layer and the doubling of the unit cell of the δ-phase. The fingerprint of the $(O_2)_4$ cluster unit is the spectrum with an additional Raman mode around 1400 cm^{-1} reflecting the antisymmetric stretching of pairs of O_2 molecules in the cluster. Previously observed principal excitations are the following: symmetric O-O stretching at around 1600 cm^{-1} and two librational modes around 340 cm^{-1} and 160 cm^{-1}, corresponding to the symmetric stretching O-O and the bending mode in the plane respectively [Lundegaard 06]. Raman spectra also revealed the emergence of several combinations of tones and overtones [Akahama 96]. Interestingly, Raman intensities of all bands are increasing with pressure up to 50 GPa, and then gradually decreasing. This resonance behaviour was attributed to the overlapping of the band gaps decreasing with the energy of the laser light [Akahama 01, Gorelli 01, Gorelli 02].

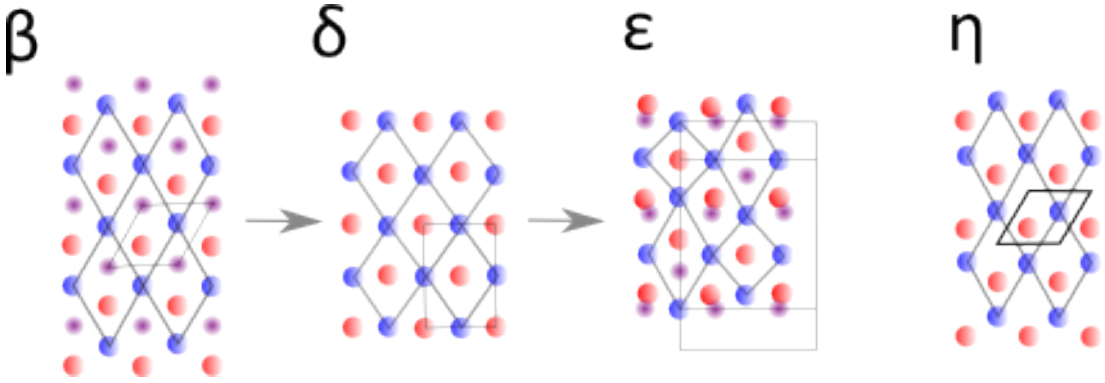

Figure 3.8 *Sequence of phase transformations of oxygen at room and high temperatures. The structures are illustrated perpendicular to the layers of parallel oxygen molecules. Different colors are used to label molecules located in different layers. The η-phase can be obtained from both β and ϵ oxygen. After reference [Lundegaard 09].*

The high-pressure metallic phase of oxygen was first observed by Desgreniers et al. [Desgreniers 90]. The insulator to metal transition happens at pressures above 95 GPa at room temperature. Also, Shimizu et al. reported superconductivity at pressures around 100 GPa and temperature of 0.6 K [Shimizu 98]. First X-ray diffraction studies indicated that the structure of the ξ-phase could be isostructural to the ϵ-phase [Akahama 95]. However, Weck et al. [Weck 02] did not confirm this assignment in their work, suggesting that the structure

should undergo a displacive transition associated with interplanar sliding and intraplanar modifications. Experimental Raman data demonstrate that molecular dissociation does not happen at least up to 134 GPa due to the high stability of the oxygen stretching mode, although with discontinuity in frequency, implying that ξ oxygen is a molecular metal [Weck 02, Goncharov 03, Akahama 95, Akahama 96, Akahama 00].

Recently, the high-temperature η and η' phases have been observed [Santoro 04, Goncharov 11]. η is stable in a narrow window at pressures above 16 GPa and temperatures above 500 K and eventually transforms either to ϵ under compression or η' with higher pressure and temperature. As with the α, β, δ and ϵ phases, it comprises of the fully ordered layered structure with the arrangement similar to hpc structure. The Raman spectrum features a single O-O stretching mode [Santoro 04, Lundegaard 09]. The η'-phase is isostructural to η. However, their stability domains do not overlap. Transition to the η'-phase is entropy driven and is connected to the dissociation of $(O_2)_4$ clusters.The Raman spectra lack sharp lattice modes, exhibiting only a broad band around 470 cm^{-1} at 1000 K and slightly red-shifted and moderately soft vibron at 1680 cm^{-1} due to the low probability of formation of intramolecular bonds which results from the bigger distance between the molecules and stronger intermolecular interactions [Goncharov 11].

3.5 Nitrogen/oxygen mixtures under pressure at low and ambient temperature

Since O_2 and N_2 diatomic molecules possess unique properties related to their structure, such as triple bonding in N_2 or magnetic moment carried in O_2, a lot of theoretical and experimental works have been devoted to the investigation of their behaviour at extreme conditions, such as high pressure or extreme temperatures. As it was discussed in the previous sections, both systems exhibit rich polymorphism up to 10 GPa, being a cross-product of quadrupolar forces, magnetic effects, bond lengths and intermolecular distances or pairing molecules and forming clusters. Pressure-induced changes result in the dominance of chemical type of interaction, thus allowing the formation of such phases as metallic oxygen or nonmolecular phases of nitrogen.

Comparatively few studies have been devoted to the investigation of the nitrogen-oxygen system under pressure although it is of direct relevance to understanding the physical and chemical interaction between simple elements with vast probabilities of application to a detonation of high-energy materials, and the synthesis of novel materials by exposing them to extreme conditions.

One of the earliest attempts to build high-pressure phase diagram of the nitrogen/oxygen binary system was undertaken by B.Baer and M.Nicol [Baer 90]. They described temperature isotherm of the nitrogen-oxygen phase diagram up to 14 GPa at 300 K with the help of Raman spectroscopy of samples prepared from mixing cooled liquids [Baer 90]. They detected several phase transitions, normally mimicking those in pure nitrogen and oxygen. It was determined that oxygen demonstrate high miscibility in the nitrogen-like phases phase below 9.5 GPa, with the more limited miscibility of nitrogen in the oxygen phases.

K. Damde and H.J. Jodl performed low-temperature measurements leading to the construction of the low-temperature tentative phase diagram up to 25 GPa at 18 K [Damde 98]. Their research was mainly focused on the nitrogen-rich mixtures and in general, confirmed the proposed idea of phases reflecting the structure of the main component of the mixture.

Minenko et al. [Minenko 04] continued the low-temperature studies on nitrogen/oxygen gas mixtures with different concentrations compressed up to 25 GPa

on nitrogen rich samples with 2% and 7% oxygen. Oxygen solubility in the ϵ-nitrogen was confirmed, with the probability of the ϵ-oxygen demixing from the ϵ-nitrogen above 15 GPa, which was previously referred to as a "new phase" [Baer 90, Baer 89].

In a more recent study, Sihackakr and Loubeyre [Sihachakr 04] continued experiments, combining several experimental methods and extending accuracy and details of previous research. They used visual observations of phase transitions, Raman spectroscopy and x-ray determination of the structures in the solid solution for determination of the phase boundaries. Samples were loaded from the gaseous mixtures. Discovered phases S1, S2, S3, S4, S5, and S6 are isostructural to the pure components. S3' is a new homogeneous phase of oxygen/nitrogen mixtures and has a hexagonal structure that does not exist for pure nitrogen or oxygen, and is described in detail in [Akahama 14]. Table 3.3 summarizes discovered phases of nitrogen/oxygen binary system and their structures.

The study of Sihachakr and Loubeyre also confirmed total miscibility in the liquid phase, large miscibility of oxygen in δ-nitrogen, and very limited ability for nitrogen substitution in the oxygen-solutions, which was less than 5% [Sihachakr 04] . Interestingly, substitution of up to 20% of nitrogen does not affect the sequence of the nitrogen-phase transitions. X-ray experiments showed that volume of the crystal cell depended significantly on oxygen substitutional solubility in the δ-nitrogen, whereas this effect was almost negligible in the β-nitrogen and δ_{loc}-nitrogen. Hence, it was concluded that O_2-N_2 interaction is quite similar to N_2-N_2 interaction and rather different from O_2-O_2 interaction which is clearly strongly dependent on the magnetic properties of oxygen below 10 GPa and the pairing of O_2 molecules above this pressure, stabilizing O_2 molecules and thus preventing N_2 molecules from substitution.

The S1 domain is characterized by the hexagonal unit cell with two molecules per cell (space group $P6_3/mmc$) which is obtained by substitution of N_2 molecules by O_2 molecules in the β-phase of solid nitrogen. Raman peaks observed in nitrogen and oxygen areas are singlets. S2 phase covers the most extensive domain of the phase diagram up to 12 GPa.

The S2 domain is related to the disordered cubic $Pm3n$ structure with eight molecules in the unit cell as in δ-nitrogen. Thus, the S2 phase is derived from

Table 3.3 *Summary of structures of nitrogen/oxygen binary system up to 12 GPa at 300 K according to references (a) [Sihachakr 04] and (b) [Akahama 14] correspondingly. Parameters: lattice constants a, b, c; V- volume of the unit cell; Z-number of molecules per unit cell.*

Phase	Description.
S1	Hexagonal $P6_3/mmc$; z=2 a=3.537±0.007 Å, c=5.844±0.007 Å, V=31.658±0.163 Å ^{3}/molecule (a)
S2	Disordered cubic Pm3n; z=8 a=6.010±0.007 Å, V=27.135±0.095 Å^3/molecule. (a)
S3	Rhombohedral R$\bar{3}$m (hexagonal cell) a=2.758 Å, c=10.200 Å, V=22.397±0.129 Å^3 /molecule. (a)
S3'	Hexagonal, a=5.630 Å, c=12.358 Å, V=24.231±0.074 Å^3 /molecule. (a) Hexagonal P6/mmm of Z = 7; a = 5.6016(4) Å, c = 6.1645(8)Å, V = 167.52(6) Å^3. (b)
S4	Orthorhombic Fmmm; z=4 a=6.704 Å, b=4.248 Å, c=2.958 Å, V=21.060±0.106 Å^3 /molecule. (a)
S5	Monoclinic C2/m; z=8 a=8.096 Å, b=5.724 Å, c=3.776 Å, b=117.26, V=19.442±0.087^3 /molecule. (a)
S6	Tetragonal (possible space group $P4_2/ncm$) a=8.075±0.007 Å, c=5.694±0.007 V=23.205±0.069 Å^3 /molecule. (a)

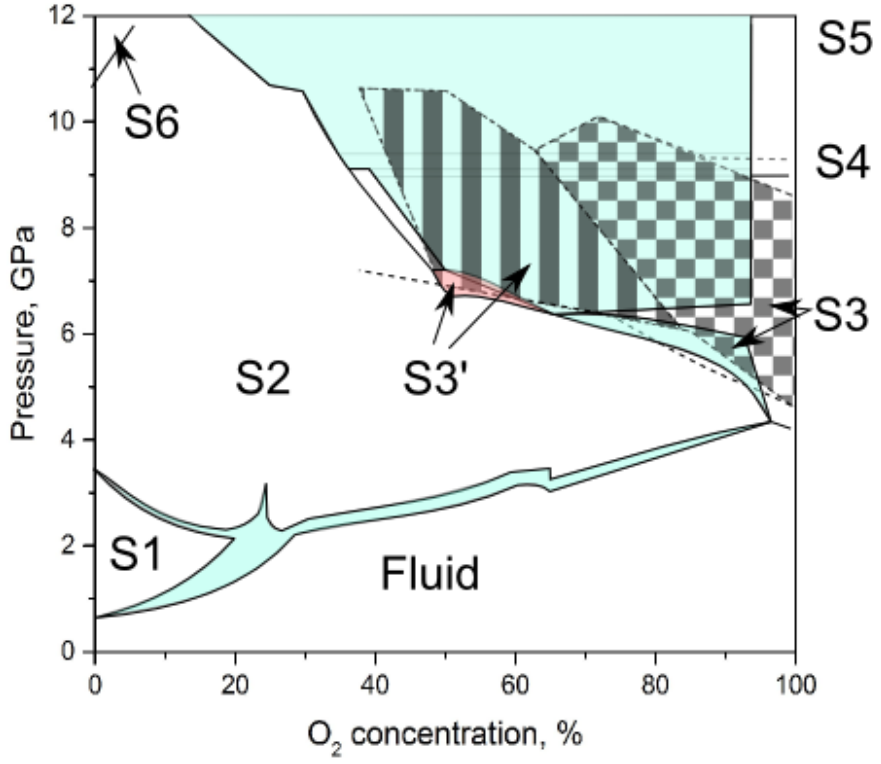

Figure 3.9 *Summary of the phase transitions in the nitrogen-oxygen binary system at room temperature based on the phase diagrams proposed in references [Sihachakr 04, Akahama 14]. The cyan areas correspond to the phase separation domains according to [Sihachakr 04]. The pink section represents the domain of hexagonal phase S3' [Sihachakr 04]. The dashed lines represent phase borders according to Akahama et al. [Akahama 14]. The striped and chess sections overlapping with the cyan domain of the phase separation [Sihachakr 04] are proposed by Akahama et al. [Akahama 14] and correspond to the hexagonal phase (analogous to S3') and β-oxygen (S3) respectively. Names of the phases are taken from the reference [Sihachakr 04]. The domain of the hexagonal S3' phase with kagome lattice is significantly extended in reference [Akahama 14] compared with previous studies. With pressure increase dissociation to ϵ-oxygen and δ-nitrogen without formation of any new compounds was suggested.*

δ-nitrogen by substitution by oxygen molecules of nitrogen. In the cubic phase with two different sites in the unit cell, vibron band splits into two. The $Pm3n$ structure of the S2 phase as δ-nitrogen has two crystallographic sites with disklike and spherelike orientations of molecules. These two different types of orientation comply with the splitting of N_2 and O_2 vibron modes which were observed in all studies mentioned earlier. Therefore, ν_1 modes corresponds to spherically disordered orientations of molecules at (0, 0, 0) and ($1/2$, $1/2$, $1/2$) positions of

the $Pm3n$ unit cell, while ν_2 corresponds to molecules with disklike orientations occupying two sites at (0, 1/4, 1/2) and (0, 3/4, 1/2) or their equivalents. The ratio between disklike and spherically disordered molecules in pure δ-nitrogen which could be inferred from the ratio of vibron intensity $\frac{\nu_1}{\nu_2}$ equals 3, which is in a first approximation an indicator of the population of molecules of sphere-like and disklike molecules on the specific sites. Results of this study show that such ratio in nitrogen/oxygen mixtures is increasing for N_2 molecules and decreasing for O_2, which consequently suggests that O_2 molecules slightly prefer to occupy disklike (ν_1) state [Sihachakr 04]]. It was documented, that relative intensities of O_2 doublet change with pressure, but N_2 vibron is not affected, which is due to vibron-vibron resonant transfer coupling in oxygen [Baer 90]. Neither of the studies reports the emergence of low-frequency peaks in $P6_3/mmc$, $Pm3n$ or $R\bar{3}m$ phases [Baer 90, Sihachakr 04].

Structure of S3 is very similar to β-oxygen with rhombohedral $R\bar{3}m$ and is formed by nitrogen doped into the oxygen cell [Sihachakr 04].

Phase S3', refined with a hexagonal unit cell with 14 molecules in it, does not correspond to any phase of pure nitrogen or oxygen [Sihachakr 04]. In further research by Akahama et al., this structure is proposed to comprise a unique kagome lattice of a geometrically frustrated magnetic system [Akahama 14]. Structural model with three molecules in the 6(i) site, two molecules in the 2(e) site and two molecules in the 4(h) site was designed, where supposedly oxygen molecules on 6(i) site form kagome-lattice [Akahama 14]. There is some disagreement about the stability of this phase in pressure and concentration range between different studies [Sihachakr 04, Akahama 14].

It was noted that under further compression hexagonal phase precipitated into monoclinic ϵ-oxygen (S5) and cubic δ-nitrogen or to the rhombohedral $R\bar{3}m$ cell of β-oxygen coexisting with other phases [Akahama 14]. At the transition to the S3' phase, two vibron bands become singlet.

S4 and S5 phases appear to be similar to the δ and ϵ phases of oxygen respectively, where S4 is orthorhombic $Fmmm$ with four molecules in the unit cell, and S5 is monoclinic with the space group $C2/m$ and eight molecules per unit cell [Sihachakr 04].

S6 phase exists in relatively dilute samples. It granted more possible interpre-

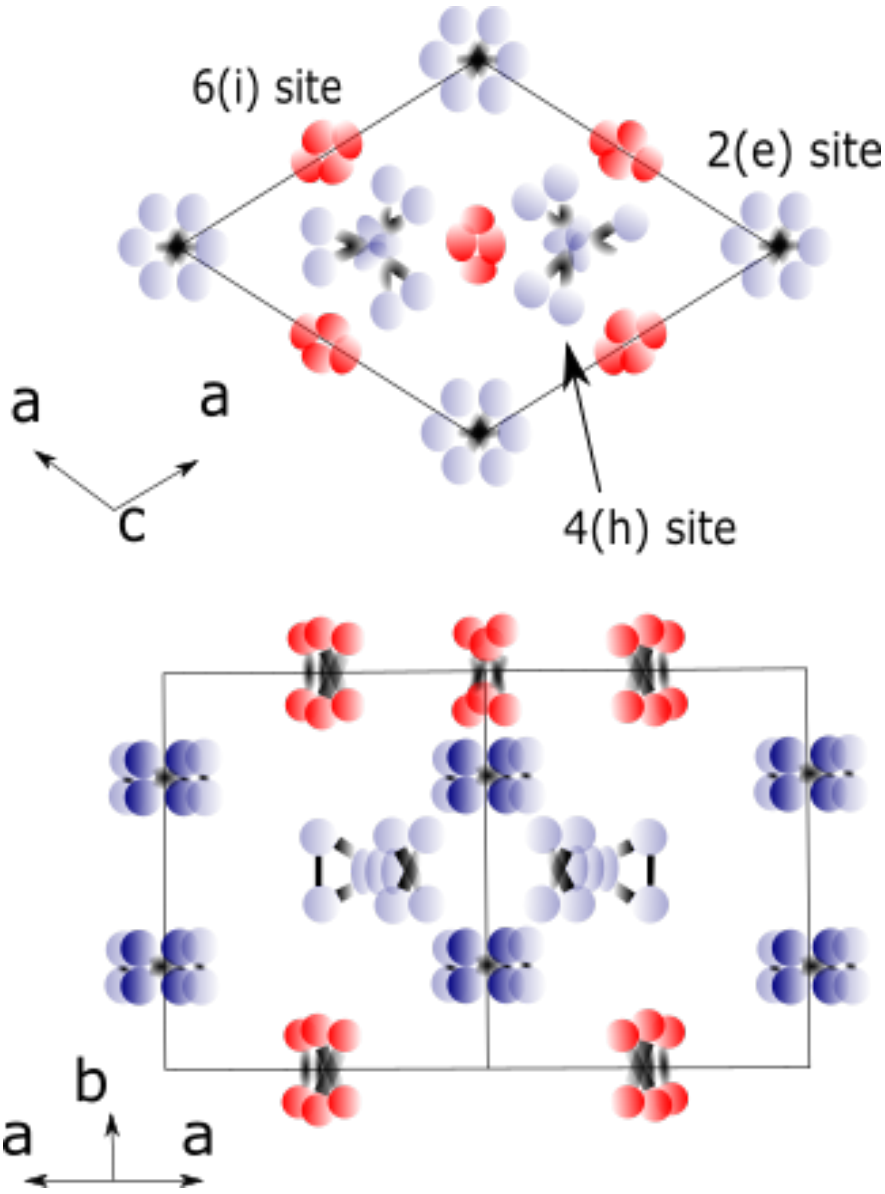

Figure 3.10 *The structural model of the S3' phase with hexagonal P6/mmm lattice. Kagome lattice is formed by O_2 molecules on the 6(i) site (red) [Akahama 14]. The scheme is courtesy of reference [Akahama 14]].*

tations in published research papers due to the ambiguous Raman spectra. X-ray analysis suggested that this phase is similar to the δ_{loc} phase of nitrogen with a possible space group $P4_2/ncm$ and minimal effect from substituting O_2 molecules on the volume of the cell [Sihachakr 04]. Baer and Nicol inferred from Raman spectra that this phase should be a variant of $Pm3n$ where O_2 molecules had a preferential occupation of sites (0,¼,½) and (0, ¾, ½) and suggested formation of oxygen clusters or chains on sites with disklike orientation [Baer 89]. Damde and Jodl documented the stability of S6 phase at low temperature [Damde 98]. This phase was reported to be stable to pressures

above 30 GPa [Baer 89, Minenko 04]. Minenko et al. assumed that drastic changes in oxygen Raman spectra characterised by the appearance of the new O_2 vibron significantly shifted to the low-energy region and librons shifted to higher frequency are features only of the ϵ-oxygen demixing from nitrogen and are related to suppression of resonance shift of oxygen by nitrogen-impurities [Minenko 04].

However, based on documented deviation from the ideal substitution in the solid solution of phase S2, corresponding to the peritectic points on the solidus line, the existence of two stoichiometric compounds $(N_2)_3O_2$ and $N_2(O_2)_2$ was proposed, however they were not observed experimentally [Sihachakr 04]. Such type of interaction as Van der Waals interaction is essential in mixtures of simple molecules and therefore the formation of new compounds is expected due to efficient packing [Loubeyre 96]. Formation of these compounds can be due to the preferential population of either component on the specific side of the structure or optimal packing with the special arrangement in a solid solution.

3.6 Nitrogen/oxygen mixtures and nitrogen oxides at high pressures and temperatures

Nitrogen/oxygen mixtures and compounds have attracted considerably less attention than their pure components although there is a lot of interest for their application due to prospective properties of the pure components and resulting materials. For example, oxygen becomes metallic [Desgreniers 90, Weck 02, Goncharov 03], nitrogen forms semiconducting nonmolecular phase [Eremets 04a, Eremets 04b], NO is of high interest due to its explosivity, and nitrogen oxides possess enhanced reactivity with the pressure increase in a broad temperature range [Manaa 05]. With the pressure increase, solids are expected to minimize their free energy by delocalizing electrons either locally (polymerization) or completely, thus transforming to a metallic state. Another possible reaction of a molecular system to pressure increase is polarization or ionization when electrostatic forces become dominant. Ionic units offer closer packing comparing to Wan der Vaals compounds. For instance, nitrogen oxides are among those materials where symmetry breaking ionization occurs as a result of pressure or temperature treatment. Importantly, phase transitions in nitrogen oxides are very kinetically and path dependent.

The most recent theoretical calculations on nitrogen/oxygen mixtures predicted the formation of three stable N-O compounds (NO_2 is stable to 91 GPa, N_2O_5 is stable to 446 GPa, NO is metastable up to 198 GPa and stable above this pressure)[Li 15, Manaa 05]. According to the simulations, most of the phases of N-O are semiconducting, whereas polymeric NO is metal and becomes a superconductor at T_c=2.0 K and 200 GPa. However, previously conducted experimental works on various nitrogen oxides showed that in most cases they decompose into nitrogen oxides (N_2O, N_2O_3, N_2O_5), nitrogen/oxygen mixtures or ionic compounds ($NO^+NO_3^-$, $NO_2^+NO_3^-$) by breaking strong covalent bonding of the molecules [Manaa 05]. Remarkably stable nitrosonium nitrate obtained in the vast majority of the high-pressure high-temperature experiments was found to be metastable in theoretical calculations [Li 15]. However, its stability might be increased with temperature, which agrees with the experimental results.

The first experiment at the beginning of nitrogen oxides high-pressure odyssey was carried out on NO, and it was discovered that under compression to 1.5 GPa

at 176 K NO is induced to form N_2O and N_2O_4 [Agnew 85].

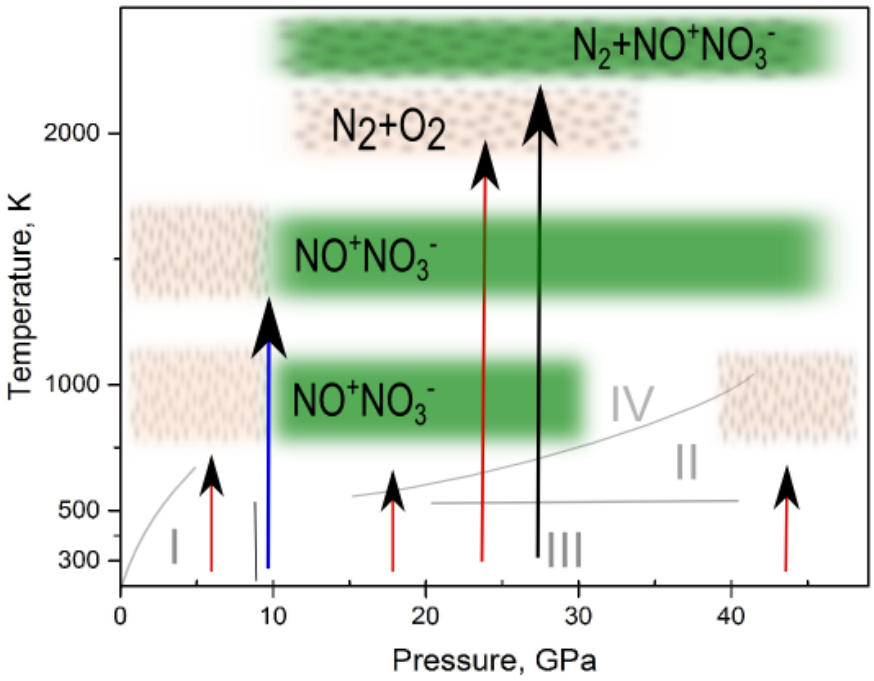

Figure 3.11 *Symbolic diagram of pressure and temperature induced phase transitions in N_2O. The grey lines indicate the phase boundaries between phases I (Pa3), II (unknown structure), III (orthorhombic Cmca) and IV (orthorhombic Pbcn) [Mills 91, Iota 04]. The green areas correspond to $NO^+NO_3^-$ in its orthorhombic phase. The patterned pink areas illustrate domains of dissociation into oxygen and nitrogen. The green patterned section depicts the area of formation of the ionic compound and nitrogen [Yoo 03]. The red arrows correspond to the experimental data obtain by Somayazulu et al. [Somayazulu 01]. The blue arrow and black arrow point at the phases observed by [Song 03b] and [Yoo 03] respectively.*

Phase diagram of N_2O is presented in Figure 3.11. N_2O at 300 K solidifies into the α-phase (Pa3) at pressures below 4 GPa and undergoes a transition to β (III, *Cmca*) above 5 GPa [Mills 91], which remains stable to 135 GPa [Iota 04]. Phase II stabilizes above 23 GPa in the narrow temperature range 100-300K. Heating above 600 K at results into transformation to phase IV. Both phases III and IV can be quenched and remain stable on decompression to 5 GPa at 300 K. N_2O-III at 5 GPa and ambient temperature can be interpreted in terms of an orthorhombic *Cmca* unit cell. Phase IV diffraction patterns were refined with two options: disordered *Pbcn* unit cell with a=54.2356(6) Å, b=55.9825(10) Å, and c=54.2232(13) Å and ordered *Pbcm* with a=54.231(2) Å, b=55.987(2) Å,

and c=54.237(1) Å. Raman spectra in phase III exhibit bending ν_2 mode around 600 cm^{-1} and asymmetric stretching ν_3 mode around 2380 cm^{-1}. Vibron ν_3 splits into four components into phase IV due to the lower symmetry crystal structure. Explanation of the structure with the ordered model suggests a potential way of transformation to an ionic compound as the result of the high level of ionicity due to the disparity between N-N and N-O lengths [Iota 04].

Heating experiments up to 54 GPa and above 2000 K showed that N_2O disproportionates into $NO^+NO_3^-$ and various products depending on the achieved pressure [Song 03b, Song 03a, Somayazulu 01, Yoo 03]. Below 10 GPa, a pressure-induced reaction of dissociation into $NO^+NO_3^-$, δ-nitrogen, β-oxygen and N/O products takes place. At 54 GPa β-N_2O disproportionates into $NO^+NO_3^-$ and η-nitrogen [Yoo 03].

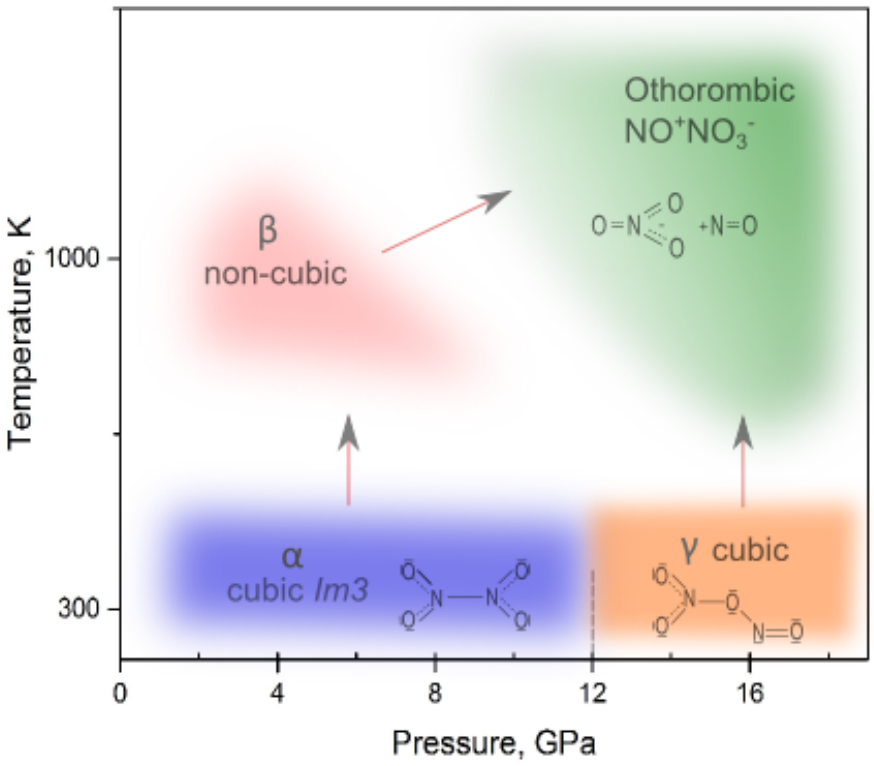

Figure 3.12 *Schematic phase diagram of N_2O_4 under high pressure and temperature. Colors correspond to different phases of molecular and ionic N_2O_4 isomers: $\alpha-N_2O_4$ (blue), β-N_2O_4 (pink), γ-N_2O_4 (orange) and ionic NO^+NO^{3-} (green). The red arrows show the pathways to obtain β-N_2O_4 and its ionic isomer by laser irradiation [Agnew 83, Agnew 85, Song 03a].*

Schematic phase diagram of N_2O_4 is presented in Figure 3.12. N_2O_4 crystallizes into the cubic Im3 N_2O_4-α phase with six molecules per unit cell [Song 03a]. Under irradiation, it was observed to transform to the β-phase with a nondefined noncubic structure [Agnew 83, Agnew 85, Song 03a]. Pressurized to 1.5-3.0 GPa,the β-phase is subjected to the transformation to ionic $NO^+NO_3^-$. At room temperature and 8.8 GPa,the α-phase transforms into the cubic γ-phase with the lower symmetry and molecular units close to D or D' isomers (Figure 3.13) [Bolduan 84] .

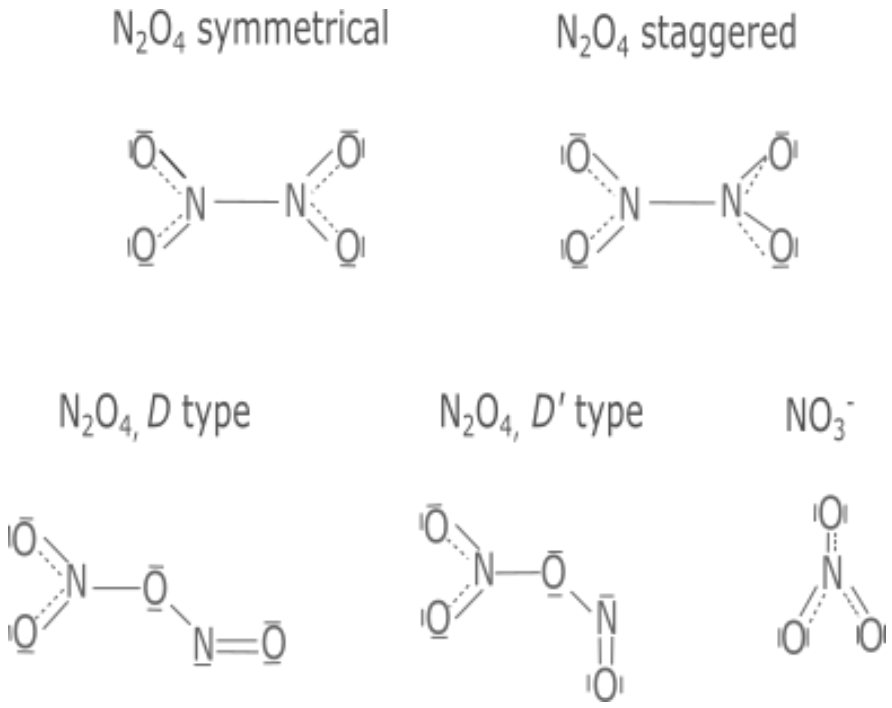

Figure 3.13 *Summary of possible isomers of N_2O_4. Different species have various Raman active modes due to the specific molecular point groups. Thus, symmetrical N_2O_4 is of D_{2h} molecular point group. Hence it has Raman active vibrations of symmetry A_g, B_{1g}, and B_{2g}. For staggered N_2O_4 of D_{2d} point group, Raman modes are of A_1, B_1, B_2, E. D type of N_2O_4 features A' and A" modes due to the C_s group, identical to D' type. And ion NO_3^- is characterized by the D_{3h} point group, featuring vibrations of A_1' and E' symmetry [Bolduan 84].*

The γ-phase can be considered as an intermediate phase between molecular α-N_2O_4 (cubic) and ionic $NONO_3$ (orthorhombic) [Song 03a]. Raman spectra exhibit enhanced low-frequency landscape, broadening of the peak at 730 cm^{-1} (NO_2 wagging mode) and new peaks at around 1100 cm^{-1} and 2200 cm^{-1} [Song 03a]. Given that no significant changes in X-Ray diffraction patterns were observed, the behaviour of the characteristic Raman features suggests that structure of the γ-phase is closer to α than to ionic compound. A vast amount of low-frequency peaks indirectly point to the disordered structure typical for

the ionic solids. Thus it was implied that this phase could be interpreted as the coexistence of the α-phase of molecular N_2O_4 and orthorhombic ionic $NONO_3$.The γ-phase is a typical example of a kinetical and path-dependent phase. When the sample is loaded at low temperatures with consequent pressure increase to at least 6 GPa at the same temperature, the γ-phase can be easily obtained. However, if the pressure is not sufficiently high, the transformation is suppressed [Song 03a].

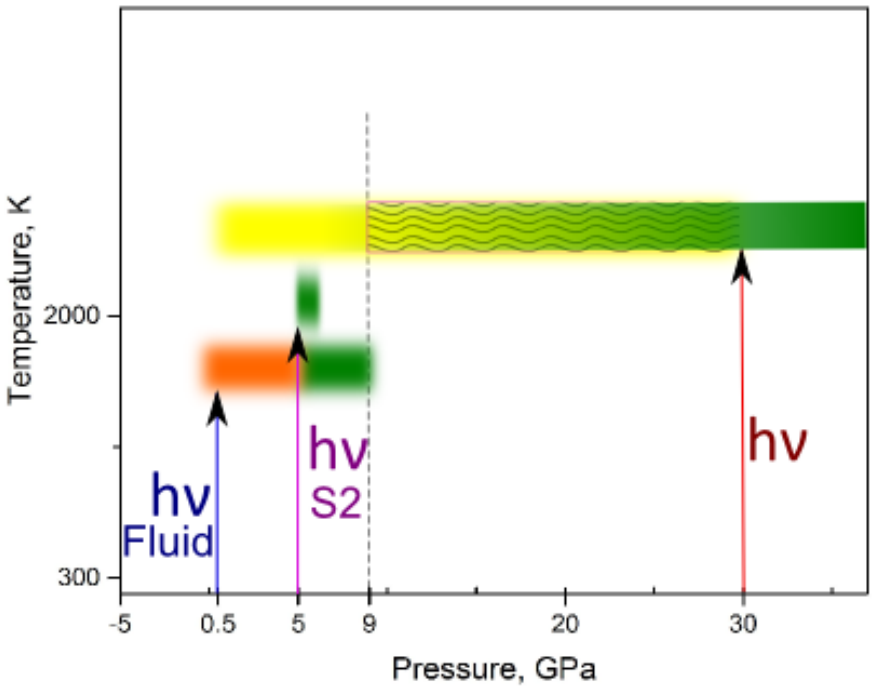

Figure 3.14 *Schematic representation of areas of synthesis of ionic compounds by laser heating directly from nitrogen/oxygen mixtures based on the research by Sihackakr et al. (purple arrow) [Sihachakr 06], Meng et al. [Meng 06] (blue arrow) and Kuznetsov et al. [Kuznetsov 09] (red arrow). Different colors correspond to different compounds. The yellow section represents the domain of $NO_2^+NO_3^-$ compound with the hexagonal $P6_3/mmc$ lattice, orange color shows the area of existence of monoclinic $NO^+NO_3^-$ with $P2_1/m$, and the green area depicts $NO^+NO_3^-$ in the orthorhombic Pmmm phase [Sihachakr 06, Meng 06, Kuznetsov 09]. The wavy pattern shows the area of coexistence of $NO_2^+NO_3^-$ and $NO^+NO_3^-$ [Kuznetsov 09]. In all these experiments laser heating was executed for the samples with different compositions and various starting phases (or at various pressures at 300K): above 10% oxygen and from S2 phase [Sihachakr 06]; fluid of 34% oxygen [Meng 06]; above 70% oxygen and above 30 GPa [Kuznetsov 09]. Temperatures of formation of the new phases are around 2000 K.*

Along with the high P-T studies of nitrogen oxides, there were studies of nitrogen/oxygen mixtures under high pressure and high temperature. Results of this

research are briefly summarized in Figure 3.14. The direct transformation from nitrogen/oxygen mixtures to the ionic compounds was reported by [Sihachakr 06] and [Meng 06]. Sihachakr et al. carried out experiments on three compositions: 25, 66 and 75% of oxygen. The chemical transformation into the iconic solid $NO^+NO_3^-$ was triggered by Nd: YAG laser irradiation of the sample in the S2-phase (solid solution with cubic Pm3n structure). Visually, solid ionic compound looked as dark reddish brown. It was noted that the reaction can be induced in the samples containing more than 10% oxygen. Raman studies revealed stretching N-O mode of NO^+ at 2240 cm^{-1}, symmetric stretch ν_1=1050 cm^{-1} band of NO_3^- group, out-plane bend mode ν_2=820 cm^{-1}, antisymmetric stretch mode ν_3=1390 cm^{-1}, in-plane deformation mode around 720 cm^{-1}. The ionic compound is stable upon decompression up to 1 GPa, where it transforms to the molecular N_2O_4 and mixture of other phases. X-ray diffraction patterns were solved as orthorhombic *Pmmm* unit cell with the cell parameters a=7.863(1) Å, b=16.519(3) Å, c =6.031(1) Å, and V=783.42 $Å^3$ cell, z=10. The appearance of the peak of the pure oxygen vibron indicated that a large amount of clathrates containing O_2 molecules (however not O_2^+ with the frequency of 1840 cm^{-1}) could be hosted in the NO^+NO^{3-} compound. However, similar behaviour for N_2 molecules was not detected [Sihachakr 06].

Parallel work of Meng et al. [Meng 06] reported the formation of $NO_2^+NO_3^-$ induced by x-ray photon radiation at pressure as low as 0.5 GPa and room temperature from the mixture of 34% nitrogen. Upon transformation, sample became opaque with distinctive grain structure. Raman spectra represented following characteristic peaks of NO_3^-: ν_4= 724.5 cm^{-1} and ν_1=1054.0 and NO_2^+: ν_2=at 523.8 cm^{-1} and ν_1= 1397.5 cm^{-1}. The structure was determined as a hexagonal $P6_3/mmc$ structure with two $NO_2^+NO_3^-$ molecules per unit cell. Observed formation of the ionic compound with less density than the α or β phases of N_2O_4 indicates that this form is thermodynamically more stable. With pressure increase, ionic $NO_2^+NO_3^-$ eventually decomposes into layered $NO^+NO_3^-$ structure at 5 GPa with the monoclinic $P2_1/m$ unit cell with two molecules per unit cell.

The most recent research was conducted on mixtures with non-precisely determined composition of more than 70% of oxygen, which were laser heated to 1300-2000 K [Kuznetsov 09]. Compression to pressures above 30 GPa and laser heating led to the formation of $NO^+NO_3^-$. Raman spectrum featured excitations associated with NO_3^- and NO^+ groups: stretching mode $\nu(NO^+)$ =2268 cm^{-1} and

the Raman bands of NO_3^- molecular complex $\nu_1(NO_3^-)$=1112 cm^{-1}, $\nu_2(NO_3^-)$=825 cm^{-1}, $\nu_3(NO_3^-)$= (1470 cm^{-1}), $\nu_4(NO_3^-)$= (750 cm^{-1}), and overtone of ν_2'=1650 cm^{-1}. From frequency-pressure dependence, two phase transitions at 5 GPa and 22 GPa were inferred. Compression below 30 GPa resulted in formation of the mixture of $NO^+NO_3^-$ and $NO_2^+NO_3^-$ with the complete conversion to $NO_2^+NO_3^-$ below 9 GPa at high temperatures. Hexagonal ($P6_3/mmc$, z=2) structure was confirmed. Raman modes are consistent with the previous results and summarized in table 3.4.

Table 3.4 *Summary of explored structures in N-O systems*

Compound / Phase	Structure	Raman modes
N_2O α I	Cubic Pa3; z=4 [Mills 91]	-
N_2O β III	Orthorhombic Cmca; a=54.987(1) Å, b=54.533(1) Å, c=56.220(1) Å; z=4 [Mills 91, Iota 04]	ν_2=600 cm^{-1} , bending doublet; ν_3=2350 cm^{-1}, asymmetric stretching; A=300 cm^{-1}, B=350 cm^{-1} [Iota 04];
N_2O II	-	ν_2=600 cm^{-1}, bending; ν_3=2350 cm^{-1}, asymmetric stretch; B_{2g}=250 cm^{-1}, Eg=380 cm^{-1} [Iota 04]

N_2O IV	Orthorhombic Pbcn; a=54.2356(6) Å, b=55.9825(10) Å, c=54.2232(13) Å; or Pbcm a=54.231(2) Å, b=55.987(2) Å, c=54.237(1) Å. [Iota 04]	ν_2=600 cm^{-1}, bending doublet; ν_3=2350 cm^{-1}, asymmetric stretch, 4 peaks; 8 low frequency modes [Iota 04];
NO^+NO^{3-}	Disordered (amorphous) [Bolduan 84]	$\nu(NO^+)$=2215 cm^{-1}, 2266 cm^{-1}; $\nu_3(NO^{3-})$=1373 cm^{-1}, antisymmetric stretch, E'; ν_1 (NO^{3-})=1046 cm^{-1}, symmetric stretch, A_1; ν_4 (NO^{3-})=717 cm^{-1}, in plane bend, E' [Bolduan 84]
NO^+NO^{3-} <5 GPa	Monoclinic $P2_1/m$; a=5.5594(8) Å, b=5.1169(7) Å, c=6.8214(9) Å, β=136.635 7°, V=133.24(2) $Å^3$, z=2(NO^+NO^{3-}), [Meng 06]	$\nu(NO^+)$=2235.4 cm^{-1}; $\nu_4(NO^{3-})$=716.5 cm^{-1}; $\nu_2(NO^{3-})$=820.1 cm^{-1}; $\nu_3(NO^{3-})$=1050.6 cm^{-1} [Meng 06]
NO^+NO^{3-} >5 GPa	Orthorhombic Pmmm; a=7.863(1) Å, b=16.519(3) Å, c =6.031(1) Å, V=783.42 $Å^3$/cell, z=10. [Sihachakr 06]	$\nu(NO^+)$= 2240 cm^{-1}, stretch N-O, A_g; $\nu_1(NO^{3-})$=1050 cm^{-1}, symmetric stretch; $\nu_2(N_2O)$=820 cm^{-1}, out-plane bend, A_g; ν_3=1390 cm^{-1}, antisymmetric stretch; $\nu_4(NO^{3-})$=720 cm-, bending, E'. [Sihachakr 06, Yoo 03], [Song 03b, Somayazulu 01]

$NO^{2+}NO^{3-}$ 0.5 GPa	Hexagonal $P6_3$ /mmc; a=5.3389(4) Å, c=6.2964(7) Å, V=155.42(2) $Å^3/mol$; Z=2 [Meng 06]	$\nu_1(NO^{3-})$=1054.0 cm^{-1}; $\nu_4(NO^{3-})$=724.5 cm^{-1}; $\nu_1(NO_2^+)$=1397.5 cm^{-1} $\nu_2(NO_2^+)$=523.8 cm^{-1} [Meng 06]
N_2O_4 α	Im3 cubic, a =7.77 Å; z=6; [Agnew 83, Song 03a]; Planar nitro molecule O_2N-NO_2 [Agnew 83]	$\nu_1(NO_2)$=1390 cm^{-1}, symmetric stretch, A_g; $\nu_2(NO_2)$=816 cm^{-1}, scissor mode, A_g; $\nu_3(N_2)$=280 cm^{-1}, N-N stretch, A_g; $\nu_5(NO_2)$=1732 cm^{-1}, antisymmetric stretch, B1g; $\nu_6(NO_2)$=507 cm^{-1}, rocking mode, B1g; $\nu_8(NO_2)$=296 cm^{-1}, wagging , B_{2g}; [Agnew 83]
N_2O_4 β	Noncubic; Planar nitro molecule O_2N-NO_2; [Agnew 83]	$\nu_1(NO_2)$=1398 cm^{-1}, symmetric stretch, A_g; $\nu_2(NO_2)$=820 cm^{-1}, scissor mode, A_g; $\nu_3(N_2)$=306 cm^{-1} , N-N stretch, A_g; $\nu_5(NO_2)$=1725 cm^{-1}, antisymmetric stretch, B1g; $\nu_6(NO_2)$=506 cm^{-1}, rocking mode, B1g; $\nu_8(NO_2)$=300 cm^{-1}, wagging mode, B_{2g}; [Agnew 83]

N_2O_4 γ	Cubic, lower symmetry, z=6 [Song 03a]	ν=730 cm^{-1} enhanced structure in the lattice mode region around 210-370 cm^{-1}; new peaks at 1104 cm^{-1} and 2208 cm^{-1} ; [Song 03a]

3.7 Summary

Now we have got a brief insight into such molecular systems as hydrogen, nitrogen and oxygen and nitrogen/oxygen mixtures, exceptionally diverse and rich with physical phenomena, although formed by simple elements. Therefore, next chapters will be devoted to the discussion of the following questions:

- Will pure rotational motion of H_2 and D_2 molecules in phase I persist unhindered across the whole pressure and temperature range of the existence of this phase? Is the nature of low-frequency excitations in phases II, IV and IV' rotational or vibrational?
- How can we compare hydrogen and deuterium P-T phase diagrams taking into account such features as the mass difference of the isotopes and delayed phase transitions to phase II in hydrogen and to phases IV and IV' in deuterium?
- What is the behaviour of nitrogen/oxygen mixtures with different concentrations compressed above 12 GPa? Are there any other phase transition, potentially related to those of pure components?
- Is it possible to form any compounds other than nitrosonium nitrate from nitrogen/oxygen mixtures by exposing the sample to high pressure and temperatures?

Chapter 4

Study of Hydrogen and Deuterium: nature of low-frequency modes and method of comparison of phase diagrams

4.1 Introduction

The effects of interactions between rotational motions and vibrations within the lattice have been extensively studied theoretically [Kranendonk 66, Silvera 80, Van Kranendonk 59, Van Kranendonk 83] and experimentally [Lorenzana 90, Hemley 90, Hemley 93, Mazin 97, Goncharov 98], altogether resulting in a formidable progress in understanding of these phenomena, but some important questions remain unclear. A unique property of quantum solid H_2, D_2 and HD is the presence of free rotational motion of the molecules against the background of weak anisotropic intermolecular forces (van der Waals forces). Theoretically, it was shown that these forces do not affect the energy of the rotational states with different J numbers [Kranendonk 66]. Nevertheless, anisotropic intermolecular forces and coupling between rotations and lattice vibrations result in energy shift and additional rupture of the degeneracy within the rotational levels [Kranendonk 66, Van Kranendonk 59, Van Kranendonk 83]. The low-frequency regions of the Raman spectra of H_2 and D_2 exhibit very distinctive features at

low pressures in quantum phases Phase I and Phase II. As pressure is increased within these phases, rotational modes smear, however, this low-frequency region shows very intense bands in the high-pressure phases IV and IV'. This intriguing behaviour triggers the interest in this experimental study.

Experiments, discussed in the contributed work, were carried out on both H_2 and D_2 at following temperatures: 10 K, 20 K, 43 K, 80 K, 150 K, and 300 K up to 150 GPa and 300 K to 400 GPa [1]

The main goal of the present chapter is the analysis of experimental Raman H_2 and D_2 features in order to get a better understanding of the rotational motion of hydrogen and deuterium molecules in various phases. In order to execute such analysis by indirect comparison of Raman features, we had to define how we compare phases of hydrogen and deuterium because of their differences. Therefore this chapter will consist of the Sections 4.2, 4.3, 4.4 devoted to the main discussion of low-frequency excitations in phases I, II, IV and IV' respectively, and Section 4.5 dedicated to the discussion of comparison of hydrogen and deuterium systems by pressure matching. The chapter will be finalized with a brief summary with the main results (Section 4.6).

4.2 Low-frequency modes fitting. Phases I and II

The nature of low-frequency excitations in hydrogen and deuterium is rather complex. At low pressures and while in Phase I, Raman spectrum of both isotopes comprises well-defined rotational peaks and lattice phonon. With pressure increase, low-frequency modes broaden and merge as will be illustrated in Figures of Section 4.3. As shown in previous theoretical and experimental research [Van Kranendonk 83], rotational levels broaden under compression due to their splitting into m sublevels because of the crystal field effect in hexagonal structure. $S_0(0)$ mode is formed by transition from J=0 to J=2, where J=2 have five sublevels with m=$\pm1, \pm2, 0$, where ±1 and ±2 are degenerate.

[1] Low-temperature experiments were conducted with the help of Dr. Liu and Dr. Dalladay-Simpson at the Institute of Solid State Physics, Chinese Academy of Sciences. The Room temperature experiments included the further assistance of Dr. M.Pena-Alvarez. Also, this chapter contains the analysis of previously collected but not analysed and/or published data by Dr. Liu, Dr. Dalladay-Simpson and Dr. Howie.

Therefore, $S_0(0)$ splits into three different contributions. $S_0(1)$ mode is formed by transition from J=1 to J=3, where J=1 have three sublevels with m=$\pm 1, 0$ (m=$\pm$1- degenerate), and J=3 have seven sublevels, with m=$\pm 1, \pm 2, \pm 3, 0$. (m=$\pm 1, \pm 2, \pm 3$ -degenerate). Therefore, $S_0(1)$ splits into eight contributions. There is no consistency in experimental literature about fitting of rotational peaks of isotopes as some sources present fitting with one contribution [Hemley 93], whilst others suggest fitting with two [Hemley 90, Mazin 97] or three [Hemley 90].

A naive notion, arising from the presence of degenerate sublevels, would lead to the conclusion that intensities of the contributions of roton S(0) should follow the ratio of 2:2:1. In fact, it was not possible to fit contributions with such ratios of intensity. So we did not fix this parameter. Observed deviation from 2:2:1 ratio could appear because of the preferred orientation of the crystal with respect to the back-scattering configuration of the Raman, or it could be related to the transformation from rotons to phonons at low temperatures.

We intend to examine how rotational peaks split with compression and if the splitting could be indicative not only of the field effect induced by compression of the hexagonal structure but also of any roton-phonon coupling, hindering rotational motion. We fit our experimental spectra into a sum of Voigt functions taking into account splitting of the sublevels. For that reason, the $S_0(0)$ band was fitted with three contributions $S(0)_1$, $S(0)_2$, $S(0)_3$, which was possible due to its fairly pronounced shape as demonstrated in Figure 4.1.

On the contrary, fitting of $S_0(1)$ band had encountered numerous difficulties. Ideally, this peak should be fitted with eight contributions. But as a result of the high overlap between these peaks and the pressure induced broadening, it is extremely hard to reliably define the positions for these contributions. Additionally, the substantial loss of intensity of $S_0(1)$ peak at low temperatures which is due to ortho-para transition makes the task of resolving the different contributions even harder. Thus, we decided to fit $S_0(1)$ excitation with two contributions ($S(1)_1$, $S(1)_2$) for deuterium and three contributions for hydrogen ($S(1)_1$, $S(1)_2$, $S(1)_3$) according to the shape of the final peaks as shown in Figures 4.1 A, B. Although these results will not be considered in the precise analysis of the low-frequency modes, they still can provide useful information for understanding how this quantum phase behaves under compression.

As mentioned before, Phase II exhibits very complex Raman spectrum, with

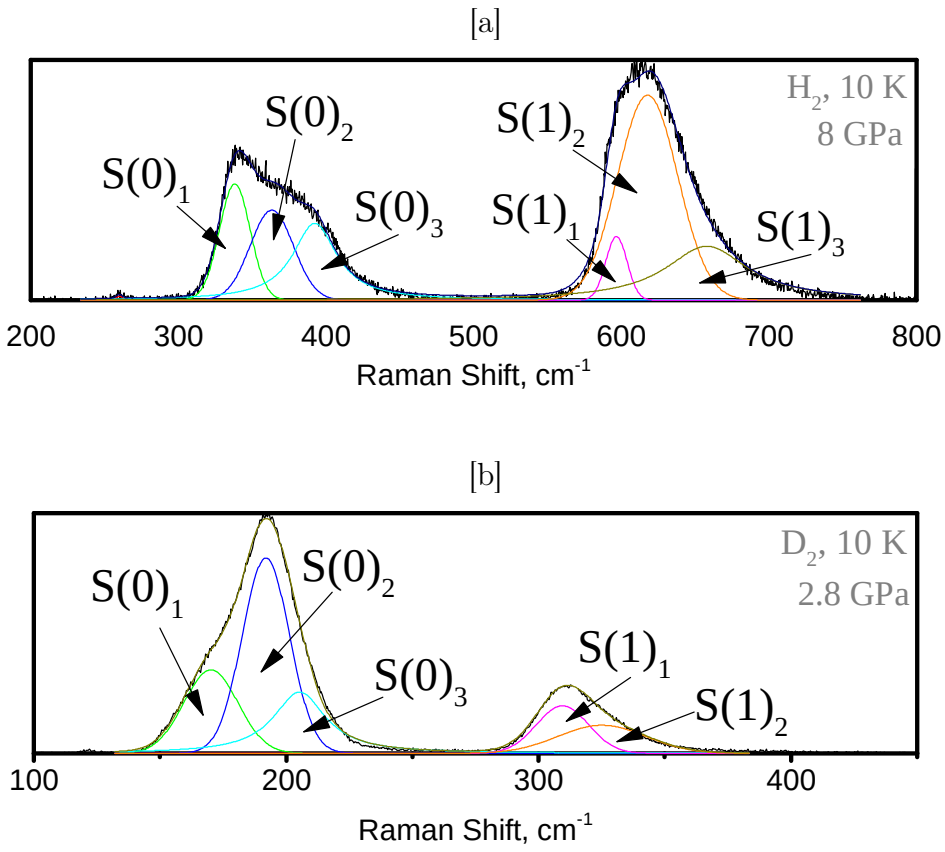

Figure 4.1 *Examples of the fittings of rotational modes of hydrogen (a) and deuterium (b) with Voigt function. S(0) peak (around 350 cm^{-1} for H_2 and 180 cm^{-1} for D_2) is fitted with three contributions for both hydrogen and deuterium, and S(1) peak (around 620 cm^{-1} for H_2 and 320 cm^{-1} for D_2) is fitted with three contributions in hydrogen and two contributions in deuterium.*

especially rich landscape in deuterium, making it difficult to distinguish between rotons and other low-frequency modes characteristic for this phase. The optimal fitting of Phase II in deuterium included eleven contributions, with three peaks which potentially belong to S(0) peak (Figure 4.4, and Figures A.2 and A.4 of Appendix B). But drastic difference between deuterium and hydrogen spectra and enormous broadening of S(0) contributions made it almost impossible to compare low-frequency modes of hydrogen and deuterium in phase II. Thus, further discussion on nature of low-frequency modes in hydrogen and deuterium will mainly focus on phase I.

Such properties of the contributed peaks as frequency, FWHM (full width at half maximum) and area were firstly obtained from the fitting of the experimental data collected at 10-40 K temperature window. This set was chosen because of

the well-pronounced peaks, therefore minimizing the error in their assignment. While fitting, it was important to control whenever possible a steady change of frequency and FWHM of the peaks, as long as the area of a peak strongly depends on experimental conditions and might not be a fair indicator. Then, these parameters were applied to the subsequent experimental runs in ascending order of temperature and refined for each data-set. This allowed us to track temperature changes on the shape and position of contributions to keep fittings consistent. Firstly, obtained parameters for each experimental set were plotted as a function of pressure. Then these dependencies were fitted with polynomial functions in order to get more data points at different pressures. Finally, these data points, obtained from polynomial dependencies, were used for further analysis.

Fittings of experimental data sets, collected at 10 K, 20 K, 40 K, 80 K, 150 K and 300 K will be discussed in details in the following chapter. Due to the great number of plots and detalization, illustrations demonstrating frequency and FWHM plotted as functions of pressure for 10 K, 20 K, 40 K, 80 K, 150 K and 300 K will be located in Appendix B.

4.3 Rotons to phonons transition. Phases I and II

As known, Phase I of hydrogen comprises a hexagonal structure with freely rotating molecules [Hazen 87], whereas in phase II rotational motion of the molecules is restricted [Mao 94]. The aim of this section is to examine whether the rotational motion is persistent in the entire domain of phase I or becomes slowly hindered upon approaching to phase II and phase III domains. It can be done indirectly, e.g., by checking whether these excitations can be described by methods applicable for unaltered rotational or vibrational modes.

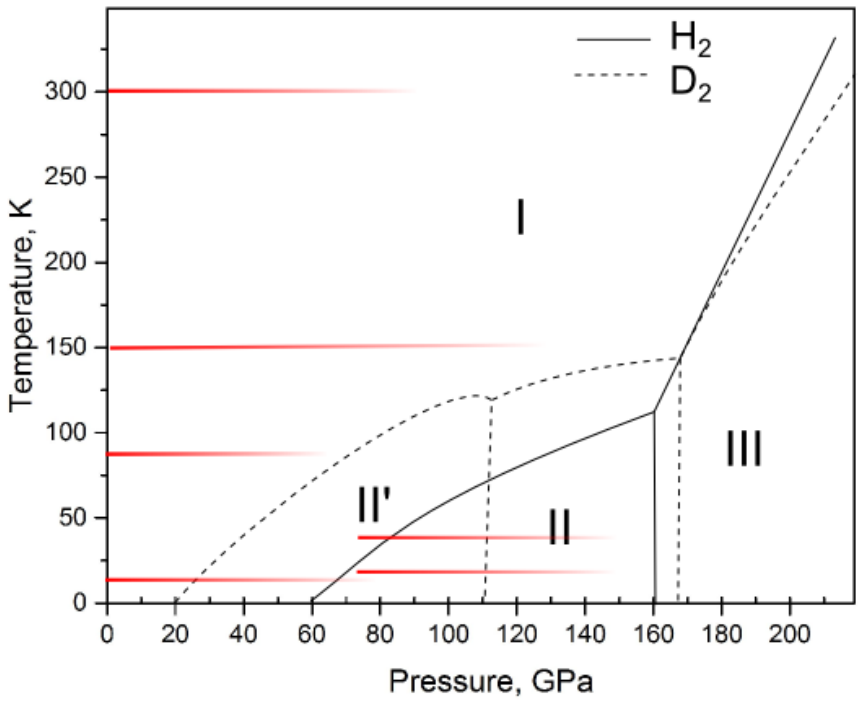

Figure 4.2 *Schematic representation of the overlapping H_2 and D_2 phase diagrams mapped in the P-T range not exceeding 400 K and 220 GPa [Liu 17]. The red lines depict pressure and temperature range of experimental data collected in this project. Dotted line is for deuterium, solid line is for hydrogen. Phase transions I-II in hydrogen and I-II' in deuterium have pressure difference of approximately 20 GPa. This difference strongly depends on the conditions of the experiment and ortho-para conversion rate (Chapter 2).*

As discussed in Chapter 2, due to the mass difference in hydrogen isotopes, the energy of rotational levels in hydrogen and deuterium scales down by a factor

of 2, whereas vibration frequency scales down by a factor of $\sqrt{2}$. Therefore, comparison of frequencies of rotational modes in the isotopes can be a first step in understanding whether these excitations arise from pure rotational motion.

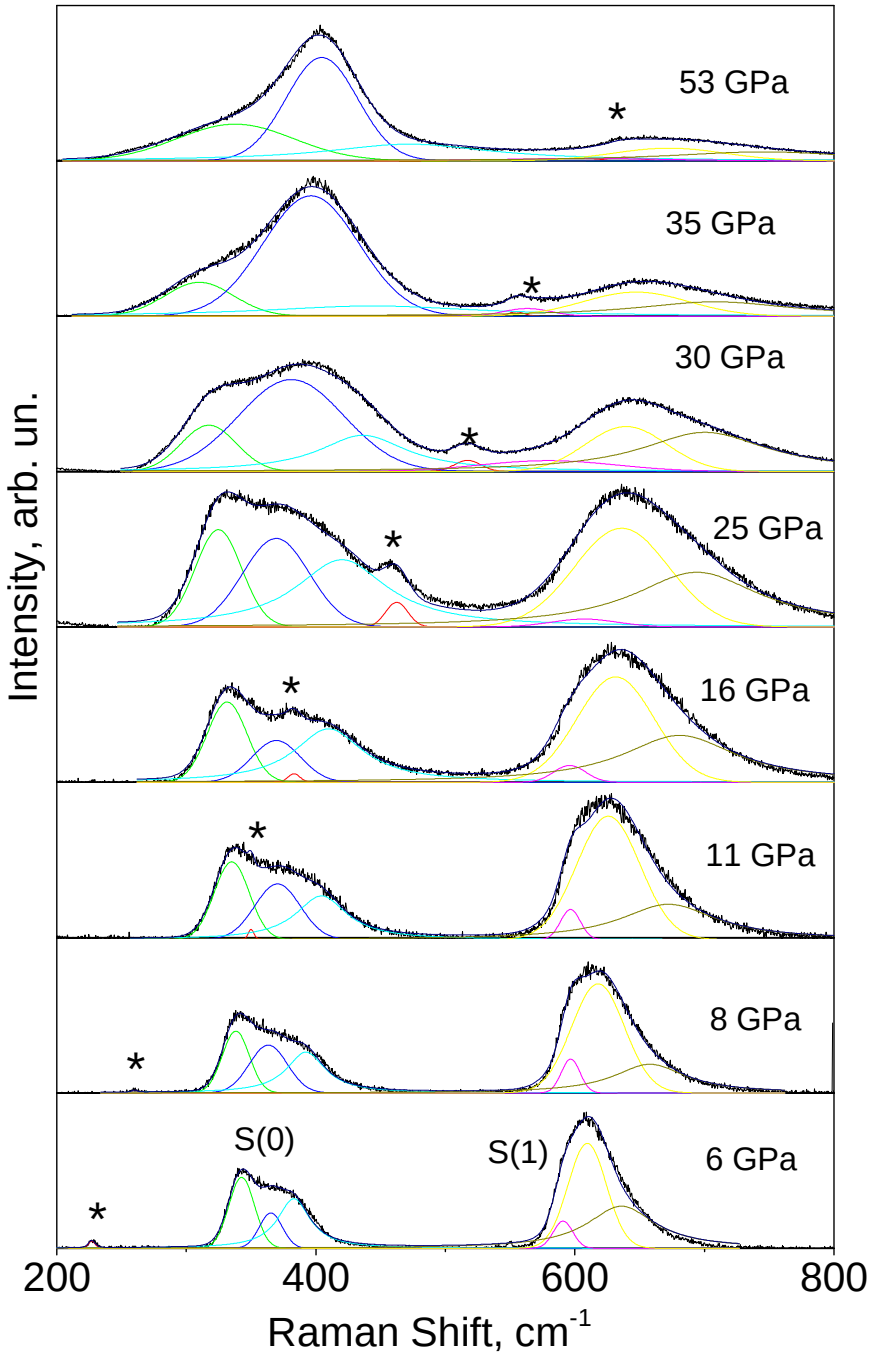

Figure 4.3 *Representative Raman spectra of hydrogen at 10 K. Peak S(0) is fitted with three contributions, as peak S(1). Phonon mode is a red peak indicated with an asterisk, and is shifting with pressure faster than rotational modes. Under compression all contributions broaden, with those of S(1) significantly losing intensity due to ortho-para conversion.*

We will begin with the analysis of low-temperature domain of phase I. First data

set to be fitted was collected at 10 K (H_2 and D_2 up to 50 GPa), 20 K (H_2 to 160 GPa) and 40 K (D_2 up to 150 GPa). As shown in Figures 4.3 and 4.4, low-frequency modes of both hydrogen and deuterium exhibit prominent peaks. We begin with fitting of this experimental run at low pressures, adjusting parameters (frequency, FWHM and area) with the pressure increase.

In hydrogen, at 6 GPa at 10 K, we observe signal from rotational peaks S(0) and S(1) at around 350 cm^{-1} and 620 cm^{-1} respectively, and the lattice mode at around 220 cm^{-1} (Figures 4.3, A.3). Under compression, phonon shifts to higher frequency, which results in the overlap of phonon peak with rotational peaks. Nevertheless, in spite of increased complexity of fitting, we were able to trace phonon peak to high pressures and estimate its influence on other peaks. We observe the increase of intensity of the first peak, associated with rotational motion, with pressure, followed by the decrease of intensity of the S(1) peak. This is related to the ortho-para conversion, which is facilitated under compression. Hydrogen is expected to undergo transformation to phase II at pressures above 50 GPa.

Whilst in phase I, deuterium behaves similarly to hydrogen. But upon transformation to phase II' around 30-35 GPa, its low-frequency modes become much more complex than those of hydrogen (Figure 4.4). Low-frequency landscape of of phase II' in deuterium is enriched with new modes, presumably coming from lattice phonons, and therefore requires fitting with additional peaks. In phase II', modes in the region between 200 and 400 cm^{-1} become much smoother and broader. Based on frequency-pressure behaviour, they were tentatively assigned as shifted peaks of S(0) (Figure A.2, A.4). Contributions of S(1) merge and significantly loose intensity, thus becoming undetectable. Phonon mode is well pronounced, as in hydrogen, and can be detected even in phase II'.

As a result of performed fitting, we determined frequency-pressure dependencies for low-frequency modes of both hydrogen and deuterium at 10 K (Figures A.1, A.2), which were fitted with polynomial functions of third order. Using these polynomials, we examined behaviour of low-frequency modes by analysing ratios ν_{H_2}/ν_{D_2} of corresponding contributions in hydrogen and deuterium.

Figure 4.5 represents such comparison for experimental data, fitted with polynomial functions, at 10 K at nominal pressures. Steep trends for all three contributions of S(0) at 10 K point downward in the direction from 2 (characteristic

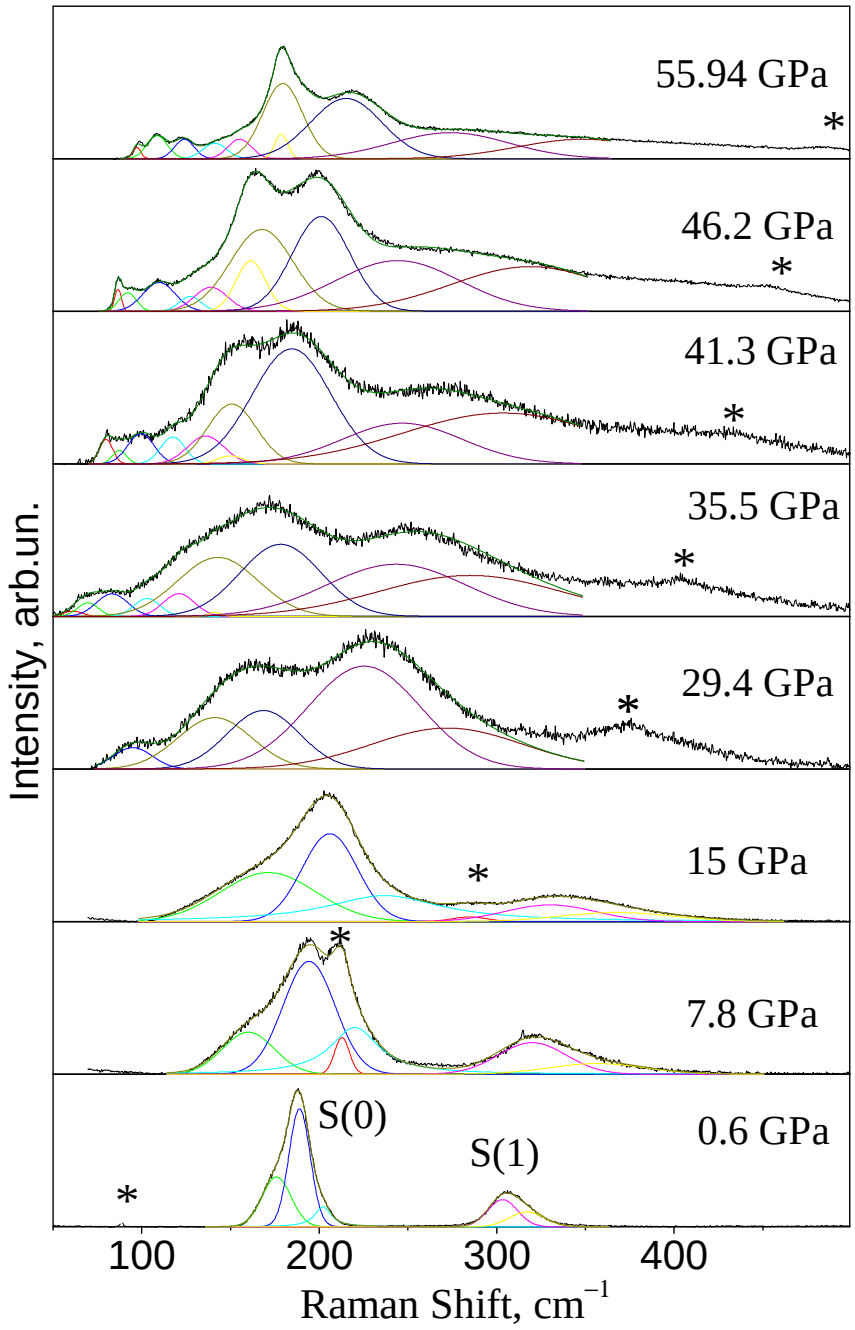

Figure 4.4 *Representative Raman spectra of deuterium at 10 K. Peak S(0) is fitted with three contributions, and peak S(1) is fitted only with two contributions due to peak of S(1) being much broader and less intense than in hydrogen. Phonon mode is a peak indicated with an asterisk, and is shifting with pressure faster than rotational peaks, as in hydrogen. Around 30 GPa, deuterium undergoes transformation to phase II', which is reflected by appearance of new low-frequency modes, most probably related to lattice phonons. Contributions, associated with S(0) peak, in 200-400 cm^{-1} range become very broad and hardly detectable, therefore they were assigned only tentatively.*

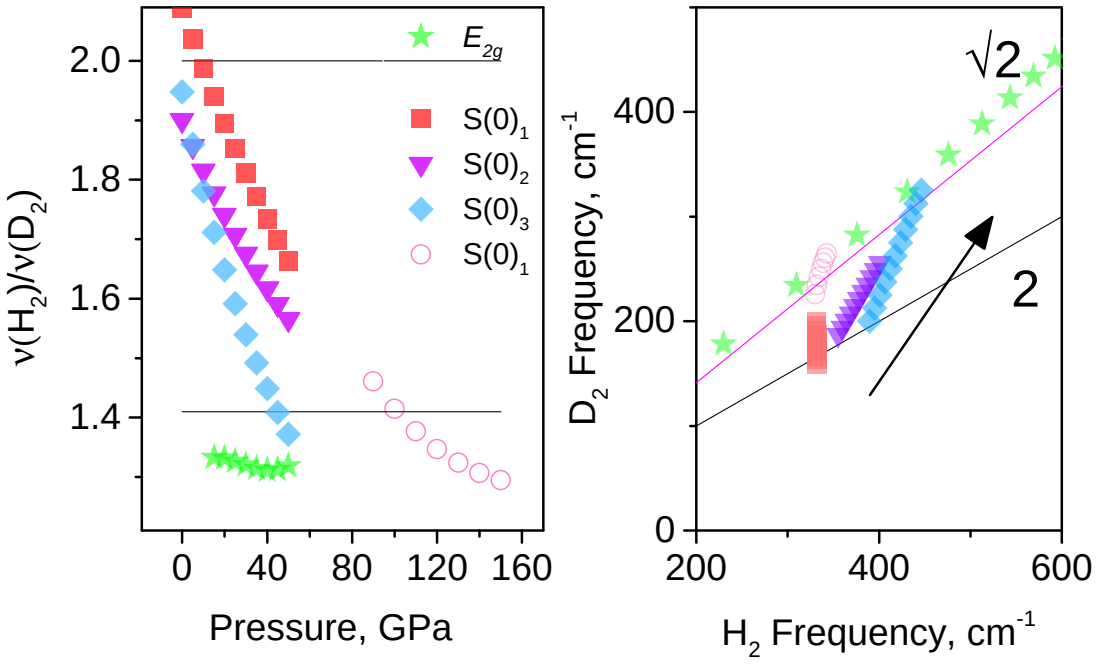

Figure 4.5 *Ratios of ν_{H_2}/ν_{D_2} plotted versus pressure and D_2 frequencies plotted versus H_2 frequencies at 10 K. Plot is based on two experiments, conducted in different pressure ranges: 0-50 GPa (phase I), and 80-160 GPa (phase II). Trends for contributions, observed in phase I, are portrayed with the solid symbols. In phase II, where it was possible to compare only $S(0)_1$ contribution,the trend for $S(0)_1$ is depicted with hollow pink circles. The arrow points in the direction of pressure increase. Trends for 10 K are very steep and are going in the direction from 2 to $\sqrt{2}$, which indicates that rotational motion becomes more hindered at lower temperatures with pressure increase.*

for rotons) to $\sqrt{2}$ (characteristic for phonons and vibrons), whereas phonon E_{2g} remains stable around 1.39. The ratio of the only detected $S(0)_1$ contribution of hydrogen and deuterium at pressures above 80 GPa (phase II in hydrogen and II' in deuterium) is located in the region of values characteristic for phonons, around 1.4 - 1.39. This curious behaviour indicates that rotational motion becomes continuously hindered with compression, and as a result rotons tend to turn into phonons.

Next temperature step that will be used for the analysis is 80 K. At this temperature, we expect transition to phase II (II' for D_2) in hydrogen and deuterium at around 100 GPa (see phase diagram in Figure 4.2). Indeed, Raman spectra at pressures up to 50 GPa do not exhibit any dramatic changes, besides from normal temperature and pressure broadening (Figures 4.6, 4.7). There are explicit differences in intensity of corresponding rotons of hydrogen

and deuterium, which again is related to the rates of ortho-para transition in isotopes. With the temperature increase, phonon peak becomes less prominent, so at some pressure steps it was assigned only approximately in the way, which allowed to keep such parameters as frequency and FWHM of all other related peaks consistent (Figures A.5, A.6).

Comparison of low-frequency modes by ratios ν_{H_2}/ν_{D_2} shows similar trend as at 10 K, with ratios of all contributions moving from 2 to $\sqrt{2}$ (Figure 4.8). Nonetheless, the slope of the trend lines is less steep than at lower temperatures (Figure 4.5). Such behaviour should not be surprising to us, in case it is related to gradual hindering of rotational motion upon transition to phase II. Indeed, at 80 K phase transition I-II occurs in pressure window of 60-100 GPa. And trend lines clearly move in the direction of $\sqrt{2}$, which they will most probably reach after transformation to phase II.

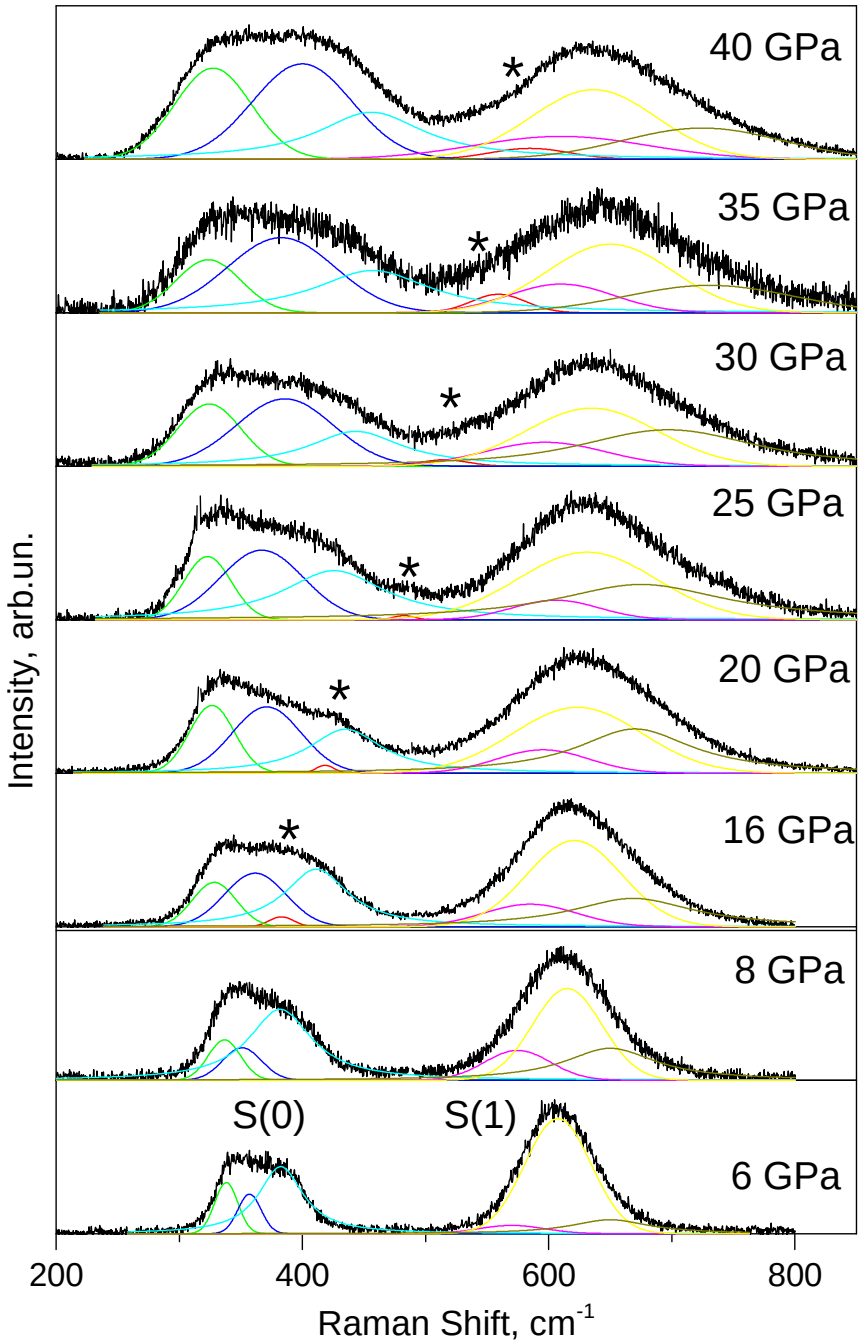

Figure 4.6 *Representative Raman spectra of hydrogen at 80 K. Peak S(1) is much more intense than at 10 K, and merges with S(0) at higher pressures. Shape of the resulting peaks becomes smoother than at lower temperatures, therefore hampering fitting of contributions. Phonon mode is marked with an asterisk.*

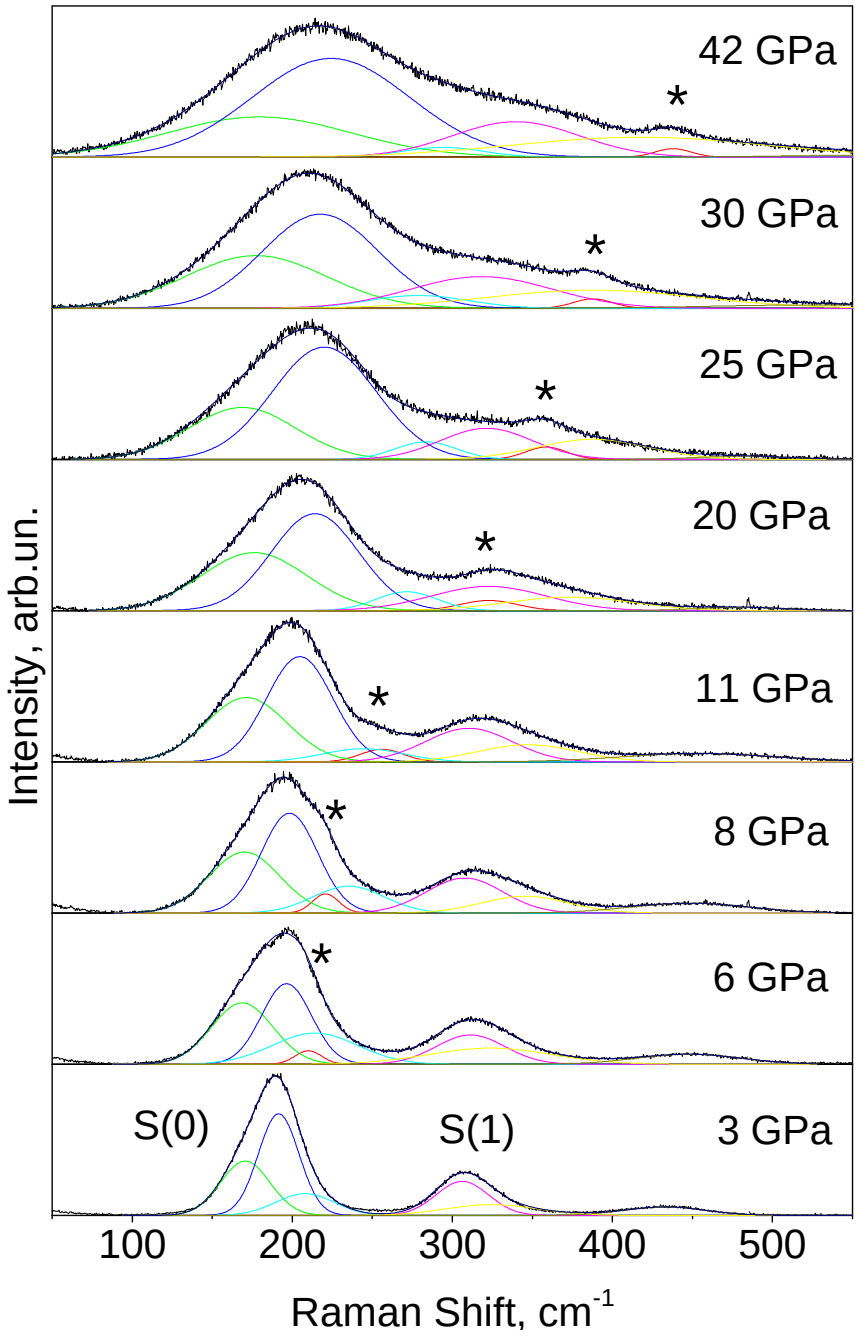

Figure 4.7 *Representative Raman spectra of deuterium at 80 K. Here, the most intense peak is S(0), as at 10 K. Therefore, it is easy to detect and trace phonon mode, marked with asterisk. At higher pressures, all contributions become much wider and peaks of the resulting profile eventually merge, which affects the accuracy of fitting.*

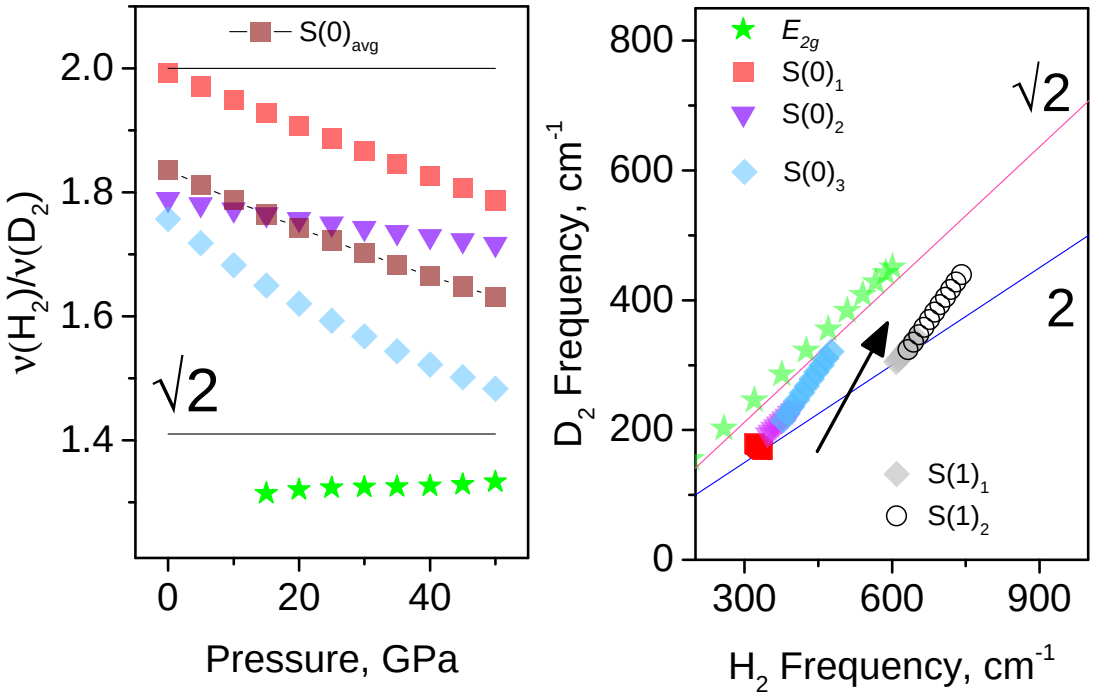

Figure 4.8 *Ratios of ν_{H_2}/ν_{D_2} plotted versus pressure and D_2 frequencies plotted versus H_2 frequencies at 80 K at pressures up to 50 GPa. Black lines with dark red squares perform the trend for the positions calculated as an average of all three contributions. Arrow points in the direction of pressure increase. Trends for all contributions still point in the direction of $\sqrt{2}$, but the slopes are less steep than at 10 K. This means that at 80 K rotons will turn into phonons at higher pressures than at lower temperatures. Thus, rotational motion becomes more hindered upon transformation to phase II, which at 80 K also occurs at higher pressures, than at 10 K.*

Pronounced differences are present at 150 K and 300 K. Firstly, phases II and II' do not exist at temperatures above 150 K in either isotope. At 150 K hydrogen and deuterium undergo transformation from quantum phase I to classical phase III at pressures around 160 GPa. In our experiments, although we reached pressures of 150 GPa for D_2 and 165 GPa for H_2 at 150 K, we did not observe transition to phase III. At 150 K, the effect of temperature and pressure broadening of low-frequency modes is very noticeable. At pressures above 50 GPa for hydrogen and 20 GPa for deuterium, resulting peaks of S(0) and S(1) merge and eventually look like a single and very broad band, as shown in Figures 4.9 and 4.10. Nevertheless, these merged bands are still located within sensible frequency range of rotational peaks, that they are formed of, which is approximately 200-900 cm^{-1} for H_2 and 50-600 cm^{-1} for D_2. This fact leads to a conclusion, that although most of contributions of rotational peaks slightly shift with pressure, the main reason for peak merging under compression is significant increase of peak width, whereas frequencies change very moderately (Figures A.7, A.8). Therefore, we were able to tentatively determine frequencies of contributions of S(0) and S(1) even when their shape became less pronounced.

Comparison by analysis of ν_{H_2}/ν_{D_2} ratios showed very interesting behaviour (Figure 4.11). Trends for all contributions have a steep slope in the pressure range from 0 to approximately 30 GPa. But under further compression slopes of the trend lines drastically change, and ratios remain relatively stable at the level between 1.7-1.9 in the pressure range from approximately 30 to 150 GPa. Significant deviation of the ratio for the first contribution $S(0)_1$ above 2, that we observe in the plot, is related to the especially high sensitivity of calculations to the obtained positions at low frequencies and inaccuracies in their estimations at higher temperatures due to the broad shape of the peaks. In general, ratios ν_{H_2}/ν_{D_2} of all contributions are located in the range closer to 2, than to $\sqrt{2}$. In other words, these excitations behave more like rotons, than phonons, although rotational movement is slightly hindered (Figure 4.11), compared to the lower temperatures (10 K and 80 K), when the rotational motion was significantly hindered with compression, which eventually led to rotons turning into phonons in phase II. And as we can see now, this behaviour differs from the behaviour of rotons at 150 K, where motion remains mainly rotational in the whole pressure range for phase I, practically until transformation to phase III.

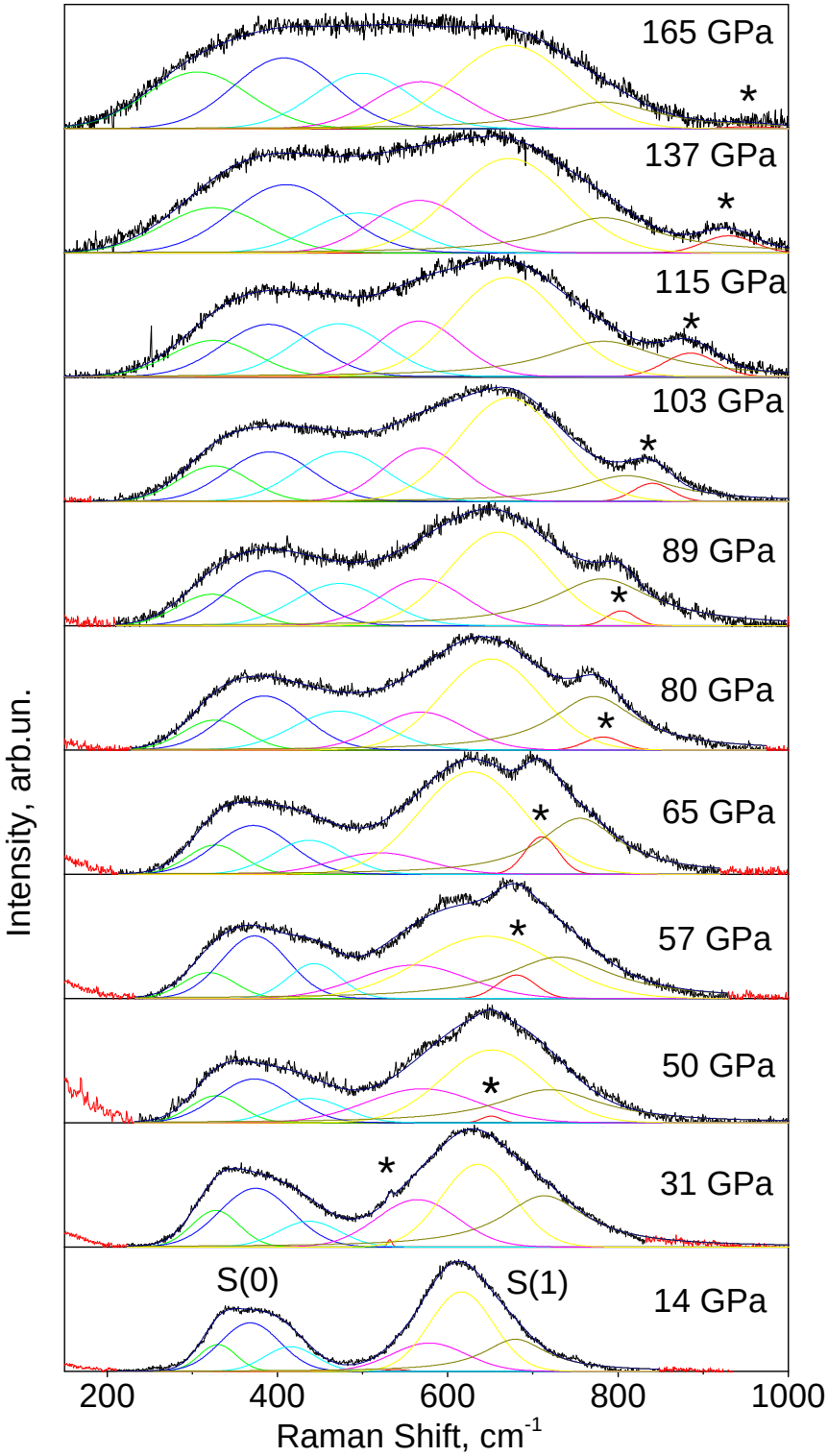

Figure 4.9 *Representative Raman spectra of hydrogen at 150 K. Under compression, contributions of S(0) and S(1) broaden, which leads to low-frequency modes looking like one wide band. Phonon band, marked with an asterisk, remains very distinct in the whole pressure range. Background, coloured in red, was masked from fitting.*

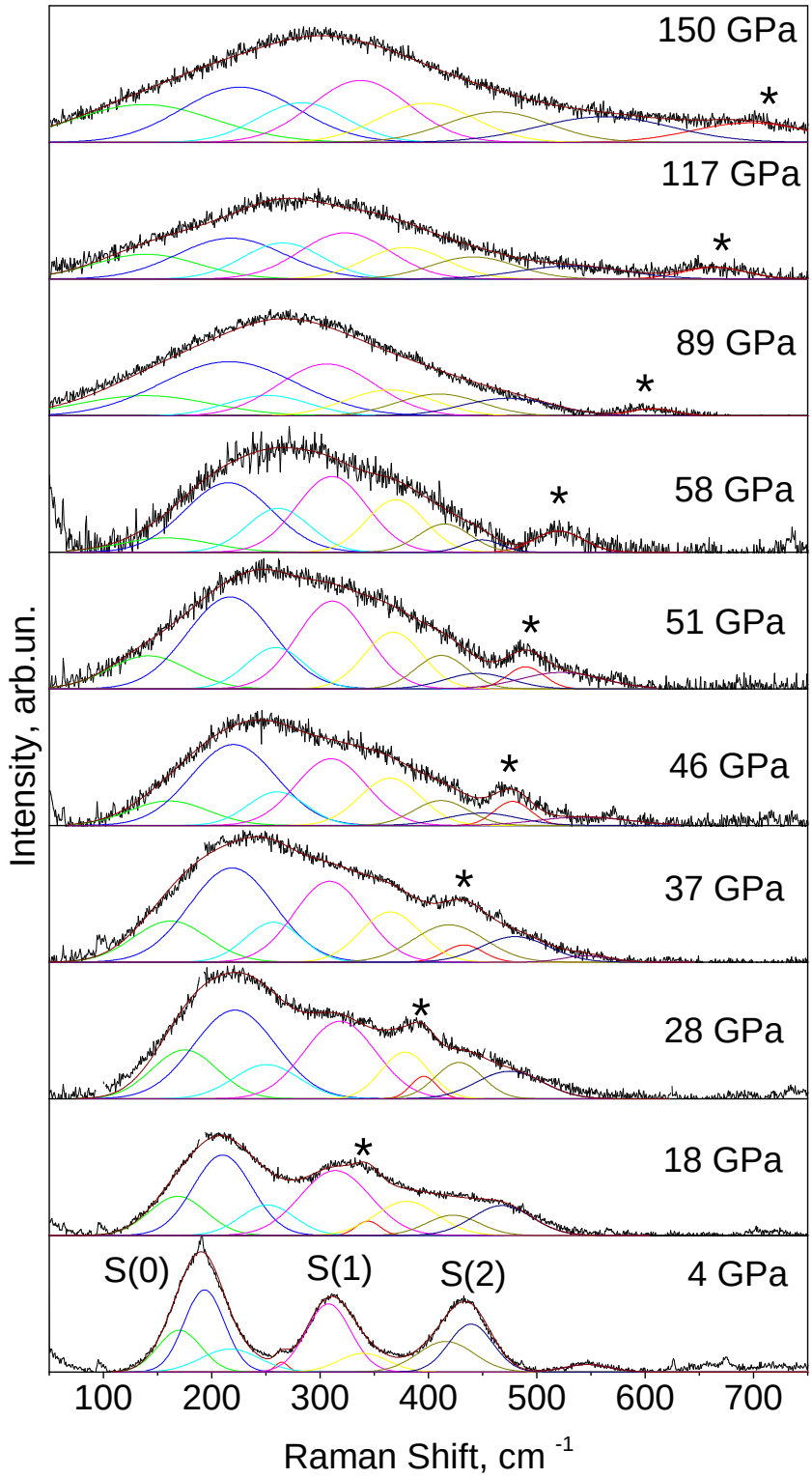

Figure 4.10 *Representative Raman spectra of deuterium at 150 K. Similar to hydrogen, contributions of S(0), S(1) and S(2) broaden under compression, resulting into single low-frequency mode on the Raman spectra. As in hydrogen, phonon band, marked with an asterisk, was traced until maximum pressures of this experiment. Background, coloured in red, was masked from fitting.*

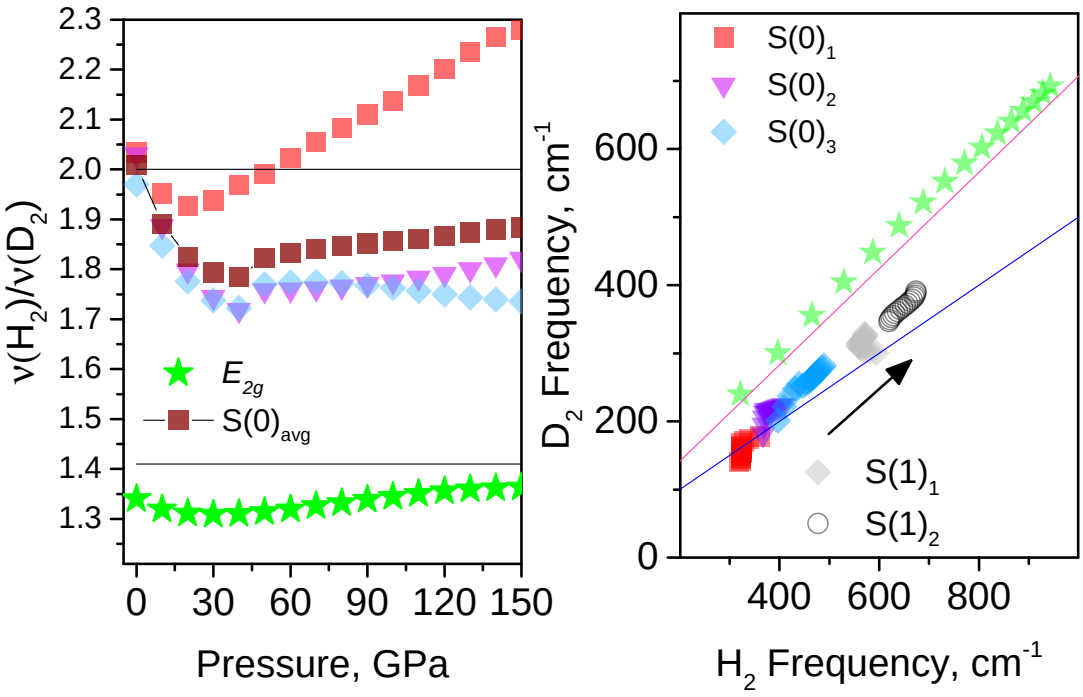

Figure 4.11 *Ratios of ν_{H_2}/ν_{D_2} plotted versus pressure and D_2 frequencies plotted versus H_2 frequencies at 150 K at pressures up to 150 GPa. The black lines with dark red squares perform ratio for the positions calculated as an average of all three contributions in hydrogen and deuterium. The arrow points in the direction of pressure increase. Ratios of most contributions tend to stay in the range 1.7-1.9, which implies that motion remains mainly rotational, although slightly hindered.*

Final data set was collected at 300 K with compression to 50 GPa (Figures 4.3 an 4.13). At room temperature S(1) and S(2) rotons are more intense, than at low temperatures, where S(0) roton is dominant. Pressure induced broadening and low intensity of S(0) makes it very hard to resolve different contributions of S(0) in both hydrogen and deuterium. Another difficulty arises from the increased intensity of peak S(1) in hydrogen and S(1) and S(2) in deuterium. Naturally, one would expect that fitting of the peak with higher intensity will help to obtain more accurate parameters. However, as discussed above, peak S(1) ideally should be fitted with eight contributions, which is not possible realistically. Thus, S(1) peak is still fitted with three contributions for hydrogen and two contributions for deuterium. Therefore, although fittings were carried out in a manner consistent with previous experiments, it is very possible that systematic errors of fitting at this temperature are bigger.

Due to the systematic errors and relatively small pressure range, comparison of hydrogen and deuterium systems at room temperature gives rather unreliable results. We can see in Figure 4.14, that trend lines tend to have remarkably different slopes. Trend line, calculated as ratio for average positions of three contributions of S(0) peak in H_2 and D_2, appears to be located between 1.7-1.8. This might indicate rotational nature of motion of molecules, but obtained results are not accurate enough to make any conclusion.

Together with the observed differences in behaviour of rotons, phonon E_{2g} at all temperatures showed typical phonon ratio close to 1.39 (Figures 4.5, 4.8, 4.11, 4.14) across the entire pressure range of the performed experiments. First of all, this indicates that suggested method of comparison gives correct results, and observed changes in rotational trends are caused by the transition to a different type of excitation. Secondly, it proves, that in our case comparison of the systems at nominal pressures is valid. Nevertheless, in this specific case phase transition to phases II in hydrogen and II' in deuterium occurred at the same pressure range (around 30- 35 GPa), which might not be true for other experiments. In these instances we propose to consider pressure scaling, as it will be discussed in the Section 4.5.

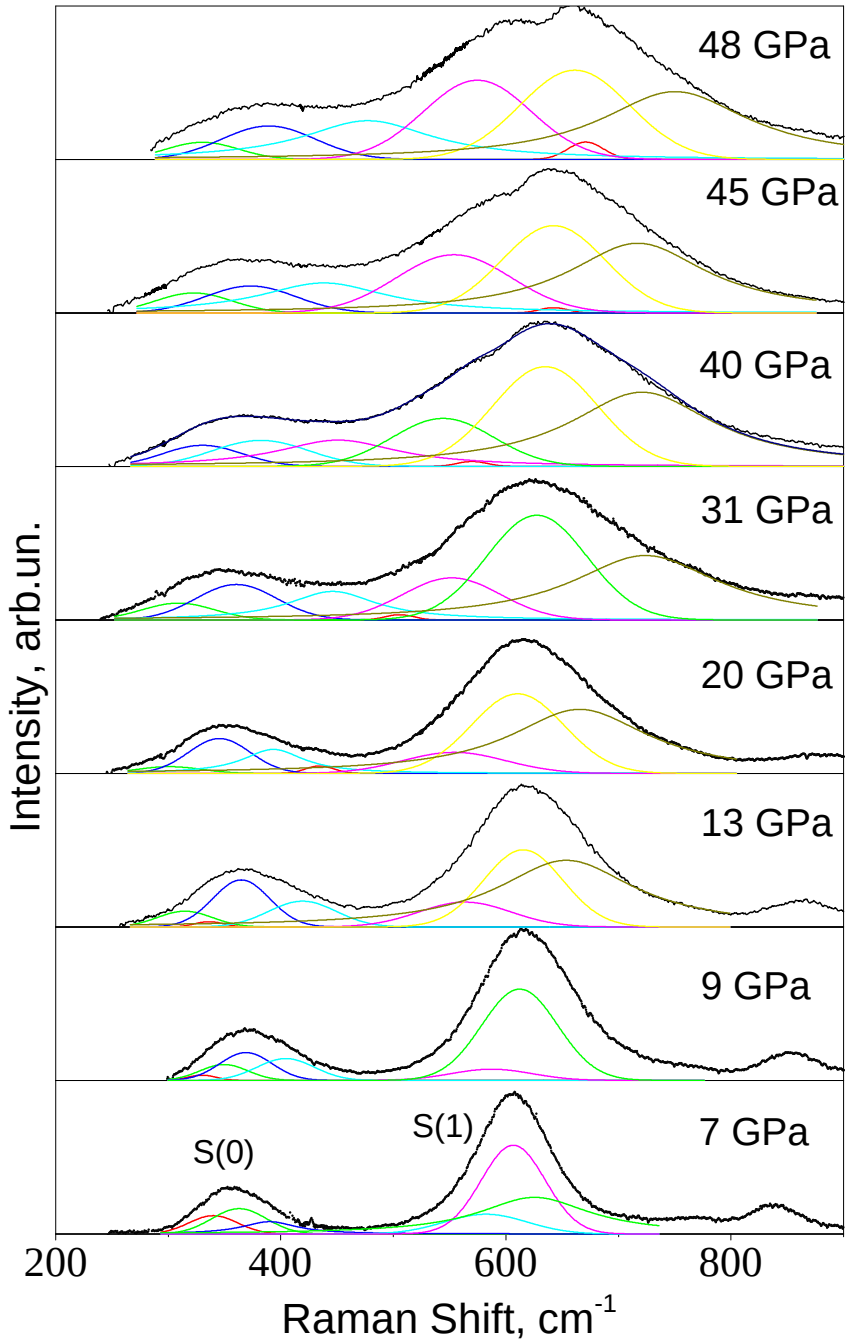

Figure 4.12 *Representative Raman spectra of hydrogen at 300 K to maximum pressure of 48 GPa. S(1) peak becomes more intense under compression. Contributions of S(0) and S(1) are very hard to resolve, therefore they were assigned only tentatively. Phonon mode is marked with an asterisk.*

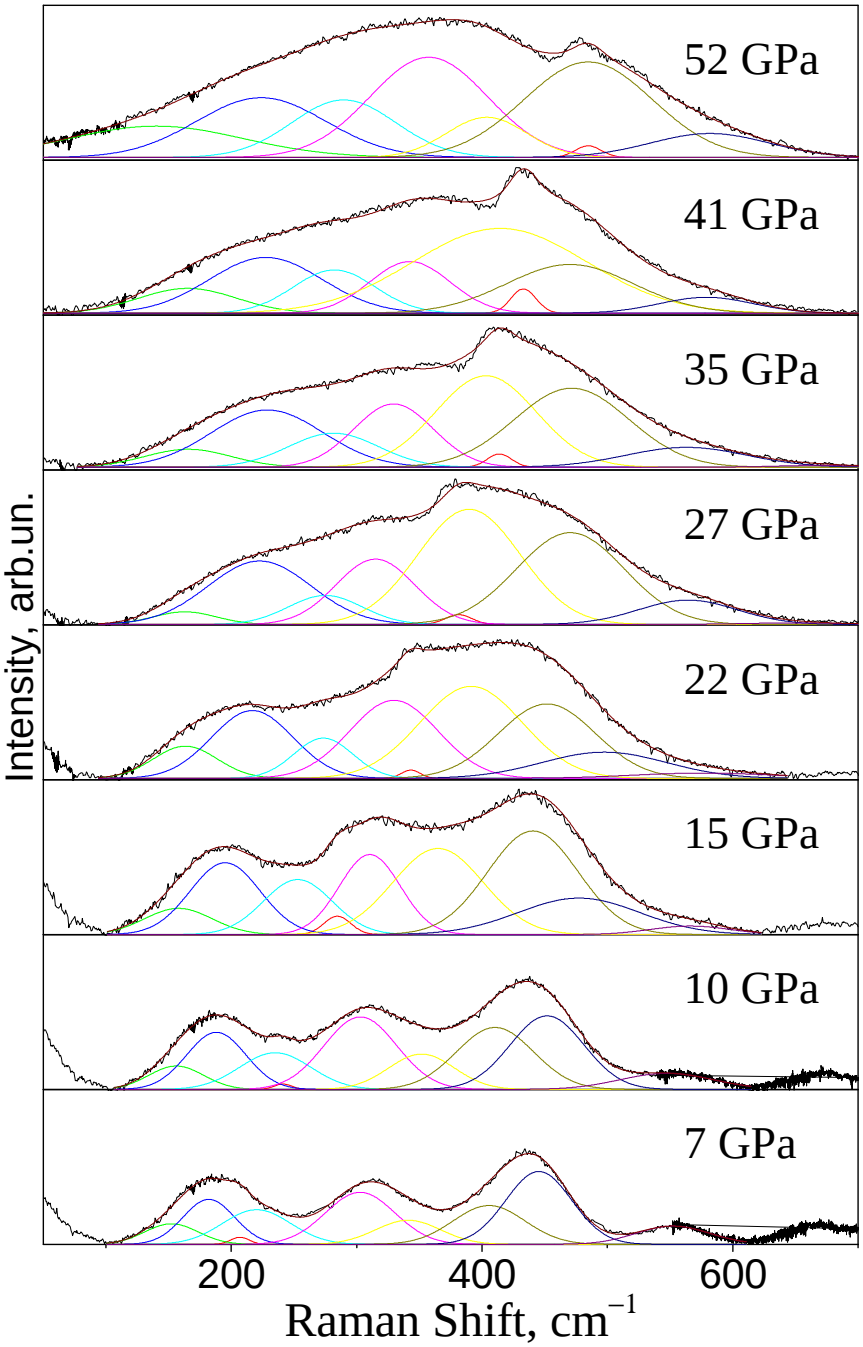

Figure 4.13 *Representative Raman spectra of deuterium at 300 K to maximum pressure of 52 GPa. In addition to roton S(1), as in hydrogen, we observe appearance of roton S(2). Peak S(2) was fitted with two contribution, suggested by the shape of the peak, in order to obtain the optimal fit. Contributions of peaks S(0) and S(1) are very hard to resolve, therefore they were assigned only tentatively. Phonon mode is marked with an asterisk.*

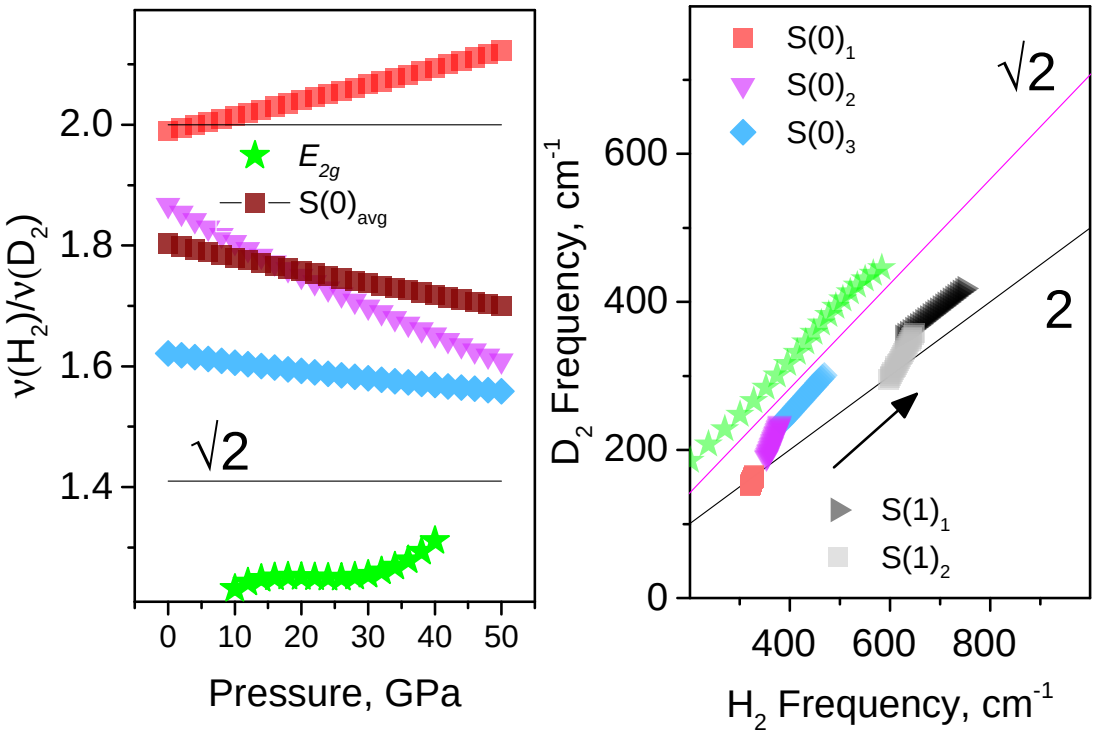

Figure 4.14 *Ratios of ν_{H_2}/ν_{D_2} plotted versus pressure and D_2 frequencies plotted versus H_2 frequencies at 300 K. Maximum pressure reached in these experiments is 50 GPa. The black lines with dark red squares perform ratio for the positions calculated as an average of all three contributions in hydrogen and deuterium. The arrow points in the direction of pressure increase. Temperature and pressure induced broadening of modes and decreased intensity of S(0) contributions resulted in systematic errors in fitting of profile with Voigt functions. We observe, that even at low pressures ratios ν_{H_2}/ν_{D_2} are not very consistent. Nevertheless, trend line which reflects calculations for average position of all contributions of S(0) peak, is still located in the range 1.7-1.8, which implies that rotation motion of the molecules prevails at these conditions.*

Summarizing all discussed above, we successfully accomplished the first attempt to analyse the rotational behaviour of the molecules in phases I and II (II' of D_2) by examination of ν_{H_2}/ν_{D_2} ratios of contributions, which compose rotons S(0) and S(1) in hydrogen and deuterium according to previous theoretical calculations [Kranendonk 66, Van Kranendonk 83, Silvera 80]. Theoretically, in the case when molecular motion is purely rotational, this ratio ν_{H_2}/ν_{D_2} should be equal 2. And for purely vibrational motion it should be equal to $\sqrt{2}$ (or 1.39, which was calculated from experimental data) [Silvera 80]. Experiments presented in the contributing work revealed the peculiar behaviour of rotons in different parts of phase I, which is reflected either by change of the ν_{H_2}/ν_{D_2} ratios for rotational peaks from 2 to $\sqrt{2}$ (or 1.39) under compression or by relative stability of these ratios in area of values, characteristic for rotons. Observed trends point to the difference between those domains of phase I, where below 150 K hydrogen and deuterium transform to phase II, and above 150 K where they undergo transformation directly to phase III.

At temperatures below 150 K, rotational motion becomes more hindered under compression, and rotons continuously become phonons. This transition takes place whilst in phase I, and presumably is accomplished after transformation from phase I to phase II (II'). In our experiments at 10 K, phase transitions to phases II and II' in hydrogen and deuterium occurred at the same pressure window, between 30-35 GPa. But ratios ν_{H_2}/ν_{D_2} reached values close to 1.4-1.39 after phase transition, only around 60 GPa, being already in phase II (II'). This phenomenon might be related to the mechanisms leading to the formation of phase II and effects of pressure induced ortho-para conversion, but more research is required to understand what influence these effects have on each other.

At higher temperatures, rotational motion seems to persist over the pressure range of phase I up to 150 GPa. Yet, the frequency ratios still show deviation from the purely free rotational motion. Such slight hindering of rotational motion might be due to the rotational levels suffering shift which arises from the coupling of rotational states with lattice vibrations and anisotropic intermolecular forces, or interference with other modes, which might become Raman active under compression.

4.4 Low-frequency modes fitting and analysis. Phases IV, IV' and V

Recent experimental discoveries of high pressure phases IV, IV' and V of hydrogen and IV and IV' of deuterium reignited the field [Eremets 11, Howie 12a, Dalladay-Simpson 16] (phase diagram can be found in Figure 3.2). Complex behaviour of hydrogen and its isotope at extreme pressures makes it very difficult to determine structure of these high pressure phases accurately. We know, that Raman spectra of both isotopes in phases IV and IV' features prominent peaks in low-frequency area [Howie 12a, Dalladay-Simpson 16]. In phase I similar peaks appear because of the rotational motion of the molecules (Section 4.3). Which then raises following questions: what are the low-frequency modes in phases IV and IV' of H_2 and D_2? Do they reflect rotational motion, and therefore quantum nature of these phases, or they are related to lattice phonons? In order to answer these questions we will do a brief analysis, using the same method as in Section 4.3.

This section presents accurate fittings of the Raman spectra of hydrogen and deuterium at pressures above 200 GPa.[2] Obtained results are in overall agreement with previously published data [Howie 12a, Howie 12b, Dalladay-Simpson 16]. Nevertheless, there are some differences, which can be explained by the difference in data interpretation.

Three low-frequency modes L_1, L_2, L_3 of phase IV are accompanied by another peak L_4 emerging in the vicinity of peak L_3 in both H_2 and D_2 (Figure 4.16,4.15). In the presented analysis peak L_4 in deuterium is detected only around 340 GPa, while Dalladay et. al. reported its emergence already at 300 GPa [Dalladay-Simpson 16].

L_3 peak was previously thought to disappear with transformation to phase V [Dalladay-Simpson 16]. On the other hand, the frequency-pressure trend with its steep increase to the higher energy region might be construed as a gradual overlap of L_3 mode with the 1-st order diamond Raman peak around 1330 cm^{-1} (see trend lines in Figures A.12, A.11 of Appendix B). In the presented way of fitting, area and FWHM of this peak are decreasing with pressure which is in a good agreement

[2]High-pressure experiments, described in this section were conducted by Dr. Howie and Dr. Dalladay-Simpson, and fitted and analysed by the author of the present thesis.

with the previous research [Dalladay-Simpson 16]. Nevertheless, in case this peak shifts in the area of the diamond band, we can speculate that FWHM and area trends are not entirely correct and instead of exhibiting massive decrease under compression above 300 GPa they might be expected to be relatively stable.

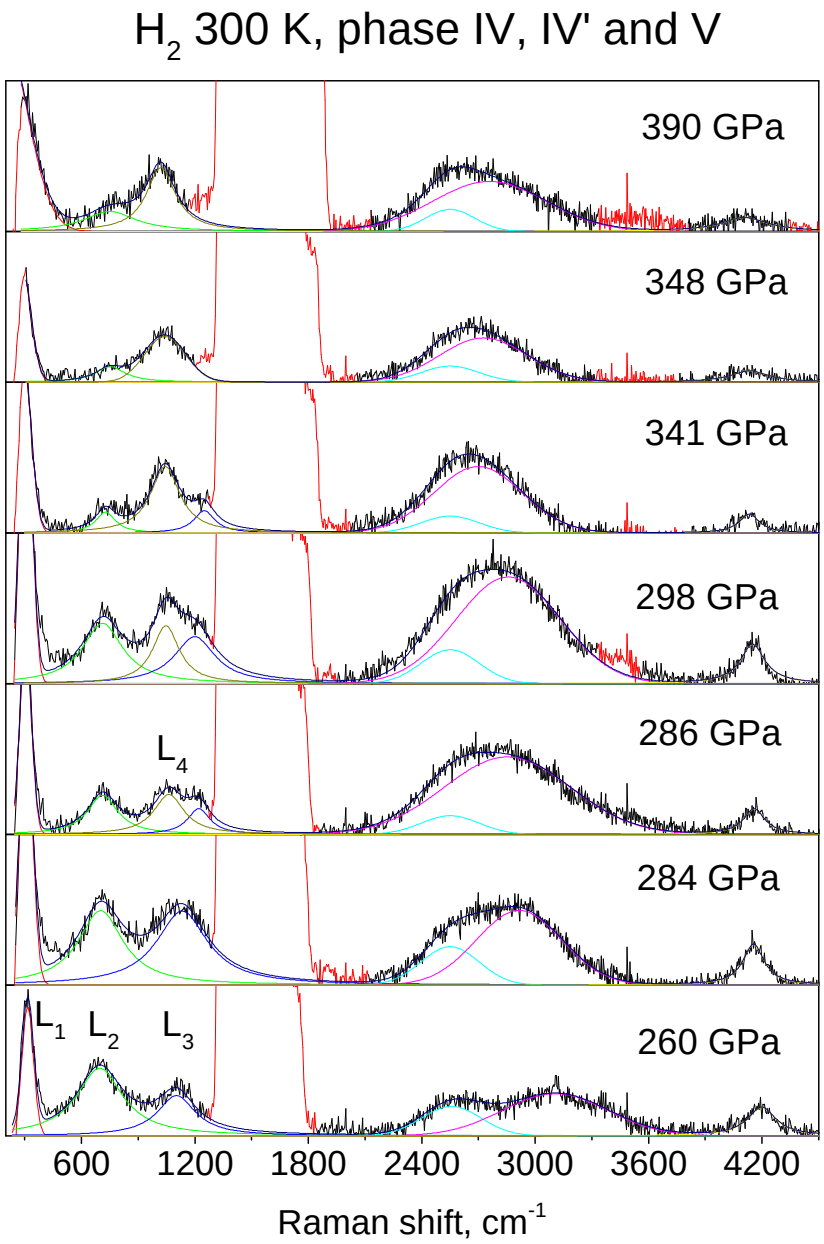

Figure 4.15 *Representative Raman spectra of H_2 at nominal pressures from 260 GPa to 390 GPa at 300 K, fitted with Voigt profiles. The first order diamond peak coloured in red is masked from fitting as few other regions. The second order diamond peak is coloured in pink and is taken into account when fitting due to overlapping with the $\nu_1(H_2)$ vibron. Frequency, FWHM and areas dependencies on pressure can be found in Appendix B, Figure A.11)*

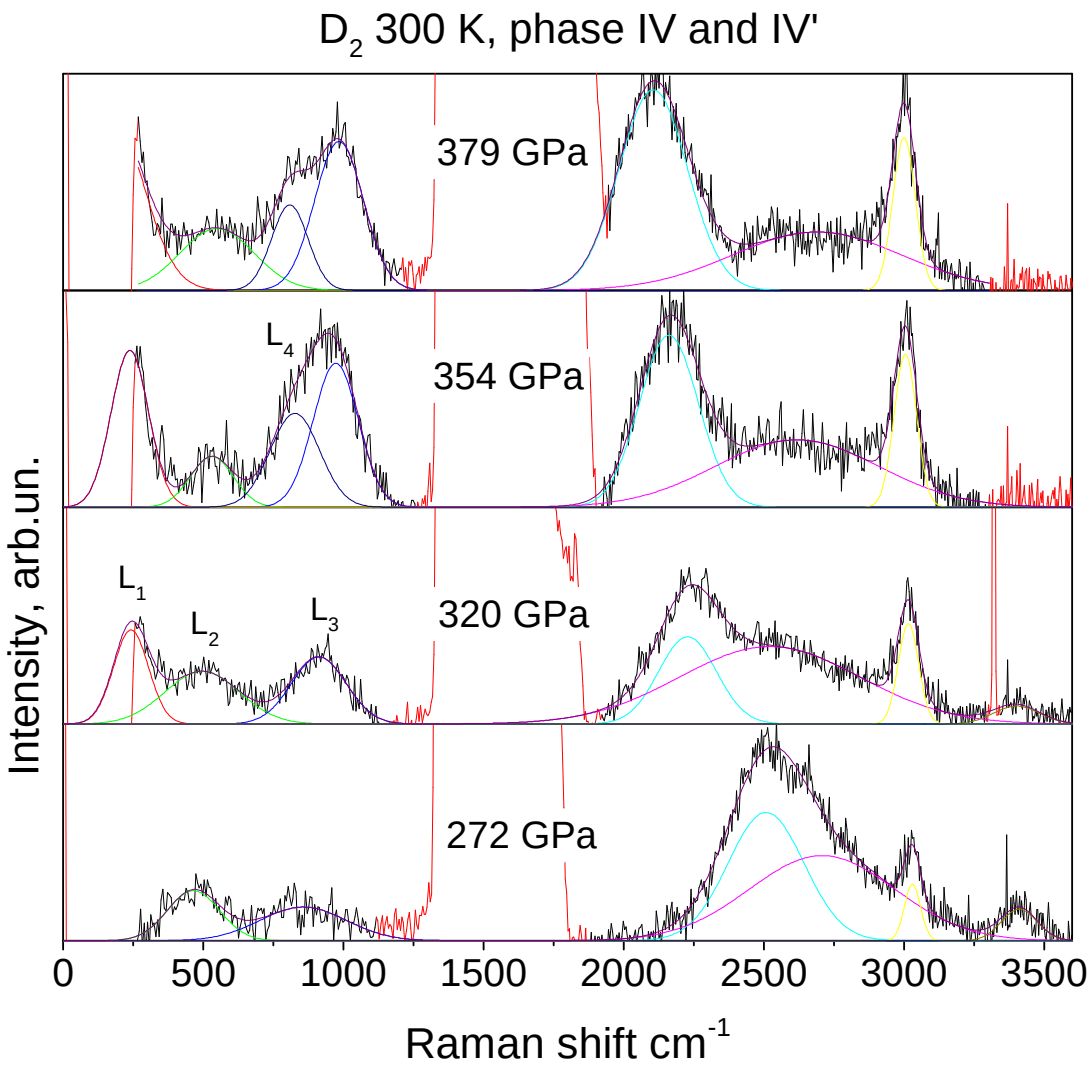

Figure 4.16 *Representative Raman spectra of D_2 at nominal pressures from 272 GPa to 379 GPa at 300 K. The first order diamond peak coloured in red is masked from fitting as few other noisy regions. The second order diamond peak is coloured in pink and is included in fitting due to overlapping with the $\nu_1(D_2)$ vibron. Frequency, FWHM and areas dependencies on pressure can be found in Appendix B, Figure A.12.*

Another refinement concerns low-frequency mode L_1. Its asymmetric shape and abrupt drop on the left side allude to the potential interference of the notch filters used for minimization of the effect of the laser signal in the collected spectra. Obviously, such parameters as FWHM and area strongly depend on how the shape of the L_1 peak is defined. Since the influence of filters cannot be eliminated, it might be too ambitious to make any assumptions about a transition to a new phase based on the changes of this peak. Summarizing all written above, the current interpretation of the transformations of the Raman spectra is questioning

the pressure range of phase transition to phase V in hydrogen and potential coexistence with phase IV' to higher pressures than it was proposed hitherto [Dalladay-Simpson 16].

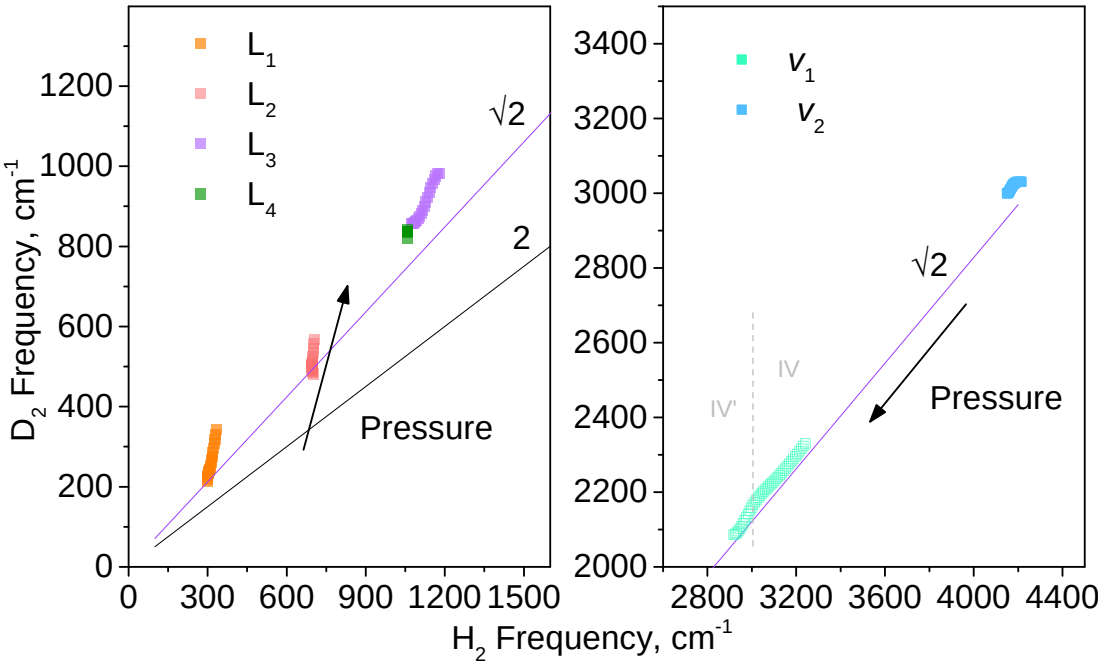

Figure 4.17 *Frequencies of D_2 low energy modes plotted versus frequencies of H_2 low energy modes and D_2 vibron versus H_2 vibrons at equivalent pressures. Location of the points above the line with slope $1/\sqrt{2}$ indicates that all excitations behave as phonons. Arrows point at the direction of pressure increase.*

As we continue the discussion about the nature of low-frequency modes, we should return to the comparison of these features in both isotopes. Transformation to phases IV and IV' in deuterium is delayed in pressure, compared to hydrogen [Howie 12a, Dalladay-Simpson 16]. This makes comparison of these high pressure phases of hydrogen and deuterium more complex. In order to make sure that we compare states with similar properties, we had to implement pressure matching, which will be discussed in Section 4.5 in details. Polynomial fittings applied to accurately defined frequency-pressure dependencies provided an opportunity to extend experimental data set for adequate data correlation. Obtained data sets were then used for the analysis by comparison of frequencies of low-frequency modes in hydrogen and deuterium. We plotted D_2 frequencies versus H_2 frequencies of corresponding modes at matched pressures, as shown in Figure 4.17. The result that we observe is rather curious. D_2 frequencies plotted versus H_2 frequencies at equivalent pressures reside above the line with the slope $1/\sqrt{2}$ for both low-frequency and high-frequency modes. Interestingly, low-frequency

modes shift very quickly from $\sqrt{2}$, which is characteristic for phonons and vibrons, but in the direction opposite to 2. In other words, these excitations are most probably not related to rotational motion. Therefore, we can conclude, that low-frequency modes of phases IV and IV' of both isotopes most probably arise from lattice vibrations.

4.5 Comparison of H_2 and D_2 systems. Pressure calibration.

Since the only difference between H_2 and D_2 is their different nuclear masses, they are expected to present similar reactivity and phase diagrams. As has been broadly shown in the literature, although H_2 and D_2 phase diagrams are similar, there are several obvious differences in the pressure ranges of H_2 and D_2 structural phases (Figure 4.18).

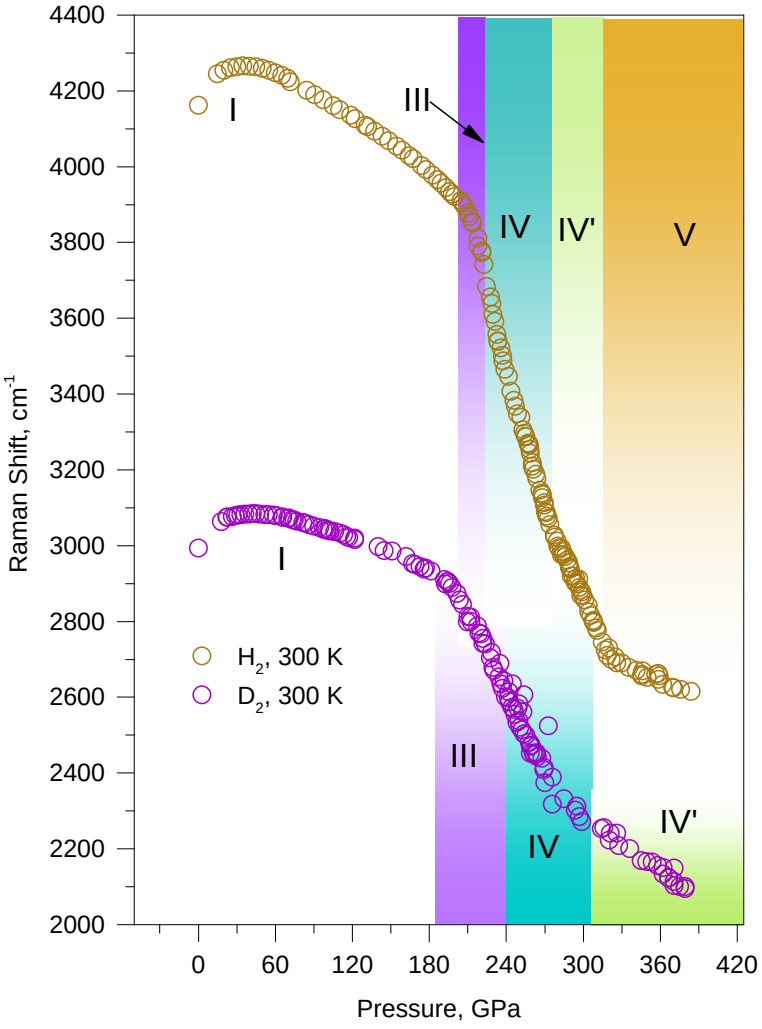

Figure 4.18 *Frequency shifts of H_2 and D_2 vibrational modes as a function of pressure at 300 K. Upper part corresponds to the H_2 vibrons, lower part of the plot represents the D_2 vibrons. Transitions from phases I-III and III-IV are found at higher pressures in deuterium compared to those of hydrogen.*

Clear examples are seen in phases II and II' of hydrogen and deuterium (Figure

4.2), which are driven by quantum effects and zero-point energy [Liu 17], and phases IV' and V of the isotopes (Figure 4.18) due to the higher rates of tunnelling in hydrogen [Howie 13]. Therefore, this raises the issue as to how these systems should be compared.

One way to approach such comparison is to use frequency of hydrogen and deuterium vibrons. Similar method has been previously suggested by Howie et al. for pressure calibration [Howie 13]. Such approach appears to be rather reliable, because vibration frequency is tied to the interatomic distance, therefore when particular frequency is reached, hydrogen/deuterium undergo phase transformation, independently of pressure measured by diamond edge or ruby fluorescence. In order to use vibrational frequencies of H_2/D_2 for such comparison, we have to normalize the shift of the vibron with the following formula:

$$\nu_{H_2 norm}(P_x) = \frac{\nu_{H_2}(P_0) - \nu_{H_2}(P_x)}{\nu_{H_2}(P_0)} \tag{4.1}$$

Normalized vibrational shifts of hydrogen and deuterium, being in the same structural state, should be equal to each other, which is supported by following logic. Vibrational nature of excitations suggests that ratio $\nu_{H_2}(P_x)/\nu_{D_2}(P_x)$ is constant at different pressures:

$$\frac{\nu_{H_2}(P_x)}{\nu_{D_2}(P_x)} = \sqrt{2} = const \tag{4.2}$$

From this dependence we can eventually obtain following relation:

$$\frac{\Delta\nu_{H_2}(P_x)}{\nu_{H_2}(P_0)} = \frac{\Delta\nu_{D_2}(P_x)}{\nu_{D_2}(P_0)}, \tag{4.3}$$

where P_0 equals 0 GPa, P_x is variable, $\Delta\nu_{H_2}$ and $\Delta\nu_{D_2}$ are relative frequency shifts in hydrogen and deuterium respectively. Relative frequency shifts $\Delta\nu_{H_2}(P_x)$ and $\Delta\nu_{D_2}(P_x)$ can be described as:

$$\Delta\nu_{H_2}(P_x) = \nu_{H_2}(P_x) - \nu_{H_2}(P_0) \tag{4.4}$$

$$\Delta\nu_{D_2}(P_x) = \nu_{D_2}(P_x) - \nu_{D_2}(P_0) \tag{4.5}$$

Taking relations 4.4 and 4.5 and substituting to 4.3, we can obtain following equation:

$$\frac{\nu_{H_2}(P_0) - \nu_{H_2}(P_x)}{\nu_{H_2}(P_0)} = \frac{\nu_{D_2}(P_0) - \nu_{D_2}(P_x)}{\nu_{D_2}(P_0)} \tag{4.6}$$

And, by substituting 4.1 to 4.6, we prove that normalized frequency of the isotopes in similar states should be equal to each other:

$$\nu_{H_2 norm}(P_x) = \nu_{D_2 norm}(P_x) \tag{4.7}$$

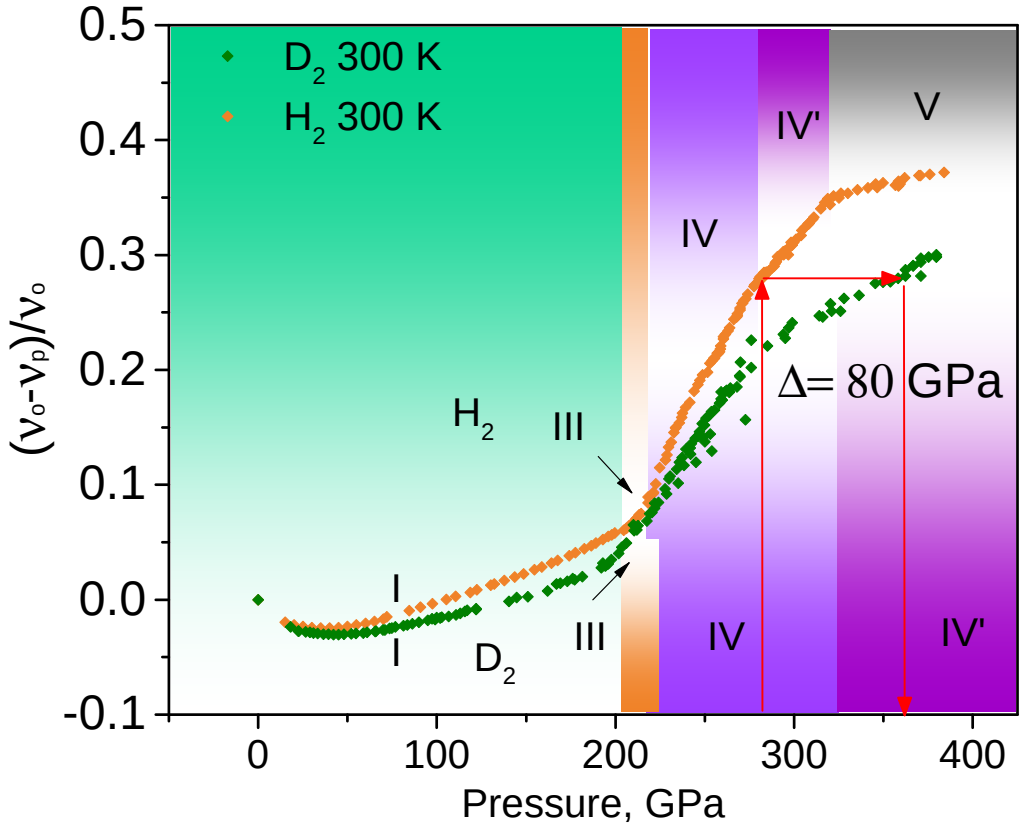

Figure 4.19 *Normalized frequency shifts $\nu_{norm}(P_x)$=$(\nu(P_0) - \nu(P_x)/\nu(P_0)$ of H_2 and D_2 as functions of nominal pressure. Different colour domains show corresponding phases in H_2 and D_2. The red line points at the pressure shift of the corresponding normalized frequency shifts in H_2 and D_2 in phase IV', equal to 80 GPa.*

In Figure 4.19 we demonstrate the normalized shift of the vibron for H_2 and D_2 as a function of pressure. It is shown that different pressures are required to reach the same phases in both isotopes as anticipated. Therefore, based on the above assumptions, we estimated the required pressure to obtain identical normalized frequency shifts in hydrogen and deuterium. The pressure shift of D_2 vibron versus pressure required to reach the equivalent H_2 vibron frequency varies from 5 GPa in phase I, to 20 GPa in phase III, reaching its maximum of more than 80 GPa in phase V of hydrogen. Unfortunately, this dependence does not follow any straight law. Hence, we attempted to describe the relationship between matching pressures by equation 4.8. Due to the complex relationship between corresponding pressures in different phases, it was not possible to characterize the normalized vibron shift vs. pressure with a single equation. We decided that the optimal solution is to use different approximations depending on the pressure range. We split the pressure range into two segments from 0 to 230 GPa and 230 GPa to 300 GPa (see Figure 4.20). In this way, we describe the D_2 vs. H_2 normalized vibron shift, or equivalent pressures required to induce in deuterium the same structural transitions as in hydrogen, through the polynomial:

$$P_{D_2} = C + \sum_{n=1}^{n=9} B_n x^n \tag{4.8}$$

Where the coefficients, B_n (n=1..9), depend on the pressure range and are listed in Table 1 A.1 of Appendix B. As shown in Figure 4.20, the calibration shows a good fit in all high-pressure phases at room temperature.

Now, it is also possible to relate frequencies of hydrogen directly to frequencies of deuterium or vice versa by the following equation, derived from fitting of experimental data at matched pressures with polynomials:

$$\nu_1(\nu_2) = C + \sum_{n=1}^{n=9} B_n x^n \tag{4.9}$$

with the coefficients for $\nu_{H_2}(\nu_{D_2})$ and $\nu_{D_2}(\nu_{H_2})$ listed in Table A.2 of Appendix B.

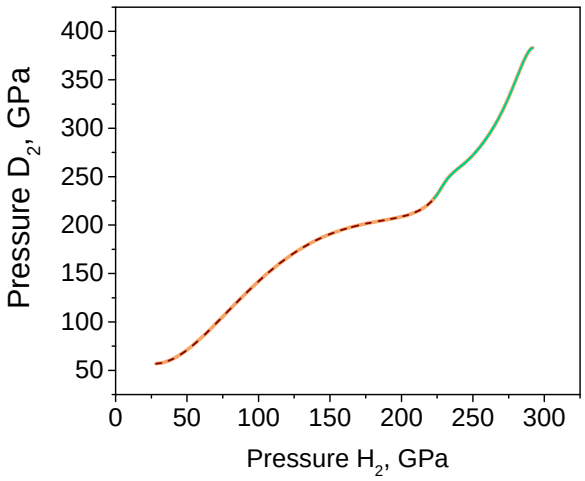

Figure 4.20 *Illustration of interdependence between H_2 and D_2 equivalent pressures (equation 4.8). Different colours of the curve segments indicate ranges from 0 to 230 GPa of hydrogen pressure and 230 GPa to 300 GPa of hydrogen pressure, which were fitted with different polynomials (see Appendix B, Table A.1 for polynomial coefficients).*

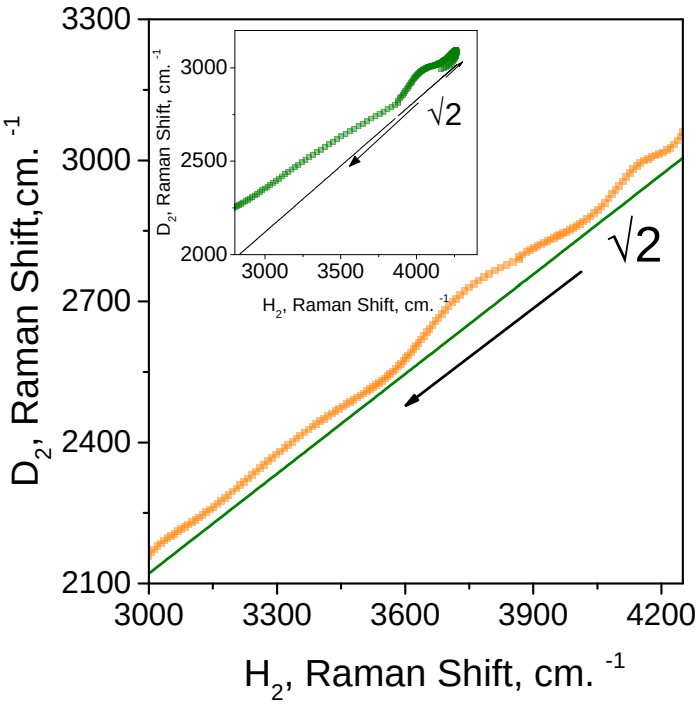

Figure 4.21 *The values of the observed vibron frequencies of D_2 plotted versus H_2 vibron frequencies from 0 to 375 GPa of matched pressures. Plotted points are obtained from polynomials calculated from experimental data. The arrows point in the direction of frequency change when pressure is increased. The black line indicates the ideal ratio between vibrational frequencies and has the slope of $1/\sqrt{2}$. Inset: vibron frequencies of D_2 plotted versus H_2 vibron frequencies before pressure matching.*

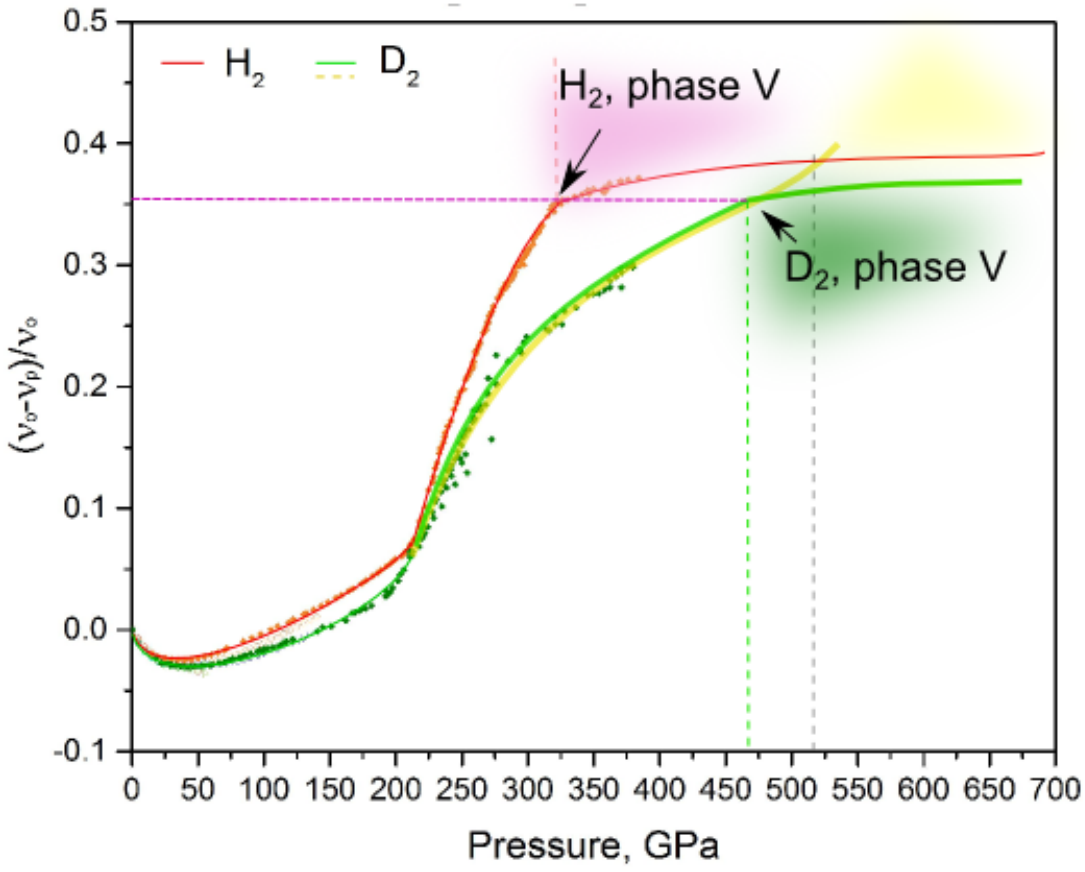

Figure 4.22 *Extrapolation of the curves for* $\Delta\nu = \frac{(\nu_0 - \nu_p)}{\nu_p}$ *in* H_2 *and* D_2 *as a function of pressure to 700 GPa. Red line indicates* H_2 *vibron relative frequency shift, whereas green and yellow is for* D_2 *vibron relative frequency shifts. Grey line indicates potential point of convergence of extrapolated curves for* H_2 *and* D_2*. As can be inferred from the plot, there are at least two options for higher pressure behaviour. Extrapolation depicted with the yellow line suggests phase transformations in* D_2 *similar to those in* H_2*, although considerably shifted to higher pressures. Alternatively, extrapolation with the green curve implies another phase transformation from phase V, occurring at the similar pressure range for both* H_2 *and* D_2 *as it happens with the phase III. The purple dashed line indicates equivalent relative frequency shift of transition to phase V in* H_2 *at approximately 320 GPa and* D_2 *at around 470 GPa.*

To check if the suggested method of matching gives satisfactory results, we will refer to the same method of analysis, as we used in Sections 4.3 and 4.4 for low-frequency modes. In Figure 4.21 trend for frequencies of hydrogen and deuterium which plotted versus each other after pressure matching differs from trend performed before pressure matching (see inset, Figure 4.21). Without pressure matching, with pressure increase trend line quickly moves from the guideline of $\sqrt{2}$, which contradicts the harmonic behaviour of the modes. On the other hand, with applied pressure matching, we obtain rather stable results,

when trend is following $\sqrt{2}$ (1.39) guideline, which agrees with its vibrational nature. Hence, suggested pressure matching method can be considered reliable.

In view of the above observations, it is interesting to speculate on H_2 and D_2 behaviour at pressures above 400 GPa. Pressure shifts of phase transitions between III, IV, IV' phases of D_2 with respect to those in H_2 suggest that phase transformation in deuterium to phase V will be delayed from 320 GPa of phase V in H_2 (Figure 4.22). This would lead to a logical conclusion, that metallization of D_2 might also occur at much higher pressures than that of hydrogen, given the relative pressure difference in phases IV' of H_2 and D_2 of approximately 80 GPa. On the other hand, in Figure 4.22 we see how after with the relative frequency shifts in lower-pressure phases I and II there is a sudden convergence of the $(\nu_0 - \nu_p)/\nu_0$ curves and almost simultaneous transition to phase III and phase IV. Examination of $(\nu_0 - \nu_p)/\nu_0$ curves of H_2 and D_2 and extrapolation of those to higher pressures results into another potential pattern of convergence at pressures above 500 GPa, presumably designating another non-described phase transition. In both cases, comparison of equivalent normalized frequency shifts and slope angles shows that the transition to phase V in deuterium is expected to occur around 470 GPa.

It is intriguing to observe how the H_2 and D_2 vibron relationship change in the different phases. As known, phases I and II are mainly governed by quantum effects, changing to dominant classical intermolecular interaction in phases III, IV, IV,' and V. Transition to the metallic state should involve other change of interaction type from mainly classical to proton-proton interaction and delocalization of electrons [Mao 94]. In other words, we might expect two phase transitions which would be governed by a change of main interplay mechanism and nuclear mass whereas the rest of phases appear due to the more efficient packing under compression. Therefore, converging of the curves of relative frequency shifts might indirectly point to such change of type of interaction, allowing to predict metallization point.

4.6 Summary

An attempt to gain greater clarity with respect to the rotational motion of hydrogen and deuterium by analysis of low-frequency excitations in Raman spectra was made. For that reason, several experiments at various temperatures and pressures were carried out in addition to those, conducted previously, and analysed in the present work. Due to the ambiguity of the understanding of phase II nature and mechanisms of formation, current project was specifically focused on phase I and phases IV and IV', which feature intense low-frequency modes.

Although because of the broadening and merging of low-energy peaks it was not possible to determine unambiguously the degree of interaction between rotational and vibrational motions, we were able to identify some behavioural trends by indirect comparison of excitation frequencies in hydrogen and deuterium. Our analysis suggested that rotational motion is hindered in the low-temperature domain of phase I before it transforms to Phase II. Trends implied that rotons might eventually become phonons when approaching border to Phase II. On the contrary, trends in phase I domain located at temperatures above 150 K point at more rotational behaviour across the whole pressure range, although it appears to be slightly frustrated. Therefore, rotons in different domains of phase I behave differently. More analysis is needed to explore the reasons for such distinctness. A similar analysis of low-frequency excitations in phases IV and IV' confirmed their vibrational nature. These modes can be explained as phonons arising from the hexagonal lattice.

In order to indirectly study low-frequency modes of hydrogen and deuterium, it was crucial to apply correct pressure scaling. For that reason, several equations which allowed estimation of equivalent pressure or frequency in both hydrogen and deuterium by introducing relative frequency shift were suggested. This method showed good results for the experiments described in the present work. Comparison of normalized frequency shifts as functions of pressure for hydrogen and deuterium presented the intriguing character as the potential convergence of the curves at the points of transition between different types of intermolecular interaction. Extrapolation of the results to pressures above 500 GPa resulted in two potential scenarios when metallization of deuterium either occurs at pressures close to those of hydrogen, or it will be significantly delayed. At the same time, both scenarios showed the transition to phase V in deuterium around 470 GPa.

To summarize, the present work elucidated the unique behaviour of rotons in different domains of phase I, as well as proved the solid structure of phases IV and IV' but confirming phonon type of low-frequency modes. The conclusions to be drawn from this analysis might help in future research, which might be needed to define the type of interaction in phase II and influence of ortho-para transition on the rotational motion of the molecules in both isotopes. Contributing work also proposed a reliable method of comparison of hydrogen and deuterium systems, which might be beneficial for further research which will include the comparison of both systems.

Chapter 5

New dense high-pressure phases in nitrogen/oxygen binary system at 300 K

5.1 Introduction

This chapter describes an extended phase P-x phase diagram of nitrogen/oxygen binary system at ambient pressure. Although, some of the measurements achieved 150 GPa, the highest recorded pressures for this system, the majority of experiments were limited to pressures up to 45 GPa. The experimental data reveals high complexity of high-pressure phase diagram and further suggests formation of new compounds. The contributing work shows an overall agreement with the previously reported sequence of phase transitions at ambient temperature. There are, however, some discrepancies in pressures and compositions.

Most of the samples were cryogenically loaded by mixing liquefied nitrogen and oxygen. Concentrations of the cryogenically loaded samples were estimated by measuring the relative intensities of the peaks in the Raman spectra of oxygen and nitrogen in fluid phase of the sample. Air sample and 25% O_2 sample were gas loaded from premixed gases with the error bar on the concentration of $\pm 2\%$.

For our convenience all experiments are divided into 5 groups according to their

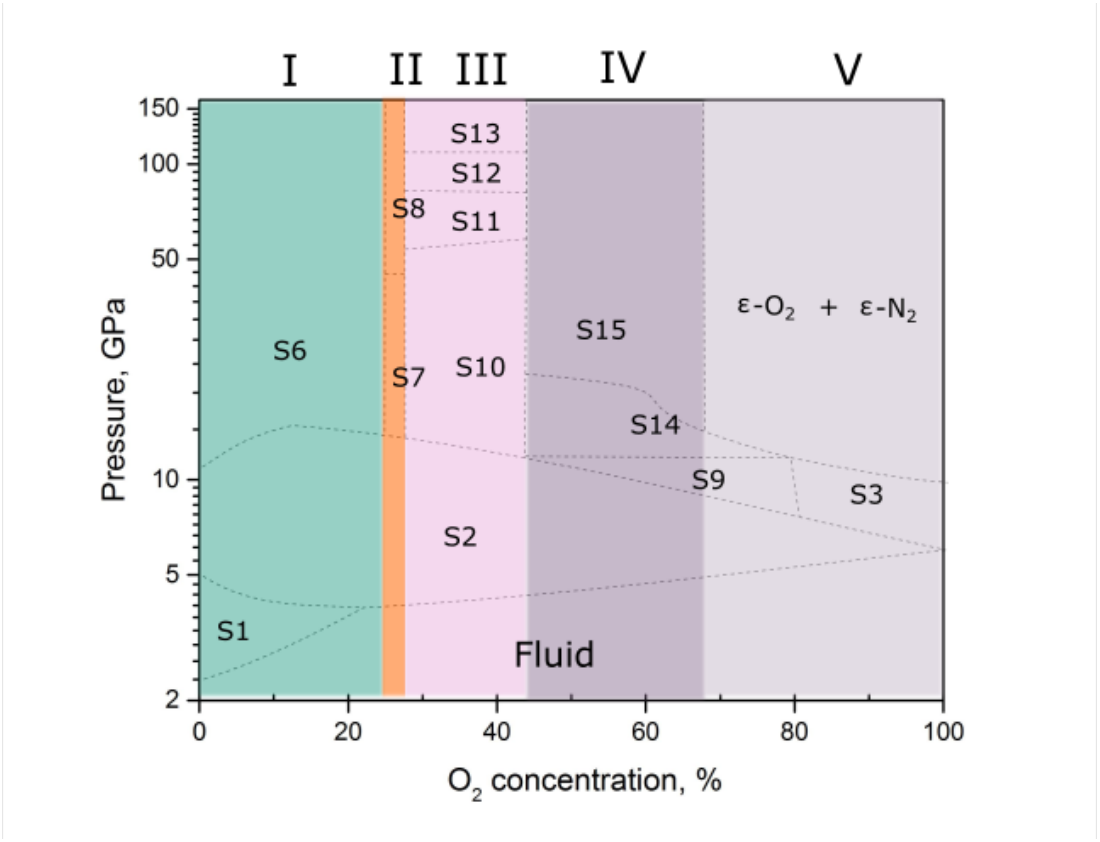

Figure 5.1 *Experimental phase diagram of the nitrogen/oxygen binary system based on our experimental results and previously reported research [Sihachakr 04, Akahama 14, Akahama 16]. Different colours represent different groups of the samples (see Table 5.1). The phase diagram will be discussed in details in the following sections.*

concentration and the similarities of the Raman spectra at pressures above 10 GPa. Group I includes samples with concentrations up to 24% of oxygen. Group II exists in a very narrow window of concentrations around 25% of oxygen and corresponds to a potentially stoichiometric compound $(N_2)_3O_2$, discussed earlier [Sihachakr 06]. Group III consists of samples with concentrations above 26% O_2 to 45% O_2. Concentrations from 45% to 70% belong to Group IV, and 70% to 100% O_2 to Group V. Phase transitions in these groups are briefly described in Table 5.1 and depicted in Figure 5.1.

To keep phase diagram coherent with the previously reported research we will continue using the same system of terminology for phases, where F is fluid, and S is solid; phases S1, S2, S3, S4, S5, S6 are the same as described in [Sihachakr 04]. Phase S3' is renamed to S9 to avoid possible confusion. This chapter will consist of sections, dedicated to each of five groups of experiments and will be finalized by the discussion of the results.

Table 5.1 *Summary of phase transitions in the conducted experiments. Samples were divided into 5 groups depending on the sequence of transformations. For concentrations with more than 50% O_2 we observed high non-homogeneity above 15 GPa, which could also be detected by visual observations. Although it was impossible to measure exact composition in different parts of the sample in solid phases, different intensity of specific features in optical spectra together with visual observation allowed to estimate composition of mixtures.*

Group	# loading	% O_2	Phase Transitions
I	12	13	F ->S2 ->S6
I	7	18	F ->S2 ->S6
I	AIR	21	F ->S2 ->S6
II	20	25	F ->S2 ->S7 ->S8
II	11	26	F ->S2 ->S7 ->S8
III	13	35	F ->S2 ->S10 ->S11 -12 ->S13
III	10	42	F ->S2 ->S10 ->S11 -12
IV	6, light	52	F ->S2 ->S9 ->S14 ->S15
IV	6, dark	52	F ->S2 ->S9 ->S14 ->S15
IV	5, light	68	F ->S2 ->S9 ->S14 ->S15
V	5, dark	68	F ->S2 ->S9 ->ϵ-O_2+ϵ-N_2
V	8	75	F ->S2 ->S9 ->ϵ-O_2+ϵ-N_2
V	4, light	82	F ->S3 ->ϵ-O_2+ϵ-N_2
V	4, dark	82	F ->S3 ->ϵ-O_2+ϵ-N_2

5.2 Group I

Nitrogen-Oxygen mixtures have already been found to behave isostructurally to phases of their pure components, albeit with slight distortions of crystal lattice due to the difference of molecule size [Sihachakr 04, Akahama 14, Baer 90]. In our nitrogen-rich experiments, with O_2 concentrations not exceeding 24% (Group I), we observe similar picture. Figure 5.2 illustrates Raman spectra over a 40 GPa range for sample with 18% O_2, undergoing phase transitions Fluid-> S2-> S6. Evidence for such phase sequence is supported by frequency changes of low and high frequency excitations, shown in Figure 5.3. Phase S2 corresponds to solid solution of O_2 in δ-nitrogen where O_2 molecules substitute N_2 on the sites of cubic Pm3n structure. Spectral modifications observed there are analogous to that of phase S2 reported in works of Baer et al. [Baer 90] and Sihachakr et al. [Sihachakr 04]. It exhibits distinctive doublets of O_2 and N_2 vibron area which are associated with two crystallographic sites with different type of order.

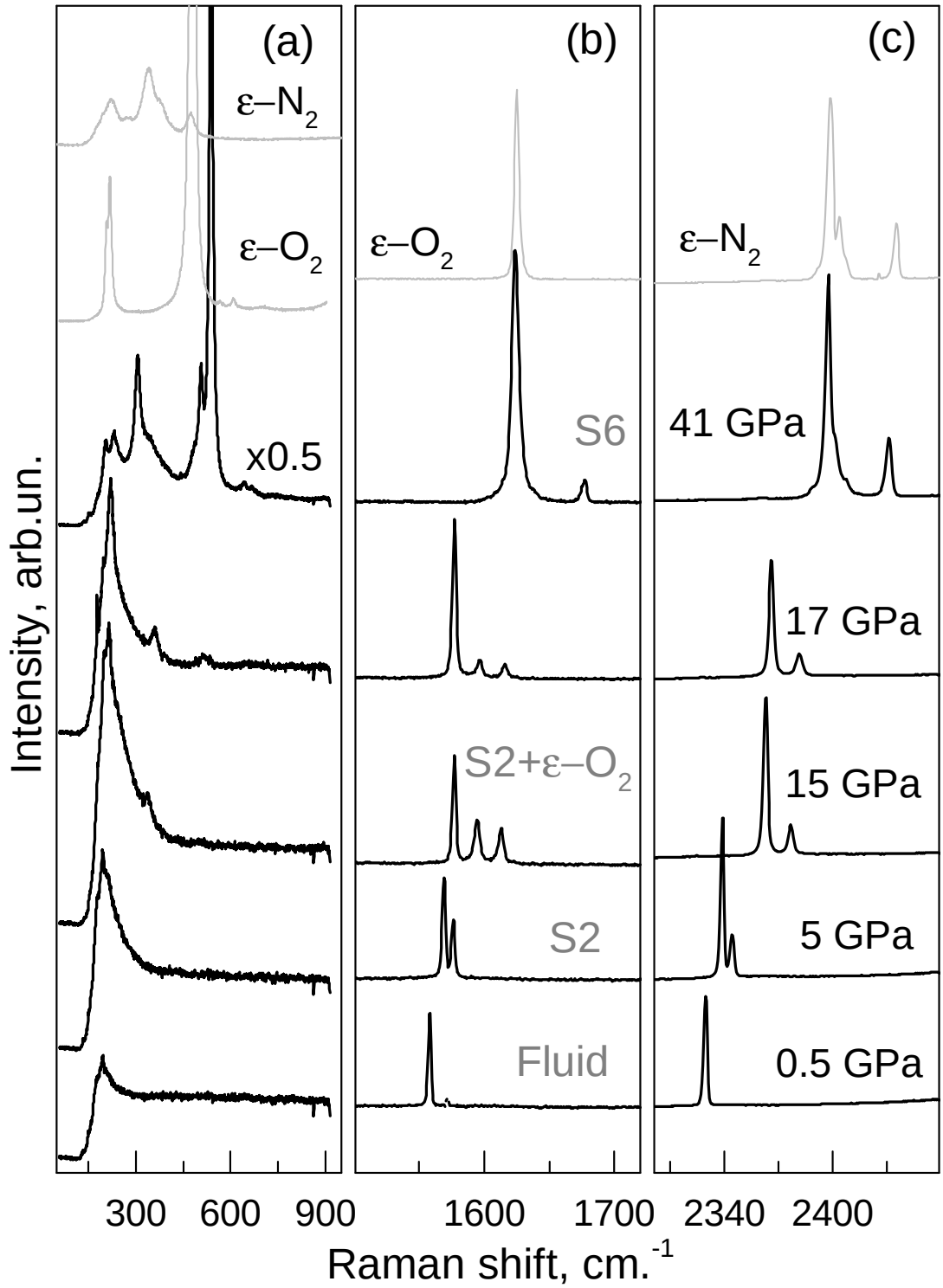

Figure 5.2 *Group I. Representative Raman spectra of 18% O_2 mixture upon compression at 300 K. Characteristic features of all phases are clearly resolved. For comparison, the top grey spectra are of pure nitrogen and oxygen at 40 GPa in their respective ϵ phases.*

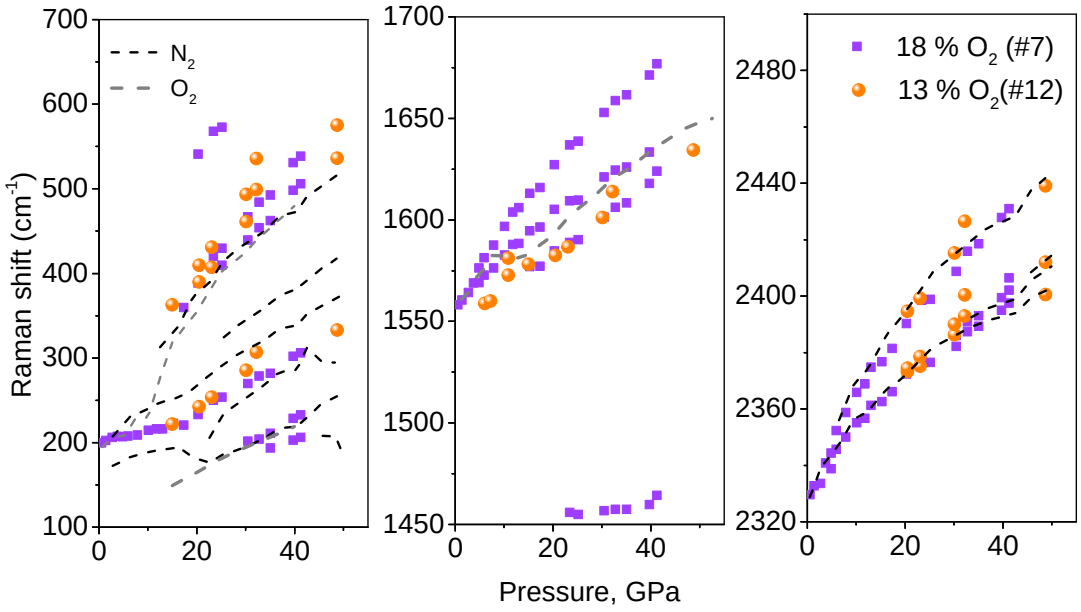

Figure 5.3 *Group I. The frequency-pressure dependence of the Raman modes of mixtures with 13% O_2 (orange balls) and 18% O_2 (purple squares) at 300 K. The grey dashed lines are for pure O_2 and N_2. Features of O_2 vibron in ϵ*-N_2 were hardly distinguishable due to the high concentration of N_2, thus not shown on the plot. Interestingly, the low-frequency spectra demonstrate overall correlation with pure species albeit peaks at 200 cm^{-1} are considerably weaker. Additionally, the O_2 peak around 400 cm^{-1} is split into a doublet. Although we suggest dissolution of S2 into alloy with ϵ-oxygen, the main ϵ-vibron of O_2 is red shifted.*

Under further compression, phase S2 undergoes a significant spectral modification, previously explained as the formation of δ-nitrogen and ϵ-oxygen as the S2 phase demixes, manifesting an O_2-triplet. However, this region of coexisting phases is stable in only a very small range of pressures, transforming above 15 GPa into phase S6, pressures characteristic for the δ-ϵ transition in N_2. The higher-pressure S6 phase is found to be stable to at least 40 GPa. The S2-S6 transition is characterised by the loss of S2 modes, the appearance of $(O_2)_4$-vibrons from the ϵ-phase at 1450 cm^{-1} and 1580 cm^{-1} (shifted from pure ϵ-oxygen), and new weak bands at 1608 cm^{-1} and 1630 cm^{-1}. This is in agreement with the low-temperature study of Minenko et al [Minenko 04]. The N_2-vibron bands appear to be similar to those in pure ϵ-nitrogen. Low-frequency spectra reveal an abundance of sharp and intense librational and phonon modes.

Figure 5.3 is representative of the amalgamated data collected in all the experimental runs on samples with 13% O_2 and 18% O_2. Both samples

undergo following transitions: Fluid -> S2 ->S6. Up to pressures of 15 GPa, the vibrational response is found to be in agreement with previously reported measurements.

Comparison of obtained Raman spectra characteristic for group I with those of pure elements is given in Figures 5.2 and 5.3. Frequency-pressure dependence indicates that ϵ-oxygen vibrational band is rather red shifted. This could be explained by a small amount of N_2 molecules dissolved in the ϵ-oxygen structure, which disturbs the interaction between O_2 molecules, diminishing resonance shift of the O_2 vibron [Minenko 04]. Oxygen doublet originates from oxygen molecules occupying two different sites in ϵ-N_2. In contrast to previous studies [Minenko 04, Baer 90, Baer 89], here we observed these peaks up to 40 GPa, with a steady intensity increase. Vibrational band of nitrogen appears to be identical to pure nitrogen. Frequencies of low-energy modes in general agree with both ϵ-oxygen and ϵ-nitrogen, with such additional peaks and splitting of the oxygen mode. Thus, we infer that phase S6 might consist of a small amount of ϵ-oxygen, ϵ-nitrogen and an alloy comprising of O_2 embedded in a rhombohedral $R\bar{3}c$ lattice of ϵ^*-N_2.

5.3 Group II

As expected from the study of Sihachakr et al. a stoichiometric compound $(N_2)_3O_2$ can be possibly formed in this area [Sihachakr 04]. This group covers a very narrow domain with concentrations close to 25% O_2. Samples with concentrations of 25% and 26% O_2 undergo transition from fluid to S2 phase, and consequently transform into S7 at 20 GPa and later to S8 above 41 GPa, compounds that exhibit immensely intense features that are uncharacteristic for other phases.

The evolution of the Raman spectra with pressure is presented in Figure 5.4 for 25% O_2 mixture and in Figure 5.5 for 26% O_2 mixture. As known, there are no phase transitions happening at approximately 20 and 40 GPa pressures in pure components (see Chapter 3). Sharp O_2 and N_2 vibron peaks from the fluid are replaced by sharp doublets characteristic of the S2 phase. Under further compression, Raman signatures of oxygen differ significantly from all other observed phases. Unlike other phases of nitrogen/oxygen system, phases S7 and S8 possess a notably simpler low-frequency landscape, with a broad peak of S7 transitioning into two broad bands at approximately 380 cm^{-1} and 550 cm^{-1} at pressures above 25 GPa (Figures 5.4 (a), 5.6).

Phase S7 is characterised by the extremely broad and asymmetric oxygen vibron with a distinctive shoulder on the higher frequency side and a broader nitrogen vibron showing less distinctive features as usually (Figures 5.4, 5.6, 5.7). In phase S8, above 40 GPa, two broad and ill-defined low-frequency bands are accompanied by a symmetric and broad O_2 vibron and a rather asymmetric N_2-vibron with a strong shoulder on the high-frequency side. Oxygen vibron mode in phases S7 and S8 is much wider than vibrational mode of pure oxygen, which is shown in Figure 5.7.

Such unique Raman landscape can be characteristic for the new stoichiometric compound, presumably $(N_2)_3O_2$. The formation of $(N_2)_3O_2$ was predicted by the observed anomaly of the site distribution for N_2 and O_2 in these mixtures. This compound can be formed in the region with 20-30% O_2 as a result of combination of the unique magnetic properties of oxygen, and preferable packing [Sihachakr 04].

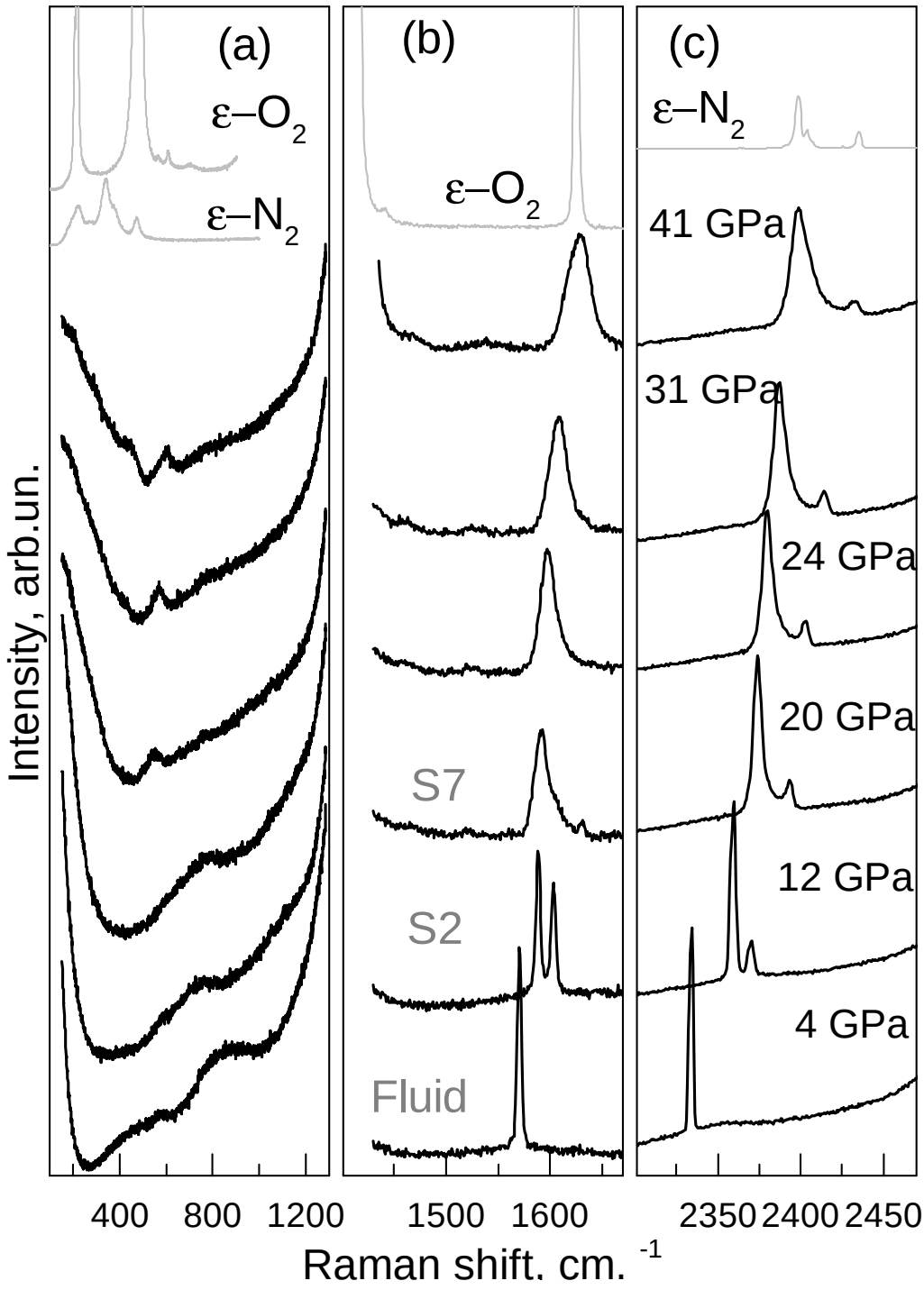

Figure 5.4 *Group II. Evolution of the low-frequency part of the Raman spectra (a), oxygen vibron (b) and nitrogen vibron (c) of nitrogen/oxygen mixture with 25% O_2 under compression to 41 GPa at 300 K. The grey lines on top indicate spectra of pure oxygen and nitrogen at 40 GPa in their respective ϵ phases. Interesting to note, that the nitrogen vibron in the mixture appear to be similar to pure ϵ-nitrogen. Although the Raman spectra of low-frequency modes change drastically from those of pure species, accompanied by a significantly broader and asymmetric oxygen vibron. All these features suggest formation of new compound with possible stoichiometric composition of $(N_2)_3O_2$ upon compression above 15 GPa predicted earlier [Sihachakr 04].*

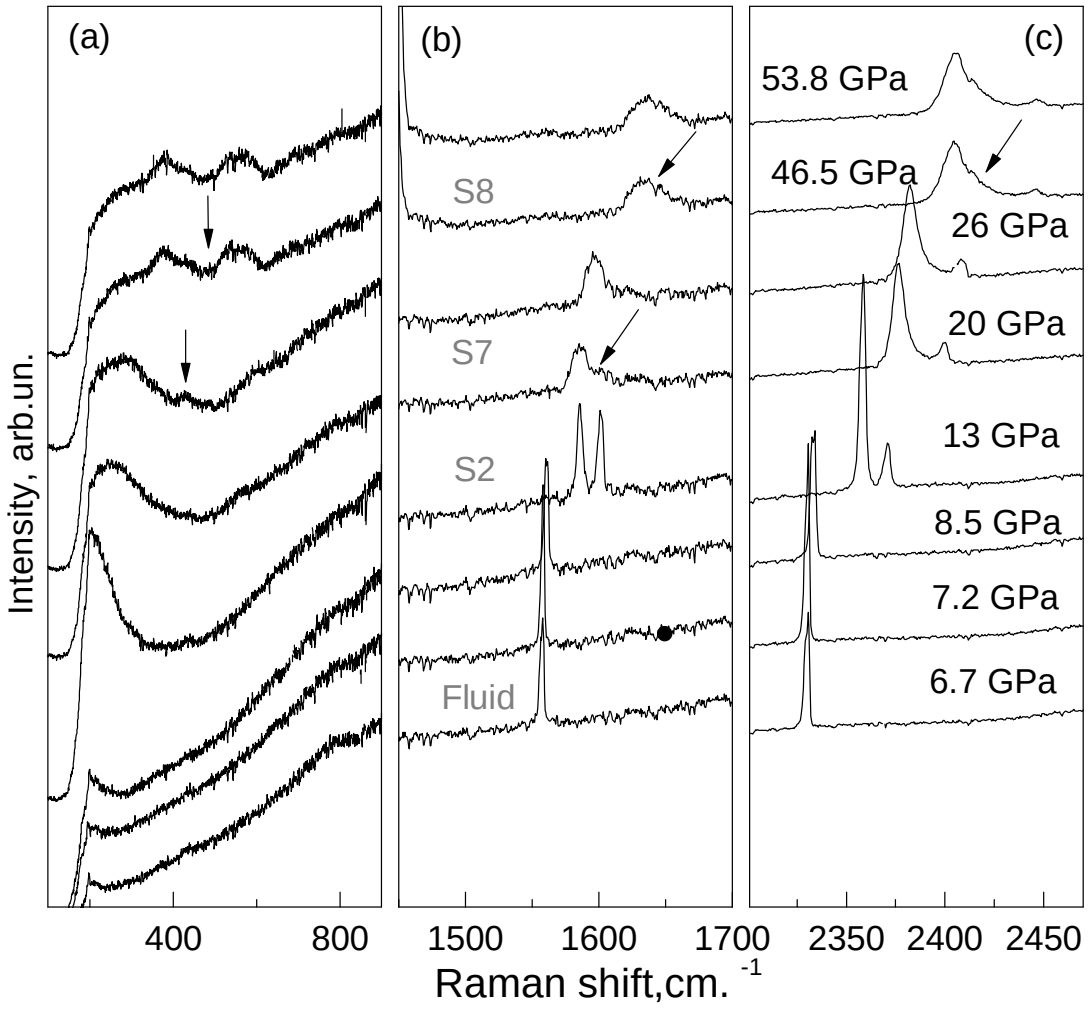

Figure 5.5 *Group II. Representative Raman spectra of nitrogen/oxygen mixture with 26% O_2 compressed to 53.8 GPa at 300 K. Phase transitions, occurred in this mixture, are following: Fluid ->S2->S7->S8. This sample was compressed to a slightly higher pressure than the previous, which allowed us to witness another phase transition S7->S8 characterized by emergence of two broad bands at around 400 cm^{-1} and 500 cm^{-1}, and the oxygen vibron, which broadens and becomes more symmetric. Nitrogen vibron becomes much broader, with less pronounced features.*

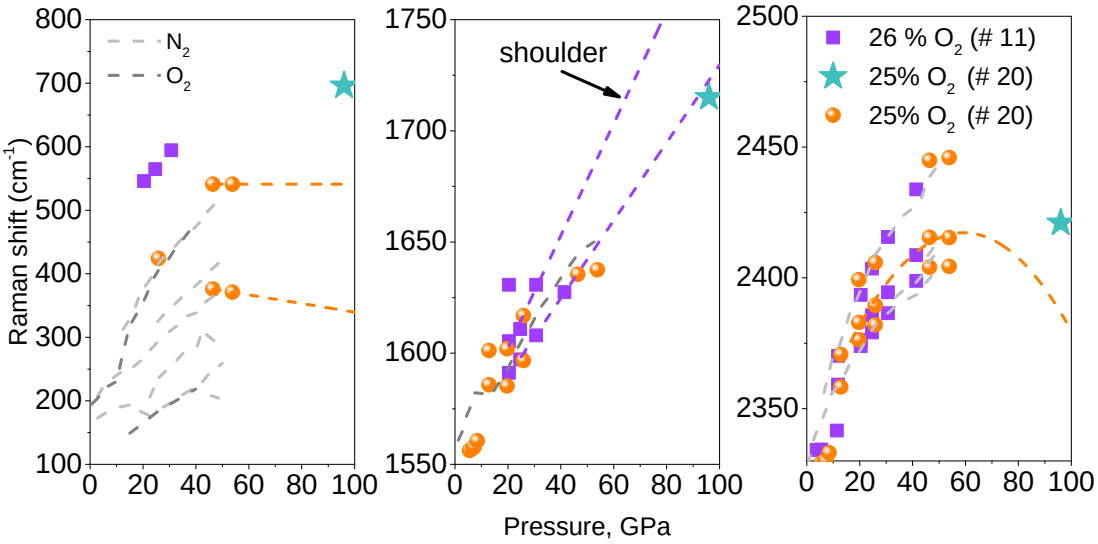

Figure 5.6 *Group II. Raman frequencies of the lattice modes, oxygen vibrons and nitrogen vibrons as functions of pressure for samples with 25% O_2 (orange balls and cyan star) and 26% O_2 (purple squares) mixtures. The dark grey dashed lines are for pure N_2 and O_2. The light dashed purple and orange lines are guidelines for eye for dependencies extrapolated to high pressures from sample with 25% O_2 mixture.*

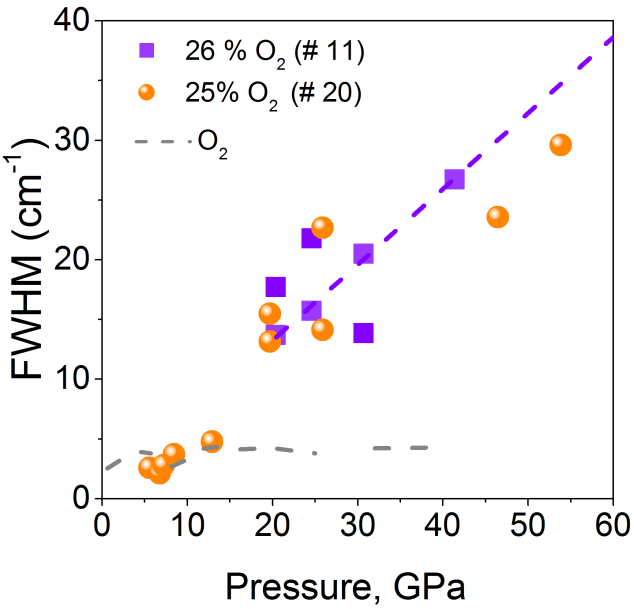

Figure 5.7 *Group II. FWHM of oxygen vibron as a function of pressure for samples with 25% O_2 (orange balls and cyan star) and 26% O_2 (purple squares) mixtures. The grey dashed line is for pure O_2. The light dashed purple line is a guideline for eye for the dependence extrapolated to high pressures from sample with 25% O_2 mixture.*

5.4 Group III

The sequence of structures, as described in Table I, observed under pressure with samples of oxygen concentrations varying in the range between 26% and 45% have been identified by unique spectral modifications of the low-frequency modes and oxygen and nitrogen vibrons up to 150 GPa. Currently, this is the highest pressure nitrogen/oxygen system has been exposed to.

Raman spectra of Group III are depicted in Figure 5.8. Several phase transitions can be observed. Mixtures with 35% O_2 generally follows pure-nitrogen transitions to 80 GPa with some exceptions. As other nitrogen-rich mixtures, the sample undergoes a transition from fluid to S2 phase, which further transforms to phase S10. The abundance of low-frequency modes however lacks one of the characteristic phonon peaks of ϵ-oxygen around 900 cm^{-1}, featuring broad triplet instead above 80 GPa. The oxygen vibron is a typical ϵ-oxygen singlet, whereas nitrogen appears to be similar to ϵ-nitrogen. Upon reaching phase S11, ϵ-nitrogen vibrational modes split into 4, which is indicative of ϵ to ζ-phase transition in nitrogen. On the transformation to ζ-phase, new lower energy excitations appear. Interestingly, intensities and positions of low-frequency Raman spectra for this group are radically different from group I and II. Two peaks (around 220 cm^{-1} and 325 cm^{-1}) appear to be very intense, moreover intensity of these peaks is increasing with pressure so that they become comparable with higher-frequency doublet at 500-600 cm^{-1}. One of possible explanations of these features could be that this phase is formed by the coexistence of ζ-nitrogen phase with a modified version of ϵ-oxygen phase, due to the different molecular environments and crystal field.

At pressures greater than 80 GPa in phase S12 there is a sudden emergence of a new oxygen vibron peak at 1602 cm^{-1}, accompanied by a series of small peaks that appear around 979 cm^{-1}. Due to the drastic increase of low-frequency excitations and no relevance to any phase transition in either pure nitrogen or oxygen at these pressures, we speculate that S12 might comprise of ζ-nitrogen and modified ϵ-oxygen, although the unit cell might be enlarged, say, doubled in size.

With the phase transition from S12 to S13, which reflects the transition from ζ-nitrogen to κ-nitrogen [Gregoryanz 07], the second oxygen vibron vanishes. The

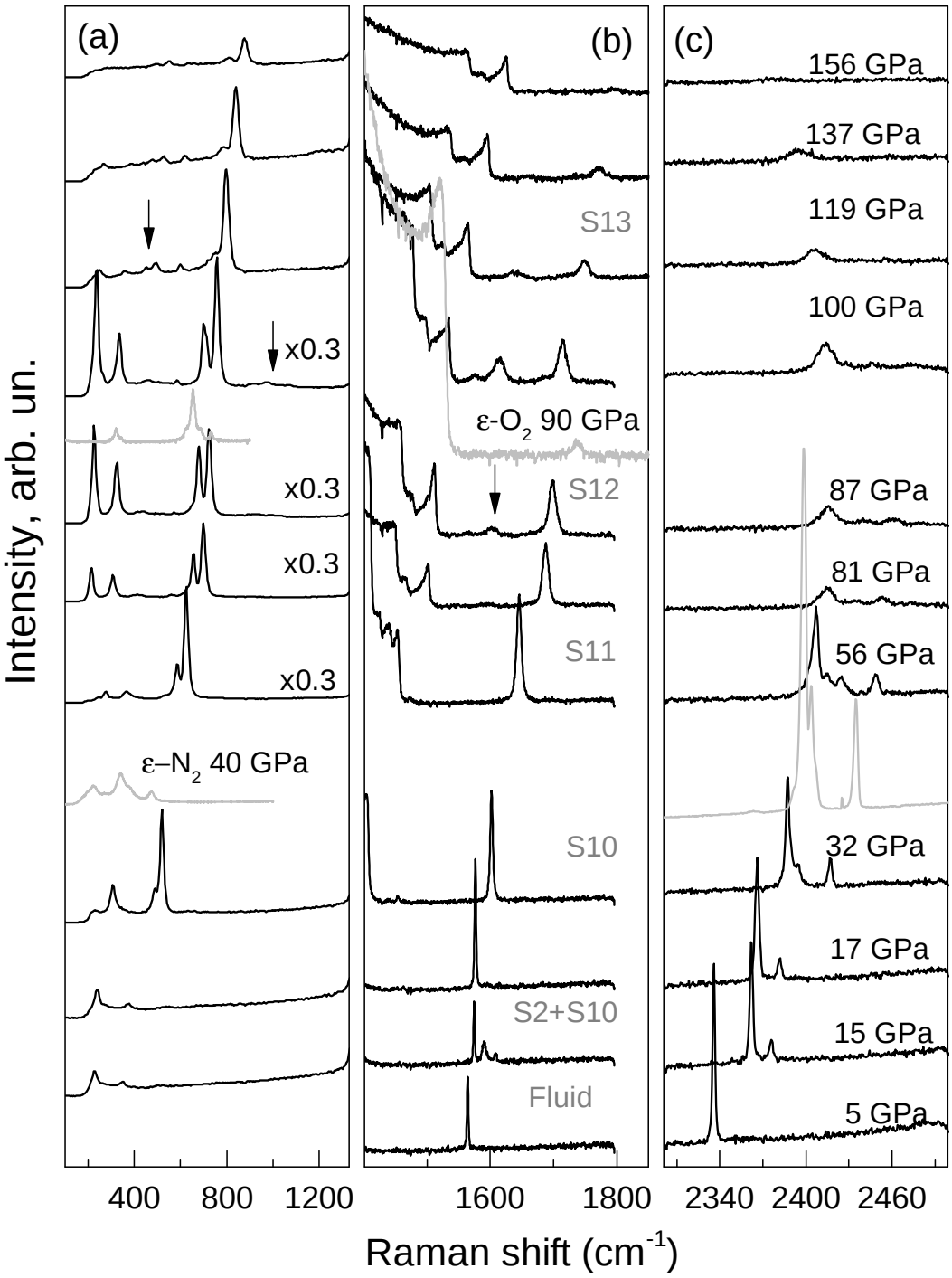

Figure 5.8 *Group III. Representative Raman spectra of the librational/lattice region (panel a) and vibrational modes (panels b, c) for a mixture of 35% O_2 concentration. The grey lines indicate spectra of pure oxygen at 90 GPa and nitrogen at 40 GPa, both in their ϵ phases. Arrows point at new peaks or dramatic changes in landscape in low-frequency and oxygen-vibron regions.*

significant loss of intensities of O-O and N-N stretching modes are accompanied

also by a marked decrease of intensities of the lattice modes with only one peak remaining very strong. This might be related to the transition of oxygen to the metallic phase, though this transition is delayed due to the high concentration of nitrogen. Interestingly, samples did not start to reflect as pure metallic oxygen, although still steadily darkening (becoming more opaque) with pressure. The frequency-pressure dependence of the nitrogen vibron indicates that the transition to the amorphous semiconducting κ-nitrogen occurs around 110 GPa (Figure 5.9). This might be an indicator that the phase S13 is amorphous and correlated with a monoclinic structure of κ-nitrogen, although including small amount of oxygen dissolved in nitrogen lattice [Gregoryanz 07].

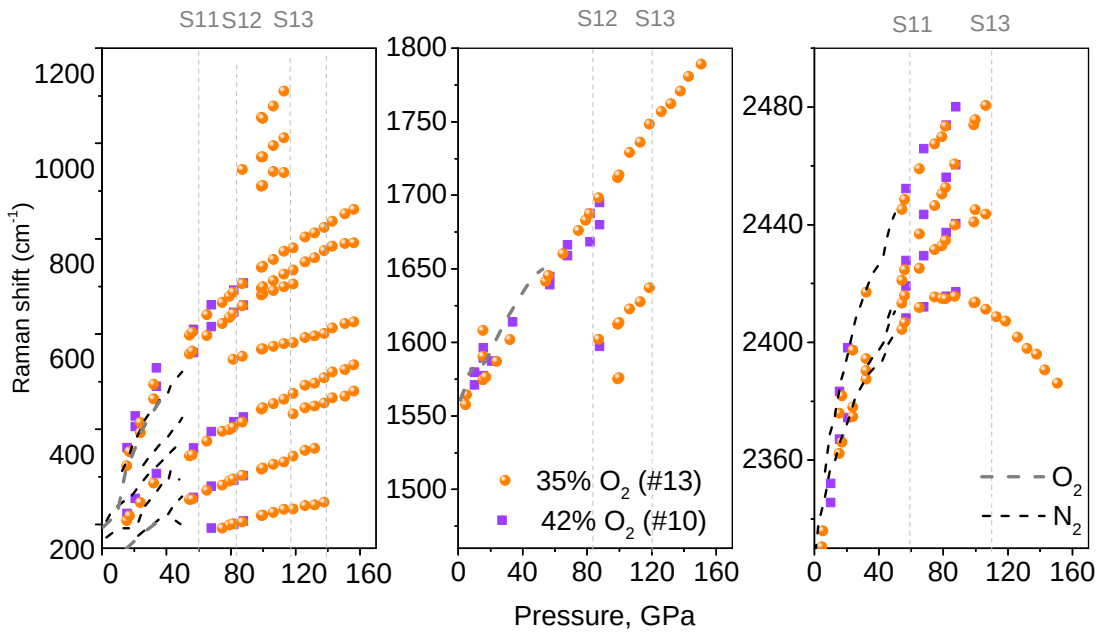

Figure 5.9 *Group III. Raman frequencies of the lattice modes, oxygen vibrons and nitrogen vibrons as functions of pressure for samples with 35% O_2 (orange balls) and 42% O_2 (purple squares) mixtures. Dark grey dashed lines are for pure N_2 and O_2. The light grey vertical lines are guidelines for eye for observed phase transitions at pressures above 60 GPa: S10 -> S11 corresponding to ϵ-ζ transition in N_2, S11 -> S12 at 80 GPa happening independently of phase transition in pure N_2 and O_2, S12 -> S13 at 120 GPa which could potentially correspond to ζ-κ transition in nitrogen. The appearance of two new oxygen vibrons at lower frequency is documented. Nitrogen vibron is similar to pure nitrogen in all phases. Lattice modes are rather rich, with few new modes emerging in S10, S11, and S12 phase, with most of them vanishing in S13 phase above 120 GPa.*

5.5 Group IV

Group IV represents phases with a more strongly marked oxygen influence, being on the oxygen-rich side of the phase diagram. Unlike experiments within groups I-III, where samples were uniform up to high pressures, samples in this group are characterised by separation into lighter and darker non-homogeneous areas with visible crystalline boundaries at pressures greater than 12 GPa, presumably after the phase transition from phase S9. Photographs of the sample with 52% O_2 at different pressures are presented in Figure 5.10. Inferred from relative Raman intensities of oxygen and nitrogen vibrons, darker parts of the samples are more oxygen-rich, whereas in the lighter parts the concentration of nitrogen is higher.

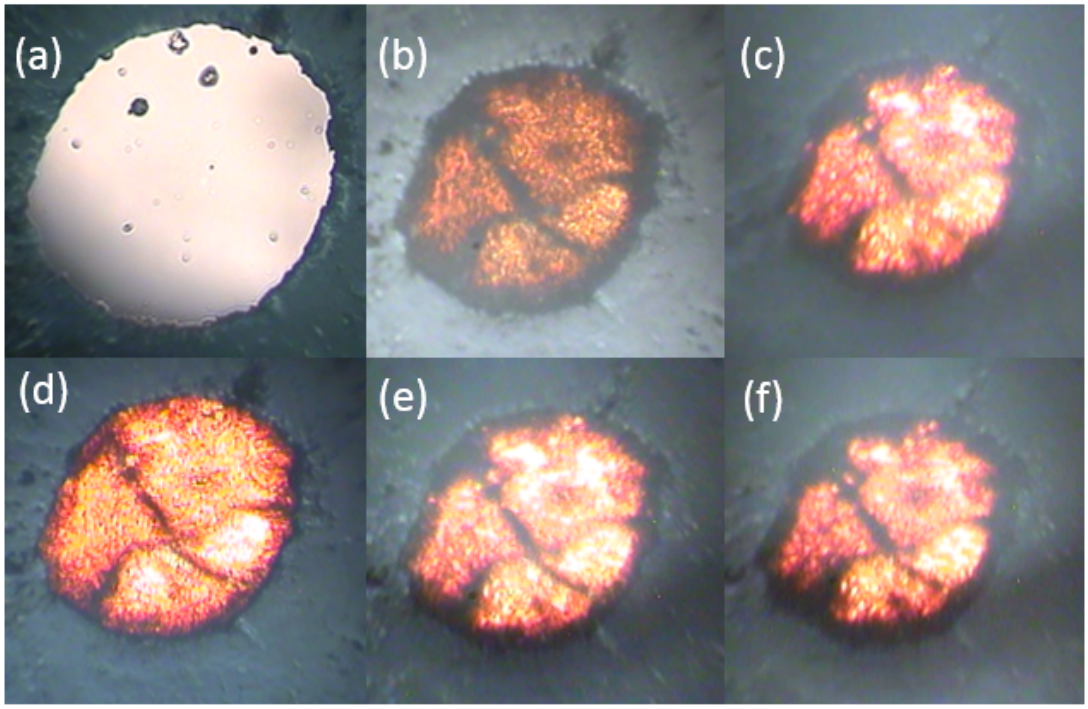

Figure 5.10 *Group IV. Microphotographs of a nitrogen-oxygen mixture with 52% O_2 at different pressures: (a) Fluid at 0.7 GPa. (b) Sample separated into the light (nitrogen-rich) and dark (oxygen-rich) parts at 15 GPa. (c), (d), (e), (f) show the sample at 20 GPa, 25 GPa, 30GPa, 40 GPa respectively. The mixture is transparent and colourless in the fluid state. With increased pressure it obtains reddish orange colour, which is specific for ϵ-phase of oxygen.*

In group IV, we observed the formation of two new phases reflected by shape and intensities of O_2 excitation and changes in low-energy part of spectra (see Figures 5.11, 5.12). This will be shown on the example of the sample with 68% O_2. The following phase transitions take place: F->S2 at 6 GPa, S2->S9 at 8 GPa, S9 ->

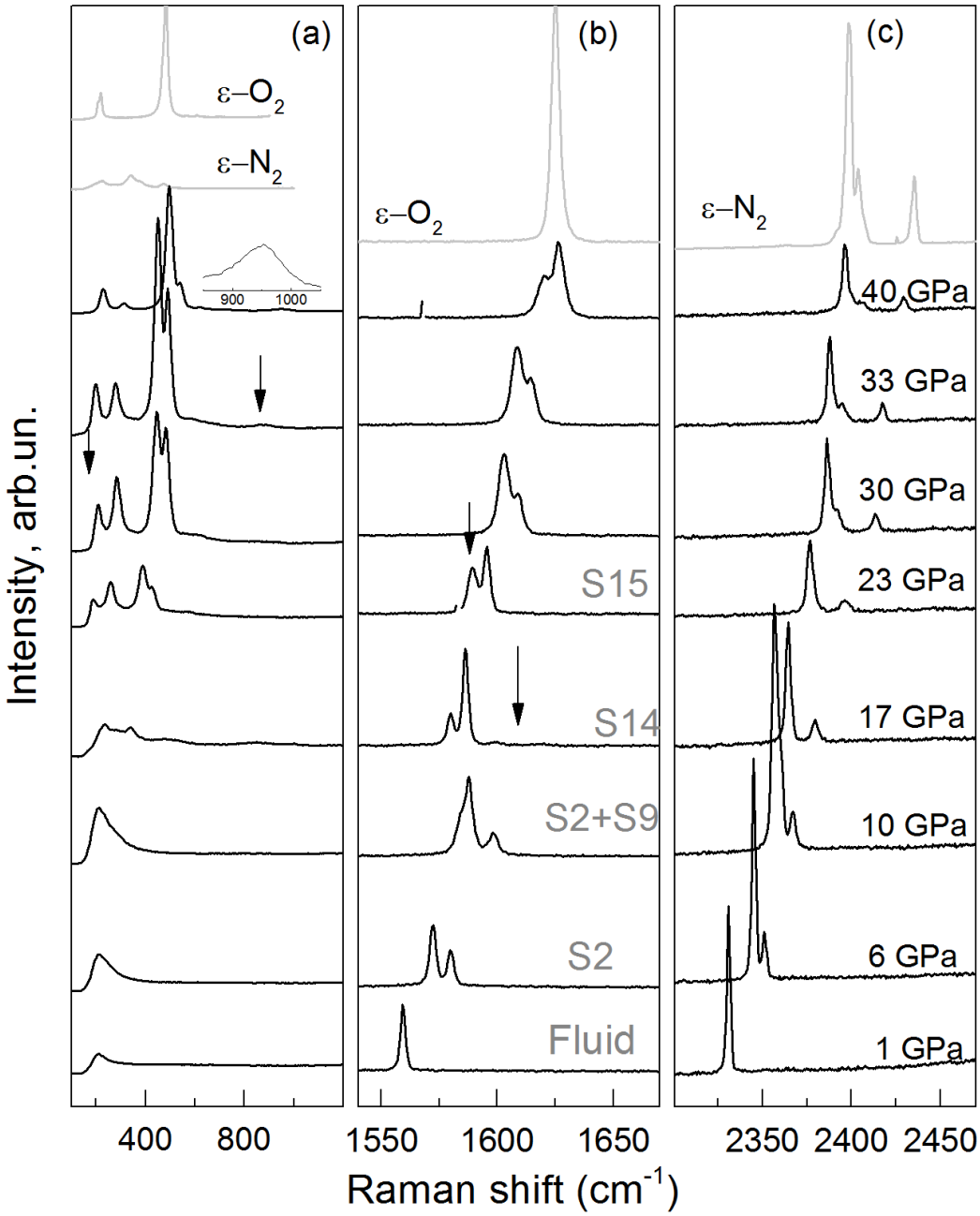

Figure 5.11 *Group IV. A pressure evolution of the Raman spectra collected in 52% O_2 mixture and in the N_2-rich part of the sample. The grey lines on top correspond to spectra of pure nitrogen and oxygen at 40 GPa in their respective ϵ phases. Inset on top of (a) emphasizes appearance of broad peak at 950 cm^{-1} which is associated with ϵ-oxygen. We observe branching of low frequency modes occurring in S15 phase as well as rise of O_2 doublet. Intensity redistribution in O_2 doublet which is presumably due to the different crystal orientation in the highly non-homogeneous mix.*

S14 at 12 GPa, and S15 remains stable above 15 GPa to at least 40 GPa. The oxygen vibrational-peak remained single in the fluid phase, then subsequently

changed to the doublet, characteristic to the S2 phase. On the S2->S9 transition the two oxygen vibron bands become a singlet again. Asymmetric shape of oxygen vibron peak at 10 GPa (Figure 5.11) with a pronounced shoulder on the left points at coexistence of two phases, one of which is reflected by a oxygen vibron doublet and another is most probably a singlet. Given the sequence of phase transitions and previous reports of hexagonal phase in similar pressure and concentration ranges, this phase can be assigned to S9, possessing kagome lattice [Akahama 14]. This phase will also be discussed in Section 5.6.

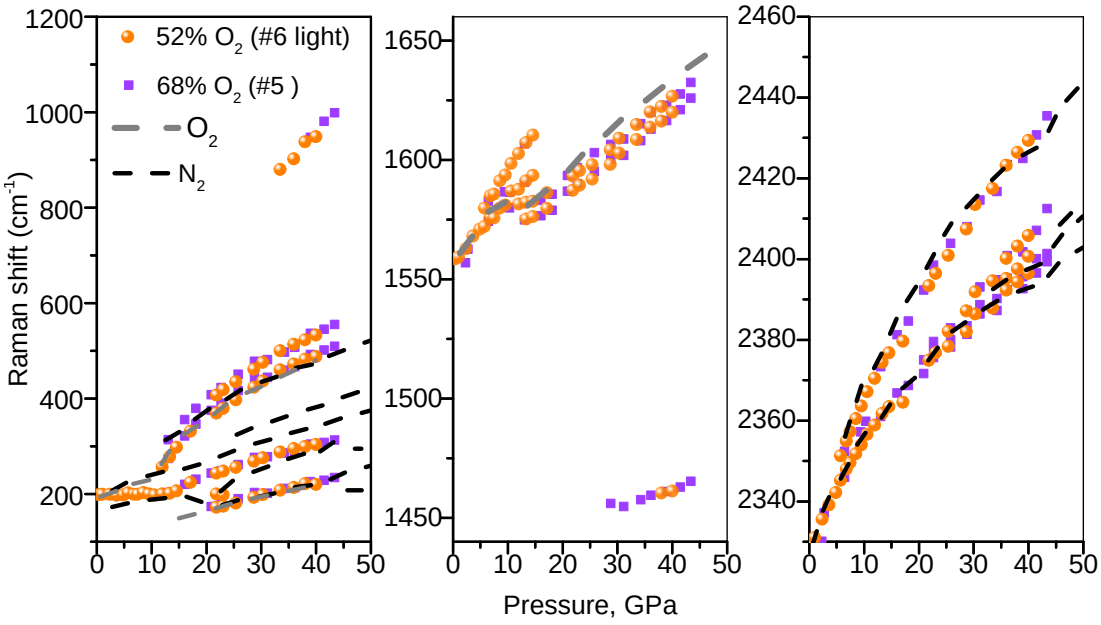

Figure 5.12 *Group IV. Frequencies of lattice modes, O_2 vibrons and N_2 vibrons plotted as functions of pressure from experiments with 52% O_2 and 62% O_2 mixtures. We collected spectra in all parts of non-homogeneous samples after transformation to S15 phase. To avoid plots being overly complicated we will present here only dependencies for nitrogen-rich parts (with transition to S15 phase) above 15 GPa. N_2 vibron reflects its pure behaviour, whereas oxygen vibron is split into a doublet, which differs from pure ϵ-oxygen vibron.*

Transition to S14 around 15-17 GPa is characterized by emergence of two weak peaks neighbouring the oxygen vibron (Figures 5.11 B, 5.12). These peaks could be similar to those corresponding to distorted ϵ^*-nitrogen phase with O_2 molecules substituting N_2 as in phase S6. On the low-frequency side of the strong peak at 1580 cm^{-1}, which could correspond to ϵ phase of oxygen, a less intense peak appears approximately 10 cm^{-1} lower in energy (see Figure 5.11 B). These changes coincide with emergence of new bands in low frequency range (Figure 5.11 A). Such rich Raman landscape suggests a rather complex structure. A possible

speculation is that S14 comprises ϵ-nitrogen, ϵ-oxygen, ϵ^*-N_2 with O_2 embedded in the lattice and some new compound.

The most pronounced effects of S14 to S15 transaction around 22 GPa are the abrupt change of frequency-pressure dependence of O_2-doublet, and emergence of intense low-frequency modes (Figures 5.11, 5.12). Although pressure- frequency dependence confirms that O_2-vibron mimic trend for its ϵ phase, albeit slightly shifted to the lower energy, the low-frequency excitations are more complex with new well-pronounced modes including one at 245 cm^{-1} and doublet at 373 cm^{-1} and 411 cm^{-1}. It is found that a remarkably broad low-frequency peak at around 800 cm^{-1} started growing after phase transition to ϵ phases of both N_2 and O above 30 GPa, after the disappearance of the N_2 vibron. All that implies that S15 could consist of ϵ-nitrogen, ϵ-oxygen and a new compound possibly related to a cluster structure.

A common feature for all samples is the significant decrease of N_2-vibron intensity in S15 and ϵ-O_2+ϵ-N_2 phases with a rate depending on the concentration of oxygen in these phases. The observed redistribution of intensities of O_2 doublet could be related to different orientation of crystals due to the non-homogeneity of sample.

5.6 Group V

Characteristic Raman spectra of this group is presented in Figure 5.13. The lattice modes of oxygen are easy to recognize due to their exceptional intensity, whereas no low-frequency modes related to an ordered structure of nitrogen were clearly resolved. A significant decrease in intensity of nitrogen vibron with increased pressure is observed; the intensity of oxygen vibron remained same or was slightly affected by pressure, but was not proportional to intensity decrease of N_2 vibron. Frequencies of the modes reflect those of pure components, as shown in Figure 5.14.

For the concentrations above 80% of O_2 all Raman signatures fit rather well with those of pure N_2 and O_2. The sequence of phase transitions in $(N_2)_0.2$ $(O_2)_0.8$ is thus exactly the same as in pure O_2. The alloy solidifies into the S3 phase with a rhombohedral structure similar to that of β-oxygen with N_2 substitution,

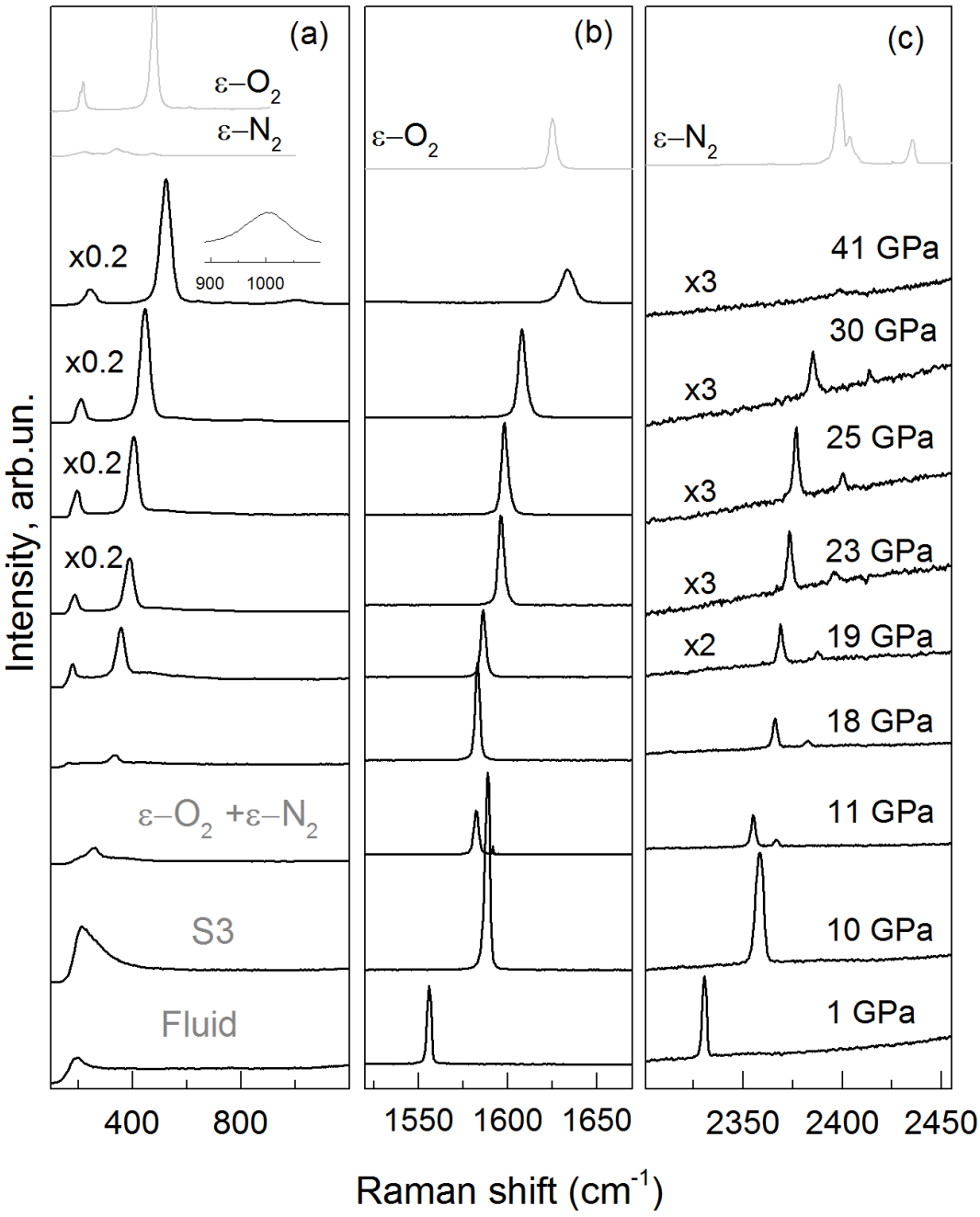

Figure 5.13 *Group V. Raman spectra of the sample with 82% O_2 mixture. The grey lines are for ϵ-nitrogen and oxygen at 40 GPa. Plot (a) demonstrates very simple landscape, characteristic for O_2. Intensity of N_2 vibron significantly drops with pressure, whereas O_2 vibron and its lattice modes exhibit intensity increase.*

and then decomposes into ϵ-oxygen and ϵ-nitrogen. Samples with less content of oxygen undergo additional transformation into S2 solid solution with a cubic Pm3n δ-nitrogen structure, which is normal for the majority of concentrations due to the exceptional stability of S2 over concentration range. According to the phase diagram of pure oxygen, β-oxygen transforms to δ-oxygen prior to transition to

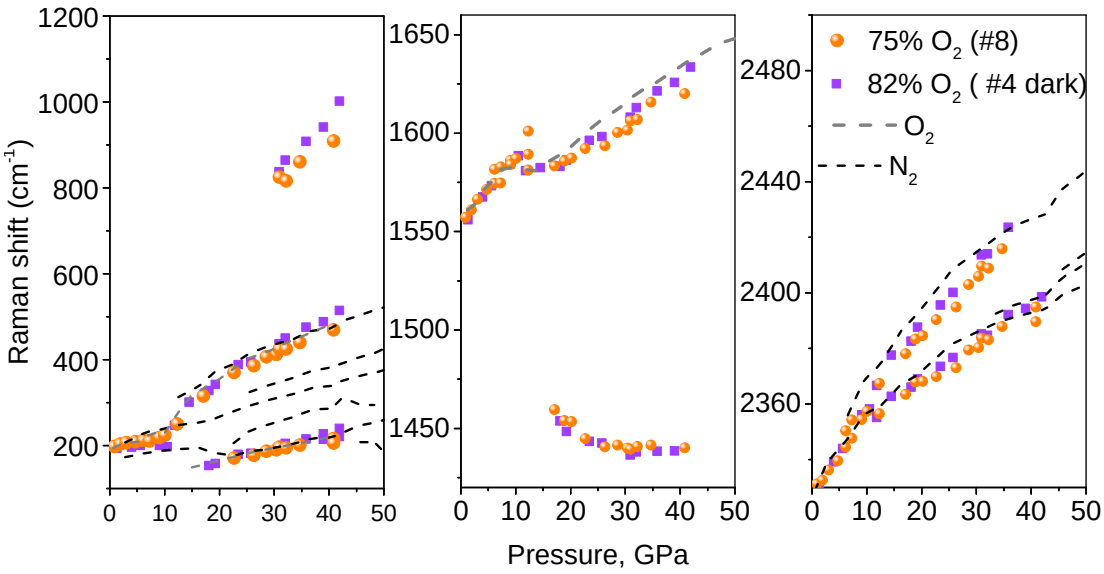

Figure 5.14 *Group V. The frequency-pressure dependence of Raman modes of mixtures with 75% O_2 (orange balls) and 82% O_2 (purple squares) at 300 K. The grey dashed lines are for pure oxygen and nitrogen. All components behave as their pure species.*

ϵ phase. But pressure steps in our experiments were not small enough to detect these changes.

Mixtures which comprise less than 80% of O_2, undergo transformation to S2, followed by transition to a phase, featuring oxygen singlet (Figure 5.15), which could be characteristic for a transition into S9 as well as S3 [Sihachakr 04, Akahama 14]. As plotted in Figure 5.15, it corresponds well to pure O_2. Similar behaviour was reported for a hexagonal phase with a kagome lattice, described elsewhere in details [Sihachakr 04, Akahama 14, Akahama 16]. Based on the sequence of transitions, we assign this phase to S9. O_2-vibron of ϵ-oxygen is shifted about 10 cm^{-1} from S9 vibron to lower wavenumbers with further compression, following a characteristic trend for the ϵ-phase, as shown in Figure 5.15. There is quite significant disagreement over concentration range for S9 phase between in our results and the previously reported research. According to reference [Akahama 14], the hexagonal phase is stable in a wide composition range, starting from 40% O_2. Yet, we did not observe this phase in samples with 52% O_2 and its formation was only observed for compositions with 68% O_2 (Group IV) and 75% O_2 (Group V).

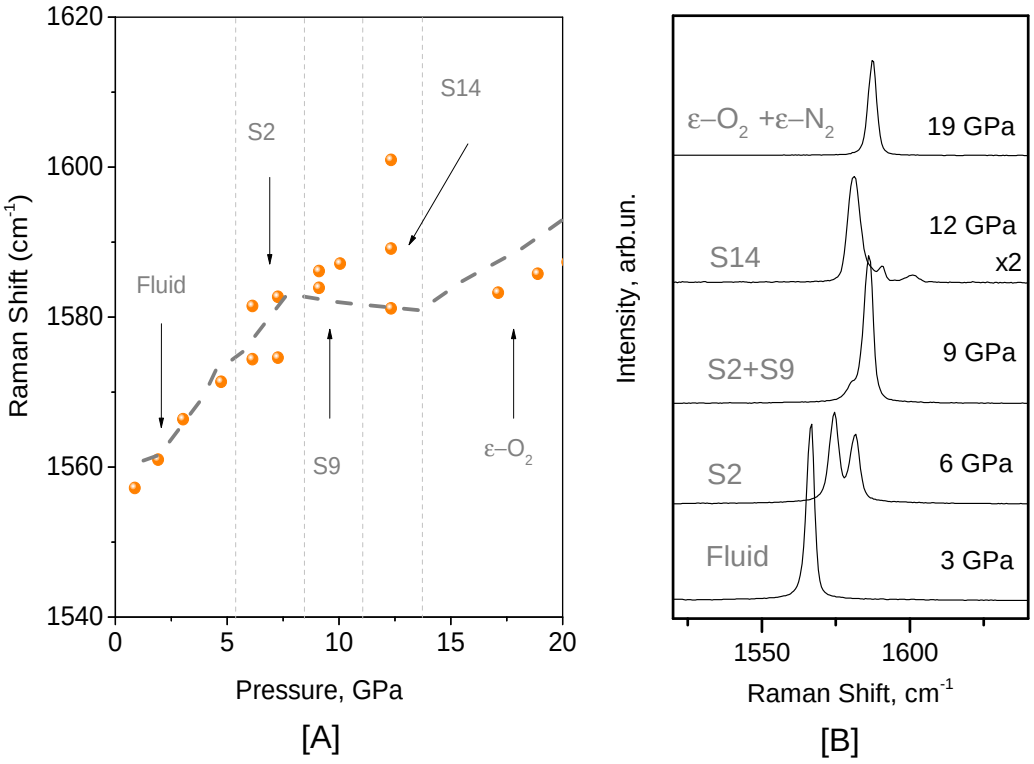

Figure 5.15 *[A] Group V. Blown up part of diagram for frequency-pressure dependence for the mixture with 75% O_2 illustrating typical behaviour of O_2 vibron, when the sample undergoes transitions Fluid -> S2 -> S9 -> S14 -> ϵ-O_2+ϵ-N_2 in the region from 0 to 20 GPa. The orange balls are for the nitrogen/oxygen mixture, the grey dashed line is for pure oxygen. [B] Group V. Raman spectra of the sample with 75% O_2 at the selected pressure steps, demonstrating radical changes of the oxygen vibron with phase transitions: Fluid -> S2 -> S9 -> S14 -> ϵ-O_2+ϵ-N_2.*

5.7 Discussion

In this work we report Raman measurements of the phase diagram of nitrogen/oxygen system at room temperature extended from 12 GPa to a maximum pressure of 150 GPa at room temperature. Mixtures with various concentrations ranging from 13% to 82% of oxygen were studied. Estimation of concentrations in the liquid phase was based on calibration of the Raman cross-sections in N_2,O_2 and N_2/O_2 mixtures to the known mix (25% O_2).

Although we avoid speculating on exact concentration of various parts of nonhomogeneous samples in solid phases, we could estimate composition based on the spectroscopic features and optical behaviour. Pressure steps were normally about 2 GPa for pressure range 0 to 15 GPa, and 5 GPa after that. Nevertheless, there might be inaccuracies with pressure determination in areas where different phases coexisted.

Visual observations showed that all samples changed colour, as their transparency evolves with pressure. Some samples inhibited separation into regions of varying opacity, which could be associated with low miscibility of N_2 in oxygen-rich samples [Sihachakr 04]. All samples apart from stoichiometric concentrations at pressures corresponding to ϵ-oxygen phase were red or dark-orange coloured.

We assigned phase transitions based on defined spectral fingerprints and thus derived P-x phase diagram (Figure 5.16). Extended phase diagram consists of seven phases, characterized in previous research (see Chapter 3 for details), and eight new high-pressure phases above 12 GPa described in the present work. Descriptions of the new phases, observed in the present work, are summarized in Table 5.2. Our experimental results in general agreed with previous research of low-pressure regions of the phase diagram.

Mixtures with the oxygen concentration higher than 80% appeared to comprise pure phases of nitrogen and oxygen. On the contrary, mixtures with increased nitrogen content possess more complex structures, which was inferred from deviations of the Raman spectra. Formation of the new phases might be due to the influence of molecular cluster structure of ϵ-oxygen. It might either coexist with other nitrogen/oxygen phases or form another structure, where oxygen clusters are trapped in the nitrogen cell, as suggested for the case

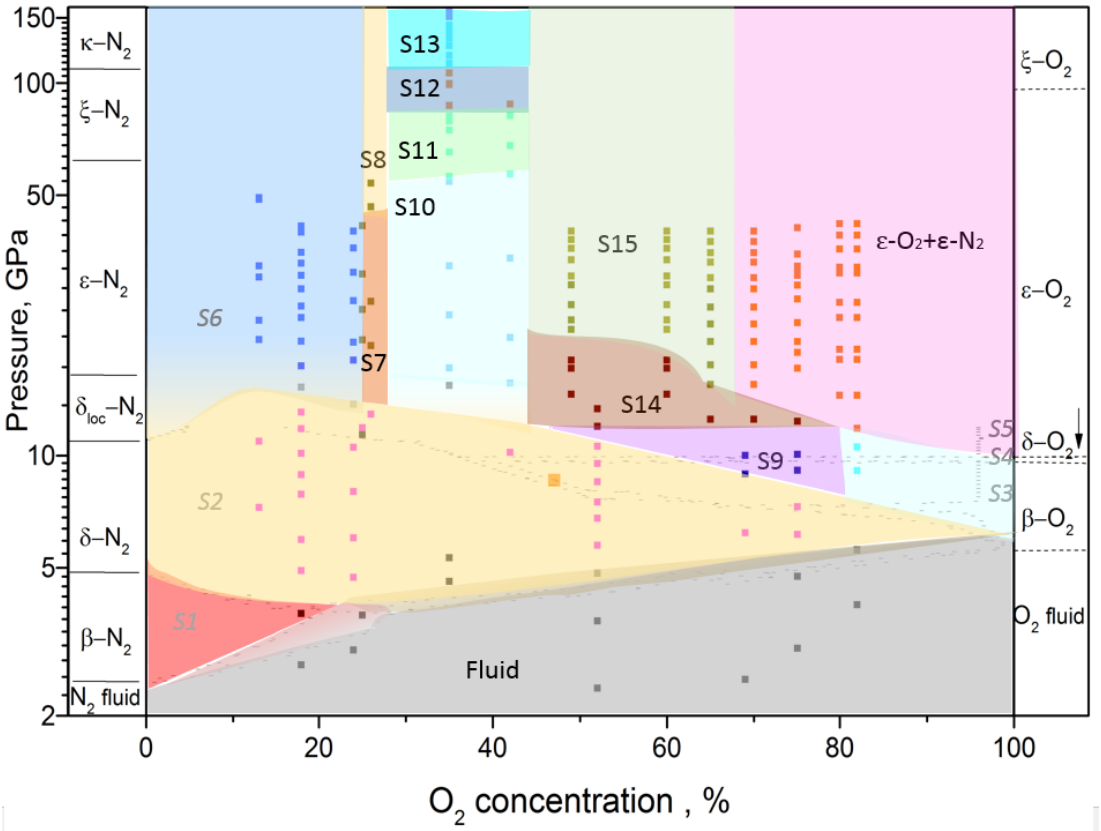

Figure 5.16 *A tentative phase diagram of the binary nitrogen/oxygen system up to 150 GPa and at ambient temperature. The grey symbols indicate phases described elsewhere [Baer 90, Sihachakr 04, Akahama 14]. The black symbols are for phases discovered in the presented study. The proposed phase diagram is overlaid with the phase diagram up to 12 GPa provided by [Sihachakr 04]. The dashed grey phase lines between phases S1-S2-S3-S4-S5-S6 are from [Sihachakr 04]. Phase domains are drawn tentatively based on the experimental data painted with filled squares. For easier analysis, structures of pure components are described on the left and right sides of the diagram. Sequence of phase transitions in general corresponds to those reported earlier. Nonetheless, there is a significant disagreement on the stability of domain S2 and S9. As long as we were able to detect the second vibron of the ϵ-oxygen phase in the majority of new phases, it is arguable that any of the phases, apart from phases S7 and S8, represents homogeneous solution. On the contrary, we suggest that in most cases solution S2 dissolves into various phases comprising pure components and either new modifications of existing phases or new solutions. Further research is required to determine exact structure of the observed phases.*

of nitrogen/oxygen transforming into $NO^+NO_3^-$ [Sihachakr 06]. In the whole concentration range, phases are stable in the pressure window from 16 to 60 GPa, when neither nitrogen nor oxygen have a phase transition and remain in their respective ϵ-phases. Subjected to further compression, mixtures undergo more phase transformations, not necessarily correlated to transitions in pure oxygen or nitrogen.

Comparison with the Raman frequencies of nitrogen oxides (NO, N_2O, NO_2, N_2O_3) showed that frequencies of Raman features of the phases, observed in the present work, do not correspond to the characteristic peaks of different nitrogen oxides in various phases (see Table 3.4). Therefore, we conclude that we did not form nitrogen oxides in the phases, reported earlier. At the same time, we witnessed the formation of new, presumably stoichiometric compound $(N_2)_3O_2$ (Group II), featuring unique Raman spectra, as it was predicted previously [Sihachakr 04].

Although we did not aim at the detailed study of low-pressure regions, which were extensively explored before, we found some discrepancies with previously published research. For instance, we observe stronger deviation in intensity ratio for O_2 vibron doublet and N_2 vibron doublet, reflecting the concentration of disk-like and sphere-like molecular distributions. In pure δ-nitrogen, the N_2-vibrons intensity ratio is $I_{\nu_2}/I_{\nu_1} = 3$ as opposed to that of 1.4 -1.7 in observed nitrogen/oxygen mixtures [Sihachakr 04]. This implies that there is a bigger O_2 population on ν_1 site of nitrogen lattice than expected.

Another disagreement is related to phase S9. Previous works already showed differences locating this phase. According to our results, it occurs in a narrower concentration range and more shifted to the oxygen-rich area than reported previously [Sihachakr 04, Akahama 14].

To summarize, compression of the nitrogen/oxygen mixtures affects the high complexity of interactions between nitrogen and oxygen molecules, thus resulting in formation of the new crystal structures. Further research is required to extend phase diagram of this binary system and identify exact composition and structure of phases.

Table 5.2 *Description of phase transitions of nitrogen/oxygen mixtures in the extended range of pressures up to 150 GPa. "S" refers to solids.*

Phase	Description	Reference
S1	hexagonal $P6_3$ /mmc	[Baer 90] [Sihachakr 04]
S2	cubic Pm3n (similar to δ-N_2)	[Baer 90] [Sihachakr 04]
S3	rhombohedral $R\bar{3}m$ (hexagonal cell)(similar to β-O_2)	[Baer 90] [Sihachakr 04]

S4	orthorhombic Fmmm (based on δ-O_2)	[Baer 90] [Sihachakr 04]
S5	monoclinic C2/m (similar to ϵ-oxygen); ϵ-oxygen+δ-N_2	[Baer 90] [Sihachakr 04]
S6	tetragonal (possible space group $P4_2/ncm$); might be consisting of ϵ-oxygen (monoclinic C2/m) + ϵ-N_2 (rhomboedral $R\bar{3}c$)+ ϵ-oxygen(host-guest structure with O_2 and N_2 molecules)	[Baer 90] [Sihachakr 04] [Minenko 04]
S7	stoichiometric compound (presumably $(N_2)_3O_2$)	present work
S8	stoichiometric compound (presumably $(N_2)_3O_2$)	present work
S9	hexagonal phase with kagome lattice /molecule	[Sihachakr 04] [Akahama 14] [Akahama 16]
S10	ϵ-oxygen (monoclinic C2/m) + ϵ-N_2 (Rhomboedral $R\bar{3}c$)	present work
S11	ζ-N_2 (Primitive orthorhombic)+ ϵ^*-oxygen	present work
S12	S12 might be comprising of ζ-N_2 and modified ϵ^{**}-oxygen with the enlarged unit cell	present work
S13	amorphous, correlated with monoclinic structure of κ-N_2, with small amount of metallic oxygen	present work
S14	ϵ-N_2+ ϵ-oxygen + ϵ^*-N_2 with O_2 embedded in the lattice + some new compound	present work
S15	ϵ-N_2+ ϵ-oxygen + new compound (possibly related to a cluster structure)	present work
>70	ϵ-oxygen+ϵ-N_2	present work

Chapter 6

Novel high-pressure high-temperature compounds of N_2/O_2 mixture

6.1 Introduction

Upon reaching high-density states with the significantly increased levels of kinetic energy, molecular solids are expected to transform into the extended solids with delocalized electrons via two mechanisms: insulator-metal transition via broadening of electronic bands triggered by pressure, or formation of densely packed polymeric covalent solids with local delocalization of electrons. Both mechanisms are known in pure elements: N_2 forms a polymeric solid, and O_2 becomes metallic. Upon further compression, extended solids can transform to amorphous or ionic solids, due ionization of valence electrons when electrostatic forces become more dominant. Such ionization can ultimately lead to dissociation to solids containing simple elements or atomic metals.

Previous research within nitrogen/oxygen system, exposed to high pressure and high temperature, showed that in most cases ionization takes place, although sometimes initial sample dissociated into pure components. For example, Somayazulu et al. [Somayazulu 01] reported dissociation of N_2O into N_2 and O_2 at temperatures above temperatures of formation of ionic $NO^+NO_3^-$. In previous

research conducted for mixtures of the N_2/O_2 system [Sihachakr 06, Meng 06, Kuznetsov 09], only ionic compounds $NO_2^+NO_3^-$, $NO^+NO_3^-$ were observed. The strong P-T path dependence, pressure, temperature and concentration range and starting phase are likely the reasons why new phases formed by dissociation, polymerization or metallization were not observed hitherto.

To probe the high-temperature high-pressure regime we performed two experiments with laser heating mixtures of N_2/O_2. One sample contained mixture with 40-60 % O_2 and was laser heated from phase S15 at 20 and 25 GPa. Another sample with 25% O_2 mixture was laser heated at 90 GPa. Details and analysis of both experiments will be discussed in the following sections.

6.2 Formation of new phases at 20 GPa and high temperatures

The investigated sample consisted of 40-60% O_2 mixture of high-purity O_2 and N_2. The composition was estimated only tentatively, based on the characteristic Raman features. The sample was cryogenically loaded from the liquid mixture of O_2 and N_2 into a piston-cylinder cell. Ruby balls were used as pressure markers. A silver coupler plate was employed (Figure 6.1).

Raman spectra from the area covered by the coupler were collected throughout the experiment to ensure that spectroscopic picture of the N_2/ O_2 mixture is not affected by processes related to the coupler. From the comparison of spectra from the coupler and transparent sample, we infer that the Raman modes, observed in the spectra of the transparent part, are not related to those of the coupler.

While being compressed up to 20 GPa at room temperature, the sample behaved as a typical mixture of Group IV, reaching phase S15 at 20 GPa (S15 consists of ϵ-nitrogen, ϵ-oxygen and the new compound which possibly has a cluster structure, see Table 5.2 of Chapter 5). At 20 GPa, the sample was laser heated from phase S15 with the beam of approximately 2.0 V for 10 min to temperature estimated as 2000 K. After laser heating, we observed separation of the sample into dark and light areas, although before heating the sample was somewhat uniform. After a slight pressure increase to 26 GPa, the sample was laser heated again with the same parameters, and subsequently pressurized to 40 GPa. Laser heating at 20

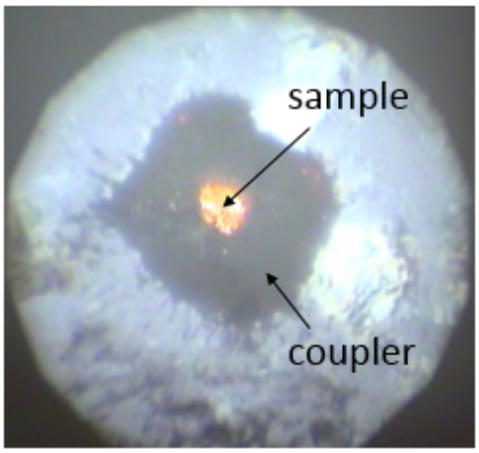

Figure 6.1 *Microphotograph of the sample with 40-60 % O_2 at 20 GPa. The dark plate in the gasket hole is the silver coupler. The sample was laser heated at 20 and 27 GPa. At 20 GPa, the sample appears to be slightly nonhomogeneous, which is standard behaviour for mixtures comprising more than 40% of O_2 in the S15 and S16 phases. After laser heating, the sample splits into visually darker and lighter parts.*

GPa caused drastic changes in the Raman spectrum of the sample, but heating at 27 GPa induced only minor alterations of the already appeared modes.

Raman spectra collected before and after laser heating are presented in Figures 6.2 and 6.3, where different modes are labelled with letters. We will refer to the phase, formed by laser heating at 20 GPa, as phase HT1, and phase, formed at 27 GPa, as phase HT2. Raman excitations of the sample, collected at 20 GPa before heating, can be assigned to the S15 phase, which presumably consists of ϵ-oxygen, ϵ-nitrogen and a new compound featuring O_2 doublet and rich low-frequency excitations (see Chapter 3 for the detailed discussion about phase S15). Laser heating at 20 GPa resulted in phase transition to HT1, reflected by the significant transformation of the Raman spectra. Dark and light parts of the sample exhibited similar Raman peaks, which were more intense in the dark part. Raman peaks of the non-transformed phase S15 (modes *a, b, g, h, k* in Figure 6.2) remained on the spectra together with the new broad peaks at around 740 cm^{-1} (mode *e*), 1107 cm^{-1} (mode *f*) and 2270 cm^{-1} (mode *i*) and sharp and narrow peaks around 270 cm^{-1} (mode *c*), 780 cm^{-1} (mode *e*) and 2300 cm^{-1} (mode *j*). Interestingly, the intensity of the O_2-vibron (mode *h*) of S15 dropped significantly, becoming nearly three times smaller than that of the N_2-vibron (mode *k*) (compared to the initial ratio $\approx$ 1:1 at 20 GPa in S15). Pressure increase to 26 GPa did not result in any significant changes apart from the regular pressure-induced shifts.

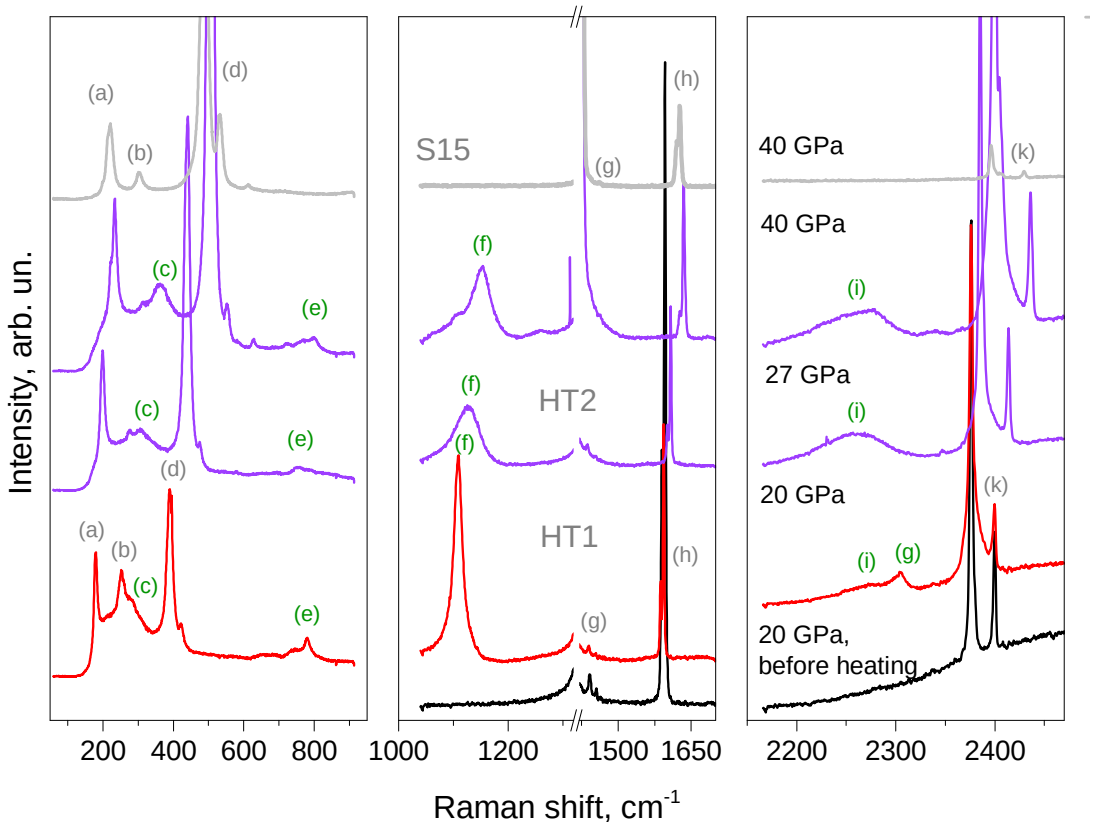

Figure 6.2 *Representative Raman spectra of the dark park of the sample which was laser heated from the S15 phase at 20 GPa, collected with grating 1800 g/mm. Black colour is for the spectrum collected in phase S15 at 20 GPa before laser heating. Red colour is for the spectrum collected in phase HT1 at 20 GPa after laser heating. Purple colour is for spectra collected in phase HT2 at 27 GPa and 40 GPa after laser heating at 27 GPa. The grey line on top indicates the spectrum of the N_2/O_2 mixture with 52% O_2 in S15 phase at 40 GPa, 300 K. Transformation to the new high P-T phase HT1 is reflected by the appearance of new modes labelled with the green letters c, e, f, i, k. Modes labelled with the grey letters a, b, d, g, h, k belong to the non-transformed S15 phase.*

Second laser heating at 27.6 GPa brought minor changes to the Raman spectra and led only to a slight broadening of peaks at 1130 cm^{-1} (mode f), and 2276 cm^{-1} (mode i), and disappearance of sharp peaks at around 270 cm^{-1} (mode b), 780 cm^{-1} (mode e) and 2300 cm^{-1} (mode j) (Figure 6.2) in the dark area, though they still could be noticed in the lighter part of the sample. Exposed to further compression to 40 GPa, the sample did not experience any considerable changes apart from the usual pressure effects as softening and broadening of the modes (Figure 6.3). We will refer to this phase as HT2 phase.

We could distinguish between peaks related to the S15 phase (comprising ϵ-oxygen, ϵ-nitrogen and new compound of S15) and peaks in phases HT1 and

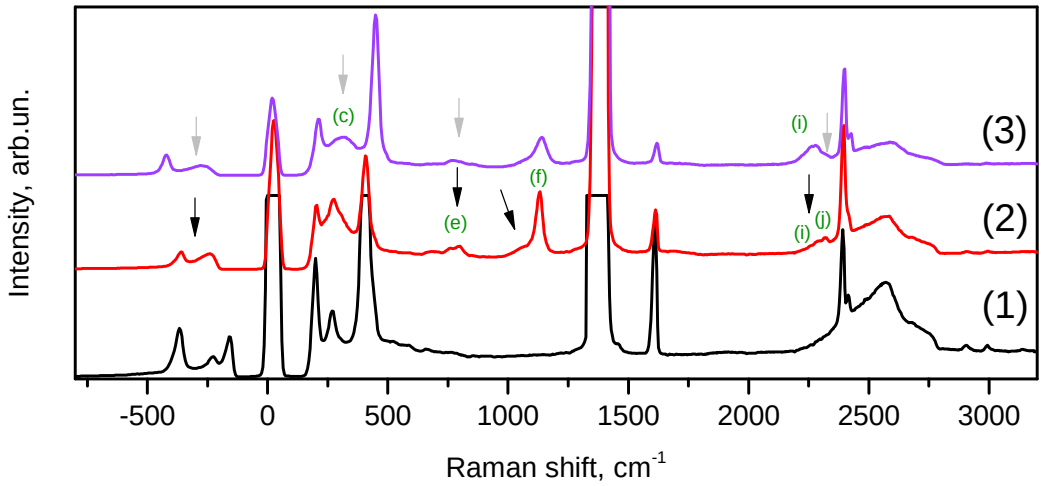

Figure 6.3 *Raman spectra collected with grating 300 g/mm from the sample at: (1) 20 GPa, S15 phase, before laser heating; (2) 20 GPa, HT1 phase, after laser heating; (3) 27 GPa, HT2 phase, after the second laser heating. The black arrows point at new peaks. The grey arrows point to the modes, softened after the second laser heating. Modes, labelled with green letters, arisen as phase transition is induced by laser heating, and are characteristic for the new high P-T compound HT1-C. Changes of the Stokes features are supported by alteration of the anti-Stokes part of the spectra.*

HT2 which were induced by heating by visual comparison of the Raman spectra (Figures 6.2, 6.3). Modes *a, b, d, g, h, k* appear to be similar to those representing phase S15 of nitrogen/oxygen mixture before at 300 K. On the other hand, modes *c, e, f, i, j* appeared after laser heating. Changes of the Stokes part of the Raman spectra with heating and compression was followed by the alteration of the anti-Stokes features (Figure 6.3). Most of the modes, that emerge after laser heating at 20 GPa, are still present after second laser heating at 27 GPa and can be traced to 40 GPa with no major changes (Figure 6.4).

Previous research indicated that nitrogen/oxygen mixtures and nitrogen oxides, exposed to high temperatures, tend to transform to ionic compounds (see Chapter 3). Brief comparison of the frequencies of the modes of phases HT1 and HT2 shows that modes of the majority of nitrogen oxides do not match with the detected excitations (see Chapter 3, Table 3.4). The most probable candidates are γ-N_2O_4 and $NO^+NO_3^-$, which are somewhat similar to the HT1 and HT2 modes not only in frequencies of the excitations, but also in their shape [Song 03b, Sihachakr 06, Meng 06, Kuznetsov 09].

In Figure 6.4, we will examine if any of the observed modes resemble excitations of N_2O_4 or $NO^+NO_3^-$, reported in previous research. Modes *i, j* around 2300

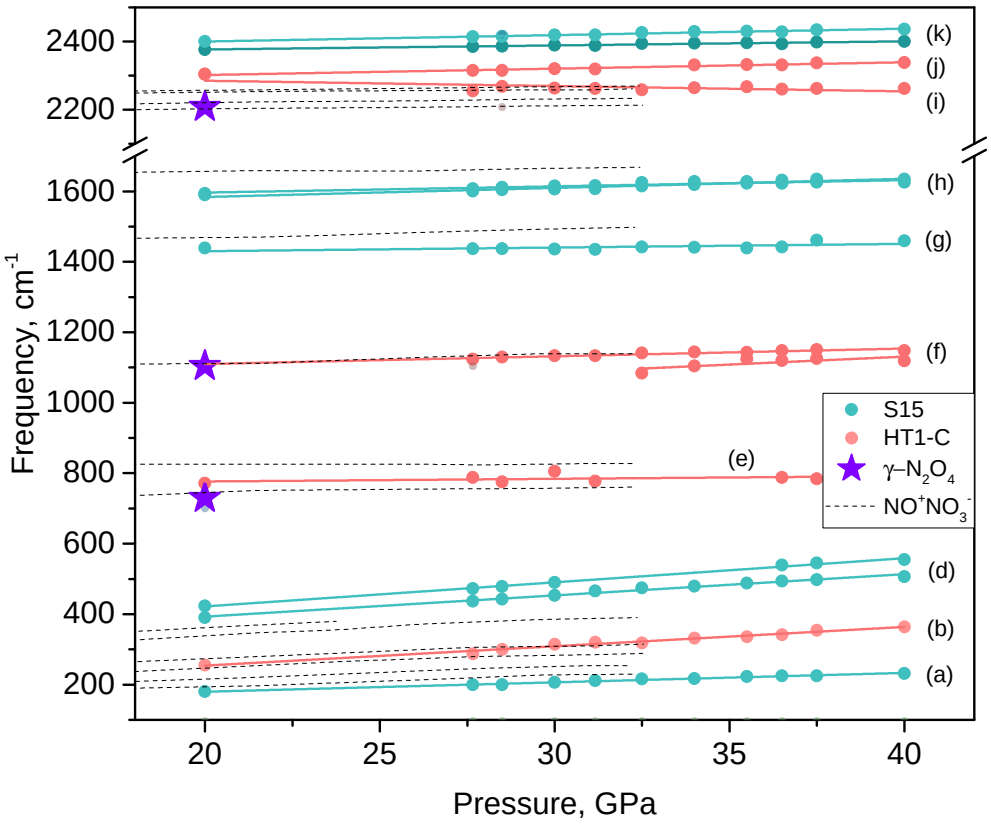

Figure 6.4 *Frequency-pressure dependence for the sample exposed to laser heating from the S15 phase at 20 GPa and 26 GPa (pink and blue balls and lines). Coloured lines are guides for eyes only. Blue is for the modes that can be related to S15 of the N_2/O_2 mix. Pink lines and balls are for the peaks associated with the new high-temperature compound. The dashed lines are for $NO^+NO_3^-$ modes from [Kuznetsov 09]. The purple stars represent positions of fundamental peaks of the γ-N_2O_4 phase, measured at 12 GPa (not including low-frequency region) [Kuznetsov 09]. Raman modes observed in the experiment are labelled with letters.*

cm^{-1} are rather close to both NO^+ vibrational mode (2270 cm^{-1}) and γ-N_2O_4 mode (2208 cm^{-1}) (Table 3.4, Chapter 3). Mode *f* at 1130 cm^{-1} matches well extrapolation of the pressure dependence for both NO_3^- symmetric stretch (ν_1) and mode of γ-N_2O_4. However, aforementioned high and low energy modes *i, j, f* are much broader than those of the γ-N_2O_4 phase and especially of the orthorhombic phase of nitrosonium nitrate reported earlier [Song 03a], which are also much more intense than the observed modes. The plausible conclusion can be that these modes are related to the formation of another molecular phase of N_2O_4 with more complex lower-symmetry structure of the molecule [Bolduan 84], which we will refer to as HT1-C. Emergence of sharp components of modes *c, e, g* after the first heating and their disappearance after the second heating can probably be because of formation of other N/O compounds as a result of first

heating at 20 GPa, which then fully transform into components of phase HT2.

In conclusion, Raman spectroscopy studies of the nitrogen/oxygen mixture with 40-60% O_2 exposed to laser heating at 20 GPa and 27 GPa revealed surprising transformation to new high P-T phases HT1 and HT2 with the formation of the new compound HT1-C, dissimilar to known forms of N_2O_4 and $NO^+NO_3^-$. It is proposed that phase HT1 is a new phase which can be formed from phase S15 by laser heating at 20 GPa, and which consists of the non-transformed S15-phase (ϵ-nitrogen, ϵ-oxygen, new S15 compound) and a mixture of the high-temperature compound HT1-C and other intermediary N-O products. By laser heating of phase HT1 at 27 GPa, it is possible to reach phase HT2, which comprises of the S15-phase(ϵ-nitrogen, ϵ-oxygen, new S15 compound) and the new high P-T compound HT1-C.

6.3 Formation of new phases at 90 GPa and high temperatures

Sample with 25% O_2 was gas-loaded to a symmetric diamond anvil cell (DAC) at 300 K and 5 GPa. The sample was steadily compressed from 5 to 41 GPa (phase S7) followed by collection of Raman spectra and then to 96 GPa on the beam line BL10XU, SPring8, Japan. Unfortunately, we lack spectroscopic information for the 41-96 GPa range. We used diamond edge calibration as a pressure marker. The colour of the sample changed from bright orange at 30 GPa to almost black at 96 GPa. At 96 GPa the sample was laser heated. We observed separation of the sample into the bright transparent part and opaque, transparent part, with the different characteristic Raman spectra in both regions (Figure 6.5). The laser power of the system was kept around 30 mW and laser exposure fixed between 10s-60s. The temperature of the heated area was estimated as approximately 3000 K.

As it was shown in Chapter 5, mixtures with 25% O_2 belong to Group II and form a new, probably stoichiometric compound at pressures above 20 GPa. They feature Raman spectra with such distinctive components as ill-defined low-frequency modes, expanded O_2-vibron, and N_2-vibron similar to ϵ-N_2 (Figure 5.4, Chapter 5).

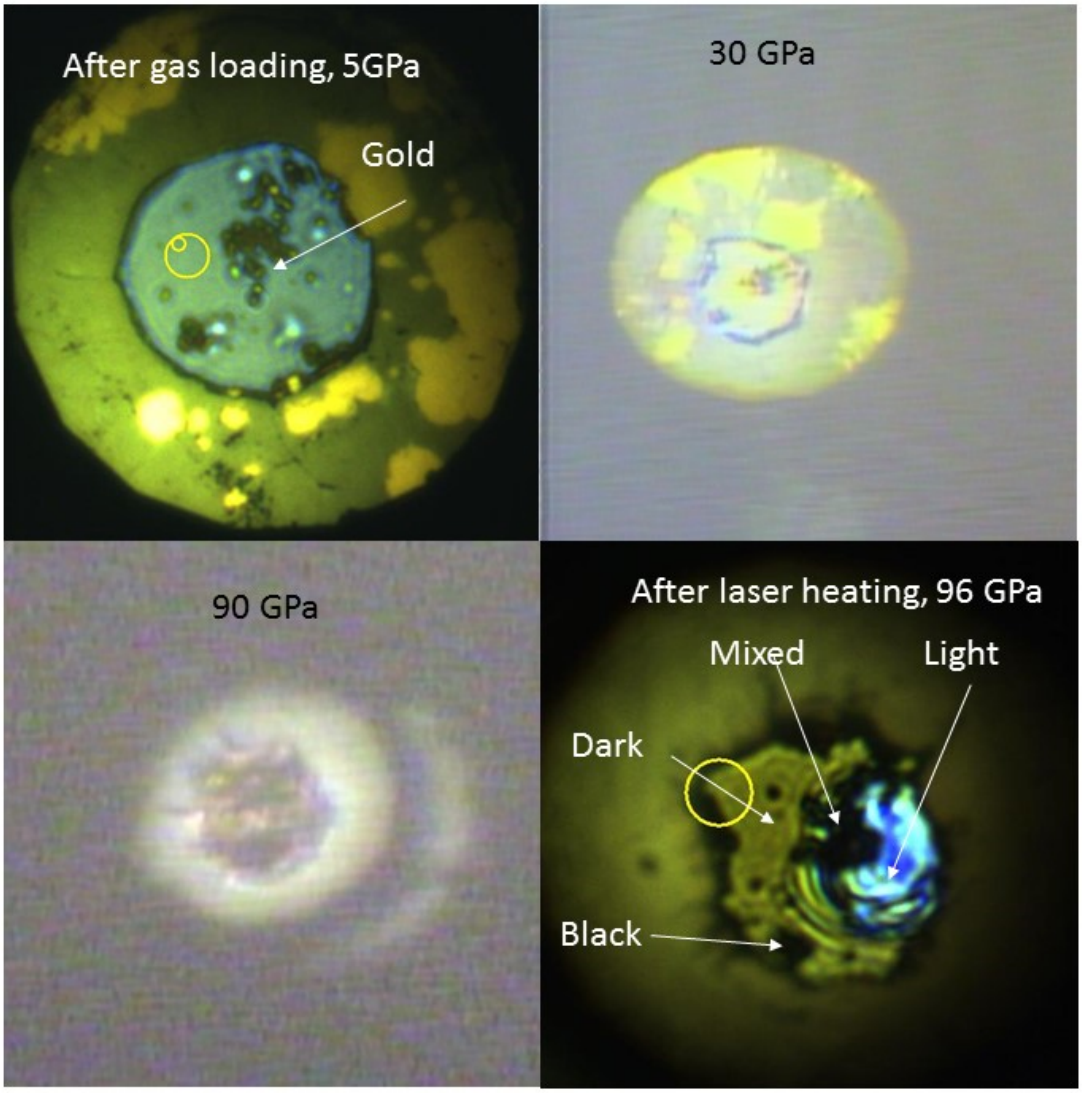

Figure 6.5 *Microphotographs of the evolution of the 25% O_2 sample at different pressures. Top left: after loading at 300 K and 5 GPa. Top right: 30 GPa, the sample is still transparent. Bottom left: at 90 GPa, the sample becomes opaque and non-uniform. Bottom right: separation of the sample into the transparent bright and opaque parts after laser heating.*

After laser heating at 96 GPa, the sample was separated into two major parts which possessed remarkably different Raman spectra (Figure 6.6). In the light part of the sample, as well as in the mixed and black parts, we observed formation of new phase HT3. It exhibits rich low-frequency landscape, consisting of sharp peaks emerging between broad modes at 417 cm^{-1} (mode a), 648 cm^{-1} (mode b), 775 cm^{-1}, 923 cm^{-1}) (mode e) and a broad band at 1260 cm^{-1} (mode f). They match very well the extrapolation of lower pressure data for the similar bands in phases HT1/HT2 in the other laser heated sample (see Figure 6.4). Another band which appears to be identical to mode i of HT2 phase at lower pressures is

the broad feature around 2260 cm^{-1}.

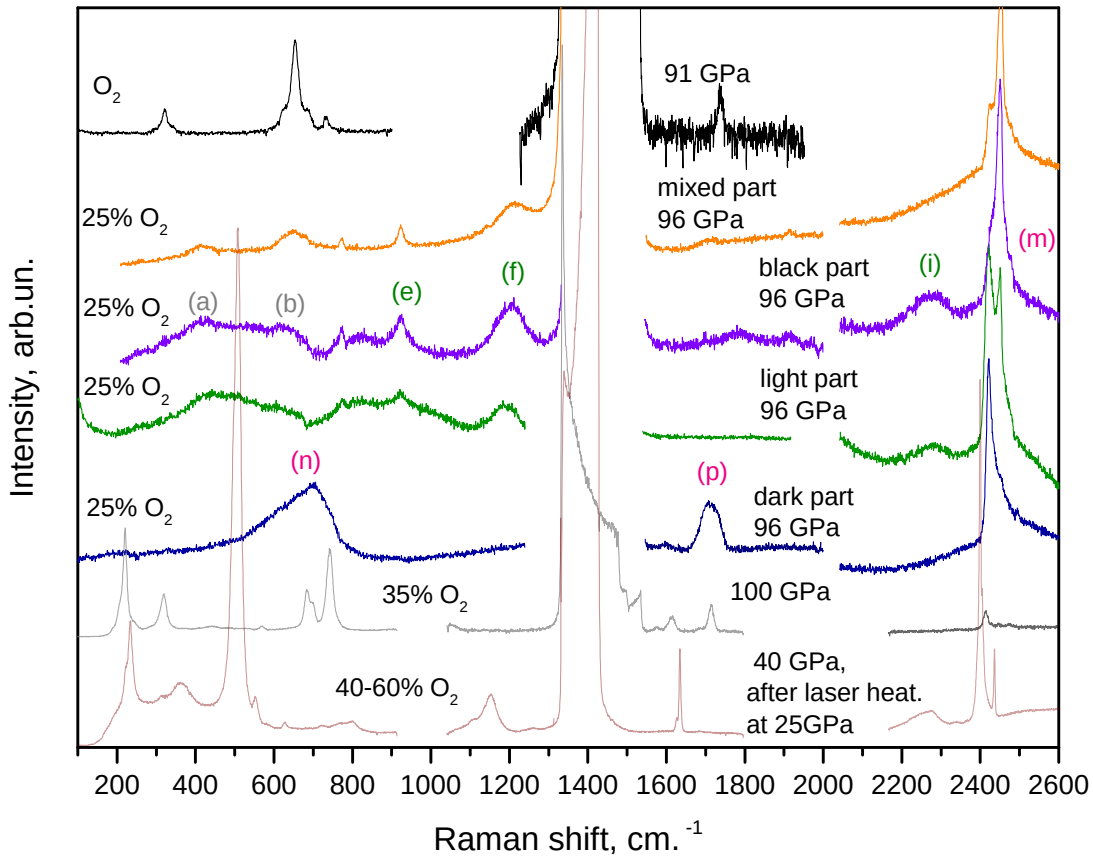

Figure 6.6 *Representative Raman spectra collected from the different parts of the laser heated sample with 25% O_2 at 96 GPa. Spectra of pure O_2 at 91 GPa (black), N_2/O_2 mixture with 35% O_2(grey) and 40-60% O_2 mixture at 40 GPa after heating at 26 GPa (light brown) are added for comparison. Green, purple and orange colours correspond to phase HT3, dark blue corresponds to phase HT4. Raman modes are labelled with letters. Modes a, b, e, f, i belong to the phase HT1/HT2, which can also be synthesized by laser heating from S15 phase at 20 GPa. Mode m belongs to the new high P-T phase of nitrogen HT3-N_2 and modes n, p belong to the novel compound HT4-C.*

Another mode *m,* emerges in the area of stretching mode of N_2 molecule. It implies that the excessive amount of nitrogen results in formation of a new molecular phase of nitrogen HT3-N_2. This band is a wide and sharp doublet and does not resemble by its shape and intensity features of any other known molecular phases of nitrogen, discussed earlier in Chapter 3. There were no low-frequency bands detected, that could be related to this nitrogen phase HT3-N_2. Also, we did not observe characteristic lower frequency peaks for either cg-N or LP-N [Tomasino 14, Eremets 04a].

Therefore, we propose that new high P-T phase HT3 consists of the new phase of

molecular nitrogen HT3-N_2 and new nitrogen/oxygen compound HT1-C, which can be also formed by heating of phase S15 at 20 GPa and appeared to be stable up to 96 GPa.

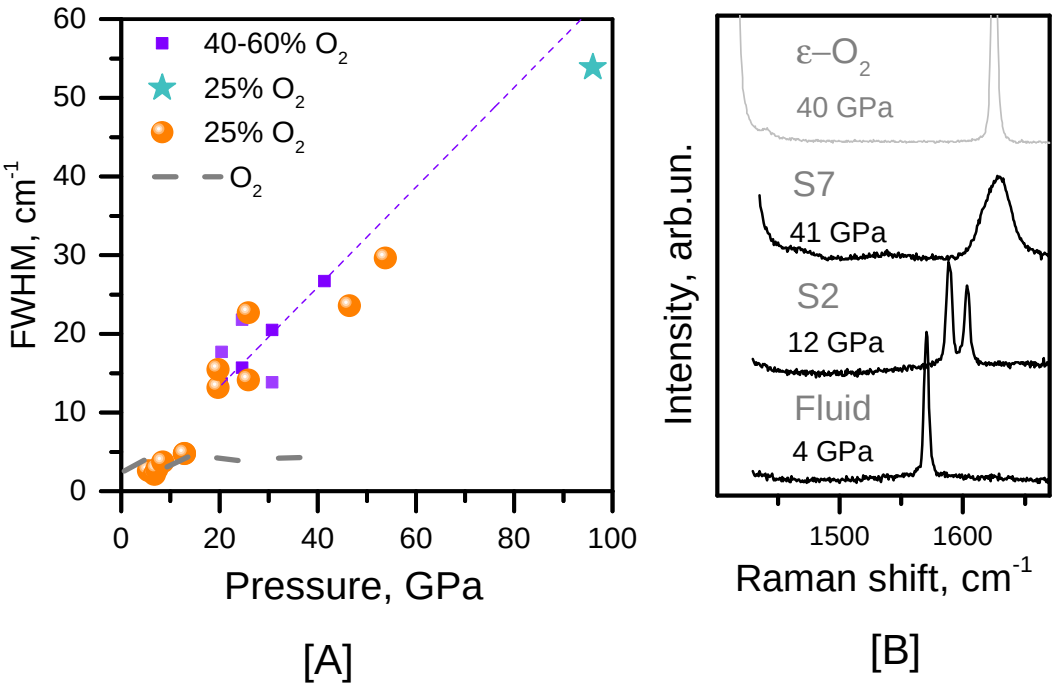

Figure 6.7 *[A] FWHM-Pressure dependence of oxygen vibron in the samples of Group II. FWHM of the pure oxygen stretching mode is depicted with the grey dashed line and is distinctly narrower than the width of O_2 excitations in the N_2/O_2 compound. The purple dashed line shows the linear extrapolation of FWHM to 90 GPa, which proves that width of the O_2 mode in the discussed sample can be considered normal for this compound, although substantially wider than that of the pure O_2-vibron. [B] Selected Raman spectra of the oxygen vibron in the sample with 40-60 % O_2. The top grey spectrum is for pure oxygen in ϵ-phase at 40 GPa and added for comparison.*

In the dark part of the sample we observe formation of another new phase HT4 (Figure 6.6). The evidence for transition to HT4 stems from the appearance of the new mode n and altered low-frequency profile together with the features of oxygen (mode p) and nitrogen (mode m). The prominent feature of the spectra of this phase is the new exceptionally extensive peak at around 700 cm^{-1} (mode n) with utter absence of any excitations at lower energies which are typical for other N_2/O_2 (Chapter 5), N_2O_4 or $NO^+NO_3^-$ phases [Song 03a, Kuznetsov 09]. There is still an extensive oxygen peak (mode p) which looks broader than pure oxygen in the ϵ-phase or oxygen modes in high-pressure phases of Group III. This is shown in Figure 6.7 where FWHM (full width at half maximum) of oxygen vibron mode p, obtained from Voigt profile, is plotted versus pressure. Unusual for the majority

of nitrogen/oxygen mixtures and their pure components, this might be a standard pressure broadening of the stoichiometric compound of the Group II discussed in Chapter 5. Also, we detected nitrogen peak with the similar shape as HT3-N_2 in the lighter part of the sample, though the higher-frequency band of the doublet lost its intensity and appeared as a shoulder. Hence, phase HT4 is composed of the novel compound and phase of nitrogen, HT4-C and HT3-N_2 respectively.

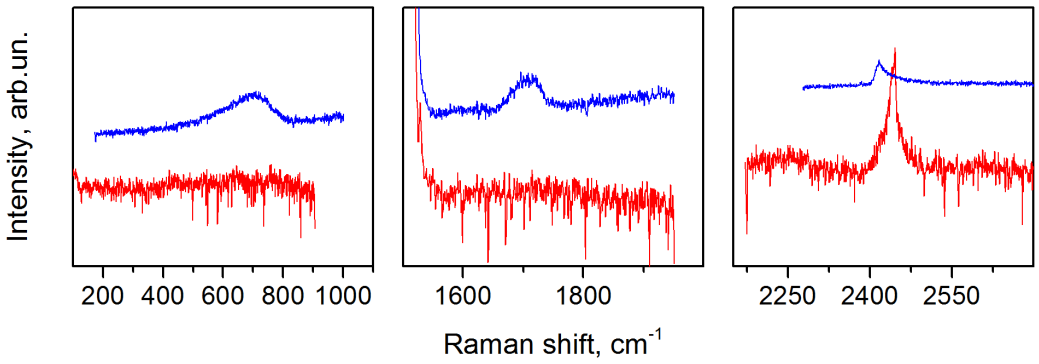

Figure 6.8 *Raman spectra taken five months later. The red line is for the spectrum collected from the light part (HT3 phase, consisting of HT3-N_2 and HT1-C after laser heating at 96 GPa). The blue line is for the spectrum of the dark part (HT4 phase). Raman spectrum of the dark part exhibits the same features as after laser heating. In the light part, we observed only N_2-vibron originating from HT3-N_2, without any other modes.*

The sample was kept at 96 GPa for five months. Interestingly, spectroscopic measurements after this period revealed substantial changes in the lighter part of the sample (Figure 6.8). Almost all the peaks apart from the intense sharp HT3-N_2 band vanished which implies instability of the HT1-C phase and its consecutive decomposition at 96 GPa and room temperature into the new nitrogen phase HT3-N_2. Excessive oxygen presumably moved to the area of HT4-C compound, indicating high mobility of O_2 molecules in the HT3 phase.

Surprisingly, spectrum of the dark part remained the same as it was five months before, displaying immensely broad asymmetric band at around 700 cm^{-1}, extensive oxygen band, and sharp and intense nitrogen feature.

6.4 Summary

From previous research shows that N_2/O_2 mixtures exposed to laser heating would likely follow ionization path and form $NO_2^+NO_3^-$ and $NO^+NO_3^-$ with distinctive Raman peaks [Sihachakr 06, Meng 06, Kuznetsov 09]. Earlier research was carried out on samples with 34% O_2 heated from fluid [Meng 06], 25%, 66%, and 77% O_2 mixtures heated from the phase S2 [Sihachakr 06] and mixtures with more than 70% O_2 heated from the phase S16 [Kuznetsov 09].

We studied two mixtures with the initial concentration of 25% O_2 and 40-60% O_2, different from the previous research. Both our samples were laser heated from the higher pressure phases, then in previously reported experimental works, at 20, 26 and 96 GPa. Our samples exhibit strikingly different behaviour from either known molecular forms of oxides under high pressure or their ionic equivalents. At the same time, in both samples we observe excitations of O-O and N-N stretching modes, indicating that exposure to temperatures close to 2000 K at pressures as high as 20 GPa and 96 GPa did not result in breaking molecular bonds of O_2 and N_2.

We report formation of four new high-pressure high-temperature phases HT1 (20 GPa), HT2 (26 GPa), HT3 and HT4 (96 GPa). HT1 might consist of S15 phase (ϵ-nitrogen, ϵ-oxygen, new S15 compound) and new compound HT1-C and N/O products. HT2 is possibly a fully transformed phase, comprising S15 phase (ϵ-nitrogen, ϵ-oxygen, new S15 compound) and new compound HT1-C, which is reflected by slight differences in Raman spectra of HT1 and HT2. HT3 and HT4 are formed by laser heating of the 25% mixture at 96 GPa. HT3 is a new phase consisting of new form of molecular nitrogen HT3-N_2 and new nitrogen/oxygen compound HT1-C, and HT4 phase contains new form of molecular nitrogen HT3-N_2 and the novel compound HT4-C.

We observed formation of the new N_2/O_2 compounds HT1-C and HT4-C and new high P-T phase of nitrogen HT3-N_2 as a result of heating to 2000 K at 20 GPa and 96 GPa respectively. We suggest that HT1-C might be another lower symmetry form of N_2O_4 based on its Raman features (peaks around 700 cm^{-1} and 2300 cm^{-1}). HT1-C can be formed from mixtures of 40-60% O_2 from phase S15 and mixtures with 25% O_2 at 96 GPa. However, this compound is unstable at 96 GPa and 300 K and eventually decomposes in the new molecular high P-T

phase of nitrogen HT3-N_2, with oxygen presumably enriching high P-T compound HT4-C.

Compound HT4-C was formed only at 96 GPa and remained stable at ambient temperature for as long as five months. It might be related to the stoichiometric compound $(N_2)_3O_2$, that can be formed from the nitrogen/oxygen mixtures with 25% O_2 (Group II).

According to the theoretical calculations [Li 15], the mixture potentially could have decomposed into monoclinic $P2_1/c$ NO_2 with molecules of N_2O_4, and polymeric N_2O_5 ($C2/c$ with planar molecules). Unfortunately, neither of proposed models was in a good agreement with our experimental data.

The presence of strong vibrational modes of O_2 and N_2 coexisting with new high-P-T compounds indicates that atomic state was not reached in our experiments. It is plausible that resulting state occurs after chemical dissociation of pressure-induced ionic phase to elemental solids. The ionic state was not observed in our case potentially due to the specific P-T path taken in the experiments.

The present data should stimulate further experimental and theoretical works to understand the mechanism of formation of the high -temperature N_2/O_2 phases, their molecular and crystal structure.

Chapter 7

Conclusion

The aim of this thesis was to study molecular systems of simple diatomics as H_2, D_2, and mixtures as the N_2/O_2 binary system at extreme conditions with the help of optical spectroscopy. As long as the thesis was composed of separate chapters, dedicated to different systems, we will continue the discussion in the same manner.

Hydrogen and deuterium. There was a limited amount of experimental studies of low-frequency modes of hydrogen and deuterium because of the unclear nature of these excitations and difficulties with the interpretation of the experimental data. The present work makes the first systematical attempt to understand the nature of low-frequency excitations in phases I, II, IV and IV' of hydrogen and deuterium by indirect analysis of their properties. Comparison of the Raman frequencies of hydrogen and deuterium at various temperatures and pressures indicates that rotational motion of the molecules in phase I becomes strongly hindered at temperatures below 150 K. However, it remains fundamentally rotational at temperatures above 150 K, although slightly impeded. Interestingly, the evolution of rotons to phonons is observed in the domain of phase I below 150 K which undergoes consequent transformation to phase II with pressure increase. Complex landscape of phase II did not allow us to execute precise analysis. Phonon nature of low-frequency modes in the phase I domain below 150 K is suggested as a first hypothesis. On the contrary, it was confirmed that low-frequency excitations of phase IV and IV' in both hydrogen and deuterium are phonons of the hexagonal lattice. Another interpretation of

the low-frequency excitations in high-pressure phases IV, IV' and V suggested that phase IV' might be a continuation of phase IV or region of coexistence of phases IV and V. Further studies of the rotational motion in phases I and II, which will consider the input of ortho-para transformation, and phases IV, IV' and V might be of particular interest for the understanding of formation mechanisms of quantum phases I and II, and mixed phases IV, IV' and V of hydrogen and deuterium, as well as differences between these systems.

In order to execute the aforementioned analysis, it was necessary to develop a method of comparison of hydrogen and deuterium systems due to significant pressure shifts in similar phases of both isotopes. As a result of multiple operations with the experimental data, several equations were proposed. They help to relate pressures needed to achieve similar states in isotopes as well as frequencies of their vibrational modes. As a bonus, this analysis showed two potential scenarios of hydrogen and deuterium behaviour at pressures above 400 GPa. On the one hand, it is possible that metallization of deuterium will be considerably delayed in pressure comparing to that of hydrogen. According to the other scenario, another phase transition will occur in both isotopes almost simultaneously at pressures above 500 GPa. In both cases, the onset of phase V in deuterium is expected to be around 470 GPa. Hopefully, the advancement of high-pressure experimental methods will allow testing these hypotheses in the nearest future.

Nitrogen/oxygen binary system. Contributing work presents the first experimental research of nitrogen/oxygen system to maximum pressures of 150 GPa at ambient temperature as well as exposed to heating. Spectroscopic studies of N_2/O_2 mixtures with various compositions allowed to determine the binary phase diagram over a range of pressures at 300 K. We observed the formation of eight new phases, existing above 12 GPa, which have not been reported previously. Distinct Raman spectra indicated that structure and composition of these phases are more diverse and complex than earlier thought. Phase transitions do not necessarily mimic those of pure components. While most of the new phases formed at 300 K under compression are solid solutions, one was identified as a new stoichiometric compound, presumably $(N_2)_3O_2$, predicted earlier [Sihachakr 04]. Laser heating experiments led to the formation of four new high P-T phases comprising novel N/O compounds HT1-C and HT4-C and new high P-T phase of nitrogen HT3-N_2. HT1-C might be another form of N_2O_4, which has proven to be unstable and eventually decomposed into new

high pressure-temperature phase of nitrogen HT3-N_2 and another N/O compound HT4-C. HT4-C compound possesses unique Raman features and might be related to the ambient temperature compound associated with $(N_2)_3O_2$. To summarize, nitrogen/oxygen binary system showed much more interesting behaviour than it was expected. Further theoretical and experimental investigations are needed to determine the crystal structure of the observed phases and novel compounds, as well as extend P-T phase diagram to the regions of metallization, amorphisation, and atomisation. Detailed X-Ray studies of the phases, detected by Raman spectroscopy, in addition to our preliminary data will be necessary for the analysis of the phases of nitrogen/oxygen binary system.

Appendix A

Study of Hydrogen and Deuterium: nature of low-frequency modes and method of comparison of phase diagrams

Table A.1 *Coefficients for polynomial dependences describing pressure needed to achieve in state of deuterium, similar to hydrogen. Polynomial equation is following:*

$$P_{D_2} = C + \sum_{n=1}^{n=9} B_n x^n$$

where the coefficients, B_n (n=1..9), depend on the pressure range and are listed below

	Pressure range 0 - 230 GPa (for H_2)	Pressure range 230 - 300 GPa (for H_2)
C	367.55609	-1.37561 * 10^7
B1	-33.55515	4.12555 * 10^5
B2	1.47521	-5.51601 * 10^3
B3	-0.03535	42.97780
B4	0.00052	-0.21334
B5	-4.85934 * 10^{-6}	0.00069
B6	2.86628* 10^{-8}	-1.41553 * 10^{-6}
B7	-1.03465 * 10^{-10}	1.68062 * 10^{-9}
B8	2.08326 * 10^{-13}	-8.81324 * 10^{-13}
B9	-1.79 * 10^{-16}	0

Table A.2 *Coefficients for polynomial dependences, which relate frequencies of hydrogen vibron to frequencies of deuterium vibrons and vice versa:*

$$\nu_1(\nu_2) = C + \sum_{n=1}^{n=9} B_n x^n$$

This equation is valid in the pressure range from 0 to 300 GPa for equivalent hydrogen pressures.

$\nu_{D2}(\nu_{H2})$		$\nu_{H2}(\nu_{D2})$	
C	-5.292 * 10^9	C	5.68196 * 10^9
B1	1.33685 * 10^7	B1	-1.99841 * 10^7
B2	-14972.868	B2	3.11555 * 10^4
B3	9.75775	B3	-28.25835
B4	-0.00408	B4	1.643 * 10^{-2}
B5	1.13317 * 10^{-6}	B5	-6.354 * 10^{-6}
B6	0.00062	B6	1.63353 * 10^{-9}
B7	2.48153 * 10^{-14}	B7	-2.693 * 10^{-13}
B8	-1.711 * 10^{-18}	B8	2.58235 * 10^{-17}
B9	5.23116 * 10^{-23}	B9	-1.098 * 10^{-21}

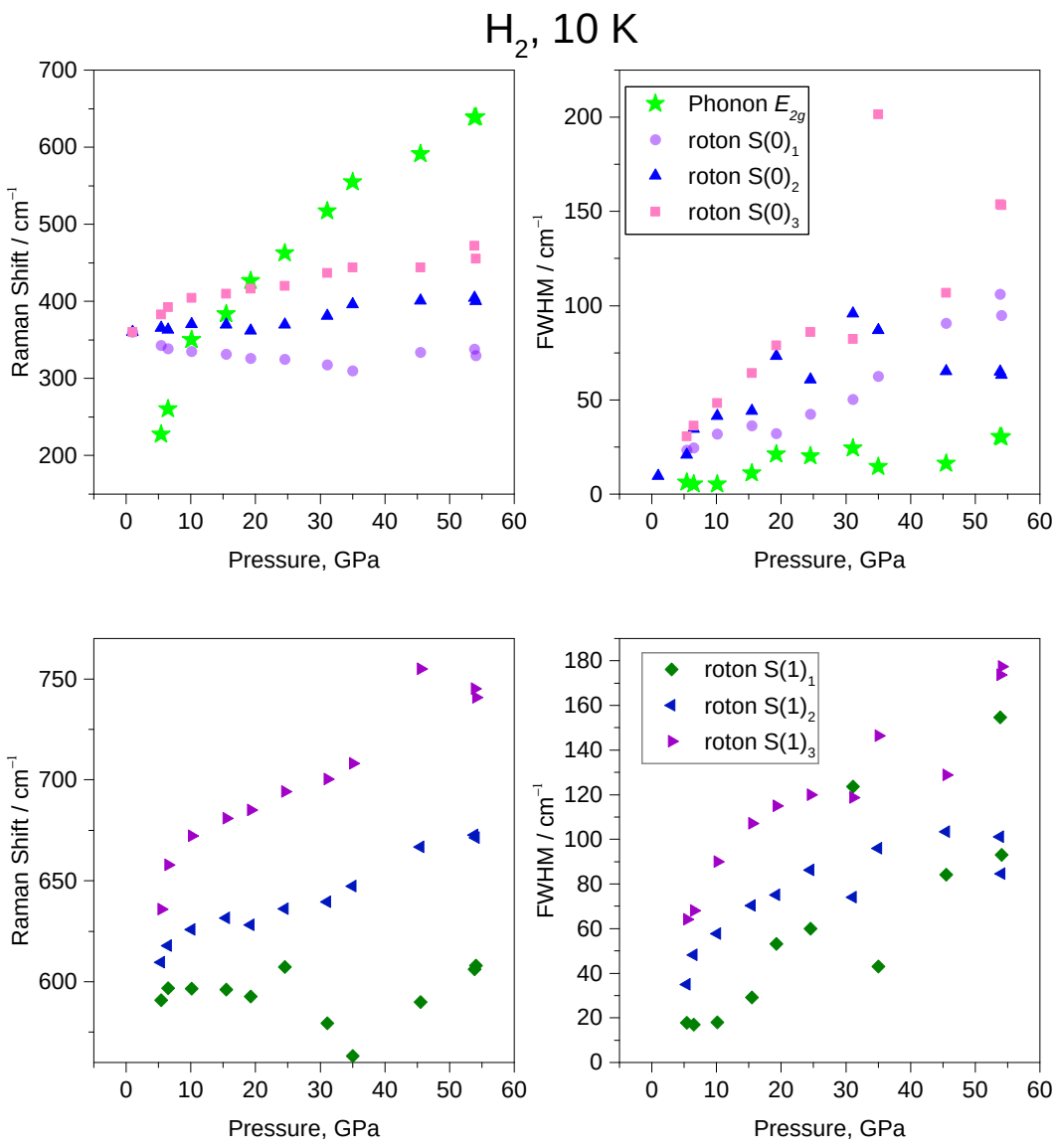

Figure A.1 *Hydrogen: Frequencies and FWHM of the sublevel contributions for peaks S(0) (top) and S(1) (bottom) plotted as functions of pressure, for the experiment executed at 10 K.*

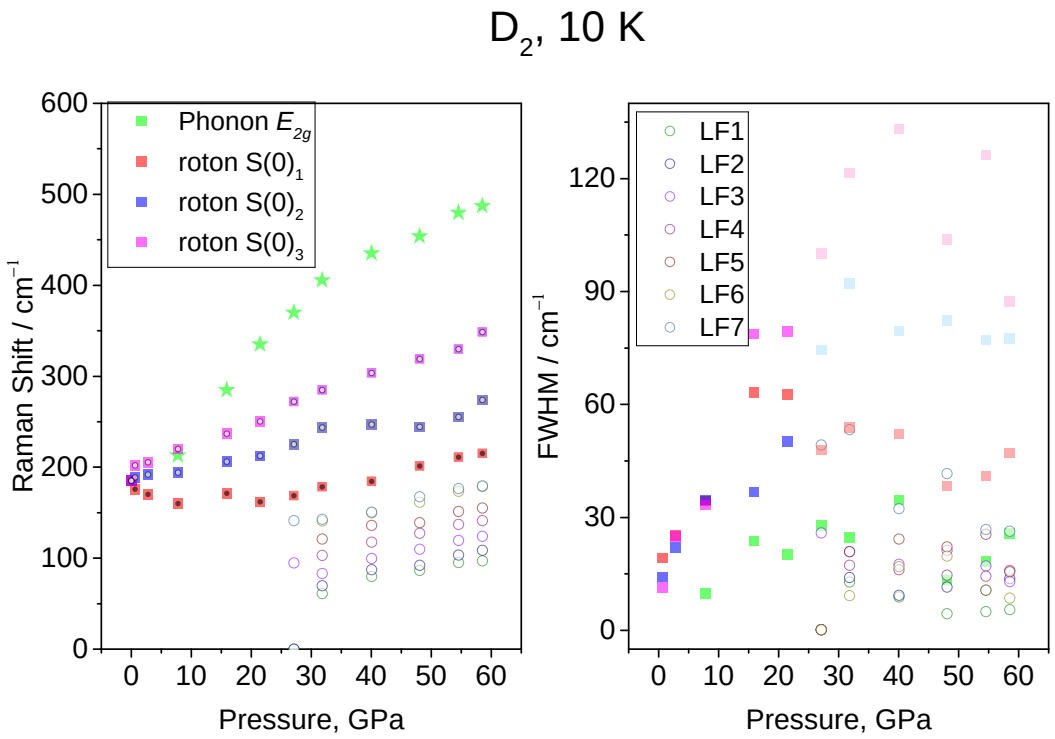

Figure A.2 *Deuterium: Frequencies and FWHM of the sublevel contributions for peak S(0) of phase I and seven additional contributions of low-frequency modes (LF) in phase II (above 30 GPa) plotted as functions of pressure, for the experiment executed at 10 K. It was not possible to accurately resolve contributions for peak S(1) at pressures above 20 Gpa, therefore it is not presented in this Figure.*

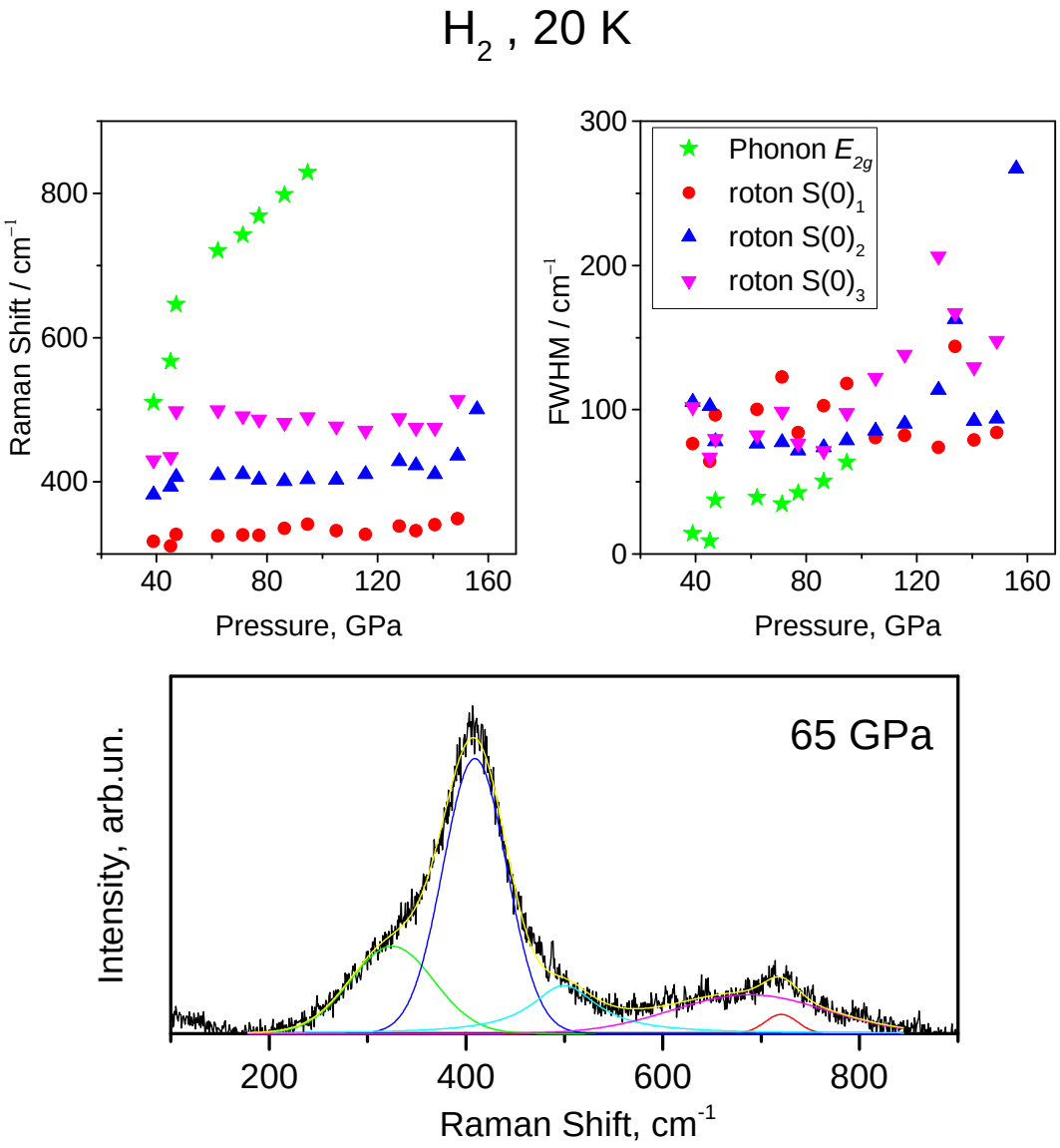

Figure A.3 *Top: Frequencies and FWHM of the sublevel contributions for peak S(0) of hydrogen at 20 K in phase II, plotted as functions of pressure. Peak S(1) was very difficult to resolve, so it is not depicted on the plots. Bottom: Example of the Raman Spectra of hydrogen in phase II at 20 K at 65 GPa with fittings of contributions of peak S(0). The red peak represents lattice phonon.*

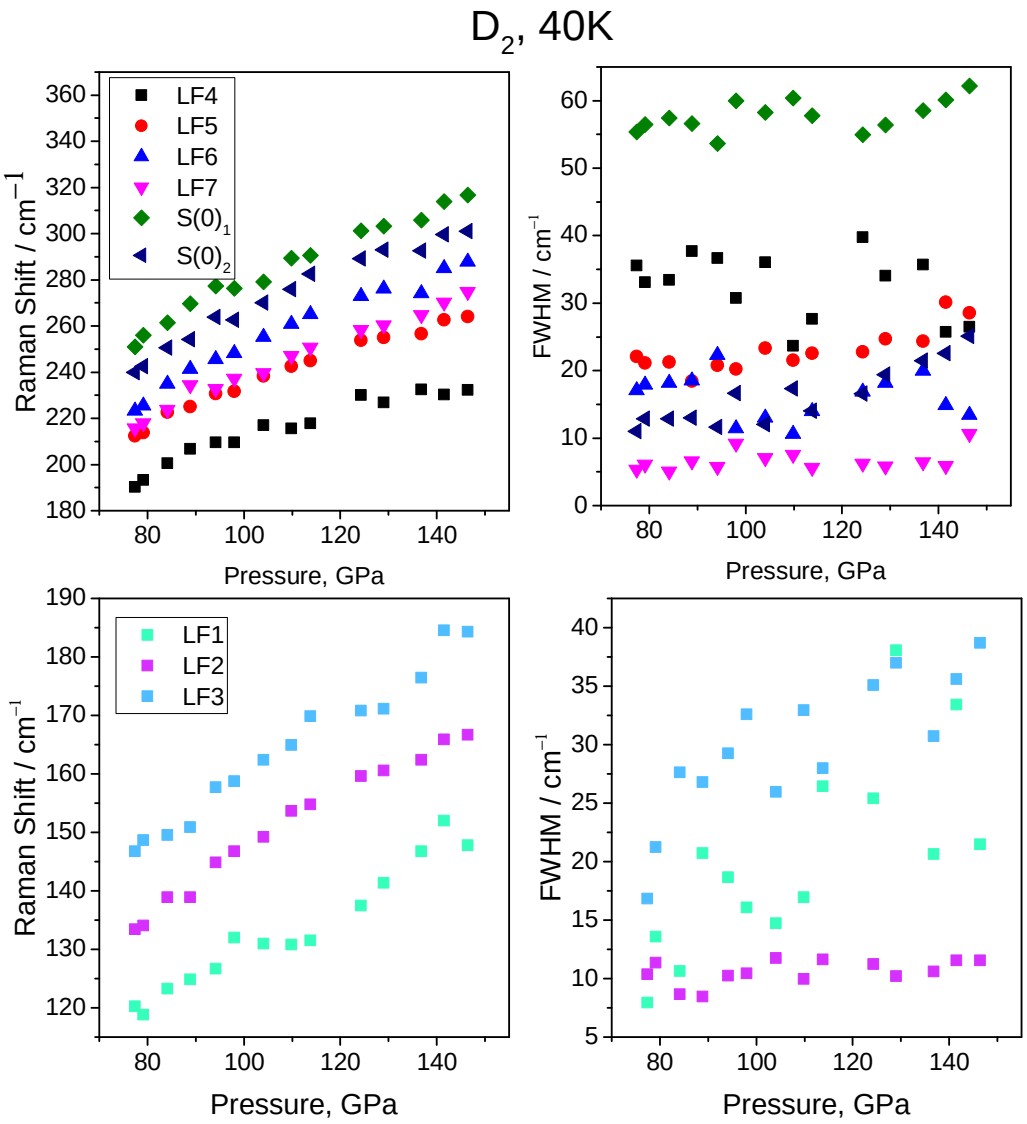

Figure A.4 *Deuterium: Frequencies and FWHM of the sublevel contributions for peak S(0) and seven additional contributions of low-frequency modes (LF) in phase II plotted as functions of pressure, for the experiment executed at 40 K.*

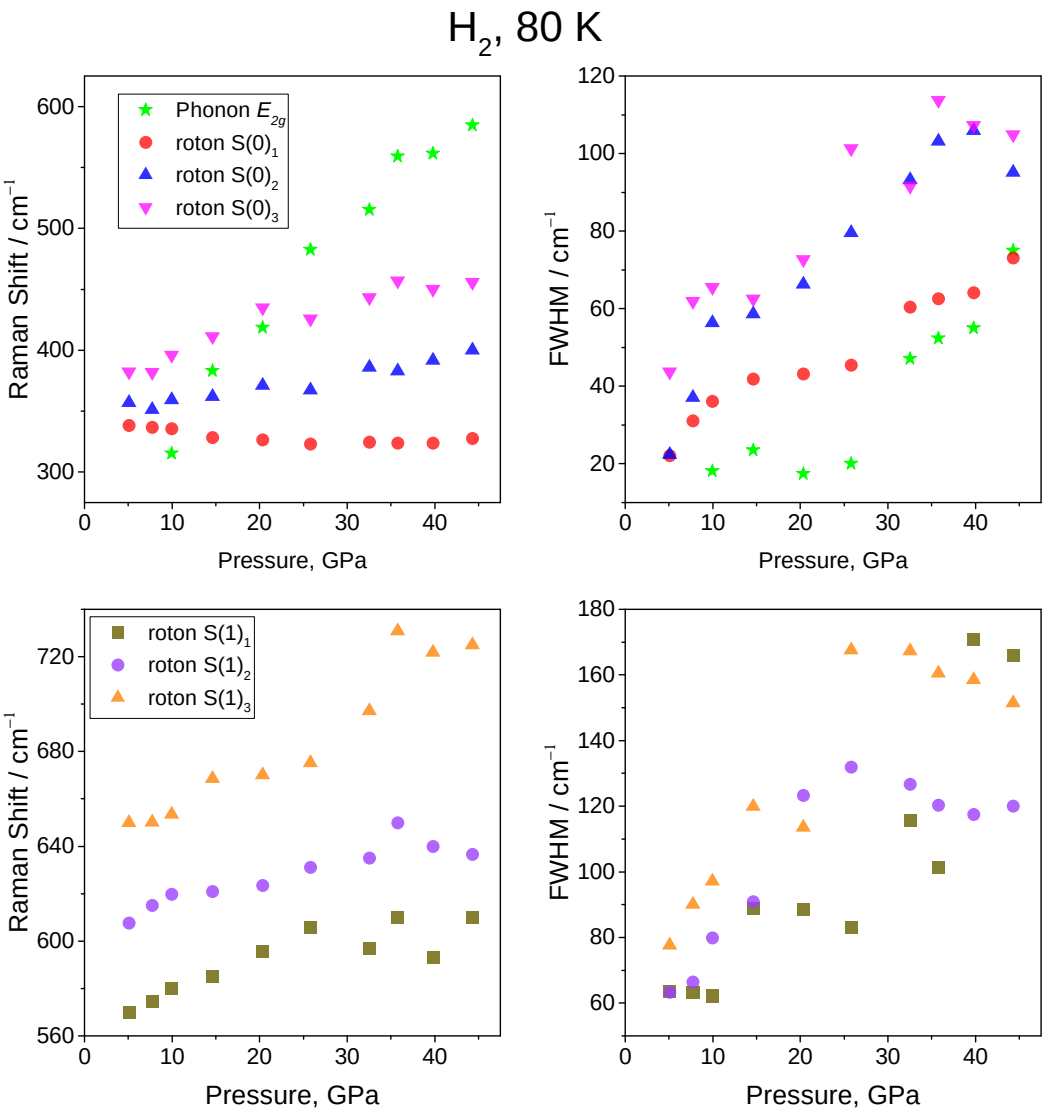

Figure A.5 *Hydrogen: Frequencies and FWHM of the sublevel contributions for peaks S(0) and S(1) of phase I plotted as functions of pressure, for the experiment executed at 80 K.*

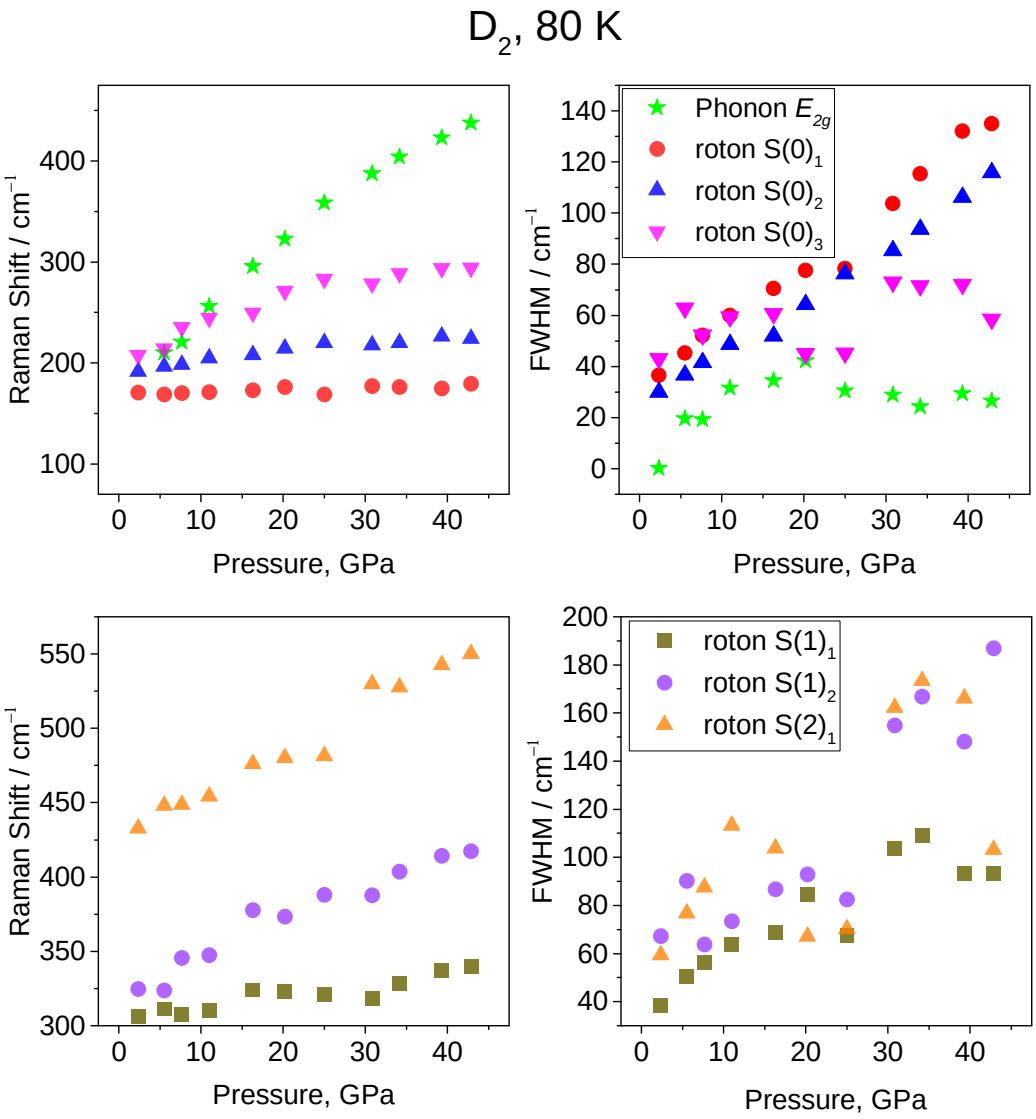

Figure A.6 *Deuterium: Frequencies and FWHM of the sublevel contributions for peaks S(0) and S(1) of phase I plotted as functions of pressure, for the experiment executed at 80 K.*

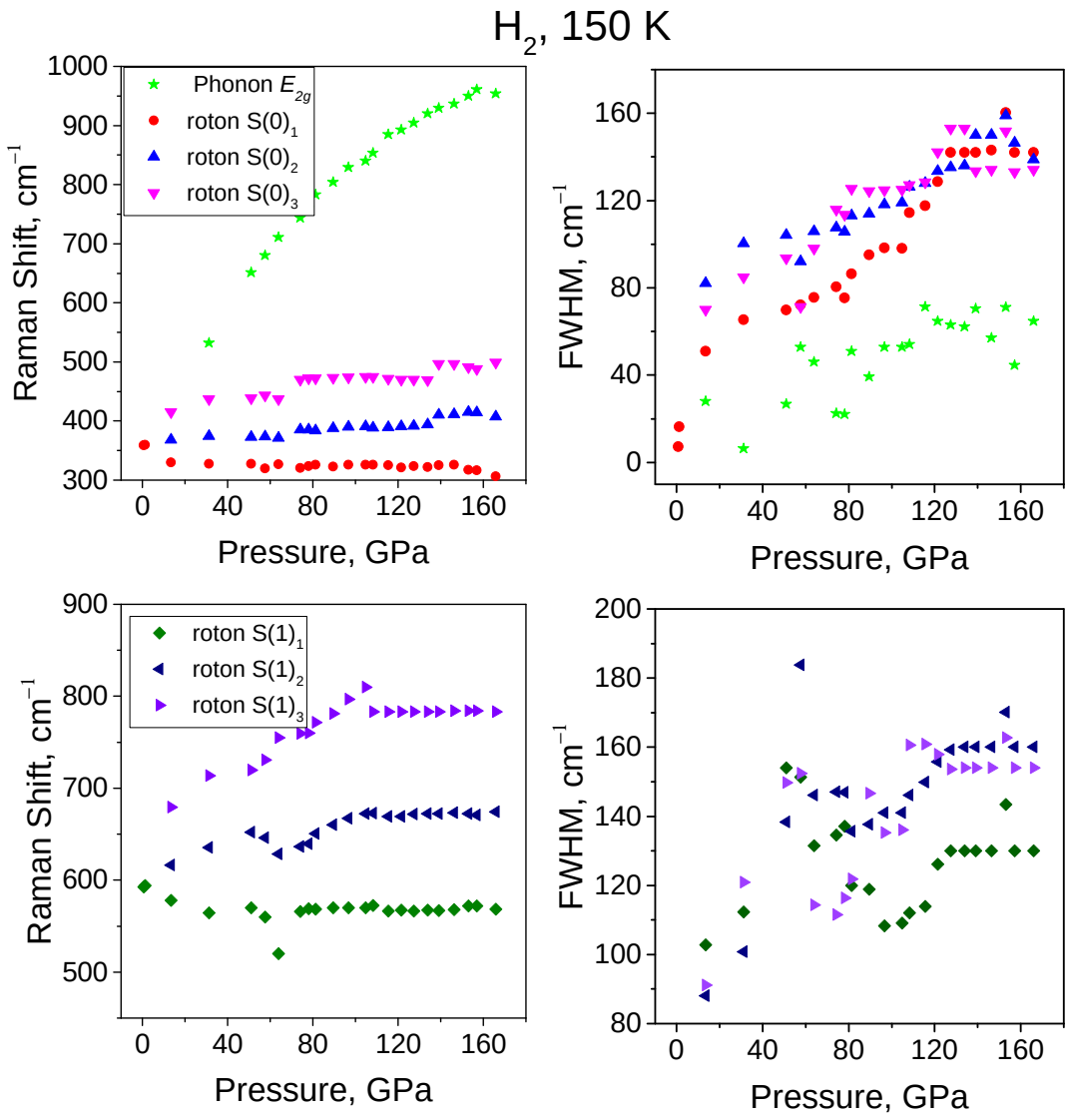

Figure A.7 *Hydrogen: Frequencies and FWHM of the sublevel contributions for peaks S(0) and S(1) of phase I plotted as functions of pressure, for the experiment executed at 150 K.*

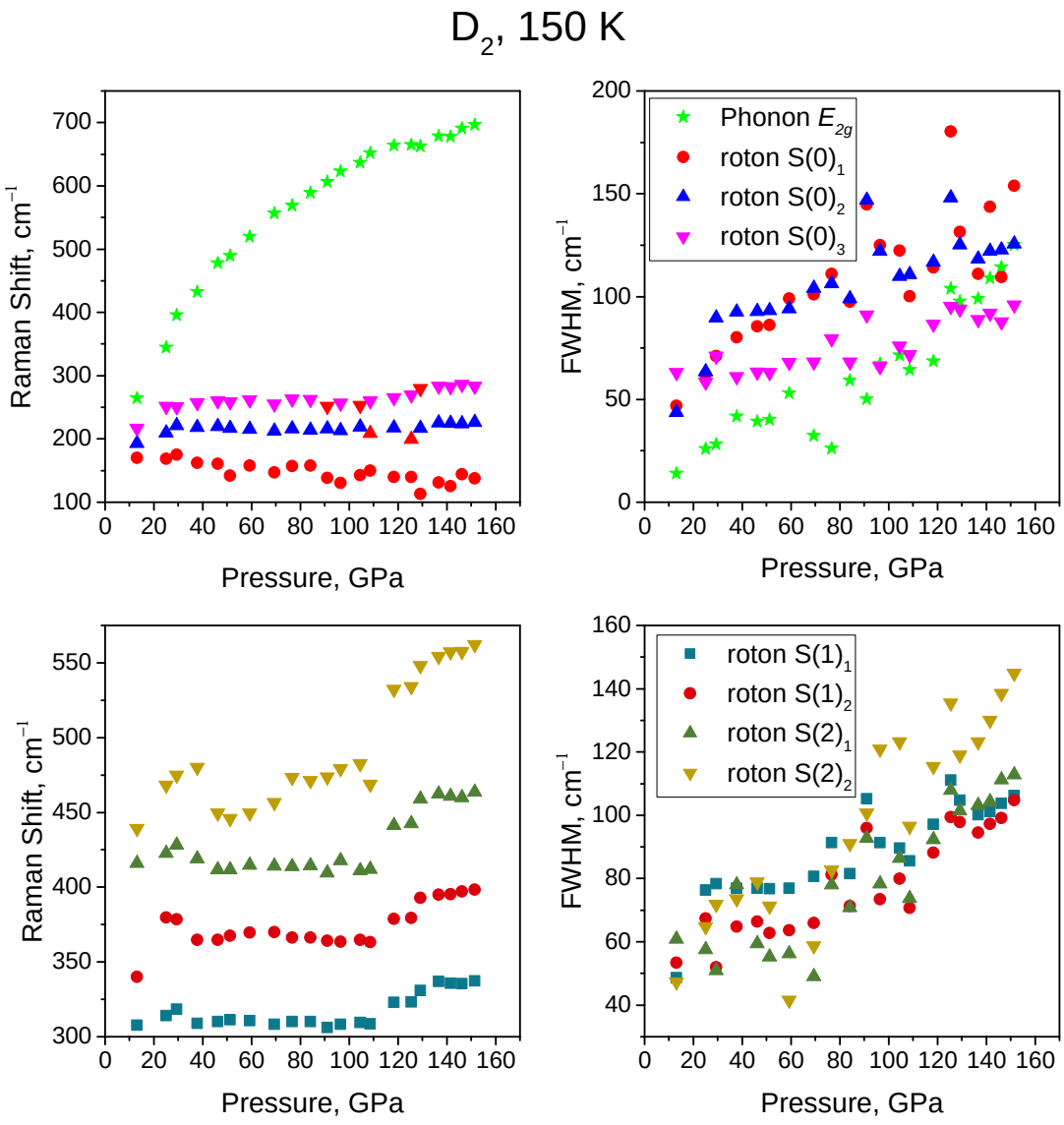

Figure A.8 *Deuterium: Frequencies and FWHM of the sublevel contributions for peaks S(0) and S(1) of phase I plotted as functions of pressure, for the experiment executed at 150 K.*

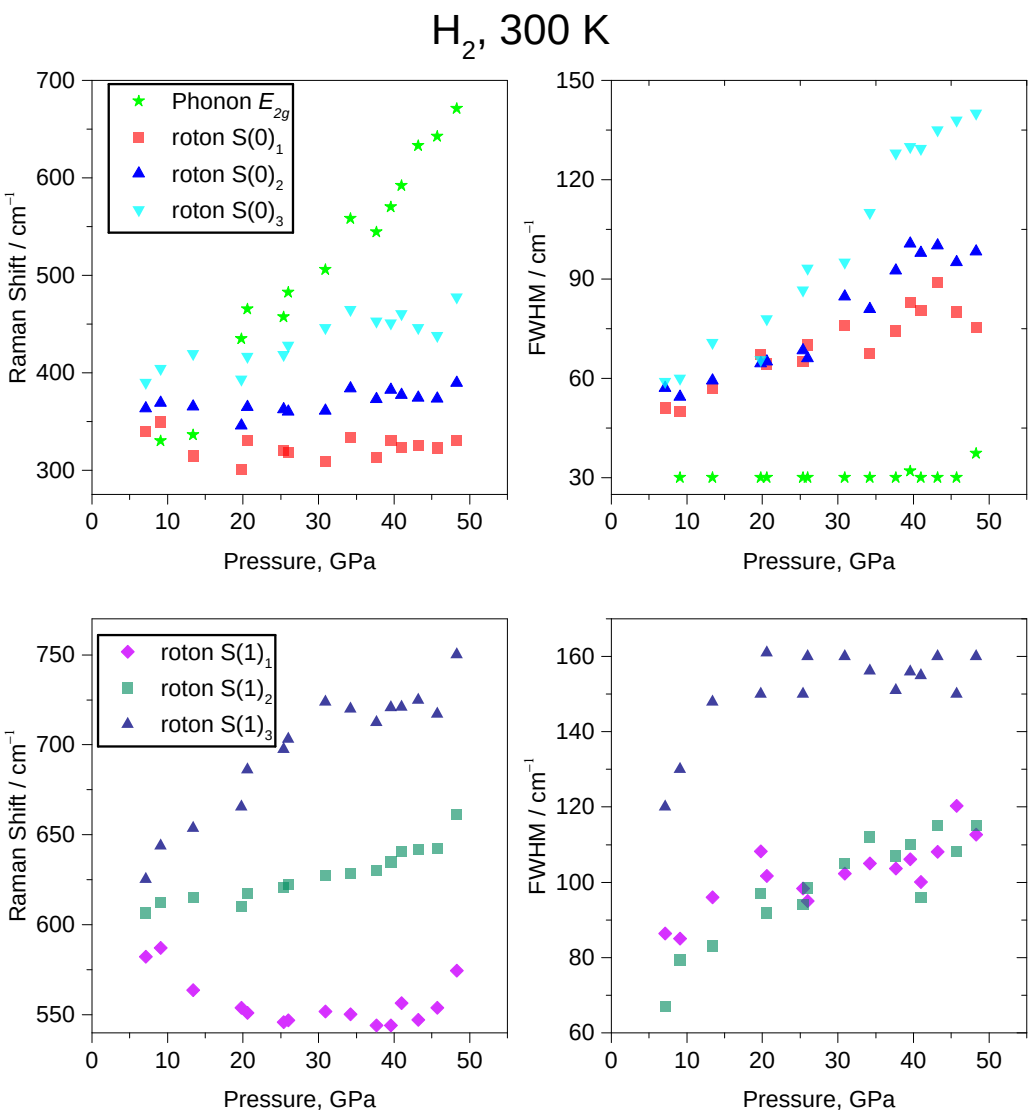

Figure A.9 *Hydrogen: Frequencies and FWHM of the sublevel contributions for peaks S(0) and S(1) of phase I plotted as functions of pressure, for the experiment executed at 300 K.*

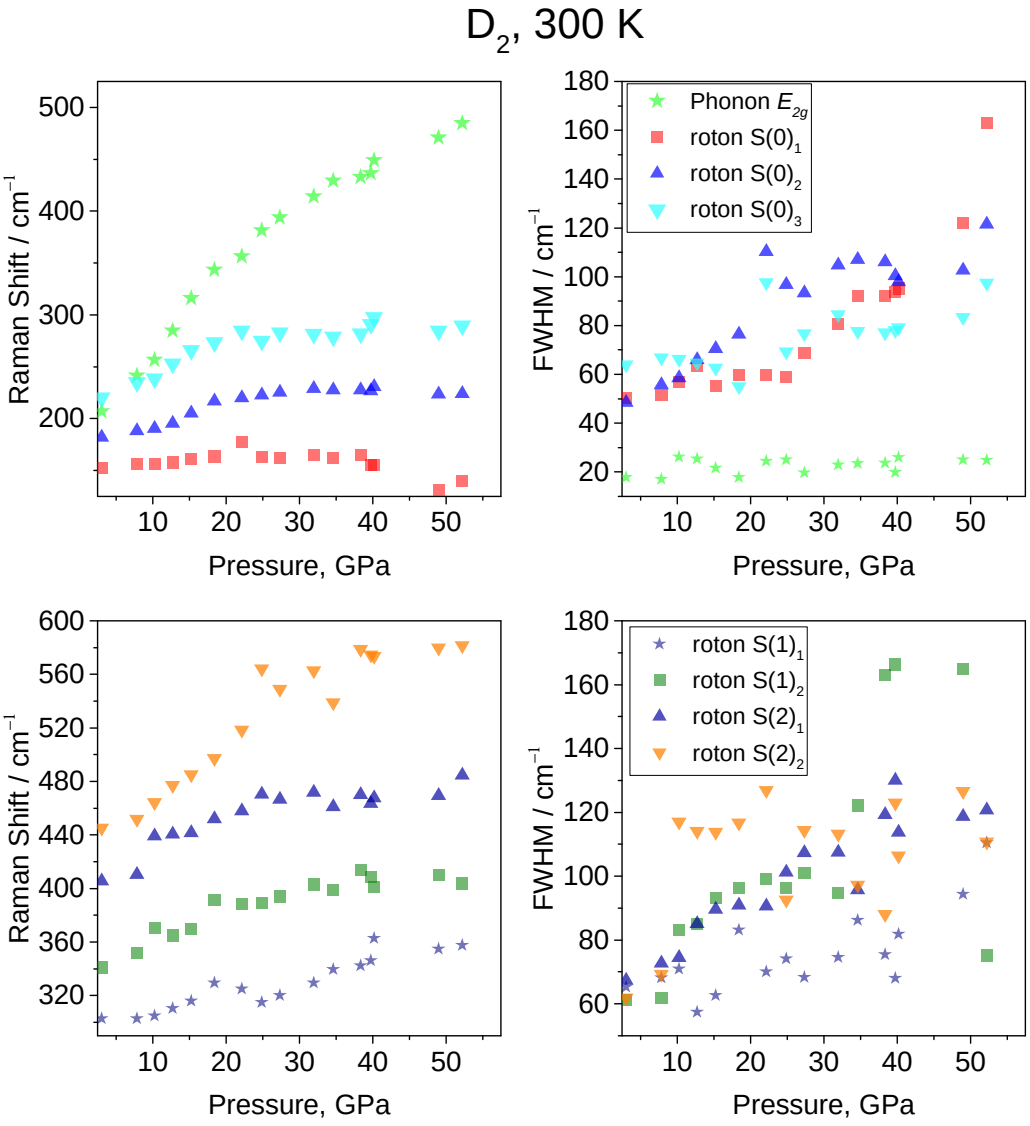

Figure A.10 *Deuterium: Frequencies and FWHM of the sublevel contributions for peaks S(0) and S(1) of phase I plotted as functions of pressure, for the experiment executed at 300 K.*

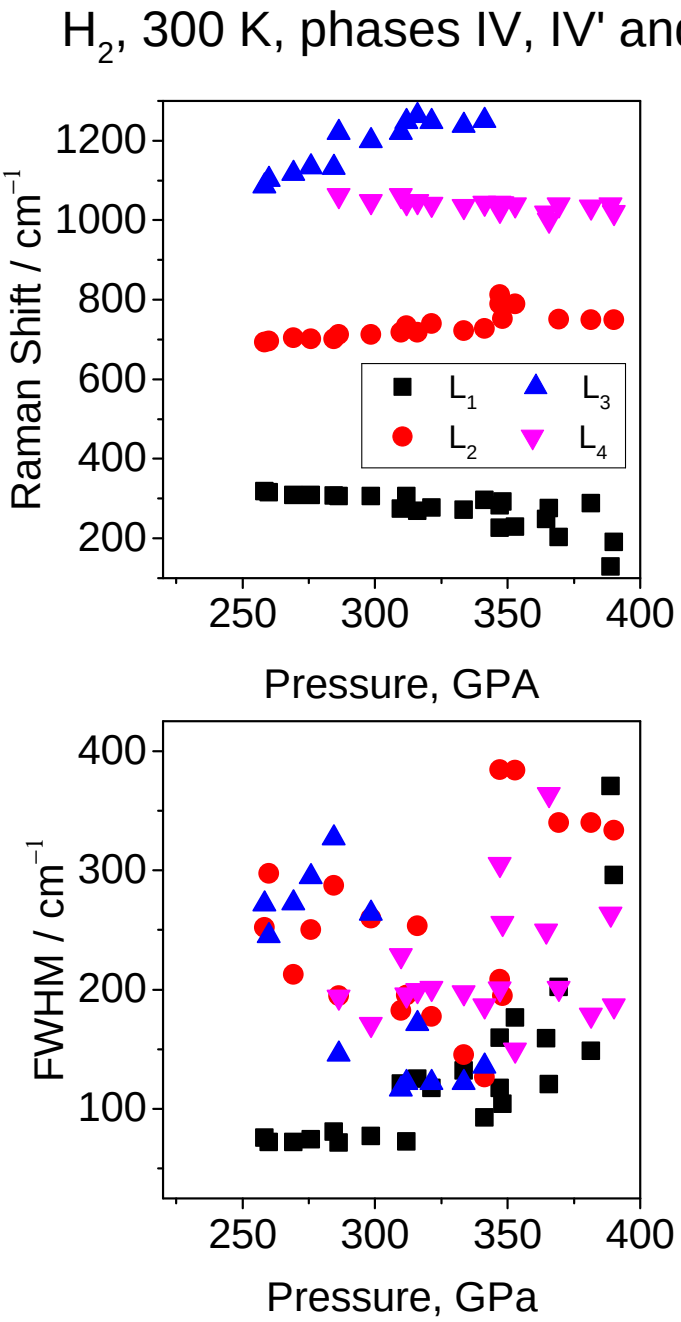

Figure A.11 *Hydrogen: Frequencies and FWHM of low-frecuency modes of phases IV, IV' and V plotted as functions of pressure, for the experiment executed at 300 K.*

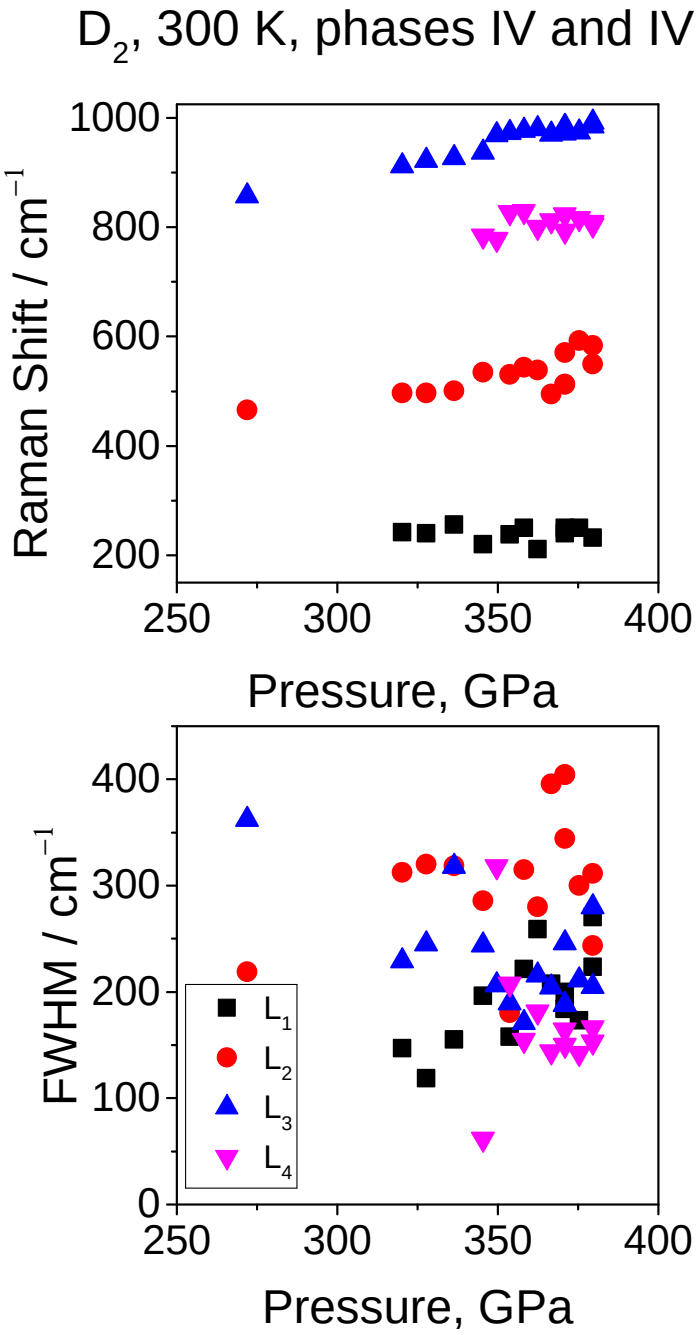

Figure A.12 *Deuterium: Frequencies and FWHM of low-frecuency modes of phases IV and IV' plotted as functions of pressure, for the experiment executed at 300 K.*

Appendix B

Publications

Polymerization of iron carbonate melts in the deep mantle

Chrystèle Sanloup[1], Jessica Hudspeth[1], Veronika Afonina[2], Benjamin Cochain[2], Zuzana Konôpková[3], Gérald Lelong[4], Laurent Cormier[4] and Chiara Cavallari[5]

[1]*Sorbonne Université, CNRS, Institut des Sciences de la Terre de Paris, F-75005, Paris, France*

[2]*SUPA, Centre for Science at Extreme Conditions and School of Physics and Astronomy, University of Edinburgh, Edinburgh, EH9 3JZ, UK*

[3]*DESY Photon Science, Notkestr. 85, 22607 Hamburg, Germany*

[4]*Sorbonne Université, CNRS, Institut de Minéralogie, de Physique des matériaux et de Cosmochimie, F-75005, Paris, France*

[5]*European Synchrotron Radiation Facility, ESRF, 71 Avenue des Martyrs, 38000 Grenoble, France*

Our understanding of the deep carbon cycle has witnessed amazing advances in the last decade, and noteworthy is the discovery of new high pressure (P) carbonate phases where carbon is tetrahedrally coordinated[1]. Petrological studies have shown that while carbonate melting mostly occurs in the upper mantle, a significant fraction of subducted carbonates reach the lower mantle and may generate melting at great depths[2]. However, little is known on the properties of molten carbonates even at ambient P, while their properties at lower mantle conditions are unknown. Here, we report the structure and density of tetrahedral $FeCO_3$ melts and glasses above 40 GPa and up to 120 GPa by means of *in situ* high P-T x-ray synchrotron diffraction combined with *ex situ* Raman and x-ray Raman spectroscopies. When melted at low P, $FeCO_3$ reacts with the silica P-transmitting medium, resulting in the

formation of silico-carbonate glasses. High P melts instead are not contaminated by silica but are still quenched as glasses. X-ray Raman spectroscopy on quenched high P glasses indicates that carbon is fully transformed to 4-fold coordination, a bond change recoverable at ambient P. No density discontinuity is observed, but an increased compaction rate over a 30 GPa range. The 3-fold to 4-fold transition is confirmed by Raman spectroscopy that do not show the characteristic CO_3^{2+} strong stretching mode but broad bands similar to low P silicate glasses, albeit at higher wavenumbers. Deep carbonate melts are therefore expected to be polymerized, highly viscous and poorly reacting with silicates in the lower mantle, in stark opposition with their low P properties.

Although the lower mantle is mostly a reducing environment with the presence of reduced Fe[3,4], significant amount of subducted carbonates are estimated to be preserved[2]. Transition to 4-fold carbon occurs in crystaline $CaCO_3$ above 130 GPa[1,5], 80 GPa for $MgCO_3$[6,7], and 50 GPa for $FeCO_3$[8], while intermediate $CaCO_3$-$MgCO_3$-$FeCO_3$ compositions form a single tetrahedral carbonate phase[9] unlike silicates.This transition induces polymerization such as sheets or 3-membered rings for $MgCO_3$[6], and chains for $CaCO_3$[1]. In contrast, our knowledge of carbonate melts structure at depth is scarce and limited to upper mantle pressures[10,11]. One main question is therefore how this 3-fold to 4-fold transition translates in the molten state, and what are the consequences on the physical and chemical properties of carbonate melts? Of particular interest is the mobility and reactivity of carbonate melts in the lower mantle, knowing that these properties underpin the key role played by carbonate melts in upper mantle geodynamics through lubrication of plate tectonics, cratonic roots[12] and ascending plumes[13].

The role of Fe in the deep carbon cycle is emphasized by the predominance of Fe-rich ferropericlase in diamond inclusions from the lower mantle[14]. The lowest transition P from 3-fold to 4-fold C in $FeCO_3$ amongst carbonates justifies its choice as the first composition to investigate. Not only this transition occurs at less challenging experimental conditions, but it might be driven by Fe high spin to low spin transition at 40.4 GPa[15], a consequence of which being the large enrichment in Fe of (Mg,Fe)-carbonates coexisting with bridgmanite to almost pure $FeCO_3$[16]. Besides, high Fe concentration stabilizes $(Ca,Mg,Fe)^{IV}CO_3$ with respect to single cation 3-fold carbonates at mid mantle conditions (30-50 GPa)[17]. Formation of Fe-carbonates in the lower mantle might also result from carbonation of Fe-oxides ((Mg,Fe)O, FeOOH) with CO_2[18,19]. Last but not least, $FeCO_3$ is a technical choice as it can be laser heated, which is required to reach lower mantle conditions without the need for additional laser coupler.

We collected *in situ* high P-T x-ray diffraction data in laser-heated diamond anvil cells at the extreme conditions beamline P02.2 at the PETRAIII synchrotron. A crystalline natural siderite sample was sandwiched between two SiO_2 layers, and laser heated for 10 s at each targeted P to induce melting. *Post mortem* electron microprobe analyses (Table 1) show that while the lowest P samples, *i.e.* 11 GPa and 15 GPa, have reacted with the SiO_2 P-transmitting medium, higher P samples have preserved their chemical integrity, and are systematically quenched as a glass (Fig.1a). High P carbonate melts are thus much less reactive than low P melts. This might not contradict the observed reactivity of high P crystalline $MgCO_3$ with SiO_2[20,21] due to the much longer heating durations (20-240 minutes against 10 s heating duration in this work); alternatively, Fe stabilizing effect on high P carbonates could be at stake. We observe no disproportionation of

Fe as was reported in the crystalline state[7,22] although not systematically[8]. This might be due to different P-T paths followed, *i.e.* flash heating here instead of continuous T increase[7,22].

The x-ray diffracted intensity data are converted into the structure factor, $S(q)$ (Fig.1a), using the Ashcroft-Langreth formalism. A striking characteristic of glassy $FeCO_3$ is its strong first sharp diffraction peak (FSDP) that persists up to the highest P investigated, indicative of a strong medium-range order. This is in stark contrast to silicate glasses that lose their medium-range order with increased P[23], but consistent with *ab initio* calculations on carbon-bearing silicate melts reporting P-induced polymerisation of carbonate species into dimers and with the silicate network[24]. A second noticeable feature is the decrease of the contribution at 4 $Å^{-1}$ attributed in molten carbonates to the O-O bond[25]. The radial distribution function $g(r)$ (Fig.1b), *i.e.* the sum of all ion-ion contributions in real space, is obtained by Fourier transforming of $S(q)$. The C-O contribution is clearly visible at 1.2-1.3 Å with none or little overlap with the second contribution (Fe-O and O-O) at $\sim$2 Å in the glass, and with some overlap in the melt.

Raman and x-ray Raman spectra were collected at ambient conditions on glassy $FeCO_3$ recovered from x-ray diffraction experiments and from additional laser-heated diamond anvil cell synthesis respectively. Two broad bands are observed in the Raman spectra (Fig.2a), very different from those of the only two carbonate systems that quench as glasses at room P[26] ($MgCO_3$-K_2CO_3 and $La(OH)_3$-$Ca(OH)_2$-$CaCO_3$-CaF_2BaSO_4) that are essential dominated by the strong CO_3^{2-} stretching mode at $\sim$1080 cm^{-1}. Instead, present Raman spectra are reminiscent of those reported for calcium silicate glasses (Fig.2a) albeit at higher Raman shift values for the broadest

band (1200-1600 cm^{-1} for glassy $FeCO_3$ *vs* 850-1100 cm^{-1}). The x-ray Raman C K-edge spectra (Fig.2b) show no presence of sp3 3-fold carbon, but the broad contribution of tetrahedrally coordinated carbon[27] is visible (Fig.2b). The 3-fold to 4-fold transition therefore occurs in molten Fe-carbonates at P less or equal to 53 GPa. This transition is preserved upon quenching to the glass state, and is recoverable at ambient conditions, opening the way to the synthesis of a new class of glassy materials.

The method to derive density from x-ray diffraction data on melts compressed in diamond-anvil cell experiments[28,29] consists in minimizing the oscillations in $g(r)$ where there should not be any signal, *i.e.* below the minimum interatomic distance. This method requires that the background, essentially the Compton signal from the diamond anvils that dominates the total diffracted intensity, is perfectly subtracted. As the C-O contribution is distinct on $g(r)$ of quenched glasses up to 83 GPa, we also ran consistency checks by fixing the C-O coordination number to 4 and simulating the C-O contribution using the obtained density values (fits on Fig.1b). Density values are reported in Fig.3 along with predictions for lower P melt properties[30], P-evolution of crystalline siderite, and with the Earth's seismological PREM model[31]. Density profile below 40 GPa is calculated using $K_{T,0}$ value of 80.23 GPa[30], consistent with that reported for molten calcite[11], and density at room P of 2500 kg·m^{-3} by assuming a similar density jump upon melting as for other carbonates for which room P density is known. Comparison with PREM model shows that Fe-carbonate melts are buoyant at all depths. Density contrast between the high P polymerized melt or glass and extrapolated equation of state for low P melt is approximately 15%, *i.e.* similar to volume collapse reported upon transition from crystalline high spin siderite I to low spin

siderite II[8]. The volume collapse is smoothed out over a $\sim$ 30 GPa range in the molten state with, as a direct consequence, a steepening of the melting curve from 55 GPa on[22]. Density of non-crystalline $FeCO_3$ remains considerably lower than that of its crystalline counter parts, even at the highest investigated P, by approximately 15%. The situation is thus very different from that of molten and crystalline silicates which density converge at deep mantle conditions[32,33], and such difference could be attributed to the very strong medium-range order preserved in tetrahedral high P carbonate melts while it is mostly collapsed by 5 GPa in silicate melts.

A consequence of the effect of Fe on the ^{III}C to ^{IV}C transition P is that crystalline Fe-poor (Ca,Mg,Fe)$^{III}CO_3$ and Fe-enriched (Ca,Mg,Fe)$^{IV}CO_3$ melts could co-exist at depth. In the case of Si isotopes, fractionation between ^{VI}Si bridgmanite and ^{IV}Si olivine structures is theoretically estimated to $\sim -1‰$ ^{28}Si at 2000 K[34]. If this effect can be scaled to C simply using mass difference considerations, then a few $‰$ ^{13}C fractionation is expected, and could potentially explain isotopic differences between calcite inclusions from super-deep diamonds[35]. This effect might be sufficient to confer a mantle-like signature to deep diamonds grown from slab-derived carbonate melts while co-existing tetrahedral crystalline carbonate are expected to get lighter.

That high P $FeCO_3$ melts quench as glasses contrasts with the behaviour observed at lower P, and suggests an important increase of carbonate melt viscosity. It is also opposite to the behaviour of molten basalt that systematically quenches as crystalline phases above 11 GPa[29] and as a glass below. The strongly reduced chemical reactivity of high P $FeCO_3$ melts with silica along with their glass-forming ability suggest that unlike at lower P, tetrahedral carbonate melts are not

pervasive, which could contribute to the longevity of carbonates in the deep mantle where allowed by oxydizing conditions or slow reduction kinetics[2].

Methods summary

We used symmetric diamond-anvil cells equipped with 70° opening Boehler-Almax seats in order to access a wider q-range up to 10 Å^{-1}, and reduce the diamond Compton contribution as Boehler-Almax anvils are only 1.5 mm thick. The x-ray monochromatic beam (42.7 keV) was focussed down to a size of 4×6 μm^2, allowing high spatial resolution in direct space. Heating was achieved by laser heating using a double-sided infra-red laser focussed down to 20 μm. The starting natural crystalline siderite sample was loaded as a 20 μm-thick platelet between two equally thick platelets of compressed SiO_2 powder. The SiO_2 platelets act as thermal insulators and P-transmitting medium. To limit iron migration away from the laser heating spot due to Soret effect, the laser shutters were opened only once the targeted power was reached, and held open for 10 s during which 10 x-ray diffraction patterns of 1 s acquisition time were recorded on a Perkin-Elmer 2-D detector. Targeted power was increased in 2 W increments from 20 to 50 W of power on each laser depending on P until complete melting of the sample (see SI. for P-T calibration). Melting was identified by disappearance of diffraction peaks apart from SiO_2 peaks, and by the appearance of diffuse scattering. Only one sample was used per P point (see SI, Fig.S1) to avoid repeated laser-heatings and preserve the chemical integrity of the sample. In order to isolate the scattered intensity from the molten $FeCO_3$ only, each sample was removed from the gasket, and the gasket put back in place to collect x-ray data on the empty cell. Obtained patterns were then scaled ver-

tically to match the baseline of x-ray patterns collected on the quenched crystalline sample still under P[36]. This last step ensures that any P effect on the background is corrected for. Amongst eight successful runs (Table1) for which full melting was observed, intensity from molten $FeCO_3$ could only be processed for the highest P run, the scattered intensity being too weak for the lower P points. All glass patterns could be processed.

X-ray Raman data were collected at an incident energy of 9.7 keV at the C K-edge on beamline ID20 of the European Synchrotron Radiation Facility (ESRF), beamsize was 15×15 μm^2. Glassy $FeCO_3$ spheres had been previously synthesized at 59 GPa using the same P02.2 laser heating system in PetraIII as for x-ray diffraction experiments. LiF was used instead of SiO_2 as a P-transmitting medium to avoid any contamination of the x-ray Raman signal by oxygen from SiO_2 as measurements at the O K-edge were initially planned. LiF salt could not be used for the x-ray diffraction experiments due to its low melting curve and relatively strong diffracted signal that would have contributed to the diffuse scattering from molten $FeCO_3$. Raman spectra were collected using 633 nm wavelength in order to preserve the samples, using more energetic lower wavelengths resulted in dissociation of the sample and detection of hematite signal.

Acknowledgements The research leading to these results has received funding from the European Community's Seventh Framework Programme (FP7/2007-2013) under grant agreements no. 312284 and 259649 (European Research Council starting grant to C.S.). Portions of this research were carried out at the light source PETRA III at DESY, a member of the Helmholtz Association (HGF). The laser heating system on beamline P02.2 is funded by the German BMBF (project number 05K10RFA). We acknowledge E. Boulard for providing the starting siderite sample, K. Glazyrin for his help with *ex situ* diamond-anvil cell laser-

heating synthesis in PETRA III, L. Rémusat at Museum National d'Histoire Naturelle (Paris, France) for gold coating of the recovered samples, the ESRF (Grenoble, France) and PETRAIII (Hamburg, Germany) for provision of synchrotron radiation facilities.

Competing Interests The authors declare that they have no competing financial interests.

Author Contributions J.H. and C.S. devised the project, C.S. processed x-ray diffraction data and wrote the paper with input from G.L. and L.C. J.H., C.S., B.C., V.A., Z.K. participated in x-ray diffraction data acquisition, M.W. designed the laser-heating system used during the experiments. J.H., G.L., L.C., C.S. participated in x-ray Raman data acquisition. J.H. collected Raman data.

Correspondence Correspondence and requests for materials should be addressed to C.S. (email: chrystele.sanloup@sorbonne-universite.fr).

1. Oganov, A., Glass, C. & Ono, S. High-pressure phases of $CaCO_3$: Crystal structure prediction and experiment. *Earth Planet. Sci. Lett.* **241**, 95–103 (2006).

2. Litasov, K. D. & Shatskiy, A. *Carbon-Bearing Magmas in the Earth's Deep Interior*, 43–82 (Elsevier, Amsterdam, The Netherlands, 2018).

3. Frost, D. *et al.* Experimental evidence for the existence of iron-rich metal in the Earth's lower mantle. *Nature* **428**, 409–412 (2004).

4. Smith, E. M. *et al.* Large gem diamonds from metallic liquid in earth's deep mantle. *Science* **354**, 1403–1405 (2016).

5. Arapan, S., De Almeida, J. S. & Ahuja, R. Formation of sp(3) hybridized bonds and stability of $CaCO_3$ at very high pressure. *Phys. Rev. Lett.* **98** (2007).

6. Oganov, A. R., Ono, S., Ma, Y., Glass, C. W. & Garcia, A. Novel high-pressure structures of $MgCO_3$, $CaCO_3$ and CO_2 and their role in Earth's lower mantle. *Earth Planet. Sci. Lett.* **273**, 38–47 (2008).

7. Boulard, E. *et al.* New host for carbon in the deep Earth. *Proc. Natl Acad. Sci. USA* **108**, 5184–5187 (2011).

8. Liu, J., Lin, J.-F. & Prakapenka, V. B. High-Pressure Orthorhombic Ferromagnesite as a Potential Deep-Mantle Carbon Carrier. *Sci. Rep.* **5** (2015).

9. Merlini, M. *et al.* Dolomite-IV: Candidate structure for a carbonate in the Earth's lower mantle. *Am. Mineral.* **102**, 1763–1766 (2017).

10. Vuilleumier, R., Seitsonen, A., Sator, N. & Guillot, B. Structure, equation of state and transport properties of molten calcium carbonate ($CaCO_3$) by atomistic simulations. *Geochim. Cosmchim. Acta* **141**, 547–566 (2014).

11. Hudspeth, J., Sanloup, C. & Kono, Y. Properties of molten $CaCO_3$ at high pressure. *Geochem. Persp. Let.* **7**, 27–31 (2018).

12. Foley, S. F. Rejuvenation and erosion of the cratonic lithosphere. *Nature Geosci.* **1**, 503–510 (2008).

13. Litasov, K. D., Shatskiy, A., Ohtani, E. & Yaxley, G. M. Solidus of alkaline carbonatite in the deep mantle. *Geology* **41**, 79–82 (2013).

14. Kaminsky, F. Mineralogy of the lower mantle: A review of 'super-deep' mineral inclusions in diamond. *Earth Sci. Rev.* **110**, 127–147 (2012).

15. Weis, C. *et al.* Pressure driven spin transition in siderite and magnesiosiderite single crystals. *Sci. Rep.* **7** (2017).

16. Lobanov, S. S., Goncharov, A. F. & Litasov, K. D. Optical properties of siderite ($FeCO_3$) across the spin transition: Crossover to iron-rich carbonates in the lower mantle. *Am. Mineral.* **100**, 1059–1064 (2015).

17. Solomatova, N. V. & Asimow, P. D. First-principles calculations of high-pressure iron-bearing monoclinic dolomite and single-cation carbonates with internally consistent Hubbard U. *Phys. Chem. Miner.* **45**, 293–302 (2018).

18. Boulard, E., Guyot, F. & Fiquet, G. The influence on Fe content on Raman spectra and unit cell parameters of magnesite-siderite solid solutions. *Phys. Chem. Miner.* **39**, 239–246 (2012).

19. Boulard, E. *et al.* CO_2-induced destabilization of pyrite-structured FeO_2H_x in the lower mantle. *Natl. Sci. Rev.* nwy032 (2018).

20. Seto, Y., Hamane, D., Nagai, T. & Fujino, K. Fate of carbonates within oceanic plates subducted to the lower mantle, and a possible mechanism of diamond formation. *Phys. Chem. Miner.* **35**, 223–229 (2008).

21. Maeda, F. *et al.* Diamond formation in the deep lower mantle: a high-pressure reaction of $MgCO_3$ and SiO_2. *Sci. Rep.* **7** (2017).

22. Cerantola, V. *et al.* Stability of iron-bearing carbonates in the deep Earth's interior. *Nat. Commun.* **8** (2017).

23. Sato, T. & Funamori, N. Sixfold-coordinated amorphous polymorph of SiO_2 under high pressure. *Phys. Rev. Lett.* **101**, 255502 (2008).

24. Ghosh, D. B., Bajgain, S. K., Mookherjee, M. & Karki, B. B. Carbon-bearing silicate melt at deep mantle conditions. *Sci. Rep.* **7** (2017).

25. Wilding, M. C. *et al.* Low-dimensional network formation in molten sodium carbonate. *Sci. Reports* **6**, 24415 (2016).

26. Sharma, S. & Simons, B. *Raman study of K_2CO_3-$MgCO_3$ glasses*, vol. 79, 322–326 (Carnegie Institute, 1979).

27. Shieh, S. R. *et al.* Electronic structure of carbon dioxide under pressure and insights into the molecular-to-nonmolecular transition. *Proc. Natl. Acad. Sci. U. S. A.* **110**, 18402–18406 (2013).

28. Eggert, J. H., Weck, G., Loubeyre, P. & Mezouar, M. Quantitative structure factor and density measurements of high-pressure in diamond anvil cells by x-ray diffraction: Argon and water. *Phys. Rev. B* **65**, 174105 (2002).

29. Sanloup, C. *et al.* Structural change in molten basalt at deep mantle conditions. *Nature* **503**, 104–107 (2013).

30. Nathan, K., Schmidt, M. W., Poli, S., Franzolin, E. & Connolly, A. D. Melting of siderite to 20 GPa and thermodynamic properties of $FeCO_3$-melt. *Chem. Geol.* **400**, 34–43 (2015).

31. Dziewonski, A. M. & Anderson, D. L. Preliminary reference Earth model. *Phys. Earth Planet. Int.* **25**, 297–356 (1981).

32. Sanloup, C. Density of magmas at depth. *Chem. Geol.* **429**, 51–59 (2016).

33. Petitgirard, S. *et al.* Fate of $MgSiO_3$ melts at core-mantle boundary conditions. *P. Natl. Acad. Sci. USA* **112**, 14186–14190 (2015).

34. Huang, F., Wu, Z., Huang, S. & Wu, F. First-principles calculations of equilibrium silicon isotope fractionation among mantle minerals. *Geochim. Cosmochim. Acta* **140**, 509–520 (2014).

35. Kaminsky, F., Matzel, J., Jacobsen, B., Hutcheon, I. & Wirth, R. Isotopic fractionation of oxygen and carbon in decomposed lower-mantle inclusions in diamond. *Mineral. Petrol.* **110**, 379–385 (2016).

36. Sanloup, C. & de Grouchy, C. J. L. *X-ray diffraction structure measurements*, 137–154 (Elsevier, Amsterdam, The Netherlands, 2018).

Synthesis and stability of hydrogen iodide at high pressures

Jack Binns,[1] Xiao-Di Liu,[2] Philip Dalladay-Simpson,[1] Veronika Afonina,[3] Eugene Gregoryanz,[1,2,3] and Ross T. Howie[1,*]

[1]*Center for High Pressure Science Technology Advanced Research, Shanghai, People's Republic of China*

[2]*Key Laboratory of Materials Physics, Institute of Solid State Physics, Chinese Academy of Sciences, Hefei, People's Republic of China*

[3]*Centre for Science at Extreme Conditions and School of Physics and Astronomy, University of Edinburgh, Edinburgh EH9 3JZ, United Kingdom*

(Received 7 August 2017; published 11 October 2017)

Through high-pressure Raman spectroscopy and x-ray diffraction experiments, we have investigated the formation, stability field, and structure of hydrogen iodide (HI). Hydrogen iodide is synthesized by the reaction of molecular hydrogen and iodine at room temperature and at a pressure of 0.2 GPa. Upon compression, HI solidifies into cubic phase I, and we present evidence for the emergence of a phase I′ above 3.8 GPa. Across the wide temperature regime presented here, HI is unstable under compression (11 GPa at 300 K, 18 GPa at 77 K), decomposing into its constituent elements, after which no further reaction between hydrogen and iodine was observed up to pressures of 60 GPa. This study provides both the constraints on the phase diagram of HI and its kinetic stability.

DOI: 10.1103/PhysRevB.96.144105

I. INTRODUCTION

The high-pressure behavior of molecular systems containing the simplest and most abundant element, hydrogen, have been the subject of an intense experimental and theoretical effort, perhaps best exemplified by the presumed insulator-to-metallic transition expected in elemental H_2 [1–4]. On the other hand, investigations into the pressurization of hydrogen-bearing species have received a significant impetus by the recent claim of high-temperature superconductivity in hydrogen sulfide (H_2S) at unprecedented high temperatures [5]. Hydrogen iodide (HI) has been proposed to exhibit both these phenomena at high pressures and low temperatures, with a claimed insulator-to-metallic transition at 50 GPa [6,7]. Additionally, compounds of HI-H_2 have been recently predicted to be stable above 50 GPa, with superconducting phases emerging above 100 GPa with a $T_c \leqslant 17.5$ K [8,9].

The hydrogen halides HCl, HBr, and HI follow a law of corresponding states and exhibit a similar solid phase sequence at ambient pressure and low temperature. Phase I at high temperatures adopts a cubic structure ($Fm\bar{3}m$) with halogen atoms forming a fcc lattice with hydrogens either in twelvefold disordered positions or rotating unhindered about these sites [10–12]. The structure of phase II, existing at intermediate temperatures, remained unresolved until neutron diffraction revealed a structure containing linear chains of twofold disordered H-$X\cdots$H hydrogen bonds [11,13]. The low-temperature/high-pressure phase III in HCl and HBr adopts a proton-ordered orthorhombic structure ($Cmc2_1$) containing zigzag chains of H-$X\cdots$H hydrogen bonds [11,14]. Phase III in HI adopts a triclinic structure ($P\bar{1}$) with stacked layers of hydrogen-bonded squares [11]. This difference is due to changes in the relative strengths of the two competing intermolecular interactions: the halogen-halogen bonding, which increases in strength from Cl to I, and the reciprocal decrease in hydrogen bonding strength [15].

An additional phase I′ exists for HBr but not for HCl, HI, or DBr. This phase is characterized by slight changes in the Raman spectra with neutron diffraction showing a transition from a spherical hydrogen scattering density in phase I to a toroidal distribution oriented about the ⟨111⟩ cubic axes [12,16].

The instability of HI, which readily dissociates into I_2 and H_2 with laser or x-ray overexposure, has hindered experimental studies at high pressures. Currently there are no high-pressure studies at room temperature, nor any x-ray structural characterization at any temperature. The stability field of the compound at high pressure has been assumed and extrapolated based on the limited low-pressure, low-temperature data and the behavior of the other hydrogen halides, HCl and HBr [7,17].

Here we present high-pressure Raman spectroscopy and x-ray diffraction experiments exploring the formation, stability field, and structures of hydrogen iodide (HI). In addition to the three known solid configurations of HI, we present evidence for a phase I′ at room temperature, structurally similar to cubic phase I, but differing in hydrogen atom distribution about the iodine atoms. A series of isothermal compressions between 300 K provide constraints on the phase diagram of HI and we find that at high pressures HI is unstable with respect to dissociation into its constituent elements thus ruling out the earlier claims of pressure-induced metallization of HI.

II. METHODS

Samples of HI were synthesized in diamond-anvil cells by the direct reaction between solid I_2 and fluid H_2. Diamond anvils with 150–250 μm culets were used for experiments, giving sample chamber diameters of between 75–100 μm. Various concentrations of I_2 were loaded in an Ar-atmosphere glove box, with a small chip of ruby or gold as a pressure calibrant [20,21]. High-purity (99.9%) H_2 was subsequently gas loaded at 0.2 GPa. Reaction of H_2 and I_2 to produce HI occurs spontaneously with time at this low pressure, or can be accelerated by irradiation with up to 200 mW of 532 nm laser light. Samples were left for 24 h to equilibrate resulting in a mixture of two fluids exhibiting clear phase

*ross.howie@hpstar.ac.cn

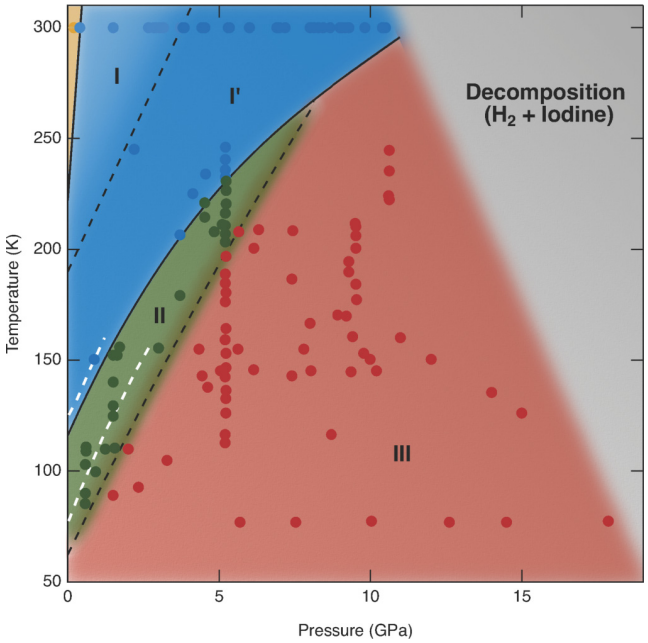

FIG. 1. *P-T* phase diagram of HI. The yellow circle represents the liquid phase. Blue, dark blue, green, and red circles represent solid phases I, I′, II, and III, respectively. The gray area indicates the *P-T* conditions of dissociation. The phase I-I′ and II-III boundaries are shown as dashed lines due to the significant overlap and ambiguity in the Raman spectra between phases. The white dashed lines show the I-II and II-III phase boundaries from Ref. [7].

separation. This process is only possible below 1 GPa, with the mixture remaining as I_2 and H_2 above this. Additionally, there would be no reformation if HI is dissociated through x-ray or laser overexposure. By careful control of the H_2 : I_2 ratio, we were able to produce samples that were completely transformed to HI. Raman spectroscopy was used to test the purity of the prepared sample, showing trace amounts of both the constituent elements. Trace amounts of I_2 and H_2, were also observed in previous studies where high purity HI was loaded directly [6,17].

Raman spectroscopy measurements were made using a custom-built microfocused Raman system. The laser power of the system was kept below 3 mW to prevent back transformation of the HI sample to I_2 and H_2 and laser exposure minimized to 0.2 s. We have found that above 1–2 GPa, photodissociation of I_2 is not possible with 200 mW of 532 nm laser light. X-ray diffraction data were collected at beam lines BL10XU, SPring-8, Japan and P02.2 ECB, PETRA, Germany [22,23]. Angle-dispersive x-ray diffraction patterns were recorded on PerkinElmer XRD1621 and Marr345 image-plate detectors with microfocused synchrotron radiation sources with energies in the range 30–43 keV. Two-dimensional image-plate data were integrated with DIOPTAS [24] to yield intensity vs 2θ plots. Patterns were indexed with DICVOL06 [25], Le Bail [26], and Rietveld [27] refinements were carried out in JANA2006 [28].

Exposure of HI to synchrotron x-ray radiation forms I_2, which contaminates the resulting diffraction pattern with numerous peaks and requires acquiring data from a new sample and/or sample position at each pressure point. Typically HI crystallizes into large single-crystal domains within the sample chamber allowing diffraction spots from HI to be easily distinguished from the powder diffraction lines due to I_2.

III. RESULTS

The pressure-temperature phase and kinetic diagram between temperatures of 300 K and 77 K is shown in Fig. 1. The vibrational modes in solid HI, as with the other hydrogen

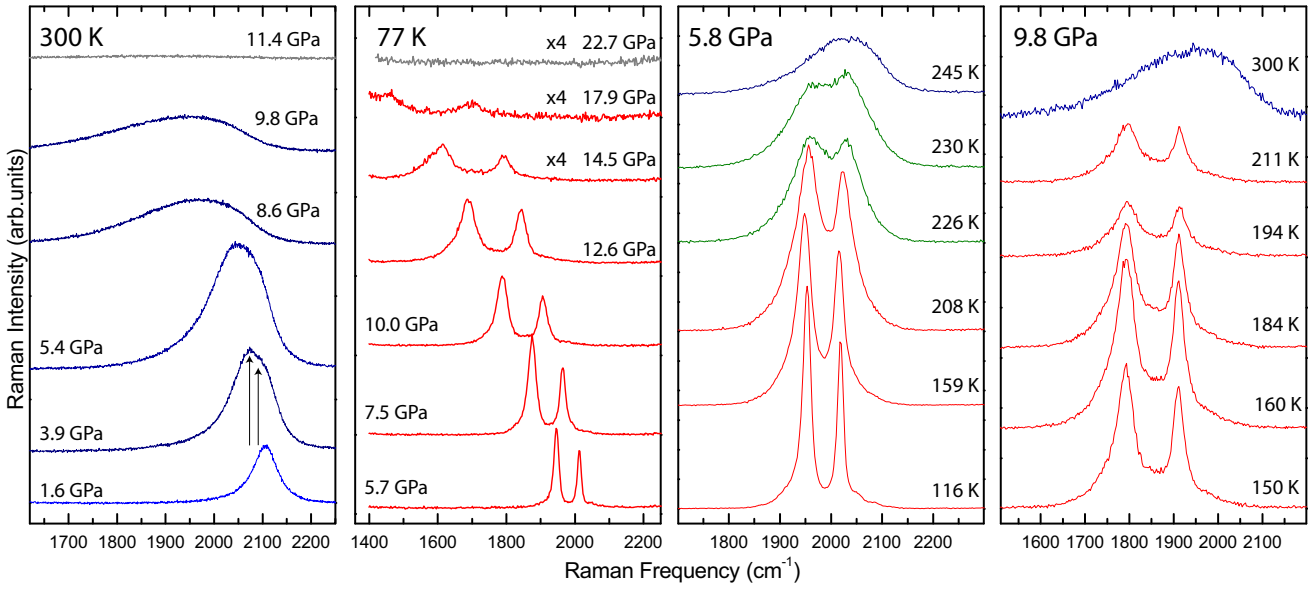

FIG. 2. Representative Raman spectra of an isothermal compression at 300 K (left panel), isothermal compression at 77 K (center left panel), an isobaric cooling/heating cycle at 5.8 GPa (center right panel) and an isobaric cooling/heating cycle at 9.8 GPa (right panel). Color indicates phases corresponding to the phase diagram in Fig. 1: light blue, phase I; dark blue, phase I′; green, phase II; red, phase III; and gray represents decomposition. Arrows indicate splitting of vibrational modes from phase I to I′.

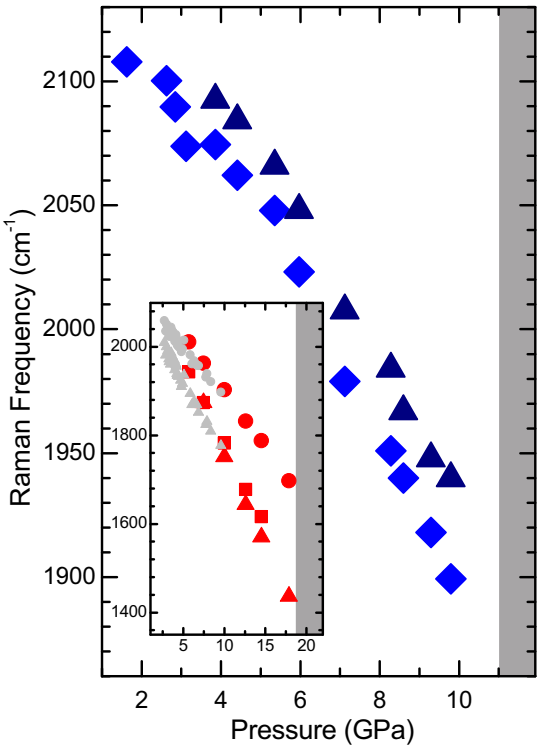

FIG. 3. Vibrational frequencies of HI on compression at 300 K, dark blue triangles indicate appearance of a second mode indicative of phase I′. Inset: Vibrational frequencies of HI on compression at 77 K, red points are from this study, while light gray points are taken from Ref. [7]. Dark gray shaded area indicates the pressure regime of decomposition

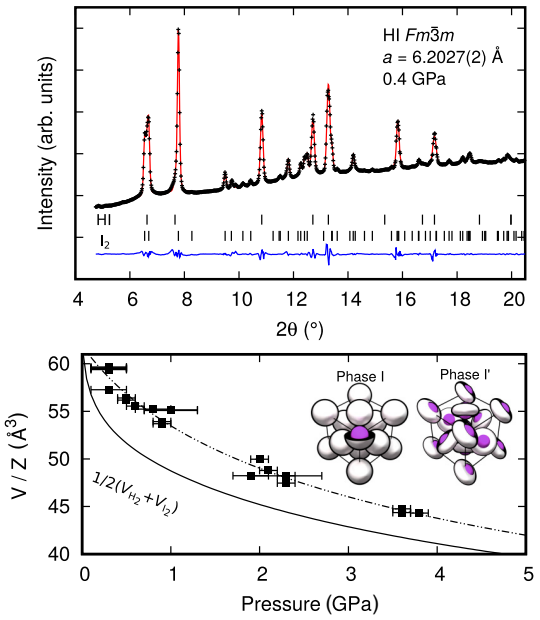

FIG. 4. (Top) Diffraction pattern of HI at 0.4 GPa, Le Bail profile refinement shown in red, difference shown in blue (wR_p = 1.68%); (bottom) HI equation of state, symbols are experimental data from individual runs. Dashed line corresponds to the calculated Birch-Murnaghan equation of state [HI: $V_0 = 248(5)$ Å^3, $K_0 = 4.7(12)$ GPa, $K_p = 5.2(11)$], solid line corresponds to the volume derived from the corresponding atomic equations of state of I_2 [18] and H_2 [19]. Inset: In phase I, hydrogen atoms freely rotate about iodine atoms (purple) represented by a shell model (white), phase I′ exhibits a toroidal distribution of disordered hydrogen atom positions oriented along the ⟨111⟩ cubic axes.

halides are due to the intramolecular H-X bond. The vibrational modes soften in the solid phase and at high pressures when intermolecular distances reduce and the strength of intermolecular interactions increases. At room temperature, the liquid phase is characterized by one symmetric vibrational mode at approximately 2110 cm^{-1}. On solidification to phase I, there is a significant broadening and softening of the mode (see Figs. 2 and 3). Despite numerous overlapping peaks, crystallization into phase I ($Fm\bar{3}m$) was confirmed by x-ray diffraction measurements (Fig. 4).

Above pressures of 3.8 GPa at 300 K, the vibrational mode of HI shows a clear splitting into two modes, separated by 20 cm^{-1}. This same splitting was observed in HBr at pressures above 2.4 GPa at 295 K and interpreted to be a transition to a phase I′ [12,16]. In HBr this transition is due to a rearrangement of the H-atom distribution with no change to the underlying fcc bromine-atom lattice of phase I, with associated symmetry change to $Pa\bar{3}$. Due to the weak x-ray scattering of H we cannot distinguish the two phases on the basis of x-ray diffraction alone. However, based on the close resemblance of the Raman spectra we propose a similar structure for HI phase I′ (Fig. 4). Interestingly, phase I′ is not seen in either DBr or HCl, suggesting that this phase is only observed in the heavier hydrogen halides.

On compression above 3.8 GPa, the asymmetry of the phase I′ vibrational band increases and there is significant broadening of both modes. The frequencies of the vibrational band decrease rapidly with pressure at a rate of -30 cm^{-1}/GPa and extrapolating the frequencies would give a pressure of 69 GPa when the frequencies would reach zero (see Figs. 2 and 3). However, the intensity of the band starts to decrease above 6 GPa and by 11 GPa the HI vibrational mode disappears completely. This, together with the increase in intensity of the Raman modes of the constituent elements H_2 and I_2, and sample darkening, are clear indicators of sample dissociation. This was confirmed by x-ray diffraction patterns from samples precompressed to above 11 GPa, which showed peaks due only to I_2. Once dissociation has taken place the sample remains as I_2 and H_2, with no indication of further reaction in both Raman spectroscopy and x-ray diffraction measurements. On decompression after dissociation, there is no reformation of HI.

Each of the solid phases of HI at low temperature can be characterized by distinct vibrational Raman spectra, which can be correlated to the ambient pressure neutron diffraction data [11,29]: phase I, a symmetric broad stretching mode; phase I′, a broad asymmetric doublet with separation of 20 cm^{-1}; phase II, two broad overlapping modes with near equal intensity and separation of approximately 65 cm^{-1}; and phase III, two sharp and distinct stretching modes (see right panel of Fig. 2). On isobaric cooling cycles we see that the phase I(I′)-II-III transition sequence is completely reversible. On entering phase II from phase I or I′, the vibrational mode

abruptly splits into two equally intense overlapping modes with separation of approximately 80 cm^{-1}. Phase II is stable over a small *P-T* regime, much like the other hydrogen halide HBr [16].

The gradual change in appearance of the vibrational modes of phase II with pressure/temperature results in some ambiguity as to at which temperatures the phase II to III transition occurs. The doublet separation gradually gets larger, each mode decreases in width, and the lower frequency mode surpasses the intensity of the higher frequency mode (see Fig. 2). On compression of phase III at 77 K, we see the similar behavior observed with the vibrational modes at room temperature: rapid softening, a fourfold increase in width, and by 17 GPa, a 95% reduction in intensity of the HI vibrons compared to 5 GPa. In phase III each vibrational mode shifts at a different rate, -26 cm^{-1}/GPa and -42 cm^{-1}/GPa. HI is slightly more stable at low temperature, with dissociation occurring above 18 GPa.

IV. DISCUSSION AND CONCLUSIONS

Despite the sensitivity to decomposition it was previously assumed that HI would remain stable up to very high pressures and enter a metallic state at low temperature [6,7]. Metallization was initially inferred by the extrapolation of absorption measurements conducted at pressures below 25.5 GPa, i.e., below the conditions at which we report dissociation. Subsequent electrical conductivity measurements carried out on a single sample show sharp drops in resistivity at 42 and 51 GPa. These drops are interpreted as a molecular-insulator to molecular-conductor transition followed by transition to a metallic state. Other conductivity measurements presented in Ref. [6] clearly correspond to the metallization of I_2 occurring at 16 GPa [30,31]. Both diagnostic techniques used in these early studies do not probe either the crystal structure or molecular behavior at high pressures, meaning that dissociation—a simpler explanation of the experimental results—was overlooked. Our combined x-ray diffraction and Raman spectroscopy measurements demonstrate that (metallic) HI cannot be present at the corresponding temperatures and pressures reported in Refs. [6,7]. The dissociation pressures of the hydrogen halides decrease down the period (HBr has been shown to dissociate at pressures above 42 GPa and HCl shown to be stable to at least 50 GPa), it can therefore be expected that the heavier hydrogen halide would dissociate at a much lower pressure [32].

At pressures close to ambient, the volume of HI (Fig. 4, bottom panel) is approximately equal to the combined volumes of H_2 and I_2. However, the high compressibility of hydrogen leads to an increasing difference between these volumes at higher pressure, whereby the experimental determined value is greater than the calculated value up to 9 GPa at 300 K. This implies that HI is unstable with respect to its constituent elements. Having the longest bond (1.60 Å vs 1.43 Å in DBr and 1.28 Å in DCl) HI is the least stable among these compounds. It appears that the decomposition of HI upon compression is not due to the intrinsic elastic or dynamical instability, e.g., HBr and HCl are stable to much higher pressures. An intrinsic stability limit is defined by the decrease in HI bonding strength therefore preventing the formation of phases with stoichiometry other than 1 : 1. This observation raises an interesting question about the predicted superconducting phases of the hydrogen iodide compounds with stoichiometry other than 1 : 1. H_2I and H_4I are both suggested to be superconducting at pressures of 100 GPa but are unlikely to be stable with respect to decomposition to their constituent elements at such conditions [8,9]. This may also hold true for the superconducting phases of HCl and HBr predicted at pressures of 280 GPa and 160 GPa, respectively [33]. At pressures up to 60 GPa and at temperatures of 80 K and 300 K, we observed no further reaction between H_2 and I_2, suggesting that much higher pressures and most probably high temperature to overcome the kinetic barrier would be required to promote formation of any the theoretically predicted H_2-I_2 compounds [8,9].

ACKNOWLEDGMENTS

This work was supported by the NSF of China (Grant No. 11404343), Natural Science Foundation of Anhui Province, China (Grant No. 1508085QA07). Parts of this research were carried out at P02.2 at DESY, a member of the Helmholtz Association (HGF). We would like to thank H.-P. Liermann and K. Glazyrin for assistance. Part of this work was performed under Proposal No. 2017A1062 at SPring-8.

[1] E. Wigner and H. B. Huntington, J. Chem. Phys. **3**, 764 (1935).
[2] M. Eremets and I. Troyan, Nat. Mater. **10**, 927 (2011).
[3] R. T. Howie, C. L. Guillaume, T. Scheler, A. F. Goncharov, and E. Gregoryanz, Phys. Rev. Lett. **108**, 125501 (2012).
[4] P. Dalladay-Simpson, R. T. Howie, and E. Gregoryanz, Nature (London) **529**, 63 (2016).
[5] A. P. Drozdov, M. I. Eremets, I. A. Troyan, V. Ksenofontov, and S. I. Shylin, Nature (London) **525**, 1 (2015).
[6] J. van Straaten and I. F. Silvera, Phys. Rev. Lett. **57**, 766 (1986).
[7] J. van Straaten and I. F. Silvera, Phys. Rev. B **36**, 9253 (1987).
[8] A. Shamp and E. Zurek, J. Phys. Chem. Lett. **6**, 4067 (2015).
[9] D. Duan, F. Tian, Y. Liu, X. Huang, D. Li, H. Yu, Y. Ma, B. Liu, and T. Cui, Phys. Chem. Chem. Phys. **17**, 32335 (2015).
[10] E. Sándor and R. F. C. Farrow, Nature (London) **14**, 171 (1967).
[11] A. Ikram, B. H. Torrie, and B. M. Powell, Mol. Phys. **79**, 1037 (1993).
[12] J. K. Cockcroft, A. Simon, and K. R. A. Ziebeck, Z. Kristallogr. **184**, 229 (1988).
[13] E. Sándor and M. W. Johnson, Nature (London) **217**, 542 (1968).
[14] E. Sándor and R. F. C. Farrow, Discuss. Faraday Soc. **48**, 78 (1969).
[15] W. Y. Zeng, Y. Z. Mao, and A. Anderson, J. Raman Spectrosc. **30**, 995 (1999).
[16] T. Kume, T. Tsuji, S. Sasaki, and H. Shimizu, Phys. Rev. B **58**, 8149 (1998).
[17] J. van Straaten and I. F. Silvera, Phys. Rev. B **36**, 9301 (1987).
[18] K. Takemura, S. Minomura, O. Shimomura, Y. Fujii, and J. D. Axe, Phys. Rev. B **26**, 998 (1982).

[19] P. Loubeyre, R. LeToullec, D. Hausermann, M. Hanfland *et al.*, Nature (London) **383**, 702 (1996).
[20] H. K. Mao, J. Xu, and P. M. Bell, J. Geophys. Res. **91**, 4673 (1986).
[21] Y. Fei, A. Ricolleau, M. Frank, K. Mibe, G. Shen, and V. Prakapenka, Proc. Nat. Acad. Sci. USA **104**, 9182 (2007).
[22] Y. Ohishi, N. Hirao, N. Sata, K. Hirose, and M. Takata, High Press. Res. **28**, 163 (2008).
[23] H.-P. Liermann, Z. Konôpková, W. Morgenroth, K. Glazyrin, J. Bednarčik, E. McBride, S. Petitgirard, J. Delitz, M. Wendt, Y. Bican *et al.*, J. Sync. Rad. **22**, 908 (2015).
[24] C. Prescher and V. B. Prakapenka, High Press. Res. **35**, 223 (2015).
[25] A. Boultif and D. Louër, J. Appl. Crystallogr. **37**, 724 (2004).
[26] A. Le Bail, H. Duroy, and J. Fourquet, Mater. Res. Bull. **23**, 447 (1988).
[27] H. M. Rietveld, J. Appl. Crystallogr. **2**, 65 (1969).
[28] V. Petříček, M. Dušek, and L. Palatinus, Z. Kristallogr. **229**, 345 (2014).
[29] A. Anderson, B. H. Torrie, and W. S. Tse, J. Raman Spectrosc. **8**, 213 (1979).
[30] A. S. Balchan and H. G. Drickamer, J. Chem. Phys. **34**, 1948 (1961).
[31] N. Sakai, K. Takemura, and K. Tsuji, J. Phys. Soc. Jpn. **51**, 1811 (1982).
[32] E. Katoh, H. Yamawaki, H. Fujihisa, M. Sakashita, and K. Aoki, Phys. Rev. B **59**, 11244 (1999).
[33] D. Duan, F. Tian, Z. He, X. Meng, L. Wang, C. Chen, X. Zhao, B. Liu, and T. Cui, J. Chem. Phys. **133**, 074509 (2010).

A&A 586, A108 (2016)
DOI: 10.1051/0004-6361/201527441

Astronomy & Astrophysics

New and updated convex shape models of asteroids based on optical data from a large collaboration network

J. Hanuš[1,2], J. Ďurech[3], D. A. Oszkiewicz[4], R. Behrend[5], B. Carry[2], M. Delbo[2], O. Adam[6], V. Afonina[7], R. Anquetin[8,45], P. Antonini[9], L. Arnold[6], M. Audejean[10], P. Aurard[6], M. Bachschmidt[6], B. Baduel[6], E. Barbotin[11], P. Barroy[8,45], P. Baudouin[12], L. Berard[6], N. Berger[13], L. Bernasconi[14], J-G. Bosch[15], S. Bouley[8,45], I. Bozhinova[16], J. Brinsfield[17], L. Brunetto[18], G. Canaud[8,45], J. Caron[19,20], F. Carrier[21], G. Casalnuovo[22], S. Casulli[23], M. Cerda[24], L. Chalamet[86], S. Charbonnel[25], B. Chinaglia[22], A. Cikota[26], F. Colas[8,45], J.-F. Coliac[27], A. Collet[6], J. Coloma[28,29], M. Conjat[2], E. Conseil[30], R. Costa[28,31], R. Crippa[32], M. Cristofanelli[33], Y. Damerdji[87], A. Debackère[86], A. Decock[34], Q. Déhais[36], T. Déléage[35], S. Delmelle[34], C. Demeautis[37], M. Dróżdż[38], G. Dubos[8,45], T. Dulcamara[6], M. Dumont[34], R. Durkee[39], R. Dymock[40], A. Escalante del Valle[85], N. Esseiva[41], R. Esseiva[41], M. Esteban[24,42], T. Fauchez[34], M. Fauerbach[43], M. Fauvaud[44,45], S. Fauvaud[8,44,45], E. Forné[28,46,†], C. Fournel[86], D. Fradet[8,45], J. Garlitz[47], O. Gerteis[6], C. Gillier[48], M. Gillon[34], R. Giraud[34], J.-P. Godard[8,45], R. Goncalves[49], Hiroko Hamanowa[50], Hiromi Hamanowa[50], K. Hay[16], S. Hellmich[51], S. Heterier[52,53], D. Higgins[54], R. Hirsch[4], G. Hodosan[16], M. Hren[26], A. Hygate[16], N. Innocent[6], H. Jacquinot[55], S. Jawahar[56], E. Jehin[34], L. Jerosimic[26], A. Klotz[6,57,58], W. Koff[59], P. Korlevic[26], E. Kosturkiewicz[4,38,88], P. Krafft[6], Y. Krugly[60], F. Kugel[19], O. Labrevoir[6], J. Lecacheux[8,45], M. Lehký[61], A. Leroy[8,45,62,63], B. Lesquerbault[6], M. J. Lopez-Gonzales[64], M. Lutz[6], B. Mallecot[8,45], J. Manfroid[34], F. Manzini[32], A. Marciniak[4], A. Martin[65,66], B. Modave[6], R. Montaigut[8,45,48,63], J. Montier[52,53], E. Morelle[27], B. Morton[16], S. Mottola[51], R. Naves[67], J. Nomen[26], J. Oey[68], W. Ogłoza[38], M. Paiella[33], H. Pallares[28,69], A. Peyrot[58], F. Pilcher[70], J.-F. Pirenne[6], P. Piron[6], M. Polińska[4], M. Polotto[6], R. Poncy[71], J. P. Previt[53], F. Reignier[72], D. Renauld[6], D. Ricci[34], F. Richard[8,45], C. Rinner[73], V. Risoldi[33], D. Robilliard[53], D. Romeuf[74], G. Rousseau[75], R. Roy[76], J. Ruthroff[77], P. A. Salom[24,42], L. Salvador[6], S. Sanchez[26], T. Santana-Ros[4], A. Scholz[16], G. Séné[6], B. Skiff[78], K. Sobkowiak[4], P. Sogorb[79], F. Soldán[80], A. Spiridakis[35], E. Splanska[6], S. Sposetti[81], D. Starkey[82], R. Stephens[83], A. Stiepen[34], R. Stoss[26], J. Strajnic[6], J.-P. Teng[58], G. Tumolo[84], A. Vagnozzi[33], B. Vanoutryve[6], J. M. Vugnon[8,45], B. D. Warner[83], M. Waucomont[6], O. Wertz[34], M. Winiarski[38,†], and M. Wolf[3]

(Affiliations can be found after the references)

Received 24 September 2015 / Accepted 22 October 2015

ABSTRACT

Context. Asteroid modeling efforts in the last decade resulted in a comprehensive dataset of almost 400 convex shape models and their rotation states. These efforts already provided deep insight into physical properties of main-belt asteroids or large collisional families. Going into finer detail (e.g., smaller collisional families, asteroids with sizes $\lesssim$20 km) requires knowledge of physical parameters of more objects.

Aims. We aim to increase the number of asteroid shape models and rotation states. Such results provide important input for further studies, such as analysis of asteroid physical properties in different populations, including smaller collisional families, thermophysical modeling, and scaling shape models by disk-resolved images, or stellar occultation data. This provides bulk density estimates in combination with known masses, but also constrains theoretical collisional and evolutional models of the solar system.

Methods. We use all available disk-integrated optical data (i.e., classical dense-in-time photometry obtained from public databases and through a large collaboration network as well as sparse-in-time individual measurements from a few sky surveys) as input for the convex inversion method, and derive 3D shape models of asteroids together with their rotation periods and orientations of rotation axes. The key ingredient is the support of more that 100 observers who submit their optical data to publicly available databases.

Results. We present updated shape models for 36 asteroids, for which mass estimates are currently available in the literature, or for which masses will most likely be determined from their gravitational influence on smaller bodies whose orbital deflections will be observed by the ESA *Gaia* astrometric mission. Moreover, we also present new shape model determinations for 250 asteroids, including 13 Hungarias and three near-Earth asteroids. The shape model revisions and determinations were enabled by using additional optical data from recent apparitions for shape optimization.

Key words. minor planets, asteroids: general – techniques: photometric – methods: observational – methods: numerical

169

† Deceased.

1. Introduction

Asteroid modeling efforts in the last decade resulted in an extensive dataset of almost 400 convex shape models and rotation states (see the review by Ďurech et al. 2015a). The majority of these models was determined by the lightcurve inversion method (LI) developed by Kaasalainen & Torppa (2001) and Kaasalainen et al. (2001). About 100 models are based on disk-integrated, dense-in-time optical data (e.g., Torppa et al. 2003; Slivan et al. 2003; Michałowski et al. 2005; Marciniak et al. 2009, 2011). Combining dense-in-time data with sparse-in-time measurements from large sky surveys, or using only sparse-in-time data, increased the number of available shape models by a factor of 4 (Ďurech et al. 2009; Hanuš et al. 2011, 2013a,c). Future data from *Gaia*, Panoramic Survey Telescope and Rapid Response System (PanSTARRS), and Large Synoptic Survey Telescope (LSST) should result in an increase of shape models by an order of at least one magnitude (Ďurech et al. 2005). The methods that will be used for analysis of these future data of unprecedented amount and quality, by the means of complex shape modeling, are similar to those applied here and developed within the scope of our recent studies.

Most asteroid shape models derived by the LI method and their optical data are available in the Database of Asteroid Models from Inversion Techniques (DAMIT[1]; Ďurech et al. 2010).

We would like to emphasize and acknowledge that the shape modeling stands on the shoulders of hundreds of observers, often amateurs, who regularly obtain photometric data with their small and mid-sized telescopes. These observations have significantly contributed to the great progress of the shape modeling field in the last decade. Although there is much more sparse than dense data available, the latter will always remain important because their much higher photometric accuracy and rotation coverage leads to higher quality shape models. This is a typical example of the great interaction between the professional and amateur community (Mousis et al. 2014).

Knowing the rotational parameters and shapes of asteroids is very important for numerous applications. The large amount of currently known asteroid models already provided a deep insight into physical properties of main-belt asteroids (MBAs) and large collisional families: (i) an excess of prograde rotators within (MBAs) larger than ~50 km in diameter, predicted by numerical simulations (Johansen & Lacerda 2010), was confirmed by Kryszczyńska et al. (2007), Hanuš et al. (2011); (ii) an excess of retrograde rotators within near-Earth asteroids (NEAs) is consistent with the fact that most of the NEAs come from the ν_6 resonance (La Spina et al. 2004). To enter the ν_6 resonance via Yarkovsky effect[2], the object must be a retrograde rotator; (iii) an anisotropy of spin-axis directions of MBAs asteroids with diameters $\lesssim$30 km and NEAs was revealed and explained by the YORP effect[3], collisions, and mass shedding (Hanuš et al. 2011; Pravec et al. 2012); (iv) a bimodality of prograde and retrograde rotators symmetric with respect to the center of the family is caused by the combined Yarkovsky, YORP, and collisional dynamical evolution (Kryszczyńska 2013; Hanuš et al. 2013a); (v) the larger dispersion of spin-axis directions of smaller ($D \lesssim 50$ km) prograde than retrograde asteroids suggests that spin states of prograde rotators are affected by resonances (Hanuš et al. 2013c); or (vi) the disruption of asteroid pairs[4] was most likely the outcome of the YORP effect that spun up the original asteroid (Polishook 2014).

With the use of convex shape models in combination with asteroidal stellar occultations and disk-resolved images obtained by space telescopes or ground-based telescopes equipped with adaptive optics (AO) systems, the size of the model can be constrained, making it possible to determine the asteroid volume. Even when the object is considerably nonconvex, the scaled convex model from occultations and AO data tends to compensate by average fitting to the disk-resolved data. As a result, the overestimation of the volume is smaller than would correspond to the convex hull. The volume can then provide, in combination with mass estimates, realistic values of bulk densities (Ďurech et al. 2011; Hanuš et al. 2013b).

The mass is one of the most challenging parameters to measure for an asteroid. Mass estimates are now available for 280 asteroids, but only 113 of these are more precise than 20% (Carry 2012; Scheeres et al. 2015). However, the situation is expected to improve significantly in the near future. The observations of the ESA *Gaia* astrometric satellite will provide masses accurate to better than 50% for ≈150 asteroids (and for ≈50 with an accuracy better than 10%; Mouret et al. 2007, 2008) by the orbit deflection method. The advantage of the masses determined by *Gaia* is in the uniqueness of the mission: we should obtain a comprehensive sample with well-described biases (e.g., the current mass estimates are currently strongly biased toward the inner main belt).

To maximize the possible outcome by means of density determinations, we focus on determination of shape models for asteroids for which accurate mass estimates are available or will most likely be determined by *Gaia*. Moreover, it is also important to update shape models for such asteroids using recently obtained optical data. By doing this, we can provide better constraints on the rotational phase (i.e., on the asteroid orientation, which is important for scaling the size) of these asteroids due to the improvement of the rotation period, and more accurate rotation state and shape parameters.

Convex models, together with thermal infrared observations, have also been used as inputs for thermophysical modeling, enabling the determination of geometric visible albedo, size, and surface properties (e.g., Müller et al. 2011; Hanuš et al. 2015). This application is particularly important because it can make use of the large sample of infrared data for more than 100 000 asteroids acquired by the NASA's Wide-field Infrared Survey Explorer (WISE). The missing input here is shape models of sufficient quality (Delbo et al. 2015).

Moreover, convex models or at least rotational states are usually necessary inputs for more complex shape modeling, which can be performed if additional data, such as stellar occultations, AO images or interferometry containing information about the nonconvexities, (Kaasalainen & Viikinkoski 2012; Carry et al. 2010a,b, 2012; Viikinkoski et al. 2015; Tanga et al. 2015) are available.

Finally, large flat areas/facets on convex shape models, represented by polyhedra, usually indicate possible concavities

[1] http://astro.troja.mff.cuni.cz/projects/asteroids3D

[2] A thermal recoil force affecting rotating asteroids (Bottke et al. 2001).

[3] Yarkovsky–O'Keefe–Radzievskii–Paddack effect, a torque caused by the recoil force from anisotropic thermal emission, can alter the rotational periods and orientation of spin axes; see, e.g., Rubincam (2000), Vokrouhlický et al. (2003).

[4] An asteroid pair consists of two unbound objects with almost identical heliocentric orbital elements that were originally part of a bound system.

(Devogèle et al. 2015). Candidates for highly irregular bodies can be identified for further studies.

In Sect. 2, we introduce the dense- and sparse-in-time optical disk-integrated data, which we used for the shape model determinations. We describe the lightcurve (convex) inversion method in Sect. 3, present updated and new shape model determinations in Sects. 4.1 and 4.2, comment on several individual solutions in Sect. 4.3, and conclude our work in Sect. 5.

2. Optical disk-integrated photometry

Similar to Hanuš et al. (2011, 2013a,c), we use two different types of optical disk-integrated data: (i) dense-in-time photometry, i.e., classical continuous multihour observations; and (ii) sparse-in-time photometry consisting of a few hundred individual calibrated measurements from several astrometric observatories, typically covering ~15 years.

Dense photometry was acquired from publicly available databases, from those of our collaborators, or directly from several individual observers. The historical data from the second half of the twentieth Century are mainly stored in the Asteroid Photometric Catalogue (APC[5]; Piironen et al. 2001). Currently, the common practice, which is used mostly by observers from the United States, is a regular data submission to the Minor Planet Center in the Asteroid Lightcurve Data Exchange Format (ALCDEF[6]; Warner et al. 2011). These data are publicly available and often also published in the Minor Planet Bulletin[7], where the synodic rotation period is reported. Many European observers send their data to the Courbes de rotation d'astéroïdes et de comètes database (CdR[8]), maintained by Raoul Behrend at Observatoire de Genève. Composite lightcurves with best-fitting synodic rotation periods are then published on the web page.

We obtained the first type of sparse-in-time photometric data for this study from the AstDyS site (Asteroids – Dynamic Site[9]) and processed the data according to Hanuš et al. (2011). We solely employ sparse data from the USNO-Flagstaff station (IAU code 689) and the Catalina Sky Survey Observatory (IAU code 703, Larson et al. 2003), weighting them with respect to dense data (unity weight) by 0.3 and 0.15, respectively. As an alternative to this type of sparse-in-time data, we use the Lowell Photometric Database (Oszkiewicz et al. 2011; Bowell et al. 2014). The photometry from several astrometric surveys, including both USNO-Flagstaff and Catalina Sky Survey, reported to the Minor Planet Center (MPC), was reprocessed; e.g., systematic effects in the magnitude calibration were removed. This enormous dataset typically consists of several hundreds of individual measurements for each of the ~320 000 asteroids that were processed so far. Although the accuracy of the recalibrated photometry is improved, the dataset for each asteroid is still a mixture of measurements from several observatories with different photometric quality. Compared to the data of USNO-Flagstaff and Catalina observatories downloaded from AstDyS, Lowell data provide an increased quantity of measurements from more observing geometries. These data, however, are, on average, of poor photometric quality, as they also contain measurements from observatories that were originally rejected in Hanuš et al. (2011) owing to low accuracy. We assigned to Lowell data the weight of 0.1. A subset of Lowell data was already analyzed by Ďurech et al. (2013) and a complex analysis of the reliability of shape models, based solely on these data, is underway (Ďurech et al. 2016). On top of that, the volunteer project Asteroids at home[10], which makes use of distributed computing and runs in the framework of Berkeley Open Infrastructure for Network Computing (BOINC), currently employs shape model computations based on Lowell data (Ďurech et al. 2015b). Thousands of individual home computational stations of volunteers are currently participating in the project.

Tables 1 and A.1 include the information about the optical data used for the shape model determination, such as the number of dense-in-time lightcurves and apparitions covered by dense-in-time observations and the number of sparse-in-time measurements from corresponding astrometric surveys. Table A.2 provides references to the dense data used for the shape model determinations and Table A.3 links the observers to their observatories.

3. Convex inversion and reproducibility

In this work, we use the lightcurve inversion method of Kaasalainen & Torppa (2001) and Kaasalainen et al. (2001), which is already a well-documented, investigated, and employed technique for asteroid shape modeling (for more details, see the review by Ďurech et al. 2015a).

The main advantage of using convex inversion is that convex models are usually the only stable or unambiguous inversion result (Ďurech & Kaasalainen 2003); they best portray the resolution level or information content of disk-integrated photometry. To demonstrate this more intuitively, consider an asteroid with a large planar region (or many regions) on the surface (e.g., an ellipsoid with a sizable chunk or chunks chopped off), and a large crater (say, half the size of the plane) at one end of the plane. Then it is impossible to tell from lightcurve data (no matter how large solar phase angles, i.e., shadows) where the crater is in the plane, or whether it is two craters half the size, or even myriads of small craters on the surface that have the same combined area as the big one (even if the crater filled most of the plane). In other words, one simply cannot say whether the lightcurves are caused just by small-scale surface roughness on a convex shape, or by huge nonconvexities that would be obvious in any disk-resolved data. Hence, any nonconvex model from disk-integrated photometric data is inevitably ambiguous, while the convex model is unambiguous. This also explains why the assumption of the nonconvexity represented by a large plane in the convex model (e.g., Devogèle et al. 2015), while often a good guess because of physical constraints, cannot usually be more than an assumption.

Convex inversion was successfully used for shape model determinations of almost 400 asteroids. On top of that, several convex models were validated by disk-resolved and delay-Doppler images or by direct comparison with images obtained by space probes (e.g., Kaasalainen et al. 2001; Carry et al. 2012). The parameter space of shape, rotation period, spin vector orientation, and scattering properties (simple three-parameter empirical model) is systematically investigated in the means of a χ^2-metric

$$\chi^2 = \sum_i \frac{\left\| L_{\mathrm{OBS}}^{(i)} - L_{\mathrm{MOD}}^{(i)} \right\|}{\sigma_i^2}, \quad (1)$$

[5] http://asteroid.astro.helsinki.fi/
[6] http://www.minorplanet.info/alcdef.html
[7] http://www.minorplanet.info/minorplanetbulletin.html
[8] http://obswww.unige.ch/~behrend/page_cou.html
[9] http://hamilton.dm.unipi.it/
[10] https://asteroidsathome.net/

Table 1. Rotational states and summary of used photometry for asteroids for which we updated their shape models based on new disk-integrated optical data.

Asteroid	λ_1 [deg]	β_1 [deg]	λ_2 [deg]	β_2 [deg]	P [h]	$N_{\rm lc}$	$N_{\rm app}$	$N_{\rm LOW}$	Original model published by
3 Juno	104	20			7.209532	38	11	332	Kaasalainen et al. (2002)
7 Iris	19	19	198	5	7.138843	39	14	372	Kaasalainen et al. (2002)
16 Psyche	32	−7			4.195948	118	19	567	Kaasalainen et al. (2002)
17 Thetis	240	22			12.26603	57	10	690	Ďurech et al. (2009)
19 Fortuna	96	56			7.44322	48	11	565	Torppa et al. (2003)
20 Massalia	304	76	124	81	8.09759	36	9	380	Kaasalainen et al. (2002)
22 Kalliope	196	4			4.148201	102	17	343	Kaasalainen et al. (2002)
23 Thalia	159	−40			12.31241	50	12	466	Torppa et al. (2003)
27 Euterpe	82	44	265	39	10.40193	54	6		Stephens et al. (2012)
29 Amphitrite	136	−20			5.390119	66	15	323	Kaasalainen et al. (2002)
39 Laetitia	322	30			5.138238	68	26	448	Kaasalainen et al. (2002)
40 Harmonia	22	34			8.90848	23	7	405	Hanuš et al. (2011)
41 Daphne	199	−30			5.98798	33	8	508	Kaasalainen et al. (2002)
42 Isis	113	45			13.58364	31	8	499	Hanuš et al. (2011)
45 Eugenia	125	−34			5.699151	101	16	574	Hanuš et al. (2013b)
54 Alexandra	152	19			7.02264	38	8	506	Warner et al. (2008b)
64 Angelina	135	6	315	5	8.75171	24	4	450	Ďurech et al. (2011)
76 Freia	138	12	319	17	9.97306	57	12	463	Marciniak et al. (2012)
87 Sylvia	82	64			5.183641	55	12	545	Kaasalainen et al. (2002), Berthier et al. (2014)
88 Thisbe	82	69			6.04132	28	8	554	Torppa et al. (2003)
94 Aurora	65	9	242	−7	7.22619	22	8	550	Marciniak et al. (2011)
95 Arethusa	119	23			8.70221	15	2	417	Ďurech et al. (2011)
107 Camilla	72	51			4.843928	34	10	543	Torppa et al. (2003)
110 Lydia	148	−39	340	−57	10.92581	53	11	398	Ďurech et al. (2007)
121 Hermione	1	16			5.550881	48	9	536	Descamps et al. (2009)
129 Antigone	211	55			4.957160	52	11	535	Torppa et al. (2003)
130 Elektra	176	−89			5.224663	56	13	358	Ďurech et al. (2007)
354 Eleonora	162	43			4.277184	64	13	482	Hanuš et al. (2011)
360 Carlova	3	56	143	67	6.18959	9	4	435	Ďurech et al. (2009)
372 Palma	234	−5	51	54	8.57964	38	8	406	Hanuš et al. (2011)
386 Siegena	289	25			9.76503	83	12	460	Marciniak et al. (2012)
409 Aspasia	2	28			9.02145	22	8	438	Warner et al. (2008b), Hanuš et al. (2013b)
423 Diotima	351	4			4.775377	58	12	540	Ďurech et al. (2007)
511 Davida	298	22			5.129365	58	17	588	Torppa et al. (2003)
532 Herculina	100	9			9.40494	74	11	410	Kaasalainen et al. (2002)
776 Berbericia	346	25			7.66701	59	11	402	Ďurech et al. (2007)

Notes. We also provide the reference to the original model and in two cases to the plausible non-convex model as well. The table gives ecliptic coordinates λ_1 and β_1 of the best-fitting pole solution, ecliptic coordinates λ_2 and β_2 for the possible second (mirror) pole solution, sidereal rotational period P, the number of dense lightcurves $N_{\rm lc}$ spanning $N_{\rm app}$ apparitions, the number of sparse-in-time measurements from Lowell $N_{\rm LOW}$, and the reference to the original model.

where the ith brightness measurement $L^{(i)}_{\rm OBS}$ (with an uncertainty of σ_i) is compared to the corresponding modeled brightness $L^{(i)}_{\rm MOD}$. The best-fitting parameter set is searched for.

A significant minimum in the parameter space indicates a unique solution. Visual examination of the fit in the period subspace is performed as well as the comparison between observed and modeled lightcurves. Additionally, the pole-ecliptic latitudes should be similar within the two pole solutions, which are typically determined as a result of the ambiguity (symmetry) presented in most lightcurve inversion models (Kaasalainen & Lamberg 2006). On the other hand, the pole-ecliptic longitudes of these so-called mirror solutions should differ by ~180 degrees. The pole ambiguity is present in the majority of our shape models.

Moreover, we also compute the principal moments of inertia of each shape model, assuming a homogeneous mass distribution, and compare these moments with the moment of inertia along the rotation axis. A reliable solution should rotate within ~10–20 degrees of the axis with the largest moment of inertia.

If available, we use a priori information about the rotation period of the asteroid from the Minor Planet Lightcurve Database[11] (Warner et al. 2009) to significantly reduce, usually by at least two orders of magnitude, computation requirements. Hence, we investigate the parameter space only in the proximity of the expected rotation period.

It should be kept in mind that none of the shape models should be taken as granted, i.e., each asteroid model contains an uncertainty (both in shape and rotation state), which increases with decreasing amount, variety, and quality of the optical data. It was already shown in Hanuš et al. (2015) that by varying a shape model within its uncertainty, one can obtain significantly different fits to the thermal infrared data by the thermophysical modeling. Thus, the shape uncertainty plays an important role for the interpretation of the thermal infrared data. This demonstrates the need of accounting for the shape model uncertainties

172

[11] http://cfa-www.harvard.edu/iau/lists/Lightcurve\discretionary-Dat.html

in all further shape model applications. Also, the overall shape model based mostly on sparse data usually contains many flat facets (areas) with rather sharp edges, thus most of the low-detail topography is hidden (i.e., we have a large uncertainty in the shape). As we use more dense data, the shape becomes smoother and has more details. This limits the application of the lower-resolution shape models based mostly on sparse data.

In the ecliptic coordinate frame, the typical pole direction uncertainties are: (i) $\lesssim 5^\circ$ in latitude β and $\lesssim 5^\circ/\cos\beta$ in longitude λ for asteroid models based on large multiapparition dense lightcurve datasets; (ii) $\sim 5-10^\circ$ in β and $\sim 5-10^\circ/\cos\beta$ in λ for models based on combined multiapparition dense data and sparse-in-time measurements; and finally; (iii) $\sim 10-30^\circ$ in β and $\sim 10-30^\circ/\cos\beta$ in λ for models based on combined few-apparition dense data with sparse-in-time measurements or only sparse-in-time data.

To sum up, we follow the same procedure for the shape model determinations as in Hanuš et al. (2011, 2013a,c). Finally, we would like to emphasize that our work can be easily reproduced by anyone who is interested. The LI code and the lightcurve data are available in DAMIT, as well as the user manual.

4. Results and discussions

4.1. Updated shape models

We updated shape models of 36 asteroids with known mass estimates or for which masses will be most likely determined by the orbit deflection method from the *Gaia* astrometric observations (Mouret et al. 2007, 2008, and personal communication with François Mignard). For each one of these asteroids, there were new available optical dense data (see Table A.2). We combined these new data with Lowell data and the already available dense photometry from DAMIT. If applicable, we replaced the original sparse data from AstDyS with the Lowell data.

In most cases, rotational states of updated shape models are similar to those of the original models in the DAMIT database. The only exceptions, which we individually commented on in Sect. 4.3, are asteroids (27) Euterpe, and (532) Herculina. We performed the LI independently from any previous shape modeling results (e.g., we did not use information about the spin axis).

Updated models provide better constraints on the rotational phase, thus these models allow us, for example, to better link recently obtained AO and occultation profiles with the orientation of the shape model at the time of the observation. This is essential for a potential scaling of the sizes of shape models to compute the volume, and consequently bulk densities. Obviously, the uncertainties in rotation period, spin axis direction, and shape model should be improved as there are more data used for the modeling.

Optimized rotation state parameters and information about optical data are listed in Table 1. References to the optical dense-in-time data can be found in Table A.2.

4.2. New shape models

The majority of our new shape model determinations is obtained by combining dense-in-time data with sparse-in-time measurements from the Lowell database. However, the fact that Lowell data contain for each asteroid a mixture of measurements from several observatories makes it difficult to find a representative weight with respect to the dense data. Indeed, a specific single value of the weight can result in an overestimation for some asteroids, while it can underestimate others. Despite these issues, we decided to use a weight of 0.1 for the Lowell data as a whole and to present corresponding shape models. As a consequence, we sometimes obtained a unique shape solution if we combined dense data and the sparse data from AstDyS (i.e., from USNO and Catalina), but not if we used the Lowell data instead. We present these shape models as well.

Moreover, 57 out of 250 shape models are based only on sparse data from USNO-Flagstaff and Catalina Sky Survey observatories. That these models can nevertheless be reliable was already shown in Hanuš & Ďurech (2012) and Hanuš et al. (2013c). As suggested there, we ran the LI search for shape and rotation state parameters with two different shape resolutions: (i) standard one; and (ii) lower one, which serves as a test of the solution stability. For this case, the asteroid's synodic rotation period is also available in the Minor Planet Lightcurve Database (LCDB, Warner et al. 2009), an additional test for the reliability can be performed. A rotation period derived by the LI (a period interval of 2–1000 h is typically scanned), which matches that already reported, points to a secure solution. In practice, all shape solutions based solely on sparse data that fulfilled our stability tests had rotation periods in an agreement with synodic periods from LCDB. This also demonstrates that our other unique solutions, for which a previous period estimate is not available, are reliable. We present nine of these shape and rotation state solutions; these are labeled in Table A.1.

We present shape models of three NEAs, which all have negative values of their pole latitudes β, and obliquities larger than 90°. The fact that they all show retrograde rotation supports the consensus that about half of the NEAs migrated through the ν_6 secular resonance, which causes an observed excess of retrograde rotators (La Spina et al. 2004).

We further present shape models of 13 asteroids that are classified as Hungarias. The majority of them (10 out of 13) exhibit retrograde rotation, which is in an agreement with the findings of Warner et al. (2014), who reported, in a sample of 53 Hungarias, a 75% representation of retrograde rotators.

Thirty-one of the derived shape models are those asteroids whose density will be measured in future or was already obtained. While for some of them, estimations on their masses are already available, the masses of the others will be determined from *Gaia* astrometric measurements. Constraining the model sizes of these asteroids using disk-resolved images, stellar occultation data, or thermophysical modeling will directly facilitate estimation of bulk densities.

Rotation state parameters and information about used optical data for all new shape model determinations are listed in Table A.1. References to the optical dense-in-time data can be found in Table A.2.

4.3. Individual asteroids

(27) Euterpe. The lightcurve amplitude of this asteroid is very low ($\lesssim$0.1 mag) and the dense data cover multiple apparitions. Thus, we decided to exclude the Lowell data from the shape modeling because they were dominated by noise. Our derived rotation period (10.40193 h) is slightly different than that derived by Stephens et al. (2012) (10.40825 h), which resulted in a different pole solution of $(\lambda, \beta) = (82, 44)^\circ$ and $(\lambda, \beta) = (265, 39)^\circ$ for the mirror solution. The solution in longitude λ is similar to that of Stephens et al. (2012), but their latitude has a different sign (−39 and −30, respectively).

(532) Herculina. Our (single) pole solution only differs by ∼180° in longitude λ from that reported by Kaasalainen et al. (2002), thus it corresponds to their mirror solution. In contrast to their solution, our model is based on additional data from 2005 and 2010 apparitions.

(537) Pauly. The rotation period of 14.15 h from the LCDB is in contradiction with our shape modeling result: our period of 16.2961 h fits the data significantly better and thus is preferred.

(596) Scheila. The observations taken on December 11th, 2010 with the Catalina Schmidt telescope exhibited a comet-like appearance (Larson 2010). This behavior was later confirmed by Jewitt et al. (2011) from the HST observations on December 27th, 2010 and on January 4th, 2011 and interpreted as caused most likely by a collision with a 35m asteroid. All photometric data used for the shape modeling date prior to this event, so the shape model does not reflect any potential changes in the shape, period, or spin orientation induced by the collision (Bodewits et al. 2014).

(8567) 1996 HW_1. The shape model of this NEAs was already determined by Magri et al. (2011) from a combination of dense lightcurves and radar Doppler images. We derived a consistent shape model and rotational state solution from combined dense and sparse data. The main difference between these two models is the fact that the Doppler images contain nonconvex signatures that were translated into their shape model. Even if our shape model is purely convex, it reliably represents the overall shape of the real asteroid. This case once again demonstrates the reliability of the convex inversion method.

(9563) Kitty. We derived the shape model of this asteroid without knowledge of a previous period estimate. However, Chang et al. (2015) recently reported period $P = 5.35 \pm 0.03$ h based on the optical data from the Intermediate Palomar Transient Factory that is in perfect agreement with our independent determination of $P = 5.38191 \pm 0.00005$ h.

5. Conclusions

In this work, we updated shape models of 36 asteroids with mass estimates by including new optical dense-in-time data in the shape modeling. For 250 asteroids, including 13 Hungarias and three NEAs, we derived their convex shape models and rotation states from combined disk-integrated dense- and sparse-in-time photometric data or from only sparse-in-time data. This effort was achieved with the help of the community of ∼100 individual observers who shared their lightcurves. All new models are now included in the DAMIT database and are available to anyone for additional studies. For nine asteroids, we provide, together with shape models and pole orientations, their first rotation period estimates.

Our work is a typical example in which a contribution of hundreds of observers, who are regularly obtaining photometric data with their small and mid-sized telescopes, was necessary to achieve presented results. The initial motivation of the observers is to derive the synodic rotation period (sometimes this is an object of a publication in the Minor Planet Bulletin), however, the shape modeling provides a welcome additional opportunity for the usage of their optical data. We acknowledge all the observers who submit their observations to the public databases and invite others to do so as well. This practice allows us an easy and straightforward access to the data and largely avoids an overlook of the precious data.

The shape models can be used as inputs for various studies, such as spin-vector analysis, detection of concavities, thermophysical modeling with the varied-shape approach by Hanuš et al. (2015), nonconvex modeling, size optimization by disk-resolved images or occultation data, or density determinations.

Shape models based only on sparse data (or combined with a few dense lightcurves) are convenient candidates for follow-up observations, both to confirm the rotation periods and to improve the shape models, which is necessary, e.g., for thermophysical modeling. Finally, we maintain a web page with a list of asteroids, for which mass estimates are available and the shape model determination still requires additional photometric data (Hanuš 2015). These objects are candidates for accurate density determination and any lightcurve support is welcome.

Acknowledgements. J.H. greatly appreciates the CNES post-doctoral fellowship program. J.H. and M.D. were supported by the project under the contract 11-BS56-008 (SHOCKS) of the French Agence National de la Recherche (ANR), JD by grant GACR 15-04816S of the Czech Science Foundation, DO by the grant NCN 2012/S/ST9/00022 of Polish National Science Center, and A. Marciniak by grant 2014/13/D/ST9/01818 of Polish National Science Center. We thank the referee, Mikko Kaasalainen, for his thorough review of our manuscript and his constructive comments and suggestions that led to a significant improvement of the text. The computations have been carried out on the "Mesocentre" computers, hosted by the Observatoire de la Côte d'Azur, and on the computational cluster Tiger at the Astronomical Institute of Charles University in Prague (http://sirrah.troja.mff.cuni.cz/tiger). Data from Pic du Midi Observatory were partly obtained with the 0.6 m telescope, a facility operated by observatoire Midi-Pyrénées and Association T60, an amateur association. The Joan Oró Telescope (TJO) of the Montsec Astronomical Observatory (OAdM) is owned by the Catalan Government and operated by the Institute for Space Studies of Catalonia (IEEC). We thank Franck Pino (INO-AZ) and Lech Mankiewicz (EU-HOU/Comenius) for the remote access to Ironwood North.

References

Alkema, M. S. 2013a, Minor Planet Bulletin, 40, 133
Alkema, M. S. 2013b, Minor Planet Bulletin, 40, 68
Alton, K. B. 2011, Minor Planet Bulletin, 38, 8
Benishek, V. 2014, Minor Planet Bulletin, 41, 126
Berthier, J., Vachier, F., Marchis, F., Ďurech, J., & Carry, B. 2014, Icarus, 239, 118
Bodewits, D., Vincent, J.-B., & Kelley, M. S. P. 2014, Icarus, 229, 190
Bottke, W. F., Vokrouhlický, D., Brož, M., Nesvorný, D., & Morbidelli, A. 2001, Science, 294, 1693
Bowell, E., Oszkiewicz, D. A., Wasserman, L. H., et al. 2014, Meteor. Planet. Sci., 49, 95
Brinsfield, J. W. 2007a, Minor Planet Bulletin, 34, 58
Brinsfield, J. W. 2007b, Minor Planet Bulletin, 34, 108
Brinsfield, J. W. 2008a, Minor Planet Bulletin, 35, 179
Brinsfield, J. W. 2008b, Minor Planet Bulletin, 35, 86
Brinsfield, J. W. 2009, Minor Planet Bulletin, 36, 64
Brinsfield, J. W. 2010a, Minor Planet Bulletin, 37, 19
Brinsfield, J. W. 2010b, Minor Planet Bulletin, 37, 50
Brinsfield, J. W. 2011, Minor Planet Bulletin, 38, 73
Brinsfield, J. W. 2012, Minor Planet Bulletin, 39, 55
Buchheim, R. K. 2005, Minor Planet Bulletin, 32, 79
Buchheim, R. K. 2007, Minor Planet Bulletin, 34, 13
Buchheim, R. K. 2014, Minor Planet Bulletin, 41, 241
Cantu, S., Adolphson, M., Montgomery, K., & Renshaw, T. 2015, Minor Planet Bulletin, 42, 28
Carry, B. 2012, Planet. Space Sci., 73, 98
Carry, B., Dumas, C., Kaasalainen, M., et al. 2010a, Icarus, 205, 460
Carry, B., Kaasalainen, M., Leyrat, C., et al. 2010b, A&A, 523, A94
Carry, B., Kaasalainen, M., Merline, W. J., et al. 2012, Planet. Space Sci., 66, 200
Chang, C.-K., Ip, W.-H., Lin, H.-W., et al. 2015, ApJS, 219, 27
Clark, M. 2010, Minor Planet Bulletin, 37, 89
Delbo, M., Mueller, M., Emery, J., Rozitis, B., & Capria, M. T. 2015, Asteroids IV, in press
Descamps, P., Marchis, F., Durech, J., et al. 2009, Icarus, 203, 88
Devogèle, M., Rivet, J. P., Tanga, P., et al. 2015, MNRAS, 453, 2232
Ďurech, J., & Kaasalainen, M. 2003, A&A, 404, 709
Ďurech, J., Grav, T., Jedicke, R., Denneau, L., & Kaasalainen, M. 2005, Earth Moon Planets, 97, 179
Ďurech, J., Kaasalainen, M., Marciniak, A., et al. 2007, A&A, 465, 331

Ďurech, J., Kaasalainen, M., Warner, B. D., et al. 2009, A&A, 493, 291
Ďurech, J., Sidorin, V., & Kaasalainen, M. 2010, A&A, 513, A46
Ďurech, J., Kaasalainen, M., Herald, D., et al. 2011, Icarus, 214, 652
Ďurech, J., Hanuš, J., Vančo, R., Oszkiewicz, D., & Bowell, E. 2013, in AAS/Division for Planetary Sciences Meeting Abstracts, 45, 304.05
Ďurech, J., Carry, B., Delbo, M., Kaasalainen, M., & Viikinkoski, M. 2015a, Asteroids IV, in press
Ďurech, J., Hanuš, J., & Vančo, R. 2015b, Astronomy and Computing, 13, 80
Ďurech, J., Hanuš, J., Oszkiewicz, D., & Vančo, R. 2016, A&A, in press, DOI: 10.1051/0004-6361/201527573
Ferrero, A., Klinglesmith, III, D. K., & Pilcher, F. 2014, Minor Planet Bulletin, 41, 33
Hanuš, J. 2015, Minor Planet Bulletin, 42, 208
Hanuš, J., & Ďurech, J. 2012, Planet. Space Sci., 73, 75
Hanuš, J., Ďurech, J., Brož, M., et al. 2011, A&A, 530, A134
Hanuš, J., Brož, M., Ďurech, J., et al. 2013a, A&A, 559, A134
Hanuš, J., Marchis, F., & Ďurech, J. 2013b, Icarus, 226, 1045
Hanuš, J., Ďurech, J., Brož, M., et al. 2013c, A&A, 551, A67
Hanuš, J., Delbo, M., Ďurech, J., & Alí-Lagoa, V. 2015, Icarus, 256, 101
Higgins, D. 2008, Minor Planet Bulletin, 35, 30
Higgins, D., & Goncalves, R. M. D. 2007, Minor Planet Bulletin, 34, 16
Higgins, D., & Pilcher, F. 2009, Minor Planet Bulletin, 36, 143
Higgins, D., & Warner, B. D. 2009, Minor Planet Bulletin, 36, 159
Higgins, D., Pravec, P., Kusnirak, P., et al. 2006a, Minor Planet Bulletin, 33, 89
Higgins, D., Pravec, P., Kusnirak, P., et al. 2006b, Minor Planet Bulletin, 33, 8
Higgins, D., Pravec, P., Kusnirak, P., Reddy, V., & Dyvig, R. 2006c, Minor Planet Bulletin, 33, 64
Jehin, E., Gillon, M., Queloz, D., et al. 2011, The Messenger, 145, 2
Jewitt, D., Weaver, H., Mutchler, M., Larson, S., & Agarwal, J. 2011, ApJ, 733, L4
Johansen, A., & Lacerda, P. 2010, MNRAS, 404, 475
Kaasalainen, M., & Lamberg, L. 2006, Inverse Problems, 22, 749
Kaasalainen, M., & Torppa, J. 2001, Icarus, 153, 24
Kaasalainen, M., & Viikinkoski, M. 2012, A&A, 543, A97
Kaasalainen, M., Torppa, J., & Muinonen, K. 2001, Icarus, 153, 37
Kaasalainen, M., Torppa, J., & Piironen, J. 2002, Icarus, 159, 369
Klinglesmith, III, D. A., Hanowell, J., Risley, E., et al. 2014, Minor Planet Bulletin, 41, 139
Klinglesmith, D. A., DeHart, A., Hanowell, J., & Hendrickx, S. 2015, Minor Planet Bulletin, 42, 101
Koff, R. A. 2001, Minor Planet Bulletin, 28, 77
Koff, R. A. 2002, Minor Planet Bulletin, 29, 25
Koff, R. A. 2004, Minor Planet Bulletin, 31, 58
Koff, R. A. 2005, Minor Planet Bulletin, 32, 32
Koff, R. A. 2006, Minor Planet Bulletin, 33, 31
Koff, R. A., & Brincat, S. M. 2000, Minor Planet Bulletin, 27, 49
Koff, R. A., & Brincat, S. M. 2001, Minor Planet Bulletin, 28, 67
Koff, R. A., Brincat, S. M., Stephens, R. D., & Pravec, P. 2001, Minor Planet Bulletin, 28, 46
Kryszczyńska, A. 2013, A&A, 551, A102
Kryszczyńska, A., La Spina, A., Paolicchi, P., et al. 2007, Icarus, 192, 223
La Spina, A., Paolicchi, P., Kryszczyńska, A., & Pravec, P. 2004, Nature, 428, 400
Larson, S. M. 2010, IAU Circ., 9188, 1
Larson, S., Beshore, E., Hill, R., et al. 2003, in BAAS, 35, AAS/Division for Planetary Sciences Meeting Abstracts 35, 982
Magri, C., Howell, E. S., Nolan, M. C., et al. 2011, Icarus, 214, 210
Marchis, F., Lainey, V., Descamps, P., et al. 2010, Icarus, 210, 635
Marciniak, A., Michałowski, T., Hirsch, R., et al. 2009, A&A, 498, 313
Marciniak, A., Michałowski, T., Polińska, M., et al. 2011, A&A, 529, A107
Marciniak, A., Bartczak, P., Santana-Ros, T., et al. 2012, A&A, 545, A131
Martinez, L. E. 2012, Minor Planet Bulletin, 39, 25
Michałowski, T., Kaasalainen, M., Marciniak, A., et al. 2005, A&A, 443, 329
Miles, R., & Warner, B. D. 2009, Minor Planet Bulletin, 36, 66
Mouret, S., Hestroffer, D., & Mignard, F. 2007, A&A, 472, 1017
Mouret, S., Hestroffer, D., & Mignard, F. 2008, Planet. Space Sci., 56, 1819
Mousis, O., Hueso, R., Beaulieu, J.-P., et al. 2014, Exp. Astron., 38, 91
Müller, T. G., Ďurech, J., Hasegawa, S., et al. 2011, A&A, 525, A145
Oey, J. 2006, Minor Planet Bulletin, 33, 96
Oey, J. 2008, Minor Planet Bulletin, 35, 132
Oey, J. 2009a, Minor Planet Bulletin, 36, 4
Oey, J. 2009b, Minor Planet Bulletin, 36, 162
Oey, J., Vilagi, J., Gajdos, S., Kornos, L., & Galad, A. 2007, Minor Planet Bulletin, 34, 81
Oey, J., Pilcher, F., Benishek, V., Higgins, D., & Pravec, P. 2012, Minor Planet Bulletin, 39, 86
Oszkiewicz, D. A., Muinonen, K., Bowell, E., et al. 2011, J. Quant. Spectr. Rad. Transf., 112, 1919
Owings, L. E. 2009, Minor Planet Bulletin, 36, 51
Owings, L. E. 2013a, Minor Planet Bulletin, 40, 104
Owings, L. E. 2013b, Minor Planet Bulletin, 40, 8
Piironen, J., Lagerkvist, C., Torppa, J., Kaasalainen, M., & Warner, B. 2001, in BAAS, 33, 1562
Pilcher, F. 2008a, Minor Planet Bulletin, 35, 51
Pilcher, F. 2008b, Minor Planet Bulletin, 35, 71
Pilcher, F. 2008c, Minor Planet Bulletin, 35, 135
Pilcher, F. 2009a, Minor Planet Bulletin, 36, 133
Pilcher, F. 2009b, Minor Planet Bulletin, 36, 25
Pilcher, F. 2009c, Minor Planet Bulletin, 36, 100
Pilcher, F. 2010a, Minor Planet Bulletin, 37, 98
Pilcher, F. 2010b, Minor Planet Bulletin, 37, 167
Pilcher, F. 2010c, Minor Planet Bulletin, 37, 119
Pilcher, F. 2010d, Minor Planet Bulletin, 37, 148
Pilcher, F. 2010e, Minor Planet Bulletin, 37, 45
Pilcher, F. 2010f, Minor Planet Bulletin, 37, 21
Pilcher, F. 2011a, Minor Planet Bulletin, 38, 183
Pilcher, F. 2011b, Minor Planet Bulletin, 38, 76
Pilcher, F. 2011c, Minor Planet Bulletin, 38, 50
Pilcher, F. 2011d, Minor Planet Bulletin, 38, 156
Pilcher, F. 2012a, Minor Planet Bulletin, 39, 57
Pilcher, F. 2012b, Minor Planet Bulletin, 39, 220
Pilcher, F. 2013a, Minor Planet Bulletin, 40, 33
Pilcher, F. 2013b, Minor Planet Bulletin, 40, 189
Pilcher, F. 2013c, Minor Planet Bulletin, 40, 85
Pilcher, F. 2013d, Minor Planet Bulletin, 40, 161
Pilcher, F. 2014a, Minor Planet Bulletin, 41, 155
Pilcher, F. 2014b, Minor Planet Bulletin, 41, 47
Pilcher, F. 2014c, Minor Planet Bulletin, 41, 250
Pilcher, F. 2015a, Minor Planet Bulletin, 42, 190
Pilcher, F. 2015b, Minor Planet Bulletin, 42, 280
Pilcher, F. 2015c, Minor Planet Bulletin, 42, 91
Pilcher, F., & Franco, L. 2014, Minor Planet Bulletin, 41, 35
Pilcher, F., & Higgins, D. 2011, Minor Planet Bulletin, 38, 32
Pilcher, F., & Jardine, D. 2009, Minor Planet Bulletin, 36, 52
Pilcher, F., Benishek, V., Delos, S., et al. 2012a, Minor Planet Bulletin, 39, 46
Pilcher, F., Delos, S., Ahrendts, G., & Barker, T. 2012b, Minor Planet Bulletin, 39, 204
Pilcher, F., Ferrero, A., & Oey, J. 2012c, Minor Planet Bulletin, 39, 228
Pilcher, F., Alvarez, E. M., Ferrero, A., et al. 2014, Minor Planet Bulletin, 41, 70
Pilcher, F., Ferrero, A., Klinglesmith, III, D. A., & Hanowell, J. 2015, Minor Planet Bulletin, 42, 90
Polishook, D. 2009, Minor Planet Bulletin, 36, 119
Polishook, D. 2014, Icarus, 241, 79
Polishook, D., Ofek, E. O., Waszczak, A., et al. 2012, MNRAS, 421, 2094
Pravec, P., Wolf, M., & Šarounová, L. 1998, Icarus, 136, 124
Pravec, P., Scheirich, P., Vokrouhlický, D., et al. 2012, Icarus, 218, 125
Pray, D. P. 2004a, Minor Planet Bulletin, 31, 34
Pray, D. P. 2004b, Minor Planet Bulletin, 31, 6
Rubincam, D. P. 2000, Icarus, 148, 2
Ruthroff, J. C. 2010, Minor Planet Bulletin, 37, 158
Ruthroff, J. C. 2011, Minor Planet Bulletin, 38, 86
Scheeres, D. J., Britt, D., Carry, B., & Holsapple, K. A. 2015, Asteroids IV. In press
Shevchenko, V. G., Chiorny, V. G., Gaftonyuk, N. M., et al. 2008, Icarus, 196, 601
Skiff, B. A., Bowell, E., Koehn, B. W., et al. 2012, Minor Planet Bulletin, 39, 111
Slivan, S. M., Binzel, R. P., Crespo da Silva, L. D., et al. 2003, Icarus, 162, 285
Stephens, R. D. 2001, Minor Planet Bulletin, 28, 5
Stephens, R. D. 2003, Minor Planet Bulletin, 30, 1
Stephens, R. D. 2005, Minor Planet Bulletin, 32, 2
Stephens, R. D. 2006, Minor Planet Bulletin, 33, 100
Stephens, R. D. 2007a, Minor Planet Bulletin, 34, 31
Stephens, R. D. 2007b, Minor Planet Bulletin, 34, 102
Stephens, R. D. 2007c, Minor Planet Bulletin, 34, 64
Stephens, R. D. 2008, Minor Planet Bulletin, 35, 60
Stephens, R. D. 2009, Minor Planet Bulletin, 36, 59
Stephens, R. D. 2010a, Minor Planet Bulletin, 37, 28
Stephens, R. D. 2010b, Minor Planet Bulletin, 37, 122
Stephens, R. D. 2012, Minor Planet Bulletin, 39, 226
Stephens, R. D. 2013, Minor Planet Bulletin, 40, 92
Stephens, R. D. 2014a, Minor Planet Bulletin, 41, 92
Stephens, R. D. 2014b, Minor Planet Bulletin, 41, 226
Stephens, R. D. 2014c, Minor Planet Bulletin, 41, 171
Stephens, R. D. 2015a, Minor Planet Bulletin, 42, 70
Stephens, R. D. 2015b, Minor Planet Bulletin, 42, 104

Stephens, R. D., & Warner, B. D. 2008, Minor Planet Bulletin, 35, 84
Stephens, R. D., & Warner, B. D. 2013, Minor Planet Bulletin, 40, 93
Stephens, R. D., Malcolm, G., Koff, R. A., Brincat, S. M., & Warner, B. 2001, Minor Planet Bulletin, 28, 1
Stephens, R. D., Warner, B. D., Megna, R., & Coley, D. 2012, Minor Planet Bulletin, 39, 2
Stephens, R. D., Coley, D., & Warner, B. D. 2014, Minor Planet Bulletin, 41, 8
Strabla, L., Quadri, U., & Girelli, R. 2011, Minor Planet Bulletin, 38, 169
Strabla, L., Quadri, U., & Girelli, R. 2012, Minor Planet Bulletin, 39, 177
Strabla, L., Quadri, U., & Girelli, R. 2013, Minor Planet Bulletin, 40, 232
Tanga, P., Carry, B., Colas, F., et al. 2015, MNRAS, 448, 3382
Torppa, J., Kaasalainen, M., Michałowski, T., et al. 2003, Icarus, 164, 346
Viikinkoski, M., Kaasalainen, M., & Durech, J. 2015, A&A, 576, A8
Vokrouhlický, D., Nesvorný, D., & Bottke, W. F. 2003, Nature, 425, 147
Warner, B. D. 1999, Minor Planet Bulletin, 26, 31
Warner, B. 2000, Minor Planet Bulletin, 27, 4
Warner, B. 2001, Minor Planet Bulletin, 28, 4
Warner, B. D. 2005a, Minor Planet Bulletin, 32, 29
Warner, B. D. 2005b, Minor Planet Bulletin, 32, 54
Warner, B. D. 2005c, Minor Planet Bulletin, 32, 4
Warner, B. D. 2006a, Minor Planet Bulletin, 33, 82
Warner, B. D. 2006b, Minor Planet Bulletin, 33, 58
Warner, B. D. 2006c, Minor Planet Bulletin, 33, 85
Warner, B. D. 2006d, Minor Planet Bulletin, 33, 35
Warner, B. D. 2007a, Minor Planet Bulletin, 34, 72
Warner, B. D. 2007b, Minor Planet Bulletin, 34, 104
Warner, B. D. 2008a, Minor Planet Bulletin, 35, 56
Warner, B. D. 2008b, Minor Planet Bulletin, 35, 163
Warner, B. D. 2009a, Minor Planet Bulletin, 36, 109
Warner, B. D. 2009b, Minor Planet Bulletin, 36, 7
Warner, B. D. 2009c, Minor Planet Bulletin, 36, 172
Warner, B. D. 2010a, Minor Planet Bulletin, 37, 112
Warner, B. D. 2010b, Minor Planet Bulletin, 37, 24
Warner, B. D. 2010c, Minor Planet Bulletin, 37, 57
Warner, B. D. 2010d, Minor Planet Bulletin, 37, 127
Warner, B. D. 2011a, Minor Planet Bulletin, 38, 142
Warner, B. D. 2011b, Minor Planet Bulletin, 38, 25
Warner, B. D. 2011c, Minor Planet Bulletin, 38, 63
Warner, B. D. 2012a, Minor Planet Bulletin, 39, 158
Warner, B. D. 2012b, Minor Planet Bulletin, 39, 16
Warner, B. D. 2012c, Minor Planet Bulletin, 39, 69
Warner, B. D. 2012d, Minor Planet Bulletin, 39, 245
Warner, B. D. 2013a, Minor Planet Bulletin, 40, 71
Warner, B. D. 2013b, Minor Planet Bulletin, 40, 137
Warner, B. D. 2014a, Minor Planet Bulletin, 41, 27
Warner, B. D. 2014b, Minor Planet Bulletin, 41, 144
Warner, B. D. 2015a, Minor Planet Bulletin, 42, 54
Warner, B. D. 2015b, Minor Planet Bulletin, 42, 115
Warner, B. D. 2015c, Minor Planet Bulletin, 42, 132
Warner, B. D., Shepard, M. K., Harris, A. W., et al. 2006, Minor Planet Bulletin, 33, 102
Warner, B. D., Behrend, R., Poncy, R., & Coliac, J.-F. 2008a, Minor Planet Bulletin, 35, 25
Warner, B. D., Durech, J., Fauerbach, M., & Marks, S. 2008b, Minor Planet Bulletin, 35, 167
Warner, B. D., Harris, A. W., & Pravec, P. 2009, Icarus, 202, 134
Warner, B. D., Stephens, R. D., & Harris, A. W. 2011, Minor Planet Bulletin, 38, 172
Warner, B. D., Harris, A. W., Stephens, R. D., & Coley, D. 2014, in AAS/Division for Planetary Sciences Meeting Abstracts, 46, 509.12

[1] Centre National d'Études Spatiales, 2 place Maurice Quentin 75039 Paris Cedex 01, France
e-mail: hanus.home@gmail.com
[2] Laboratoire Lagrange, UMR7293, Université de la Côte d'Azur, CNRS, Observatoire de la Côte d'Azur, Blvd de l'Observatoire, CS 34229, 06304 Nice Cedex 4, France
[3] Astronomical Institute, Faculty of Mathematics and Physics, Charles University in Prague, V Holešovičkách 2, 18000 Prague, Czech Republic
[4] Astronomical Observatory Institute, Faculty of Physics, A. Mickiewicz University, Słoneczna 36, 60-286 Poznań, Poland
[5] Geneva Observatory, 1290 Sauverny, Switzerland
[6] Aix Marseille Université, CNRS, OHP (Observatoire de Haute Provence), Institut Pythéas (UMS 3470), 04870 Saint-Michel-l'Observatoire, France
[7] Centre for Science at Extreme Conditions, The University of Edinburgh, Erskine Williamson Building, Peter Guthrie Tait Road, Edinburgh, EH9 3FD, UK
[8] Association T60, Observatoire du Pic du Midi, 65200 Bagnères-de-Bigorre, France
[9] Observatoire des Hauts Patys, 84410 Bédoin, France
[10] Observatoire de Chinon, Mairie de Chinon, 37500 Chinon, France
[11] Villefagnan Observatory, France
[12] Harfleur Observatory, France
[13] 490 chemin du gonnet, 38440 Saint Jean de Bournay, France
[14] Observatoire des Engarouines, 1606 chemin de Rigoy, 84570 Malemort-du-Comtat, France
[15] Collonges Observatory, 90 allée des résidences, 74160 Collonges, France
[16] SUPA, School of Physics & Astronomy, North Haugh, St Andrews, KY16 9SS, UK
[17] Via Capote Observatory, Thousand Oaks, CA 91320, USA
[18] Le Florian, Villa 4, 880 chemin de Ribac-Estagnol, 06600 Antibes, France
[19] Observatoire de Dauban, 04150 Banon, France
[20] Levendaal Observatory, Uiterstegracht 48, 2312 TE Leiden, The Netherlands
[21] European Southern Observatory, La Silla, Coquimbo, Chile
[22] Eurac Observatory, Bolzano/Bozen, Italy
[23] Vallemare di Bordona, Rieti, Italy
[24] Observatorio Astronómico Caimari, 07144 Costitx, Spain
[25] Observatoire de Durtal, 49430 Durtal, France
[26] OAM - Mallorca, 07144 Costitx, Spain
[27] 20 parc des Pervenches, 13012 Marseille, France
[28] Agrupación Astronómica de Sabadell, Apartado de Correos 50, PO Box 50, 08200 Sabadell, Barcelona, Spain
[29] Observatorio El Vendrell, 1193 Trragona, Spain
[30] AFOEV (Association Française des Observateurs d'Etoiles Variables), Observatoire de Strasbourg 11, rue de l'Université, 67000 Strasbourg, France
[31] Observatori d'Ager, 08014 Barcelona, Spain
[32] Stazione Astronomica di Sozzago, 28060 Sozzago, Italy
[33] Santa Lucia Stroncone, 05039 Stroncone, Italy
[34] Institut d'Astrophysique de l'Université Liège, Allèe du 6 Aout 17, 4000 Liège, Belgium
[35] Haleakala-Faulkes Telescope North, Hawaii, USA
[36] Seine-Maritime, Le Havre, 76600 Haute-Normandie, France
[37] Village-Neuf Observatory, 9bis rue du Sauvage, 68300 Saint-Louis, France
[38] Mt. Suhora Observatory, Pedagogical University. Podchorążych 2, 30-084, Cracow, Poland
[39] Shed of Science Observatory, 5213 Washburn Ave. S, Minneapolis, MN 55410, USA
[40] Waterlooville, UK
[41] Observatoire St-Martin, 31 grande rue, 25330 Amathay Vésigneux, France
[42] Observatorio CEAM, Caimari, Canary Islands, Spain
[43] Florida Gulf Coast University, 10501 FGCU Boulevard South, Fort Myers, FL 33965, USA
[44] Observatoire du Bois de Bardon, 16110 Taponnat, France
[45] Association T60, 14 avenue Edouard Belin, 31400 Toulouse, France
[46] Osservatorio l'Ampolla, Tarragona, Spain
[47] International Occultation Timing Association, Montgomery, AL, USA
[48] Club d'Astronomie de Lyon Ampere (CALA), Place de la Nation, 69120 Vaulx-en-Velin, France
[49] Linhaceira Observatory, Portugal
[50] Hong Kong Space Museum, Tsimshatsui, Hong Kong, PR China
[51] Institute of Planetary Research, German Aerospace Center, Rutherfordstrasse 2, 12489 Berlin, Germany
[52] Astroqueyras, Mairie, 05350 Saint-Véran, France
[53] 51 Centre astronomique de la Couyère, La Ville d'ABas, 35320 La Couyère, France
[54] Hunters Hill Observatory, 7 Mawalan Street, Ngunnawal ACT 2913, Australia

[55] Observatoire des Terres Blanches, 04110 Reillanne, France
[56] Department of Physics, University of Strathclyde, 16 Richmond Street, Glasgow G1 1XQ, UK
[57] Guitalens Observatory, 5 chemin d'En Combes, 81220 Guitalens, France
[58] Observatoire Les Makes, G. Bizet 18, 97421 La Rivière, France
[59] 980 Antelope Drive West, Bennett, CO 80102, USA
[60] Institute of Astronomy of Kharkiv Karazin National University, Kharkiv 61022, Sumska Str. 35, Ukraine
[61] Severní 765, 50003 Hradec Králové, Czech republic
[62] Uranoscope, Avenue Carnot 7, 77220 Gretz-Armainvilliers, France
[63] Observatoire OPERA, France
[64] Instituto de Astrofísica de Andalucía, CSIC, Apdo. 9481, 08080 Barcelona, Spain
[65] Mulheim-Ruhr, Germany
[66] Tzec Maun Foundation Observatory, Mayhill, New Mexico, US
[67] Observatorio Montcabrer, C/Jaume Balmes nb 24, Cabrils 08348 Barcelona, Spain
[68] Kingsgrove, NSW, Australia
[69] Sant Gervasi Observatory, 08022 Barcelona, Spain
[70] 4438 Organ Mesa Loop, Las Cruces, NM 88011, USA
[71] Rue des Ecoles 2, 34920 Le Crès, France
[72] 11 rue François-Nouteau, 49650 Brain-sur-Allonnes, France
[73] Ottmarsheim Observatory, 5 rue du Lièvre, 68490 Ottmarsheim, France
[74] Université Claude BERNARD Lyon 1. Observatoire de Pommier, POMMIER, 63230 Chapdes-Beaufort, France
[75] 4 rue de la Bruyère, 37500 La Roche Clermault, France
[76] Observatoire de Blauvac, 293 chemin de St Guillaume, 84570 Blauvac, France
[77] Shadowbox Observatory, 12745 Crescent Drive, Carmel, IN 46032, USA
[78] Lowell Observatory, Flagstaff, AZ 86001, USA
[79] Savigny-le-Temple, France
[80] Observatorio Amanecer de Arrakis, MPC274 Alcalá de Guadaíra, Sevilla, Spain
[81] Gnosca Observatory, 6525 Gnosca, Switzerland
[82] DeKalb Observatory, 2507 CR 60, Auburn, IN 46706, USA
[83] Center for Solar System Studies, 9302 Pittsburgh Ave, Suite 105, Rancho Cucamonga, CA 91730, USA
[84] School of Physics and Astronomy, University of Edinburgh, James Clerk Maxwell Building, Peter Guthrie Tait Road, Edinburgh, EH9 3FD, UK
[85] European Space Astronomy Centre, ESA, PO Box 78, 28691 Villanueva de la Cañada, Madrid, Spain
[86] Ironwood North, Hawaii, USA
[87] Centre de Recherche en Astronomie, Astrophysique et Géophysique, BP 63 Bouzereah, Algiers
[88] Astronomical Observatory of Jagiellonian University, ul. Orla 171, 30-244 Kraków, Poland

Bibliography

[Agnew 83] SF Agnew, BI Swanson, LH Jones, RL Mills & D Schiferl. *Chemistry of nitrogen oxide (N_2O_4) at high pressure: observation of a reversible transformation between molecular and ionic crystalline forms.* The Journal of Physical Chemistry, vol. 87, no. 25, pages 5065–5068, 1983.

[Agnew 85] Stephan F Agnew, BI Swanson, LH Jones & RL Mills. *Disproportionation of nitric oxide at high pressure.* The Journal of Physical Chemistry, vol. 89, no. 9, pages 1678–1682, 1985.

[Akahama 95] Yuichi Akahama, Haruki Kawamura, Daniel Häusermann, Michael Hanfland & Osamu Shimomura. *New high-pressure structural transition of oxygen at 96 GPa associated with metallization in a molecular solid.* Physical review letters, vol. 74, no. 23, page 4690, 1995.

[Akahama 96] Yuichi Akahama & Haruki Kawamura. *High-pressure Raman spectroscopy of solid oxygen.* Physical Review B, vol. 54, no. 22, page R15602, 1996.

[Akahama 00] Yuichi Akahama & Haruki Kawamura. *High-pressure infrared spectroscopy of solid oxygen.* Physical Review B, vol. 61, no. 13, page 8801, 2000.

[Akahama 01] Yuichi Akahama, Haruki Kawamura & Osamu Shimomura. *Structural phase transitions of solid oxygen at low temperature and high pressure.* Physical Review B, vol. 64, no. 5, page 054105, 2001.

[Akahama 07] Yuichi Akahama & Haruki Kawamura. *Diamond anvil Raman gauge in multimegabar pressure range.* High Pressure Research, vol. 27, no. 4, pages 473–482, 2007.

[Akahama 10a] Yuichi Akahama & Haruki Kawamura. *Pressure calibration of diamond anvil Raman gauge to 410 GPa.* In

Journal of Physics: Conference Series, volume 215, page 012195. IOP Publishing, 2010.

[Akahama 10b] Yuichi Akahama, Manabu Nishimura, Haruki Kawamura, Naohisa Hirao, Yasuo Ohishi & Kenichi Takemura. *Evidence from x-ray diffraction of orientational ordering in phase III of solid hydrogen at pressures up to 183 GPa.* Physical Review B, vol. 82, no. 6, page 060101, 2010.

[Akahama 14] Yuichi Akahama, Takeo Maekawa, Toshiyuki Sugimoto, Hiroshi Fujihisa, Naohisa Hirao & Yasuo Ohishi. *High-pressure phase diagram of N_2 and O_2 binary system: formation of kagome-lattice of O_2.* In Journal of Physics: Conference Series, volume 500, page 182001. IOP Publishing, 2014.

[Akahama 16] Y Akahama, D Ishihara, H Yamashita, H Fujihisa, N Hirao & Y Ohishi. *Phase stability and magnetic behavior of hexagonal phase of N_2-O_2 system with kagome lattice under high pressure and low temperature.* Physical Review B, vol. 94, no. 6, page 064104, 2016.

[Baer 89] Bruce J Baer & Malcolm Nicol. *New phase of an oxygen-nitrogen alloy at high pressure and room temperature detected by Raman spectroscopy.* The Journal of Physical Chemistry, vol. 93, no. 5, pages 1683–1687, 1989.

[Baer 90] Bruce J Baer & Malcolm Nicol. *High-pressure binary phase diagram of nitrogen-oxygen at 295 K determined by Raman spectroscopy.* Journal of Physical Chemistry, vol. 94, no. 3, pages 1073–1078, 1990.

[Barbee III 93] TW Barbee III. *Metastability of atomic phases of nitrogen.* Physical Review B, vol. 48, no. 13, page 9327, 1993.

[Barrett 67] CS Barrett, L Meyer & J Wasserman. *Antiferromagnetic and Crystal Structures of Alpha-Oxygen.* The Journal of Chemical Physics, vol. 47, no. 2, pages 592–597, 1967.

[Bini 00] Roberto Bini, Lorenzo Ulivi, Jörg Kreutz & Hans J Jodl. *High-pressure phases of solid nitrogen by Raman and infrared spectroscopy.* The Journal of Chemical Physics, vol. 112, no. 19, pages 8522–8529, 2000.

[Boehler 00] Rev Boehler. *High-pressure experiments and the phase diagram of lower mantle and core materials.* Reviews of Geophysics, vol. 38, no. 2, pages 221–245, 2000.

[Boehler 04] Reinhard Boehler & Koen De Hantsetters. *New anvil designs in diamond-cells.* High Pressure Research, vol. 24, no. 3, pages 391–396, 2004.

[Boehler 06] Reinhard Boehler. *New diamond cell for single-crystal x-ray diffraction.* Review of Scientific Instruments, vol. 77, no. 11, page 115103, 2006.

[Bolduan 84] F Bolduan, HJ Jodl & A Loewenschuss. *Raman study of solid N2O4: temperature induced autoionization.* The Journal of chemical physics, vol. 80, no. 5, pages 1739–1743, 1984.

[Burakhovich 77] IA Burakhovich, IN Krupskii, AI Prokhvatilov, Yu A Freiman & AI Erenburg. *Elementary excitation spectrum and phase transitions of solid oxygen.* JETP Lett, vol. 25, no. 1, 1977.

[Cromer 81] Don T Cromer, Robert L Mills, D Schiferi & Larry A Schwalbe. *The structure of N2 at 49 kbar and 299 K.* Acta Crystallographica Section B: Structural Crystallography and Crystal Chemistry, vol. 37, no. 1, pages 8–11, 1981.

[Dalladay-Simpson 16] Philip Dalladay-Simpson, Ross T Howie & Eugene Gregoryanz. *Evidence for a new phase of dense hydrogen above 325 gigapascals.* Nature, vol. 529, no. 7584, page 63, 2016.

[Damde 98] Klaus Damde & Hans-Jörg Jodl. *Mixtures of (N 2) 1- x:(O 2) x at High Pressures and Low Temperatures.* Journal of low temperature physics, vol. 111, no. 3-4, pages 327–337, 1998.

[Desgreniers 90] Serge Desgreniers, Yogesh K Vohra & Arthur L Ruoff. *Optical response of very high density solid oxygen to 132 GPa.* Journal of Physical Chemistry, vol. 94, no. 3, pages 1117–1122, 1990.

[Donohue 61] J Donohue. *A refinement of the positional parameter in α-nitrogen.* Acta Crystallographica, vol. 14, no. 9, pages 1000–1001, 1961.

[Drummond 15] Neil D Drummond, Bartomeu Monserrat, Jonathan H Lloyd-Williams, P López Ríos, Chris J Pickard & Richard James Needs. *Quantum Monte Carlo study of the phase diagram of solid molecular hydrogen at extreme pressures.* Nature communications, vol. 6, page 7794, 2015.

[Dubrovinsky 12] Leonid Dubrovinsky, Natalia Dubrovinskaia, Vitali B Prakapenka & Artem M Abakumov. *Implementation of micro-ball nanodiamond anvils for high-pressure studies above 6 Mbar.* Nature communications, vol. 3, page 1163, 2012.

[Dubrovinsky 15] L Dubrovinsky, N Dubrovinskaia, E Bykova, M Bykov, V Prakapenka, C Prescher, K Glazyrin, H-P Liermann, M Hanfland, Marcus Ekholm*et al.* *The most incompressible metal osmium at static pressures above 750 gigapascals.* Nature, vol. 525, no. 7568, page 226, 2015.

[Dunstan 89] DJ Dunstan. *Theory of the gasket in diamond anvil high-pressure cells.* Review of Scientific Instruments, vol. 60, no. 12, pages 3789–3795, 1989.

[Eremets 96] MI Eremets. High pressure experimental methods. Oxford University Press, 1996.

[Eremets 01] Mikhail I Eremets, Russell J Hemley, Ho-kwang Mao & Eugene Gregoryanz. *Semiconducting non-molecular nitrogen up to 240 GPa and its low-pressure stability.* Nature, vol. 411, no. 6834, page 170, 2001.

[Eremets 04a] MI Eremets, AG Gavriliuk, NR Serebryanaya, IA Trojan, DA Dzivenko, R Boehler, HK Mao & RJ Hemley. *Structural transformation of molecular nitrogen to a single-bonded atomic state at high pressures.* The Journal of chemical physics, vol. 121, no. 22, pages 11296–11300, 2004.

[Eremets 04b] Mikhail I Eremets, Alexander G Gavriliuk, Ivan A Trojan, Dymitro A Dzivenko & Reinhard Boehler. *Single-bonded cubic form of nitrogen.* Nature materials, vol. 3, no. 8, page 558, 2004.

[Eremets 07] MI Eremets, AG Gavriliuk & IA Trojan. *Single-crystalline polymeric nitrogen.* Applied physics letters, vol. 90, no. 17, page 171904, 2007.

[Eremets 11] MI Eremets & IA Troyan. *Conductive dense hydrogen.* Nature materials, vol. 10, no. 12, page 927, 2011.

[Fahlman 11] Bradley D Fahlman. *Nanomaterials.* In Materials Chemistry, pages 457–583. Springer, 2011.

[Forman 72] Richard A Forman, Gasper J Piermarini, J Dean Barnett & Stanley Block. *Pressure measurement made by the utilization of ruby sharp-line luminescence.* Science, vol. 176, no. 4032, pages 284–285, 1972.

[Freiman 04] Yu A Freiman & Hans-Jörg Jodl. *Solid oxygen.* Physics Reports, vol. 401, no. 1-4, pages 1–228, 2004.

[Frost 16] Mungo Frost, Ross T Howie, Philip Dalladay-Simpson, Alexander F Goncharov & Eugene Gregoryanz. *Novel high-pressure nitrogen phase formed by compression at low temperature.* Physical Review B, vol. 93, no. 2, page 024113, 2016.

[Fujihisa 06] Hiroshi Fujihisa, Yuichi Akahama, Haruki Kawamura, Yasuo Ohishi, Osamu Shimomura, Hiroshi Yamawaki, Mami Sakashita, Yoshito Gotoh, Satoshi Takeya & Kazumasa Honda. *O_8 cluster structure of the epsilon phase of solid oxygen.* Physical review letters, vol. 97, no. 8, page 085503, 2006.

[Goettel 89] Kenneth A Goettel, Jon H Eggert, Isaac F Silvera & William C Moss. *Optical evidence for the metallization of xenon at 132 (5) GPa.* Physical review letters, vol. 62, no. 6, page 665, 1989.

[Goncharenko 05] Igor N Goncharenko. *Evidence for a magnetic collapse in the epsilon phase of solid oxygen.* Physical review letters, vol. 94, no. 20, page 205701, 2005.

[Goncharov 98] Alexander F Goncharov, Russell J Hemley, Ho-kwang Mao & Jinfu Shu. *New high-pressure excitations in parahydrogen.* Physical review letters, vol. 80, no. 1, page 101, 1998.

[Goncharov 00] Alexander F Goncharov, Eugene Gregoryanz, Ho-kwang Mao, Zhenxian Liu & Russell J Hemley. *Optical evidence for a nonmolecular phase of nitrogen above 150 GPa.* Physical review letters, vol. 85, no. 6, page 1262, 2000.

[Goncharov 03] Alexander F Goncharov, Eugene Gregoryanz, Russell J Hemley & Ho-kwang Mao. *Molecular character of the metallic high-pressure phase of oxygen.* Physical Review B, vol. 68, no. 10, page 100102, 2003.

[Goncharov 08] Alexander F Goncharov, Jonathan C Crowhurst, Viktor V Struzhkin & Russell J Hemley. *Triple point on the melting curve and polymorphism of nitrogen at high pressure.* Physical review letters, vol. 101, no. 9, page 095502, 2008.

[Goncharov 11] Alexander F Goncharov, N Subramanian, TR Ravindran, Maddury Somayazulu, Vitali B Prakapenka & Russell J Hemley. *Polymorphism of dense, hot oxygen.* The Journal of chemical physics, vol. 135, no. 8, page 084512, 2011.

[Gorelli 99] Federico A Gorelli, Lorenzo Ulivi, Mario Santoro & Roberto Bini. *The ε phase of solid oxygen: evidence of an O_4 molecule lattice.* Physical review letters, vol. 83, no. 20, page 4093, 1999.

[Gorelli 00] Federico A Gorelli, Lorenzo Ulivi, Mario Santoro & Roberto Bini. *Antiferromagnetic order in the δ phase of solid oxygen.* Physical Review B, vol. 62, no. 6, page R3604, 2000.

[Gorelli 01] Federico A Gorelli, Lorenzo Ulivi, Mario Santoro & Roberto Bini. *Spectroscopic study of the ε phase of solid oxygen.* Physical Review B, vol. 63, no. 10, page 104110, 2001.

[Gorelli 02] Federico A Gorelli, Mario Santoro, Lorenzo Ulivi & Michael Hanfland. *Crystal structure of solid oxygen at high pressure and low temperature.* Physical Review B, vol. 65, no. 17, page 172106, 2002.

[Gregoryanz 01] Eugene Gregoryanz, Alexander F Goncharov, Russell J Hemley & Ho-kwang Mao. *High-pressure amorphous nitrogen.* Physical Review B, vol. 64, no. 5, page 052103, 2001.

[Gregoryanz 02] Eugene Gregoryanz, Alexander F Goncharov, Russell J Hemley, Ho-kwang Mao, Maddury Somayazulu & Guoyin Shen. *Raman, infrared, and x-ray evidence for new phases of nitrogen at high pressures and temperatures.* Physical Review B, vol. 66, no. 22, page 224108, 2002.

[Gregoryanz 07] Eugene Gregoryanz, Alexander F Goncharov, Chrystele Sanloup, Maddury Somayazulu, Ho-kwang Mao & Russell J Hemley. *High P-T transformations of nitrogen to 170 GPa.* The Journal of chemical physics, vol. 126, no. 18, page 184505, 2007.

[Hanfland 85] M Hanfland & K Syassen. *A Raman study of diamond anvils under stress.* Journal of applied physics, vol. 57, no. 8, pages 2752–2756, 1985.

[Hanfland 92] M Hanfland, RJ Hemley, HK Mao & GP Williams. *Synchrotron infrared spectroscopy at megabar pressures: vibrational dynamics of hydrogen to 180 GPa.* Physical review letters, vol. 69, no. 7, page 1129, 1992.

[Hanfland 98] M Hanfland, M Lorenzen, C Wassilew-Reul & F Zontone. *Structures of molecular nitrogen at high pressures.* The Review of High Pressure Science and Technology, vol. 7, pages 787–789, 1998.

[Hazen 87] RM Hazen, HK Mao, LW Finger & RJ Hemley. *Single-crystal x-ray diffraction of n-H 2 at high pressure.* Physical Review B, vol. 36, no. 7, page 3944, 1987.

[Hemley 90] RJ Hemley, HK Mao & JF Shu. *Low-frequency vibrational dynamics and structure of hydrogen at megabar pressures.* Physical review letters, vol. 65, no. 21, page 2670, 1990.

[Hemley 93] Russell J Hemley, Jon H Eggert & Ho-kwang Mao. *Low-frequency Raman spectroscopy of deuterium to megabar pressures at 77-295 K.* Physical Review B, vol. 48, no. 9, page 5779, 1993.

[Hemley 00] Russell J Hemley & Przemyslaw Dera. *Molecular crystals.* Reviews in Mineralogy and Geochemistry, vol. 41, no. 1, pages 335–419, 2000.

[Howie 12a] Ross T Howie, Christophe L Guillaume, Thomas Scheler, Alexander F Goncharov & Eugene Gregoryanz. *Mixed molecular and atomic phase of dense hydrogen.* Physical Review Letters, vol. 108, no. 12, page 125501, 2012.

[Howie 12b] Ross T Howie, Thomas Scheler, Christophe L Guillaume & Eugene Gregoryanz. *Proton tunneling in phase IV of hydrogen and deuterium.* Physical Review B, vol. 86, no. 21, page 214104, 2012.

[Howie 13] Ross T Howie, Eugene Gregoryanz & Alexander F Goncharov. *Hydrogen (deuterium) vibron frequency as a pressure comparison gauge at multi-Mbar pressures.* Journal of Applied Physics, vol. 114, no. 7, page 073505, 2013.

[Iota 04] V Iota, JH Park & CS Yoo. *Phase diagram of nitrous oxide: Analogy with carbon dioxide.* Physical Review B, vol. 69, no. 6, page 064106, 2004.

[Jodl 85] HJ Jodl, F Bolduan & HD Hochheimer. *Pressure dependence of intramolecular and intermolecular mode frequencies in solid oxygen determined by Raman studies.* Physical Review B, vol. 31, no. 11, page 7376, 1985.

[Jordan 64] TH Jordan, WD Streib, HW Smith & WN Lipscomb. *Single-crystal studies of β-F_2 and of γ-O_2.* Acta Crystallographica, vol. 17, no. 6, pages 777–778, 1964.

[Kolos 68a] W Kolos & L Wolniewicz. *Improved theoretical ground-state energy of the hydrogen molecule.* The Journal of Chemical Physics, vol. 49, no. 1, pages 404–410, 1968.

[Kolos 68b] W Kolos & L Wolniewicz. *Vibrational and rotational energies for the B 1 Σ u+, C 1 Π u, and a 3 Σ g+ states of the hydrogen molecule.* The Journal of Chemical Physics, vol. 48, no. 8, pages 3672–3680, 1968.

[Kotakoski 08] J Kotakoski & K Albe. *First-principles calculations on solid nitrogen: A comparative study of high-pressure phases.* Physical Review B, vol. 77, no. 14, page 144109, 2008.

[Kranendonk 66] J Van Kranendonk & VF Sears. *Theory of the interaction between the lattice vibrations and the rotational motion in solid hydrogen.* Canadian Journal of Physics, vol. 44, no. 2, pages 313–335, 1966.

[Kuznetsov 09] A Yu Kuznetsov, L Dubrovinsky, A Kurnosov, MM Lucchese, W Crichton & CA Achete. *High-Pressure Synthesis and Study of and Ionic Solids.* Advances in Physical Chemistry, vol. 2009, 2009.

[Landsberg 28] Gr Landsberg & L Mandelstam. *Über die lichtzerstreuung in kristallen.* Zeitschrift für Physik, vol. 50, no. 11-12, pages 769–780, 1928.

[Letoullec 88] R Letoullec, JP Pinceaux & P Loubeyre. *The membrane diamond anvil cell: a new device for generating continuous pressure and temperature variations.* International Journal of High Pressure Research, vol. 1, no. 1, pages 77–90, 1988.

[Lewis 92] Steven P Lewis & Marvin L Cohen. *High-pressure atomic phases of solid nitrogen.* Physical Review B, vol. 46, no. 17, page 11117, 1992.

[Li 15] Dongxu Li, Artem R Oganov, Xiao Dong, Xiang-Feng Zhou, Qiang Zhu, Guangrui Qian & Huafeng Dong. *Nitrogen oxides under pressure: stability, ionization, polymerization, and superconductivity.* Scientific reports, vol. 5, page 16311, 2015.

[Lipp 07] Magnus J Lipp, J Park Klepeis, BJ Baer, Hyunchae Cynn, William J Evans, Valentin Iota & C-S Yoo. *Transformation of molecular nitrogen to nonmolecular phases at megabar pressures by direct laser heating.* Physical Review B, vol. 76, no. 1, page 014113, 2007.

[Liu 17] Xiao-Di Liu, Ross T Howie, Hui-Chao Zhang, Xiao-Jia Chen & Eugene Gregoryanz. *High-Pressure Behavior of Hydrogen and Deuterium at Low Temperatures.* Physical review letters, vol. 119, no. 6, page 065301, 2017.

[Lorenzana 90] Hector E Lorenzana, Isaac F Silvera & Kenneth A Goettel. *Orientational phase transitions in hydrogen at megabar pressures.* Physical review letters, vol. 64, no. 16, page 1939, 1990.

[Loubeyre 96] Paul Loubeyre. *Compounds of simple molecular systems at high pressure.* International Journal of High Pressure Research, vol. 14, no. 4-6, pages 353–361, 1996.

[Lundegaard 06] Lars F Lundegaard, Gunnar Weck, Malcolm I McMahon, Serge Desgreniers & Paul Loubeyre. *Observation of an O_8 molecular lattice in the ϵ-phase of solid oxygen.* Nature, vol. 443, no. 7108, page 201, 2006.

[Lundegaard 09] Lars F Lundegaard, Christophe Guillaume, Malcolm I McMahon, Eugene Gregoryanz & Marco Merlini. *On the structure of high-pressure high-temperature η-O_2.* The Journal of chemical physics, vol. 130, no. 16, page 164516, 2009.

[Ma 09] Yanming Ma, Artem R Oganov, Zhenwei Li, Yu Xie & Jani Kotakoski. *Novel high pressure structures of polymeric nitrogen.* Physical review letters, vol. 102, no. 6, page 065501, 2009.

[Mailhiot 92] C Mailhiot, LH Yang & AK McMahan. *Polymeric nitrogen.* Physical Review B, vol. 46, no. 22, page 14419, 1992.

[Manaa 05] M Riad Manaa. Chemistry at extreme conditions. Elsevier, 2005.

[Mao 76] Ho-Kwong Mao & Peter M Bell. *High-pressure physics: the 1-megabar mark on the ruby R1 static pressure scale.* Science, vol. 191, no. 4229, pages 851–852, 1976.

[Mao 94] Ho-kwang Mao & Russell J Hemley. *Ultrahigh-pressure transitions in solid hydrogen.* Reviews of modern physics, vol. 66, no. 2, page 671, 1994.

[Martin 86] Richard M Martin & Richard J Needs. *Theoretical study of the molecular-to-nonmolecular transformation of nitrogen at high pressures.* Physical Review B, vol. 34, no. 8, page 5082, 1986.

[Mattson 04] William D Mattson, Daniel Sanchez-Portal, Simone Chiesa & Richard M Martin. *Prediction of new phases of nitrogen at high pressure from first-principles simulations.* Physical review letters, vol. 93, no. 12, page 125501, 2004.

[Mazin 97] II Mazin, Russell J Hemley, AF Goncharov, Michael Hanfland & Ho-kwang Mao. *Quantum and classical orientational ordering in solid hydrogen.* Physical review letters, vol. 78, no. 6, page 1066, 1997.

[McMahan 85] AK McMahan & R LeSar. *Pressure dissociation of solid nitrogen under 1 Mbar.* Physical review letters, vol. 54, no. 17, page 1929, 1985.

[Meng 06] Yue Meng, Robert B Von Dreele, Brian H Toby, Paul Chow, Michael Y Hu, Guoyin Shen & Ho-kwang Mao. *Hard x-ray radiation induced dissociation of N_2 and O_2 molecules and the formation of ionic nitrogen oxide phases under pressure.* Physical Review B, vol. 74, no. 21, page 214107, 2006.

[Merrill 74] Leo Merrill & William A Bassett. *Miniature diamond anvil pressure cell for single crystal x-ray diffraction studies.* Review of Scientific Instruments, vol. 45, no. 2, pages 290–294, 1974.

[Mills 80] RL Mills, DH Liebenberg, JC Bronson & LC Schmidt. *Procedure for loading diamond cells with high-pressure gas.* Review of Scientific Instruments, vol. 51, no. 7, pages 891–895, 1980.

[Mills 86] RL Mills, Bart Olinger & DT Cromer. *Structures and phase diagrams of N_2 and CO to 13 GPa by x-ray diffraction.* The Journal of chemical physics, vol. 84, no. 5, pages 2837–2845, 1986.

[Mills 91] RL Mills, Bart Olinger, DT Cromer & R LeSar. *Crystal structures of N2O to 12 GPa by x-ray diffraction.* The Journal of chemical physics, vol. 95, no. 7, pages 5392–5398, 1991.

[Minenko 04] Maksym Minenko, Jörg Kreutz, Thorsten Hupprich & Hans-Jörg Jodl. *Raman Investigation of the N_2-O_2 Binary System as a Function of Pressure and Temperature.* The Journal of Physical Chemistry B, vol. 108, no. 20, pages 6429–6440, 2004.

[Nicol 79] Malcolm Nicol, KR Hirsch & Wilfried B Holzapfel. *Oxygen phase equilibria near 298 K.* Chemical Physics Letters, vol. 68, no. 1, pages 49–52, 1979.

[Pickard 07] Chris J Pickard & Richard J Needs. *Structure of phase III of solid hydrogen.* Nature Physics, vol. 3, no. 7, page 473, 2007.

[Pickard 09] Chris J Pickard & RJ Needs. *High-pressure phases of nitrogen.* Physical review letters, vol. 102, no. 12, page 125702, 2009.

[Pickard 12] Chris J Pickard, Miguel Martinez-Canales & Richard J Needs. *Density functional theory study of phase IV of solid hydrogen.* Physical Review B, vol. 85, no. 21, page 214114, 2012.

[Piermarini 75] Ge J Piermarini, S Block, JD Barnett & RA Forman. *Calibration of the pressure dependence of the R 1 ruby fluorescence line to 195 kbar.* Journal of Applied Physics, vol. 46, no. 6, pages 2774–2780, 1975.

[Raman 28a] Chandrasekhara Venkata Raman & Kariamanikkam Srinivasa Krishnan. *A new type of secondary radiation.* Nature, vol. 121, no. 3048, page 501, 1928.

[Raman 28b] Chandrasekhara Venkata Raman & Kariamanikkam Srinivasa Krishnan. *The optical analogue of the Compton effect.* Nature, vol. 121, no. 3053, page 711, 1928.

[Rekhi 99] Sandeep Rekhi, Leonid S Dubrovinsky & Surendra K Saxena. *Temperature-induced ruby fluorescence shifts up to a pressure of 15 GPa in an externally heated diamond anvil cell.* High Temperatures-High Pressures, vol. 31, no. 3, pages 299–305, 1999.

[Rivers 08] Mark Rivers, Vitali B Prakapenka, Atsushi Kubo, Clayton Pullins, Christopher M Holl & Steven D Jacobsen. *The COMPRES/GSECARS gas-loading system for diamond anvil cells at the Advanced Photon Source.* High Pressure Research, vol. 28, no. 3, pages 273–292, 2008.

[Robertson 30] Robert Robertson & JJ Fox. *Infra-red spectrum of diamond by infra-red spectrometer and Raman methods.* Nature, vol. 125, no. 3158, page 704, 1930.

[Sanloup 13] Chrystèle Sanloup, James WE Drewitt, Zuzana Konôpková, Philip Dalladay-Simpson, Donna M Morton, Nachiketa Rai, Wim van Westrenen & Wolfgang Morgenroth. *Structural change in molten basalt at deep mantle conditions.* Nature, vol. 503, no. 7474, page 104, 2013.

[Santoro 04] Mario Santoro, Eugene Gregoryanz, Ho-kwang Mao & Russell J Hemley. *New phase diagram of oxygen at high pressures and temperatures.* Physical review letters, vol. 93, no. 26, page 265701, 2004.

[Schiferl 81] David Schiferl, DT Cromer & RL Mills. *Structure of O_2 at 5.5 GPa and 299 K.* Acta Crystallographica Section B: Structural Crystallography and Crystal Chemistry, vol. 37, no. 7, pages 1329–1332, 1981.

[Schiferl 83] David Schiferl, DT Cromer, Robert R Ryan, Allen C Larson, Richard LeSar & RL Mills. *Structure of N_2 at 2.94 GPa and 300 K.* Acta Crystallographica Section C: Crystal Structure Communications, vol. 39, no. 9, pages 1151–1153, 1983.

[Schuch 70] AF Schuch & RL Mills. *Crystal structures of the three modifications of nitrogen 14 and nitrogen 15 at high pressure.* The Journal of Chemical Physics, vol. 52, no. 12, pages 6000–6008, 1970.

[Shen 16] Guoyin Shen & Ho Kwang Mao. *High-pressure studies with x-rays using diamond anvil cells.* Reports on Progress in Physics, vol. 80, no. 1, page 016101, 2016.

[Shimizu 98] K Shimizu, K Suhara, M Ikumo, MI Eremets & K Amaya. *Superconductivity in oxygen.* Nature, vol. 393, no. 6687, page 767, 1998.

[Sihachakr 04] D Sihachakr & P Loubeyre. *N_2/O_2 mixtures under pressure: A structural study of the binary phase diagram at 295 K.* Physical Review B, vol. 70, no. 13, page 134105, 2004.

[Sihachakr 06] Davina Sihachakr & Paul Loubeyre. *High-pressure transformation of N_2/ O_2 mixtures into ionic compounds.* Physical Review B, vol. 74, no. 6, page 064113, 2006.

[Silvera 80] Isaac F Silvera. *The solid molecular hydrogens in the condensed phase: Fundamentals and static properties.* Reviews of Modern Physics, vol. 52, no. 2, page 393, 1980.

[Silvera 81] Isaac F Silvera & Rinke J Wijngaarden. *New low-temperature phase of molecular deuterium at ultrahigh pressure.* Physical Review Letters, vol. 47, no. 1, page 39, 1981.

[Smekal 23] Adolf Smekal. *Zur quantentheorie der dispersion.* Naturwissenschaften, vol. 11, no. 43, pages 873–875, 1923.

[Somayazulu 01] Maddury Somayazulu, Achintya Madduri, Alexander F Goncharov, Oliver Tschauner, Paul F McMillan, Ho-kwang Mao & Russell J Hemley. *Novel broken symmetry phase from N 2 O at high pressures and high temperatures.* Physical Review Letters, vol. 87, no. 13, page 135504, 2001.

[Song 03a] Yang Song, Russell J Hemley, Ho-kwang Mao, Zhenxian Liu & Dudley R Herschbach. *New phases of N_2O_4 at high pressures and high temperatures.* Chemical physics letters, vol. 382, no. 5-6, pages 686–692, 2003.

[Song 03b] Yang Song, Maddury Somayazulu, Ho-kwang Mao, Russell J Hemley & Dudley R Herschbach. *High-pressure structure and equation of state study of nitrosonium nitrate from synchrotron x-ray diffraction.* The Journal of chemical physics, vol. 118, no. 18, pages 8350–8356, 2003.

[Stinton 09] GW Stinton, I Loa, LF Lundegaard & MI McMahon. *The crystal structures of δ and δ nitrogen.* The Journal of Chemical Physics, vol. 131, no. 10, page 104511, 2009.

[Sun 13] Jian Sun, Miguel Martinez-Canales, Dennis D Klug, Chris J Pickard & Richard J Needs. *Stable all-nitrogen metallic salt at terapascal pressures.* Physical review letters, vol. 111, no. 17, page 175502, 2013.

[Tomasino 14] Dane Tomasino, Minseob Kim, Jesse Smith & Choong-Shik Yoo. *Pressure-induced symmetry-lowering transition in dense nitrogen to layered polymeric nitrogen (LP-N) with colossal Raman intensity.* Physical review letters, vol. 113, no. 20, page 205502, 2014.

[Uddin 06] Jamal Uddin, Verónica Barone & Gustavo E Scuseria. *Energy storage capacity of polymeric nitrogen.* Molecular Physics, vol. 104, no. 5-7, pages 745–749, 2006.

[Van Kranendonk 59] J Van Kranendonk. *Rotational and vibrational energy bands in solid hydrogen.* Physica, vol. 25, no. 7-12, pages 1080–1094, 1959.

[Van Kranendonk 83] Jan Van Kranendonk. *Solid hydrogen.* 1983.

[Vincenzo 13] Schettino Vincenzo & Bini Roberto. Materials under extreme conditions: molecular crystals at high pressure. World Scientific, 2013.

[Vos 91] Willem L Vos & Jan A Schouten. *On the temperature correction to the ruby pressure scale.* Journal of applied physics, vol. 69, no. 9, pages 6744–6746, 1991.

[Wang 10] Zhao Wang, Duanwei He, Wei Zhang, Wenqiang Li, Wenyong Li, Jiaqian Qin, Li Lei, Yongtao Zou & Xiangdong Yang. *Portable high pressure sapphire anvil cell for gas hydrates research.* Review of Scientific Instruments, vol. 81, no. 8, page 085102, 2010.

[Wang 12] Xiaoli Wang, Yanchao Wang, Maosheng Miao, Xin Zhong, Jian Lv, Tian Cui, Jianfu Li, Li Chen, Chris J Pickard & Yanming Ma. *Cagelike diamondoid nitrogen at high pressures.* Physical review letters, vol. 109, no. 17, page 175502, 2012.

[Webb 76] AW Webb, DU Gubser & LC Towle. *Cryostat for generating pressures to 100 kilobar and temperatures to 0.03 K.* Review of Scientific Instruments, vol. 47, no. 1, pages 59–62, 1976.

[Weck 02] G Weck, P Loubeyre & R LeToullec. *Observation of structural transformations in metal oxygen.* Physical review letters, vol. 88, no. 3, page 035504, 2002.

[Weck 17] Gunnar Weck, Frédéric Datchi, Gaston Garbarino, Sandra Ninet, Jean-Antoine Queyroux, Thomas Plisson, Mohamed Mezouar & Paul Loubeyre. *Melting Curve and Liquid Structure of Nitrogen Probed by X-ray Diffraction to 120 GPa.* Physical review letters, vol. 119, no. 23, page 235701, 2017.

[Weir 59] CE Weir, ER Lippincott, A Van Valkenburg & EN Bunting. *Infrared studies in the 1-to 15-micron region to 30,000 atmospheres.* J. Res. Natl. Bur. Stand. A, vol. 63, pages 55–62, 1959.

[Wolniewicz 66] L Wolniewicz. *Vibrational-rotational Study of the Electronic Ground State of the Hydrogen Molecule.* The Journal of Chemical Physics, vol. 45, no. 2, pages 515–523, 1966.

[Xu 86] JA Xu, HK Mao & PM Bell. *High-pressure ruby and diamond fluorescence: observations at 0.21 to 0.55 terapascal.* Science, vol. 232, no. 4756, pages 1404–1406, 1986.

[Xu 00] Ji-an Xu & Ho-kwang Mao. *Moissanite: A window for high-pressure experiments.* Science, vol. 290, no. 5492, pages 783–785, 2000.

[Yagi 01] Takehiko Yagi, Tadashi Kondo, Tetsu Watanuki, Osamu Shimomura & Takumi Kikegawa. *Laser heated diamond anvil apparatus at the Photon Factory and SPring-8: Problems and improvements.* Review of Scientific Instruments, vol. 72, no. 2, pages 1293–1297, 2001.

[Yao 08] Yansun Yao, S Tse John & Kaori Tanaka. *Metastable high-pressure single-bonded phases of nitrogen predicted via genetic algorithm.* Physical Review B, vol. 77, no. 5, page 052103, 2008.

[Yoo 03] CS Yoo, V Iota, H Cynn, M Nicol, JH Park, T Le Bihan & M Mezouar. *Disproportionation and other transformations of N_2O at high pressures and temperatures to lower energy, denser phases.* The Journal of Physical Chemistry B, vol. 107, no. 24, pages 5922–5925, 2003.

[Young 91] David A Young. Phase diagrams of the elements. Univ of California Press, 1991.

[Zahariev 05] F Zahariev, A Hu, J Hooper, F Zhang & T Woo. *Layered single-bonded nonmolecular phase of nitrogen from first-principles simulation.* Physical Review B, vol. 72, no. 21, page 214108, 2005.

Publications

J. Hudspeth, V. Afonina, B. Cochain, Z. Konopkova, G. Lelong, L. Cormier, C. Cavallari. "Polymerization of iron carbonate melts in the deep mantle." *Nature* , (Awaiting publication).

J. Binns, X.-D. Liu, P. Dalladay-Simpson, V. Afonina, E. Gregoryanz, and R.Howie. "Synthesis and stability of hydrogen iodide at high pressures." *Physical Review B*, **96**, 144105 (2017).

J. Hanus, J. Durech, V. Afonina et al. "New and updated convex shape models of asteroids based on optical data from a large collaboration network." *Astronomy and Astrophysics*, **586**, A108 (2016).